Quasar Cosmology and Physics

ELTVEDT, ALICE,MARILYN

Quasar Cosmology and Physics

Alice Eltvedt

Abstract: In this thesis, we develop the VST ATLAS Quasar Survey, based on the VST ATLAS+NEOWISE imaging surveys and consisting of $\sim 1,229,000$ quasar (QSO) candidates with $16 < g < 22.5$ over ~ 4700 deg^2. We also probe the halo mass profiles of galaxy clusters, galaxies and Luminous Red Galaxies (LRGs) via the gravitational lensing of background VST ATLAS quasars. We show that disagreement between various authors as to whether the results of such cross-correlations are in tension with ΛCDM depend on whether a standard model HOD is assumed rather than simply assuming that galaxies trace mass. In the case of galaxy clusters we find that their mass profiles are well fitted by HODs with a 1-halo term based on the NFW profile. In the case of galaxies, we find that their mass profiles may be marginally more poorly fitted by HOD's with 1-halo NFW profiles. In an attempt to study the 1-halo term directly, we measure the magnification bias of LRGs and find that the observed lensing amplitude may be too small to be explained by a standard HOD+NFW model at the smallest scales. We finally exploit the VST ATLAS QSO Survey to perform measurements of the QSO halo mass via the 2-point angular auto-correlation function and comparing with the mass clustering correlation function for the ΛCDM model, the cross-correlation with the Planck Cosmic Microwave Background (CMB) lensing convergence maps and scaling the model fits of comparable works, and finally by fitting HOD model parameters to our QSO auto-correlation function and from the derived QSO halo mass function estimating a QSO halo mass. These measurements give QSO halo masses of $M_{halo} = 8.5 \times 10^{11}\mathrm{h}^{-1}M_{\odot}$, $M_{halo} = 8.3 \times 10^{11}h^{-1}\mathrm{M}_{\odot}$, and $M_{halo} = 2.5 \times 10^{12}\mathrm{h}^{-1}M_{\odot}$ respectively. We further find that the sharp peak of our QSO halo mass function implies most ($\approx 2/3$) QSOs have halo masses within a factor of ≈ 3 of this average mass. Finally, we perform stacked reverberation mapping of QSOs in the eROSITA eFEDS field via optical to Broad Line cross-correlations and optical to X-ray cross-covariance. Simply by virtue of their existence, the $2-4\sigma$ peaks we find in these analyses provide further support for a narrow QSO black hole mass function. The continuum to Broad Line peak lags are 58 ± 39 days for H_{β}, 59 ± 28 days for MgII, 35 ± 25 days for CIV, and we see a peak at a continuum-X-ray lag of 35 ± 12 days at $3-4\sigma$ significance and a smoother more continuous feature is seen at negative lags between -100 and -10 days

at similarly high significance. The results for H_β and CIV are in good agreement with other authors while the MgII lag is somewhat lower in these data than previous estimates. The X-ray lags are unexpectedly high, and the sharp X-ray peak being close to the CIV lag seems to suggest that X-rays may be associated as much with Broad Line Region scales as those of an $\approx 10\times$ smaller accretion disk.

Quasar Cosmology and Physics

Alice Eltvedt

A thesis presented for the degree of
Doctor of Philosophy

Centre for Extragalactic Astronomy
Department of Physics
Durham University
United Kingdom

May 2024

Contents

List of Figures

List of Tables

Declaration

The work in this thesis is based on research carried out in the Centre for Extragalactic Astronomy, Department of Physics, Durham University, United Kingdom. No part of this thesis has been submitted elsewhere for any other degree or qualification and it is all my own work unless referenced to the contrary in the text.

The content presented in Chapter 2 has been published in the form of a paper:

Alice M Eltvedt, T Shanks, N Metcalfe, B Ansarinejad, L F Barrientos, R Sharp, U Malik, D N A Murphy, M Irwin, M Wilson, D M Alexander, Andras Kovacs, Juan Garcia-Bellido, Steven Ahlen, David Brooks, Axel de la Macorra, Andreu Font-Ribera, Satya Gontcho a Gontcho, Klaus Honscheid, Aaron Meisner, Ramon Miquel, Jundan Nie, Gregory Tarlé, Mariana Vargas-Magaña, Zhimin Zhou, **The VST ATLAS quasar survey I: Catalogue of photometrically selected quasar candidates**, *Monthly Notices of the Royal Astronomical Society*, Volume 521, Issue 3, May 2023, Pages 3384–3404, https://doi.org/10.1093/mnras/stad516

A previous version of the content presented in Chapters 2 and 3 has also been a part of my MSc by Research thesis (2020).

The contents of Chapters 3, 4, and 5 are in preparation for submission to MNRAS.

The author of this thesis was primarily responsible for all aspects of this publication. The work in Chapters 2, 3, 4, and 5 were carried out in collaboration so the pronoun 'we' is used, although the work was led by the author.

Acknowledgements

I would like to thank my supervisors Tom Shanks, Nigel Metcalfe, and Dave Alexander for all of the time and effort they took to teach and guide me throughout my PhD, sharing their wealth of knowledge and enthusiasm for research. Tom, thank you for constantly pushing me to improve. Your passion for research and hunger for uncovering potential new science has been an incredible motivation throughout these years and I feel lucky to have been able to spend this time working with you. Thank you for facilitating observing trips, conference talks, and ensuring that I would have every opportunity to learn and grow as a researcher and person.

I am also grateful to the Durham astronomy department for creating such a wonderful environment for my PhD. Thank you to Behzad for your constant support, friendship, help, and encouraging words whenever I needed them. Thank you to Ellen, Amy, Jake, Vicky, Jack, Lizelke, Miguel, Giorgio, Aidan, Joaquin, Matteo, Emmy, Makun, Carolina, and Willem for being the best group of people I could embark on this PhD with. Your friendships, the many days and evenings filled with long discussions, laughs, dancing, and maybe some crying, made the past years absolutely incredible. Thank you for sharing so many happy, stressful, tired, funny, and exciting moments with me!

Thank you Durham University Sport for your support throughout my PhD. Dave Caldwell, thank you for always making time to see me and offering so much encouragement. Thank you to the water polo team for creating such a fun and welcoming space to jump into.

I would like to thank all of my collaborators that I've worked with these past years. Thank you Alfredo for all of your observing help with DECam. I would especially like to thank Rob, Umang, and Harry in Australia. Thank you for your exceptional hospitality, warmth, delirious observing night games, and the fantastic roadtrip talks and playlists.

I wouldn't be at this point in my life without my family. I am so lucky to have the parents and siblings that I do who make me feel so incredibly loved and valued. Mami and Daddy,

you have always made me believe that I can do whatever I set my mind to. Thank you for providing me with unending love and support throughout my entire life. I have never once doubted that I can try anything, because you will always be there for me to pick me up, cheer me on, and make sure that I get up and try again. This PhD would have been very difficult had it not been for you letting me come home during the covid lockdowns, making sure that I have everything I need to keep working, taking me on fantastic adventures, and providing a loving space to thrive in. Mickey, thank you for all of the philosophical discussions, jokes, and for placing your trust in me with parts of your life as well. Maya, thank you for the unending laughs, baking experiences, photo opps, and friendship. Layla, your contagious happiness is remarkable. Thank you for being an unending source of love, kindness, and excitement.

Finally, I'd like to thank my husband, Oli. You have made my life so much better in every single way. You are the kindest, funniest, hard working, and loving partner. Thank you for taking care of me, for creating a loving home with me, and for supporting me. I could not be more grateful to experience life with you. I can't wait for everything that comes next for us.

Chapter 1

Introduction

1.1 Standard Cosmological Model

The currently accepted standard cosmological model developed from Einstein's (1917) theory of general relativity and Friedmann's (1922) model of an expanding universe. Underpinning such models is the Cosmological Principle, which assumes that the Universe is homogeneous and isotropic at large scales. The discovery of Hubble's law (Hubble, 1929) gave observational evidence supporting this model of an expanding universe. This law relates cosmological redshift to distance (Hubble, 1929) in the following manner:

$$z = \frac{H_0}{c} r \tag{1.1.1}$$

where z is redshift, c is the speed of light, r is distance, and H_0 is a constant called the Hubble constant. The value of H_0 has been a topic of debate, however most recent determinations put it at $\sim 70 \mathrm{kms}^{-1}\mathrm{Mpc}^{-1}$. As redshift is interpreted at $z << 1$ as a Doppler shift, where a redshift means an object is moving away from the observer and a blueshift means an object is moving towards the observer, Hubble's law can also be written as $v = zc = H_0 r$. Hubble's distance estimates of galaxies, plotted on what is called a Hubble diagram, showed the linear relation between distance and redshift. These observations have since been repeated many times with galaxies and supernovae. An updated figure showing these observations is shown in Figure 1.1, where distance is plotted on the x-axis and velocity on the y-axis.

The Cosmological Principle represents the start to solving Einstein's (1916) field equations, which relate the curvature of spacetime to the mass-energy in the universe. The Robertson-

Walker metric (also referred to as the Friedman-Lemaître-Robertson-Walker metric; (Robertson, 1935; Walker, 1937), was developed in the 1930's to describe this homogeneous and isotropic Universe and takes the form of a 4-dimensional metric with three spatial components and one time component. For general relativity, this metric, expressed in spherical coordinates is as follows (Peacock, 1999; Ryden, 2016):

$$ds^2 = -c^2dt^2 + a(t)^2[dr^2 + S_k^2(r)d\Psi^2] \tag{1.1.2}$$

where $-c^2dt^2$ is the time component, with c being the speed of light, and $a(t)^2[dr^2+S_k^2(r)d\Psi^2]$ is the spatial component. Here, $a(t) = \frac{1}{1+z}$, is a dimensionless scale factor that describes the expansion of the universe as a function of time and is set to $a(t_0) = 1$ at present time, t_0, where t is the cosmological proper time and r is the proper distance at time t_0. The $a(t)$ term is also related to the Hubble parameter as $H(t) = \frac{\dot{a}}{a}$. The $S_k^2(r)$ term describes the curvature of spacetime, and can be calculated for the three possibilities; $k = 0$ for a flat infinite space, $k = 1$ for a universe with positive curvature and therefore finite volume, and $k = -1$ for a universe with negative curvature and therefore infinite volume. The $d\Psi^2$ parameter is an angular function in spherical polars $d\Psi^2 = d\theta^2 + sin^2\theta d\phi^2$. The assumption of the Cosmological Principle means that the geometry of spacetime is described by $a(t)$ and k.

Derived from Einstein's (1916) Field Equations, Friedmann (1922) developed an exact relation between the parameters which relates the curvature of spacetime to the energy density, or contents, of the Universe. This Friedmann Equation, also referred to as the most important equation in cosmology, evaluated at present time ($t = t_0$) is as follows:

$$H_0^2 = (\frac{\dot{a}}{a})^2_{t=t_0} = \frac{8\pi G}{3c^2}\epsilon_0 - \frac{kc^2}{R_0^2} \tag{1.1.3}$$

Note that $\epsilon(t)$ represents the proper, as opposed to the comoving, energy density, with $\epsilon(t) \equiv \rho(t)c^2$.

Here, H_0^2 contains the velocity of expansion of the kinetic part of the universe, where H_0 is the Hubble constant. The first term on the right hand side of the equation describes the gravitational (potential) part of the universe. The total energy density of the universe is denoted by ϵ_0 and the $\frac{k}{R_0^2}$ term describes the magnitude of curvature of space. In the case where the universe is assumed to be spatially flat, the $\frac{kc^2}{R_0^2}$ term drops out. Therefore, the critical energy density of the universe can be defined as:

$$\epsilon_{crit}(t) = \frac{3}{8}\frac{H^2(t)}{\pi G} \tag{1.1.4}$$

There had been an addition of a cosmological constant to the Friedmann Equation, which adds $+\frac{\Lambda}{3}$ to the right hand side of Eq. 1.1.3. Einstein originally invoked the cosmological constant as without it, the universe couldn't be static. However, Einstein removed the cosmological constant after the discovery that the universe is actually expanding. This constant does return in various other cosmological models as well as with the addition of dark energy, but at a different value. As we can determine the Hubble constant to within a $\pm 5\%$ (Riess et al., 2022; Efstathiou et al., 2023), we can therefore calculate the associated critical density of the Universe. A dimensionless density parameter is then defined as the ratio of the density of the universe to the critical density:

$$\Omega(t) = \frac{\epsilon(t)}{\epsilon_c(t)} = \frac{8\pi G\epsilon(t)}{3H^2(t)} \tag{1.1.5}$$

The standard cosmological model is comprised of three energy density components. These components are matter density, $\Omega_M \sim \frac{\rho_m}{\rho_{crit}}$ (~ 0.3 today with a baryonic matter density of ~ 0.045), the dark energy density, Ω_Λ (~ 0.7 today), and the radiation density, Ω_{rad} ($\sim 8.5 \times 10^{-4}$ today). All three density parameters (matter, dark energy, and radiation) depend differently on the expansion rate of the universe, with the mass density, $\rho_m(z) \propto \rho_{m(0)}(1+z)^3$, radiation density $\rho_{rad}(z) \propto \rho_{rad(0)}(1+z)^4$, and dark energy density $\rho_\Lambda(z) \propto \rho_{\Lambda(0)}$ (see e.g. Peacock (1999), Ryden (2016)). Taking these parameters into account, we can rewrite the Friedmann Equation as:

$$H(z) = H_0[\Omega_{m,0}(1+z)^3 + \Omega_{\Lambda,0} + \Omega_{rad,0}(1+z)^4 + \Omega_{k,0}(1+z)^2]^{\frac{1}{2}} \tag{1.1.6}$$

The curvature component, $\Omega_{k,0}(1+z)^2$, is zero for a flat universe, however is relevant when looking at various other possible models of the universe. We can use Eq. 1.1.6 to model the expansion of the universe relative to time for various scenarios of the combination of cosmological parameters.

Evidence for the possible existence of dark matter was first noted by Zwicky (1933)) who observed a high velocity dispersion of galaxies in the Coma cluster, and then by Rubin et al. (1977) whose research showed that the flat rotation curves of galaxies require more mass to be present than is visible. It is now known that only a small fraction of the matter density is made

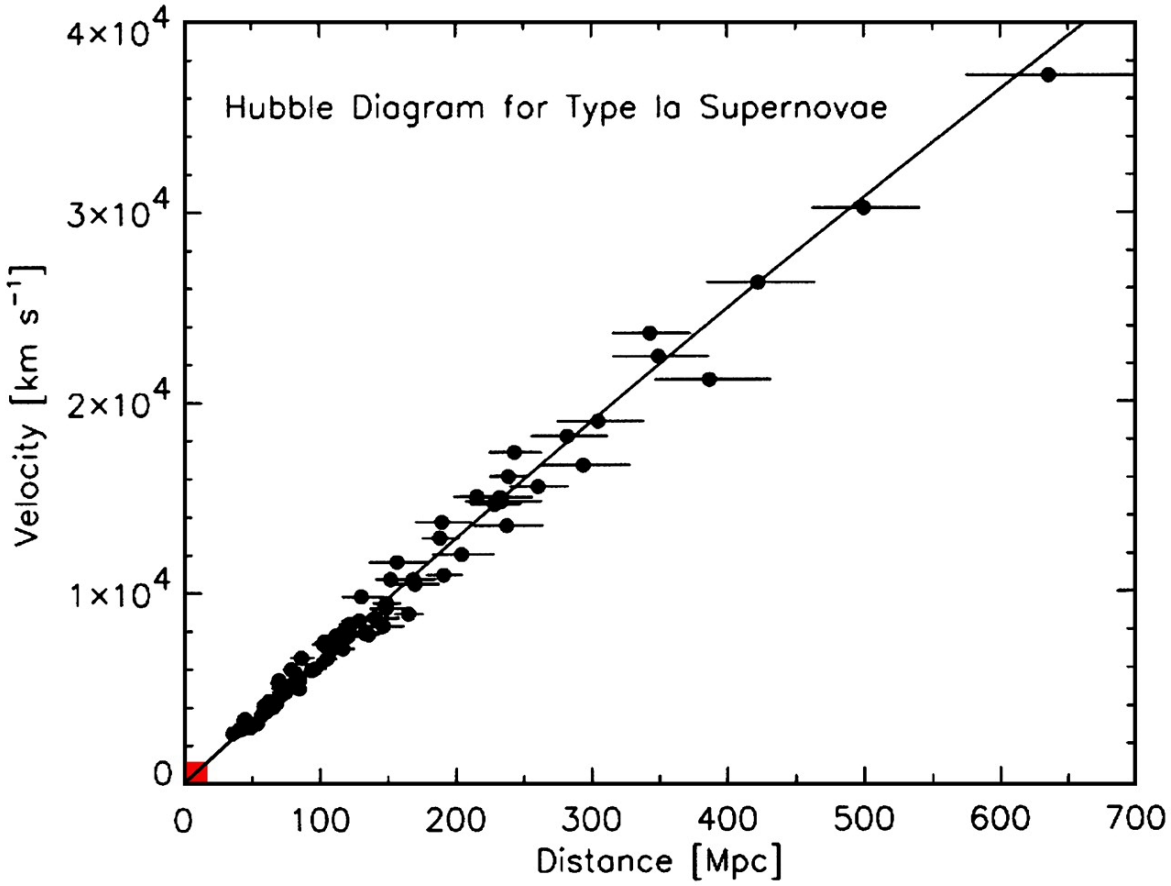

Figure 1.1: A Hubble diagram from Kirshner (2004) showing velocity (cz) vs. luminosity distance. The red square in the lower left region of the figure shows the area in which Hubble's original 1929 diagram was measured. The linear relation in Eq. 1.1.1 is only expected at z<0.1.

up of baryonic matter. Therefore, there must be some other form of mass in the Universe and this has had a great impact on our understanding of structure formation and the evolution of the universe as it significantly increases the Ω_m value. The ΛCDM standard model of the universe defines this non-baryonic matter which dominates ρ_m as non-relativistic cold dark matter. The dark matter component would slow down the expansion of the universe based on the Hubble relation. The dark energy component, Λ, is responsible for the accelerated expansion of space in this framework.

1.2 Testing the Cosmological Model

The Dark Energy density of the universe, Ω_Λ, can be investigated by looking at the accelerated expansion of the universe, i.e. by comparing the redshifts and distances of Type Ia supernovae with distances estimated via their standard candle properties, or by comparing angular-diameter distances with redshift using the BAO scale as a standard rod. This relation, first

remarked upon by Hubble, can be shown via a Hubble diagram, seen in Fig. 1.1, where we see the distance vs. velocity of Type Ia Supernovae. The distance is determined via the luminosity distance, defined as $d_L = (\frac{L}{4\pi f})^{\frac{1}{2}}$. Type Ia Supernovae are called standard candles as their luminosity is known.

There are several observational methods to determine the mass density parameter of the Universe. As previously mentioned, galaxy rotation curves and galaxy velocity dispersions in clusters have been used to determine the need for dark matter. The observed cluster mass function, which describes the number density of galaxy clusters above a certain mass, is also a powerful probe of the mass density of the Universe as these galaxy clusters are believed to have been formed in peaks in the mass-density fluctuations that trace the dark matter distribution (Peacock 1999, Bahcall & Cen 1992, 1993). Gravitational lensing, which will be further described in Section 1.2.1, is also a powerful probe of matter in the universe as light is deflected, or bent, around objects in its path. We can determine the baryonic fraction of mass in the universe via mass-to-light ratios and CMB temperature fluctuations, which depend on baryon-to-photon ratios (Ryden, 2016).

Evidence for the Big Bang model, and the ΛCDM model in particular, is based on the observations of the expanding Universe and the existence of the CMB with its acoustic peaks. However, modern cosmology requires answers to critical questions in order to test further the standard ΛCDM model of the universe. Both Dark Matter and Dark Energy are required for the model to fit observations, and finding indisputable observational proof of what exactly these are is a main goal of modern astronomy. Tests of the standard cosmological model include: measuring the expansion history of the universe, mass distribution and clustering in the universe, investigations into the Hubble constant, and gravitational lensing to see whether the observed mass in the universe confirms the presence of Dark Matter (like Kaiser (1998), Kaiser & Squires (1993), Myers et al. (2003)). We will be utilizing the magnification bias caused by weak gravitational lensing, clustering analyses, and Halo Occupation Distribution models in this thesis to determine various halo masses and mass functions. These techniques are introduced below.

1.2.1 Weak Lensing

The phenomenon of light bending in a gravitational field, gravitational lensing, is predicted by general relativity (Einstein, 1916). A foreground mass, such as galaxies and galaxy clusters, act as a lens to a background source, distorting the background objects. The geometry of a

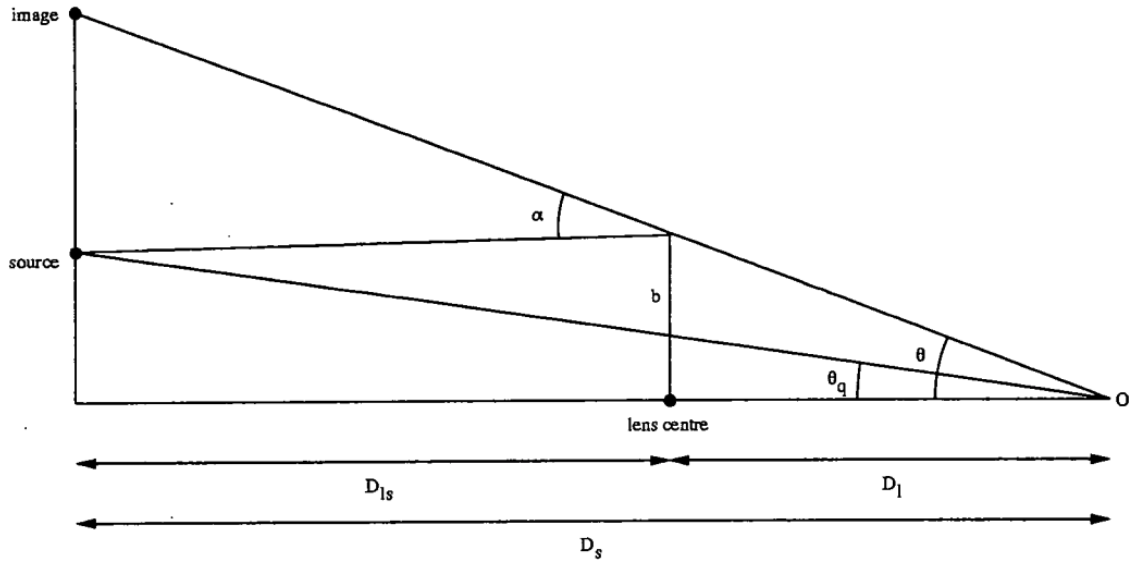

Figure 1.2: A diagram of the geometry of gravitational lensing, taken from Croom (1997).

gravitational lens is shown in Fig. 1.2, where the observer is denoted by O on the right, the angle to the source is θ_q, and the observed angle to the lensed image is θ. The radius of the lens is defined as b, D_s is the angular diameter distance from the observer to the source, D_{ls} is the angular diameter distance from the source to the lens. For a mass, $M(< b)$, which is defined as the mass contained within the radius of the lens, the deflection angle (α) of sources by foreground lenses is given by the Einstein deflection law as:

$$\alpha = \frac{4GM(< b)}{bc^2} = \frac{D_s}{D_{ls}}(\theta - \theta_q), \tag{1.2.1}$$

Gravitational lenses are classified into strong lensing, where multiple images or arcs of the background objects are detected (e.g. Lynds & Petrosian 1986), weak lensing, where larger numbers background sources are statistically distorted around foreground objects (e.g. Tyson et al. 1990), and micro lensing, where only the apparent brightening of background sources is detected. Weak lensing is a powerful probe of the mass density of the universe, and can be used to measure the observed mass and the mass distribution in the universe. Not only can we measure the masses of the lens, but the effect of lensing also has an impact on the background density of high redshift objects we observe (Narayan, 1989; Broadhurst et al., 1995).

The weak lensing approach we will be using is magnification bias and counting the sky den-

sity of quasars (QSOs; further introduced in Section 1.3) in the line of sight of galaxies and clusters of galaxies (Narayan, 1989; Myers et al., 2003). We can then use the resulting positive and negative correlations to estimate the masses of the foreground objects. The high luminosity of QSOs proves them to be very useful cosmological tools as background sources to foreground structure, with the first example of a strongly lensed QSO found by Walsh et al. (1979). We exploit this property of QSOs in this thesis using QSOs as background sources in weak lensing analyses in Chapter 3 as well as direct tracers of the mass distribution in QSO clustering analyses in Chapter 4.

1.2.2 Halo Occupation Distribution Models

Halo Occupation Distribution (HOD) models are a way of codifying the relationship between galaxies and dark matter. These models describe the probability that a halo with a specified mass contains a number of galaxies, N, as well as the distribution of these galaxies in the dark matter haloes (Berlind et al., 2003; Zheng et al., 2005). HODs were first used to populate halos in ΛCDM N-body simulations in order to describe galaxy and large structure formation. HODs are needed because the ΛCDM halo mass function is much steeper at the small mass end than either the galaxy luminosity function or the galaxy stellar mass function. In addition, there are also too many high mass halos compared to either of those observations. Therefore, a HOD would generally not allow very low mass halos to be populated by galaxies at all. The numbers of galaxies per halo throughout the higher mass range is determined by comparing real/observed galaxy clustering as a function of galaxy luminosity with simulated galaxy distributions created by applying HODs to ΛCDM halo mass functions. In this thesis, we shall not only be determining the HODs from galaxy clustering, but also from lensing of QSOs (and the CMB) by foreground galaxies and galaxy clusters, to see if the HODs implied from clustering are consistent with the lensing results.

This is the main place where we will be testing cosmological parameters in this work. Specifically, we will be addressing the issue that when the assumption is made that galaxies trace the mass, it is found that a higher matter density than predicted by ΛCDM, $\Omega_m \approx 1$, is required to explain the high amplitude of the QSO lensing results of e.g. Myers et al. (2003). However, Scranton et al. (2005) claims that this problem can be solved with a lower matter density that is consistent with ΛCDM, $\Omega_m \approx 0.3$, by introducing a HOD model that is already known to fit the observed galaxy clustering. We want to check this claim that the observed QSO

lensing results can be reconciled with the ΛCDM model by comparing the new VST ATLAS galaxy-galaxy and galaxy-QSO correlation functions to predictions based on the galaxy HOD frameworks of Scranton et al. (2005); Zheng et al. (2007); Zheng & Weinberg (2007); Zheng et al. (2009).

1.3 Quasar Physics

A further overall aim of this thesis is to make new investigations of the physics invoked to explain the unique nature of QSOs, so we now briefly describe the main properties that led to the current standard QSO model. First discovered by Schmidt (1963, 1965), quasi-stellar objects or QSOs, are the most luminous subset of the broader population of objects termed Active Galactic Nuclei (AGN). Due to their high luminosity and fast X-ray variability, QSOs are believed to be powered by the accretion of matter onto a supermassive, $\gtrsim 10^6 M_{\odot}$, black hole (Lynden-Bell & Rees, 1971; Alexander & Hickox, 2012)). The bolometric luminosity of an AGN, L_{bol}, is dependent on the mass accretion rate, $\dot{M}$ via $L_{bol} = \epsilon \dot{M} c^2$ where ϵ is the mass-energy efficiency conversion, and the upper limit of this luminosity is given by the Eddington limit, L_{Edd}. The Eddington ratio, $\lambda = \frac{L_{bol}}{L_{Edd}}$, correlates the AGN bolometric luminosity with its Eddington luminosity, or critical luminosity. The Eddington ratio value of $\lambda = 1$ indicates that the QSO is radiating at the maximum luminosity for its black hole mass. The unified model of AGN, presented by Antonucci (1993), outlines the structure of different types of AGN based on the orientation to our line of sight, a schematic of which is shown in Figure 1.3 (a). A second schematic is shown in Figure 1.3 (b), which highlights the various components of an AGN and the scales at which these can be found. In both Fig. 1.3 (a) and (b) we see the central black hole surrounded by an accretion disk (Shakura & Sunyaev, 1973). This accretion disk is responsible for thermal continuum emission at mainly UV and optical wavelengths. This continuum emission is absorbed by the dusty torus around the accretion disk and is re-emitted as Infrared radiation (IR). Although the true structure of the X-ray emitting region is not fully understood, it is thought to come from the innermost regions of the accretion disk nearest the central black hole, labeled the corona in Fig. 1.3(b). The Broad Line Region (BLR) lies within the dusty torus and the Narrow Line Region (NLR) lies outside, as suggested by observations of QSOs in polarised light (Antonucci, 1993). Fast moving, high density gas clouds in the BLR are ionized by the continuum emission from the accretion disk, which leads to the broad emission lines seen in the UV, optical, and near-IR. Similarly, the continuum from the accretion disk ionizes low density gas clouds in the

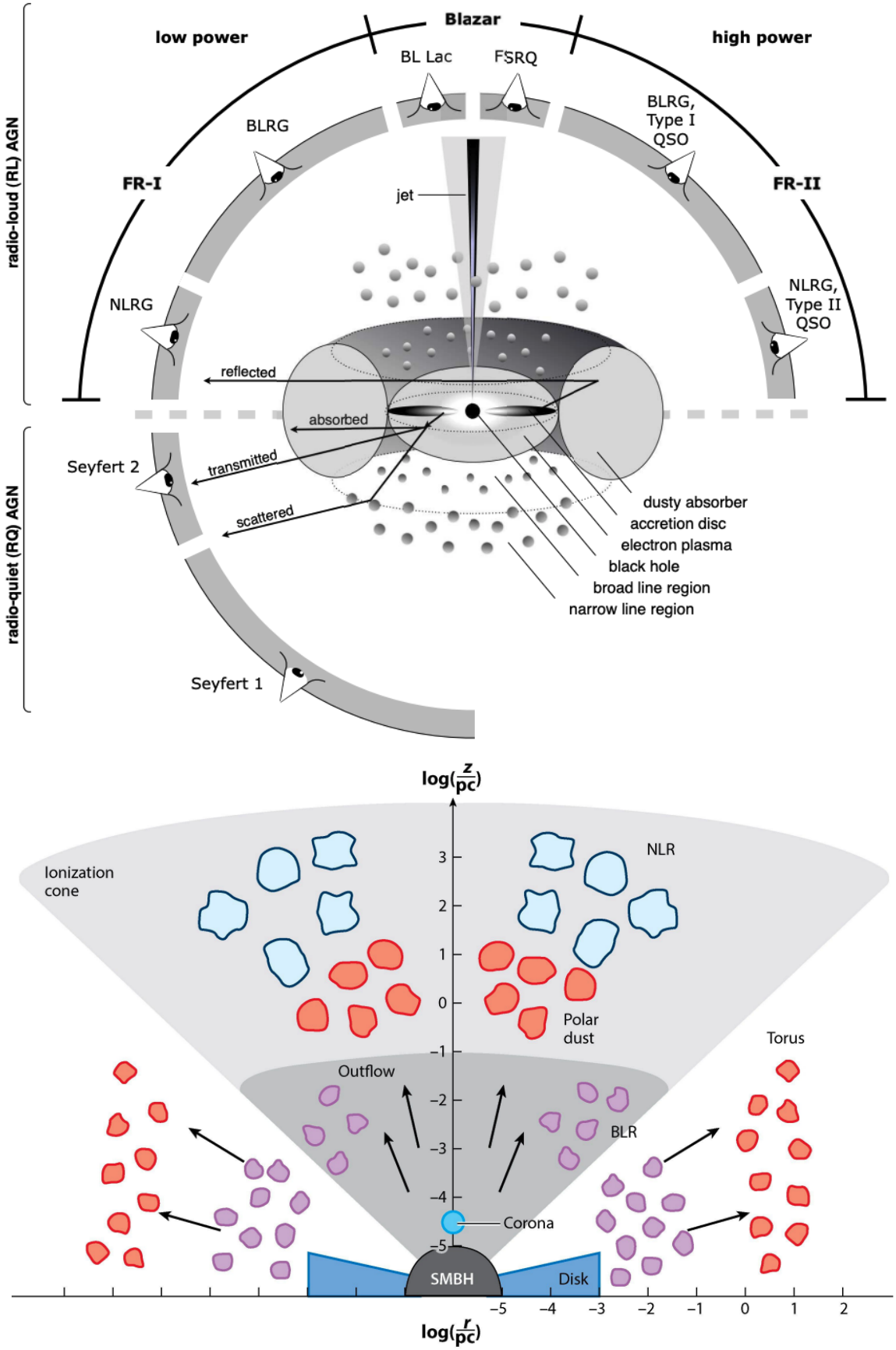

Figure 1.3: (a) Idealised standard model of an AGN, taken from Figure 1 of Beckmann & Shrader (2013), highlighting how viewing angle plays a major role in the identification of AGN. (b) A second model showing the main components and approximate scales of these components, adapted from Ramos Almeida & Ricci (2017).

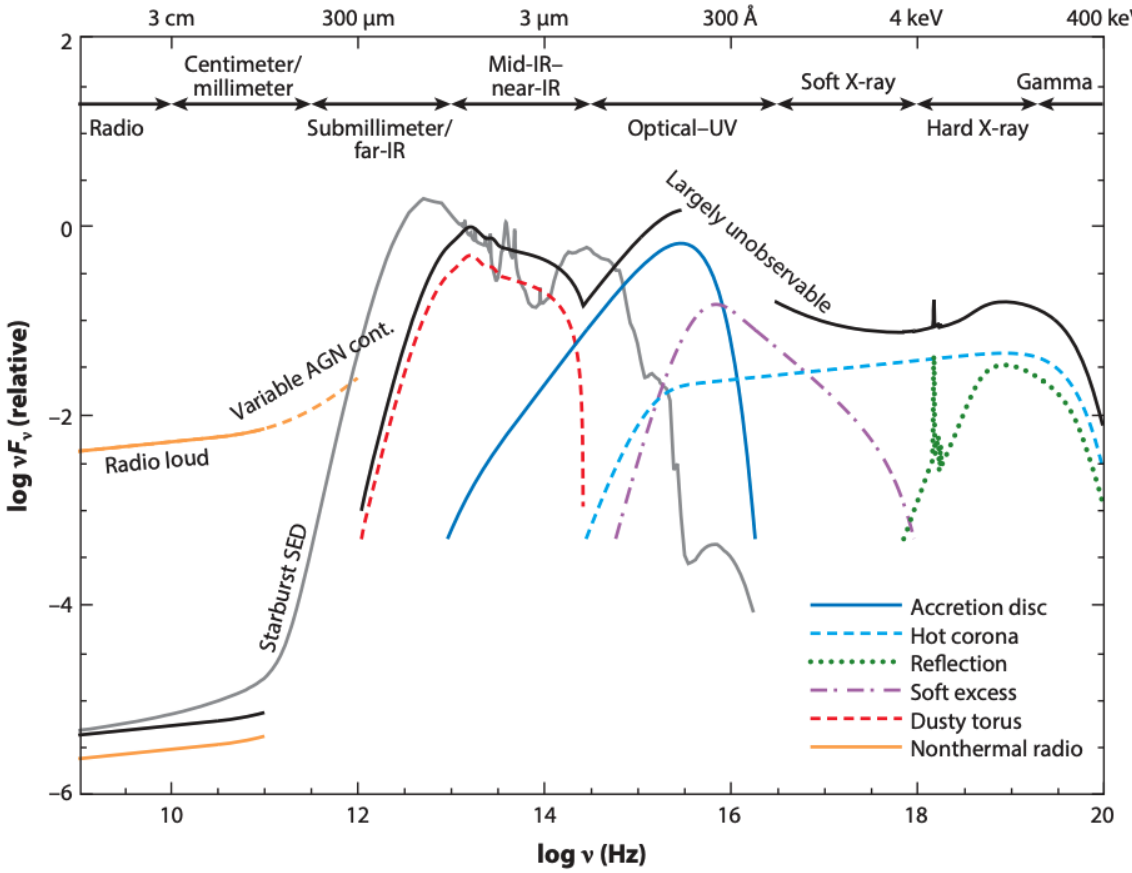

Figure 1.4: Taken from Hickox & Alexander (2018), which was adapted from Harrison (2014), this figure shows the spectral energy distribution of an AGN. Here we see the wide range of wavelengths that can be emitted by an AGN, leading to many possible AGN classifications and methods of selection.

NLR to produce UV, optical, and IR narrow emission lines. In Fig. 1.3(a) we also see the relativistic jet and the type of identification an observer may make based on the viewing angle of the AGN. For example, a Type I QSO has both narrow and broad emission lines, whereas a Type 2 QSO will only show narrow emission lines. The resulting spectral energy distribution (SED), showing the contributions from the various components of an AGN, is shown in Fig. 1.4. All of this is contained in a host galaxy and host dark matter halo. QSOs are unique in the broad emission lines they show in the optical and infrared, and the strong continua seen over the full range of the electromagnetic spectrum (Padovani, 2017). By combining selection methods at these various wavelengths, we are able to create a catalogue of QSOs in Chapter 2 with high completeness.

QSO activity is typically seen at redshifts at which we cannot spatially resolve the nucleus of the AGN. Even the Event Horizon Telescope Collaboration et al. (2019) was only able to image the Milky Way and the nearby M87 nuclei at respective distances of r∼8kpc and

r∼15Mpc. We shall see in this thesis that another route towards resolving these regions, even in distant QSOs, is reverberation mapping, which we introduce in Section 1.3.2 and use in Chapter 5. This relies on another characteristic of AGN, which is that their properties are also known to vary with time.

1.3.1 QSO Black Hole Mass Function via QSO clustering

We utilize QSO clustering in order to determine the QSO host halo masses via measurements of the QSO bias as well as via HODs. Models of structure formation predict the clustering of massive objects based on Gaussian fluctuations (e.g. Press & Schechter 1974; Kaiser 1984). Therefore, these massive objects, such as QSOs, are biased tracers of the underlying mass distribution in the universe. QSO clustering amplitudes are dependent on the QSO host halo mass, with a larger clustering amplitude implying a higher halo mass. Building on previous works, such as e.g. Martini & Weinberg (2001) and Ferrarese (2002), we assume a relation between halo mass and central black hole mass and can then utilize these clustering results to determine black hole masses. An integral part of understanding QSOs involves determining the evolution of the QSO halo mass function, or QSO Black Hole Mass Function (BHMF), $\phi(M_{BH})$, which describes the number density of black holes of various masses per unit volume within a certain redshift range. As QSOs are only the most luminous subset of AGN, the total BHMF is populated with many more objects. The BHMF can also be determined via the galaxy-BH scaling relation as, at first order, all galaxies with a bulge component are assumed to host a central black hole (Shankar et al., 2009). We utilize QSO clustering and CMB lensing in this thesis to determine the QSO halo mass function. Previous studies such as Chehade et al. (2016) and Shanks et al. (2011) have suggested that QSO clustering is approximately independent of luminosity (see Fig. 1.5) and thus that the black hole mass range may be small. Here, we aim to check this result by making a new determination of the QSO halo mass function using CMB lensing as well as QSO clustering, which is more definitive than the average bias routes used before.

1.3.2 Reverberation Mapping

One way to determine black hole masses indirectly is through reverberation mapping (e.g. Blandford & McKee (1982)). The process of reverberation mapping utilizes many epochs of continuum observations and spectroscopy on single objects in order to measure the time lag between flares in the continuum reaching the BLR. This time lag is then used to estimate

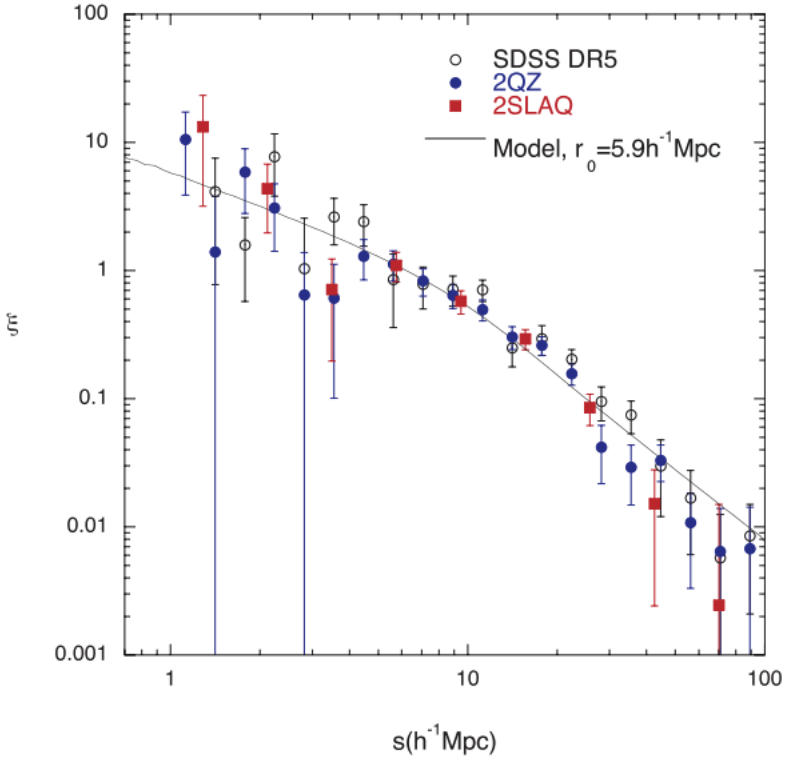

Figure 1.5: Taken from Figure 1 of Shanks et al. (2011), these results from three separate studies show the luminosity independence of QSO clustering. This is due to all three studies showing similar clustering amplitudes although they have varying absolute magnitude limits, with SDSS having the brightest limit and 2SLAQ the faintest, for similar redshift distributions which peak at z≈1.4.

the radius of the BLR. We can then use this reverberation mapped radius along with the velocity measured from the width of the broad line to determine black hole masses via the Virial Theorem:

$$M_{BH} \approx \frac{r_{BLR} < v^2 >}{G} \tag{1.3.1}$$

In this thesis, we use a novel technique of 'stacked' reverberation mapping, first introduced by (Fine et al., 2012, 2013), where we stack the cross-correlation functions of the continuum-Broad Line variations across ∼1000 QSOs in our sample. This is much more observationally efficient than single object reverberation mapping and allows us to probe QSOs at higher redshifts. Results from Fine et al. (2013) show that the stacked reverberation mapping technique competes well with the traditional reverberation mapping in recovering lags. We therefore construct a sample of QSOs in the eROSITA eFEDS field to perform optical-to-Broad Line stacked reverberation mapping to measure the radius of the BLR as well as optical-to-X-ray stacked reverberation mapping with the initial aim to measure the radius of the accretion disk. There are also studies such as that of, e.g. Edelson et al. (2019) and Cackett et al. (2020), investigating *ugriz* inter-band lags on the assumption that these are dominated by light from the accretion disc (but see Netzer 2022, and references therein). Such studies find that the u band leads the g band and similarly the others in order of wavelength as might be expected from blackbody radiation from cooler material at increasing radii in the accretion disc. Here we combine these inter-band, continuum-Broad Line and continuum-X-ray reverberation mapping results to make a new model of QSO nuclei reaching the scales from the event horizon to the BLR.

1.4 Thesis Motivation and Outline

There are five main parts of this thesis. First, we establish QSO catalogues for VST ATLAS in Chapter 2. This survey is based on VST ATLAS+NEOWISE photometry (Shanks et al., 2015; Schlafly et al., 2019) to covers $\sim 4700\text{deg}^2$ of Southern sky. These catalogues, along with the DECaLS Legacy Survey DR10, lead to target selections for the 4MOST Cosmology Redshift Survey (Merloni et al., 2012; de Jong et al., 2019; Richard et al., 2019) the details of which are described in Appendix D. Our second aim is to use ATLAS to test whether the large amount of observed galaxy-QSO lensing is caused by a higher Ω_m or HOD in standard model. This is described in Chapter 3. Then, in Chapter 4 we use our QSO catalogues to in-

fer the QSO BHMF. In Chapter 5 we apply optical, BL, and X-ray reverberation mapping to QSOs in the eROSITA eFEDS field (Liu et al., 2022). We are interested to see if the stacked reverberation mapping approach works, as that would offer significant support for a narrow QSO BHMF. Finally, the QSO stacked reverberation mapping allows for the investigation of accretion disk and BLR radii and therefore models of QSO nuclei. Our conclusions and future work are shown in Chapter 6.

Chapter 2

VST ATLAS QSO Survey: Catalogue

2.1 Introduction

Here, we develop selection criteria for a photometrically selected QSO catalogue based on VST ATLAS (Shanks et al., 2015) +unWISE neo6 (Schlafly et al., 2019) following e.g. Croom et al. (2001) and Richards et al. (2004). We aim to achieve a sky density at $g < 22.5$ of 130 deg^{-2} at $z < 2.2$ and 30 deg^{-2} at $z > 2.2$ over ≈ 4700 deg^2, comparable to the sky densities projected by the Dark Energy Spectroscopic Instrument experiment (DESI) (DESI Collaboration et al., 2016) and observationally confirmed by Chaussidon et al. (2022a). We utilize methods outlined in Chehade et al. (2016) and develop further selection techniques by comparing our results to X-ray QSOs from Bielby et al. (2012) in the William Herschel Deep Field (WHDF) (Metcalfe et al., 2001), and preliminary DESI data from DESI DR1.

We shall report on the lensing of VST ATLAS QSOs by foreground galaxies and galaxy clusters in Chapter 3. We also detect lensing of the cosmic microwave background (CMB) by the QSOs in Chapter 4. This catalogue also aims to be part of the spectroscopic fiber targeting of the upcoming 4MOST Cosmology Redshift Surveys (4CRS; Richard et al. 2019), where it will be combined with 2800 deg^2 from the Dark Energy Survey (DES) (Dark Energy Survey Collaboration et al., 2016) to give 7500 deg^2 at 160 deg^{-2} for QSO cosmology projects, further described in Appendix D.

In Section 2.2 we describe the imaging and spectroscopic surveys we use to create and test our QSO catalogue. We describe QSO selection methods based on the 2QDESp and WHDF

surveys, which we utilize to start, test, and adapt our QSO selections in Section 2.3. Section 2.4 details the final VST-ATLAS QSO catalogue selections. Section 2.5 contains a spectroscopic completeness analysis of our VST-ATLAS QSO catalogue, using preliminary DESI data as well as our own preliminary data from AAT 2dF. We present the final VST-ATLAS QSO candidate catalogue in Section 2.6. Finally, we finish our analysis in Section 2.7 where we utilize the ANNz2 photometric redshift code to determine a $z < 2.2$ and $z > 2.2$ redshift sample. We discuss our results in Section 2.8.

2.2 Data

2.2.1 Imaging Surveys

VST ATLAS

The ESO VST ATLAS data we utilize in this work is from the DR4 ATLAS catalogue released in 2019, plus data below DEC of -20, which will be part of the DR5 release. ATLAS is a photometric survey which images ~ 4700 deg^2 of the Southern sky ($\approx$2000 deg^2 in the Northern Galactic Cap, NGC, and $\approx$2700 deg^2 in the Southern Galactic Cap, SGC, in the *ugriz* bands, designed to probe similar depths as the Sloan Digital Sky Survey (SDSS) (e.g. York et al., 2000). The imaging was performed with the VLT Survey Telescope (VST), which is a 2.6-m wide-field survey telescope with a $1^\circ \times 1^\circ$ field of view. It is equipped with the OmegaCAM camera (Kuijken et al. 2002), which is an arrangement of 32 CCDs with $2k \times 4k$ pixels, resulting in a $16k \times 16k$ image with a pixel scale of $0.''21$. The two sub-exposures taken per 1 degree field are processed and stacked by the Cambridge Astronomy Survey Unit (CASU). This pipeline provides catalogues with approximately 5σ source detection that include fixed aperture fluxes as well as extended source magnitudes (Kron and Petrosian) and morphological classifications. The processing pipeline and resulting data products are described in detail by Shanks et al. (2015). We create band-merged catalogues using TOPCAT (Taylor, 2005). For our quasar catalogue, we utilize a $1.''0$ radius aperture magnitude (aper3 in the CASU nomenclature) as well as the Kron magnitude in the $g-$band, and the morphological star-galaxy classification supplied as a default in the CASU catalogues in the $g-$band. This classification is discussed in detail by González-Solares et al. (2008). The u-band data in DR4 consist of 2×120s exposures in the ≈ 700 deg^{-2} area at Dec< -20 deg in the NGC and 2×60s exposures elsewhere. We utilize the 2×60s u-band exposures of the complementary ATLAS Chilean Survey (ACE, Barrientos et al in prep.) to increase the

u-band exposure time to 240s exposure throughout the entire DR4 area. We combine the ATLAS and Chilean $u-$band data by averaging their magnitude values weighted by the relative seeing on the two exposures. Approximately 1000 deg^2 of the DR4 SGC area and NGC area at Dec>-20 deg did not have Chile u-band data at the time of this work. In these areas we simply use the shallower ATLAS DR4 data. To ensure as many objects as possible have u-band measurements, we do not detect objects independently on the u images but instead we 'force' photometry at the positions of all the g-band detections. To avoid problems with detector saturation at brighter magnitudes, in what follows we restrict the ATLAS data to objects with $g > 16$. The area covered by VST ATLAS, as well as the surveys we are utilizing in the analyses of this paper can be seen in Fig. 2.1. We correct all of the magnitudes for Galactic dust extinction using the relation $A_x = C_x E(B-V)$, for each pass band (x), using the C_x values defined in Schneider et al. (2007) and the Planck $C_x E(B-V)$ map (Planck Collaboration et al., 2014).

unWISE

The NASA satellite Wide-field Infrared Survey Explorer (WISE; Wright et al. 2010, mapped the entire sky in four pass-bands $W1$, $W2$, $W3$, and $W4$ at 3.4, 4.6, 12, and 22μm respectively, with 5σ point source limits at $W1 = 16.83$ and $W2 = 15.60$ mag in the Vega system. The Near-Earth Object Wide-field Infrared Survey Explorer (NEOWISE; Mainzer et al. 2011) mission continued surveying the sky in the $W1$ and $W2$ bands, and the telescope was commissioned again for the NEOWISE-Reactivation (NEOWISER; Mainzer et al. 2014) mission. The unWISE catalogue (Schlafly et al., 2019; Meisner et al., 2021) presents the coadded, unblurred $W1$ and $W2$ images of WISE, NEOWISE, and NEOWISER for $\sim$2 billion objects over the full sky. The other full-sky WISE/NEOWISE coadded dataset is presented in the AllWISE catalogue, which is blurred to the WISE PSF. The unblurred unWISE catalogue preserves the WISE resolution and detects sources approximately 0.7 magnitudes fainter than AllWISE in $W1$ and $W2$, ie 5σ limits of $W1 = 17.5$ and $W2 = 16.3$ in the Vega system. This deeper imaging is made possible through the coaddition of all available $3-5\mu m$ WISE+NEOWISE imaging, increasing the total exposure time by a factor of ~ 5 relative to AllWISE (Schlafly et al., 2019). We use the pre-release version of DR3 of the unWISE catalogue (neo6), provided by E. Schlafly, in this work, matched with a 3" radius to the VST ATLAS photometry. We correct for Galactic dust extinction using the same $E(B-V)$ values described above (Planck Collaboration et al., 2014), with 0.18 and 0.16 coefficients for W1 and W2 respectively taken from Yuan et al. (2013).

To allow checks of unWISE quasar selection, we also download data from the DECaLS Legacy Survey DR9 release (Dey et al., 2019a) as this is the data which has been used by DESI Collaboration et al. (2016) in their science, targeting, and survey design. This includes the $W1$ and $W2$ WISE fluxes using 'forced' photometry of the neo6 data at the locations of Legacy Survey's optical sources in the unWISE maps. Being 'forced', these data go somewhat deeper than the unWISE neo6 catalogue, but, of course, only exist for objects with optical photometry.

William Herschel Deep Field (WHDF)

To perform an analysis of X-ray selected quasars, we use the William Herschel Deep Field (WHDF) data provided by Metcalfe et al. (2001). This data covers a $16' \times 16'$ area of sky with data in the $UBRIZHK$ bands and goes several magnitudes deeper than our VST ATLAS data. Unfortunately, particularly for U and B, the passbands are very different from those used in the VST ATLAS survey. To overcome this we matched to the SDSS Stripe 82 photometry (described in Pier et al. 2003), whose passbands are very similar to VST ATLAS. Although this is less deep than the WHDF photometry, for $B < 23.5$, $\approx$95% of our WHDF objects have Stripe 82 photometry. We retain the star/galaxy separation information from the deeper, original, WHDF data.

This is then combined with a 75ksec Chandra ACIS-I X-ray exposure (Vallbé Mumbrú, 2004; Bielby et al., 2012) and the mid-infrared (MIR) 3.6 and 4.5μm Spitzer SpIES data (Timlin et al., 2016) to provide 0.5-10 keV X-ray fluxes and the equivalent of $W1$ and $W2$ band magnitudes.

2.2.2 Spectroscopic Surveys

2QZ

The 2dF QSO Redshift Survey (2QZ; (Boyle et al., 2002; Croom et al., 2005), covers approximately 750 deg^2 of the sky, with $\approx$ 480 deg^2 overlap with VST-ATLAS. It used the 2-degree Field (2dF) multi-object spectrograph at the Anglo Australian Telescope (AAT) to target sources, and discovered $\approx$ 23000 QSOs at $z < 3$. The areas targeted for 2QZ are contained within the 2dF Galaxy Redshift Survey sky coverage (Colless et al. (2001), 2dFGRS). The 2QZ catalogue utilizes photometric colour cuts to select QSO targets. Therefore, we can use the 2QZ quasar catalogue to test for completeness of our new catalogue as it spans a redshift

range of $0.3 < z < 2.2$, which includes our target redshift range. At higher redshifts, the completeness of the 2QZ survey rapidly drops as the Lyman-alpha forest enters the u-band. Additional incompleteness may be due to AGN dust absorption. See Croom et al. (2005) for further description of the 2QZ QSO survey.

2QDESp

The 2QDES Pilot Survey (2QDESp) (Chehade et al., 2016) was the first survey to use VST ATLAS photometry to target QSOs. They attempted to target QSOs up to $g < 22.5$, with high completeness up to $g \approx 20.5$ with an average QSO sky density of $\approx$70 deg^{-2} in the redshift range of $0.8 < z < 2.5$. The target depth of $g \leq 22.5$ was to probe the clustering properties of intrinsically faint quasars as this was a relatively unexplored depth for the targeted redshift range at that time.

As 2QDESp used VST ATLAS data, albeit an earlier release, we will base our selection methods on the 2QDESp selection criteria as we aim to find sources at these faint magnitudes with a higher sky density. We are able to select fainter targets as we use the unWISE catalogue in conjunction with VST ATLAS photometry, instead of the AllWISE all-sky source catalogue used by 2QDESp. We also have deeper u-band data and we encompasses the full ATLAS area, which was not completed at the time of 2QDESp.

DESI

The Dark Energy Spectroscopic Instrument (DESI) (DESI Collaboration et al., 2016) is a Stage IV dark energy measurement using baryon acoustic oscillations and other techniques that rely on spectroscopic measurements. The main spectroscopic survey is conducted on the Mayall 4-metre telescope at Kitt Peak National Observatory. With a target selection based on DECaLS DR9 photometry, DESI has a target depth of $r < 23$. We utilize DECaLS DR9 photometry to check our VST-ATLAS photometry as well as the "main" survey data in the seventh internal data release of DESI spectra, Guadalupe (which will be released in DR1), to perform checks of our QSO candidate selection. This data has an $\approx$144 deg^2 overlap with ATLAS. We shall also use DESI Guadalupe spectroscopy covering the WHDF to increase the numbers of known quasars with redshifts in the WHDF area, beyond those previously reported by Vallbé Mumbrú (2004) and Bielby et al. (2012).

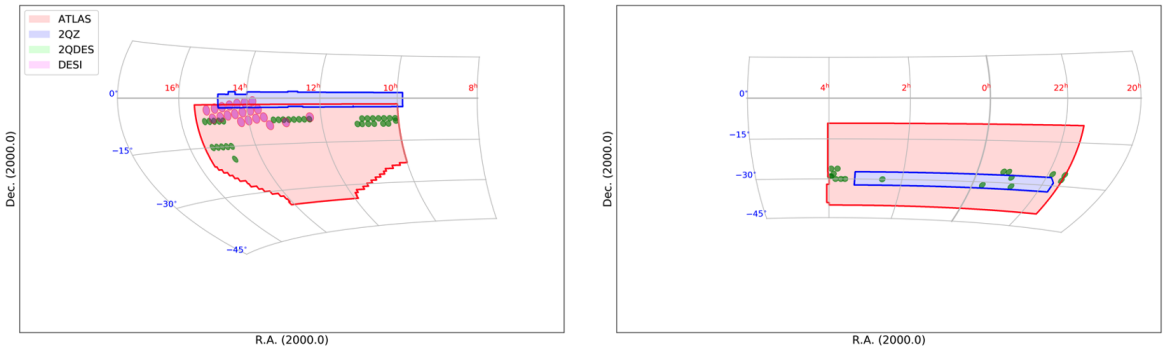

Figure 2.1: The sky coverage of VST ATLAS NGC is shown in red, including 2000 deg^2 in the NGC in the left hand panel and 2700 deg^2 in the SGC in the right hand panel. The map also shows areas where other surveys used in this work overlap VST ATLAS. The 2dF Quasar Survey (2QZ, Croom et al. 2005) area is shown in blue, the 2dF QSO Dark Energy Survey pilot (2QDESp, Chehade et al. 2016) area in green and the area covered by DESI, by the time of the internal release used here, in magenta.

2dF

We are able to test our final QSO selection using the 2-degree Field (2dF) fibre coupler feeding 392 fibres over 3 deg^2 into the AAOmega spectrograph (Sharp et al., 2006) at the Anglo Australian Telescope (AAT). The spectrograph uses a dichroic beam-splitter at 5700Å and the fibres have a 2.″1 diameter. We utilize the multi-object mode and the 580V and 385R gratings, giving a wavelength range from 3700-8800Å with a spectral resolution of ≈1300. We observed two trial VST ATLAS fields, NGC-F1 and NGC-F2, with the observational details being given in Section 2.5.2.

2.3 Optimizing QSO Selection via 2QDES + WHDF

To create the VST ATLAS QSO catalogue, we start from photometric selection methods in multiple colour spaces based on previous work using VST ATLAS+AllWISE catalogues. We utilize both the ultra-violet excess (UVX) and the mid-infrared excess (MIRX) properties of QSOs to create photometric colour cuts for our target selection, following Chehade et al. (2016). We test the completeness of these selections using QSO identified in the deeper WHDF data at X-ray, optical, and MIR wavelengths. We then adjust these improved selections to allow for the brighter flux limits that apply to VST ATLAS and unWISE relative to the WHDF, always aiming to minimise stellar and galaxy contamination while maximizing completeness of the quasar sample. We perform these colour cuts in the regions covered by VST-ATLAS and unWISE in both the NGC and SGC survey areas in the Southern hemi-

sphere. UVX colour cuts were previously used by 2QZ and SDSS (Ross et al., 2012) to select quasars in the redshift range of $z < 2.2$. We then follow Chehade et al. (2016) in combining UV and MIR photometry to make our QSO selections. The continued inclusion of UV criteria differentiates this work from e.g. the extended Baryon Oscillation Spectroscopic Survey (eBOSS) (Dawson et al., 2016) and DESI who use only MIRX selection (Yèche et al., 2020). As noted in Section 2.2, we use spectroscopic surveys such as 2QZ, 2QDESp, eBOSS, DESI and new 2dF observations to optimise the ATLAS selection and compare selection efficiencies with results from these other spectroscopic surveys.

2.3.1 2QDESp QSO Selection

Our initial ATLAS selections are based on the UVX and MIRX QSO selections made by Chehade et al. (2016) who utilized a combination of VST-ATLAS and WISE photometry in ≈ 150 deg^2 of the Southern hemisphere for their analysis, complementing their selection with the XDQSO code for quasar classification. We replace AllWISE with the deeper unWISE to improve this photometric selection and expand the area covered over the full VST-ATLAS footprint. This thesis does not include an XDQSO selection as it would require some recalibration for the deeper photometry in the $u-$, $W1-$, and $W2-$ bands we are utilizing.

The original colour selections from Chehade et al. (2016) are as follows. The VST ATLAS photometry is in AB magnitudes and the unWISE photometry is in Vega magnitudes. The UVX/optical selection is given in Eq. 2.3.1:

$$\begin{aligned} -1.0 \leq (u-g) \leq 0.8 \\ -1.25 \leq (g-r) \leq 1.25 \\ (r-i) \geq 0.38 - (g-r) \end{aligned} \tag{2.3.1}$$

The selections exploiting mid-IR excess are given in Eq. 2.3.2:

$$\begin{aligned} &(i-W1) \geq (g-i) + 1.5 \;\&\; -1.0 \leq (g-i) \leq 1.3 \;\&\; (i-W1) \leq 8 \\ &\&\; [(W1-W2) > 0.4 \;\&\; (g < 19.5) \;||\; \\ &(W1-W2) > -0.4 * g + 8.2 \;\&\; (g > 19.5)] \end{aligned} \tag{2.3.2}$$

These selections are graphically displayed in Fig. 1 of Chehade et al. (2016). Following the colour selections outlined above, we note that the maximum confirmed quasar sky density achieved by Chehade et al. (2016) was $\sim$90 deg^{-2} for $z < 2.2$ QSOs. This leaves us below our target density of 130 deg^{-2} at $z < 2.2$ (plus 30 deg^{-2} at $z > 2.2$), motivating us to further improve these selections and use them in conjunction with better data.

2.3.2 William Herschel Deep Field (WHDF) QSO Selection

Our first attempt to refine our QSO selection is based on objects in the extended WHDF (Metcalfe et al. 2001, 2006). Although a small, $\sim 16' \times 16'$ area, here we have high signal-to-noise optical data which is several magnitudes fainter than the VST-ATLAS data that benefits star/galaxy separation accuracy and is still ≈ 1 mag deeper when using SDSS Stripe 82 data for *ugri* photometry (see Section 2.2.1). Since the WHDF also has deeper MIR and X-ray imaging, it presents an ideal opportunity to try to optimize our selection methods in this well-observed field. To do this, we start from the R-selected star and galaxy image lists provided on the WHDF webpage [1] and match this catalogue to the MIR 3.6 and 4.5μm Spitzer SpIES data (Timlin et al., 2016) to get an equivalent to $W1$ and $W2$ band photometry. Unless otherwise stated, all magnitudes and colours are corrected for galactic extinction. We next match the Stripe 82 *ugriz* data to the R image lists. We are then able to develop our selection cuts in the WHDF field starting from those described by Chehade et al. (2016) and given in eqs. 2.3.1 and 2.3.2 above.

WHDF X-ray & DESI QSO Population

Firstly, we need to establish the number of known quasars on the WHDF. We consider the X-ray selected sample of WHDF quasars given in Table 2 of Bielby et al. (2012) (see also Vallbé Mumbrú 2004), which lists 15 spectroscopically confirmed quasars, their Chandra X-ray fluxes and spectroscopic redshifts. Together with the WHDF morphological and SDSS Stripe 82 photometric properties of these objects, these parameters are all included in Table A.1 in the Appendix. Of these Chandra X-ray QSOs, 12 are detected brighter than our target limit of $g < 22.5$. These include 10 that are morphologically classified as stellar sources in the WHDF photometric catalogue, and 2 which are classified as extended sources. Additionally, 11 of these 12 quasars are in our 'QSO tracer' target redshift range of $0.3 < z < 2.2$. These 12 confirmed quasars occupy an X-ray-optical overlap area of 214 arcmin^2 or 0.0594 deg^2, implying a $16 < g < 22.5$ quasar sky density of 202 ± 58 deg^{-2} from the list of Bielby et al. (2012). Finally, we note that 10 of these 12 X-ray quasars[2] are detectable to the nominal eROSITA 0.5-10 keV X-ray flux limit of 1×10^{-14} ergs cm^{-2} s^{-1}, corresponding to a sky density of 168 ± 53 deg^{-2}.

[1] (http://astro.dur.ac.uk/ nm/pubhtml/herschel/herschel.php)
[2] WHDFCH099 and WHDFCH113 have $S_X(0.5-10\,\mathrm{keV}) < 1 \times 10^{-14}$ ergs cm^{-2} s^{-1}.

Table 2.1: WHDF completeness and contamination statistics for various QSO cut selections to the ATLAS $g < 22.5$ mag limit in all cases. Class 'All' means 'Stellar' plus 'Extended'. All rows refer to the full redshift range.

Class	Cut	X-ray limit (0.5-10keV) (ergs cm^{-2} s^{-1})	Completeness	Contamination	QSO density (deg^{-2})	Notes
Stellar	X-ray	1×10^{-15}	11/12→92%	0/11→0%	185	>3σ X-ray, 16<g<22.5 stellar, <3″
Stellar	X-ray	$> 1 \times 10^{-14}$	8/12→67%	0/8→0%	135	
Stellar	DESI	-	9/12→75%	-	152	
Stellar	*grW*	-	11/12→92%	8/19→42%	185	
Stellar	ugr/UVX	-	8/12→67%	8/16→50%	135	
Extended	X-ray	1×10^{-15}	4/4→100%	6/10→60%	67	>3σ X-ray, 16<g<22.5 extended, <3″
Extended	X-ray	$> 1 \times 10^{-14}$	3/4→75%	4/7→57%	51	
Extended	DESI	-	2/4→50%	-	34	
Extended	*grW*	-	3/4→75%	7/10→70%	51	
Extended	ugr/UVX	-	3/4→75%	27/30→90%	51	
All	X-ray	1×10^{-15}	15/16→94%	6/21→29%	253	>3σ X-ray, 16<g<22.5, <3″
All	X-ray	$> 1 \times 10^{-14}$	11/16→69%	4/15→27%	185	
All	DESI	-	11/16→69%	-	185	
All	*grW*	-	14/16→88%	15/29→52%	236	
All	ugr/UVX	-	11/16→69%	35/46→76%	185	

In addition to the Chandra X-ray population of quasars, we also have preliminary DESI Guadalupe internal release data in the WHDF. Here we selected objects that were targeted as QSOs and confirmed spectroscopically as QSOs in these DESI data. These 13 quasars are listed in Table A.2. Note that these data are only preliminary and so future DESI public releases may identify more quasars. But in DESI, there are 11 QSOs to a depth of $g < 22.5$, which gives a density of 185 ± 56 deg^{-2}, close to the above X-ray sample of Bielby et al. (2012). Of these 11 QSOs, 9 are morphologically classified as stellar and 2 as extended.

There are seven $g < 22.5$ QSOs in common between the DESI and the X-ray QSO catalogues. Of the stellar QSOs with $g < 22.5$, the DESI and X-ray selected samples find respectively 2 and 3 QSOs that are undetected by the other technique. Hence we identify a total of 12 stellar QSOs on the WHDF, leading to a stellar QSO density of 202 ± 58 deg^{-2}. None of the morphologically extended QSOs with $g < 22.5$ are in common, meaning there are 4 extended QSOs spectroscopically identified, with 2 in X-ray and 2 in DESI for a total extended QSO sky density of 67 deg^{-2}. The total number of $g < 22.5$ stellar+extended QSOs on the WHDF is thus 16, corresponding to an overall X-ray+DESI quasar sky density of 269 ± 67 deg^{-2}.

We note that three out of the four $g < 22.5$ DESI quasars missing from Table A.1 are detected in the X-ray at fainter X-ray fluxes. This increases the overall X-ray completeness from 11/16=69% at the eROSITA $S_X(0.5 - 10\,\mathrm{keV}) > 1 \times 10^{-14}$ ergs cm^{-2} s^{-1} limit to 15/16=94% at the fainter $S_X(0.5-10\,\mathrm{keV}) > 1\times10^{-15}$ ergs cm^{-2} s^{-1} Chandra limit. The X-ray completeness can be compared to the overall DESI completeness of 11/16=69%. Table 2.1 provides a full summary of cut completeness and contamination, subdivided by stellar and extended source morphology.

Based on this analysis and subject to the preliminary nature of the DESI internal release, our provisional conclusion is that a joint optical/MIR and eROSITA X-ray selection will give an estimated quasar candidate density which is $\approx 45\%$ higher than simply using the X-ray or DESI optical/MIR selections alone. In particular, we can expect an $\approx 45\%$ increase in sky density by adding eROSITA X-ray selection to an optical/MIR survey such as DESI to $g < 22.5$. Of course, this estimate does not account for any QSOs which may be missed by both techniques.

WHDF Motivated QSO Cuts

We now turn our attention to how many of these QSOs are picked up by our photometric selection technqiue, and whether we can optimise this. To test this, we start from the initial $ugri + giW1W2$ photometric cuts, as derived from previous work done by Chehade et al. (2016) and described in Section 2.3.1, on the 16 confirmed QSOs.

Stellar Cuts

We show the 16 WHDF quasars first in the context of the WHDF stellar sources in the same magnitude range in the $u - g : g - r$ plane (see Fig. 2.2). As the WHDF/Stripe 82/SpiES photometry is deeper and less noisy than VST ATLAS/neo 6, we change the $g - r > -1.25$ colour cut of Chehade et al. (2016) to $g - r > -0.4$ to reflect the reduced contamination in this area.

$$\begin{aligned} -0.5 \leq (u - g) \leq 0.8 \\ -0.4 \leq (g - r) \leq 1.35 \end{aligned} \tag{2.3.3}$$

We then similarly show the 16 WHDF QSOs in the $g - r : r - W1$ plane[3] in Fig. 2.3 where our mid-IR, $grW1$ selections are:

$$(r - W1) > 1.6 * (g - r) + 2.1 \;\&\; (i - W1) \leq 8 \tag{2.3.4}$$

In both figures, the UVX and MIRX ($grW1$) selections are shown as dashed green lines and objects classified as stellar sources are shown in light gray. The stellar locus can be clearly seen in both colour spaces. The X-ray sources are shown as blue circles and the DESI

[3]Here we have moved from the $g - i : i - W1$ plane of Chehade et al. (2016), for the practical reason that more faint QSOs are detected in ATLAS r rather than i. (see Section 2.4).

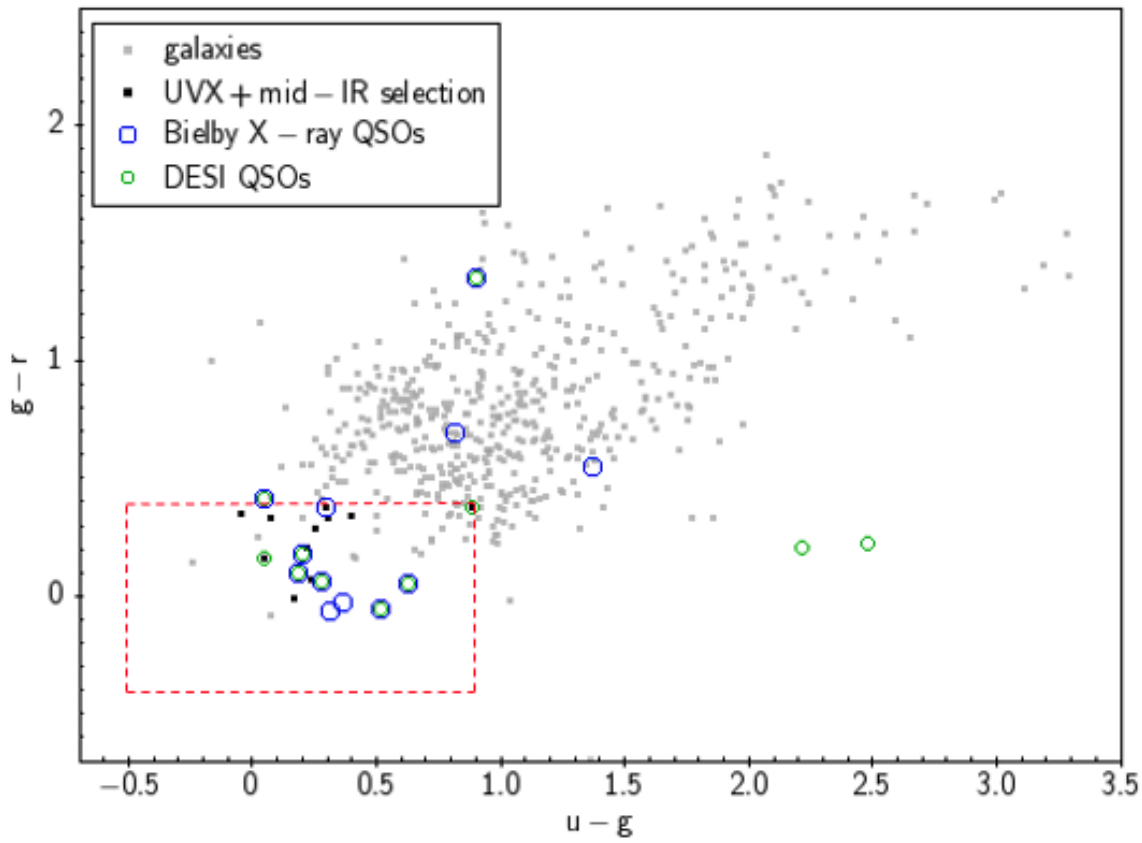

Figure 2.2: Colour selections performed on stellar sources in the extended WHDF in the *ugr* colour space. WHDF objects with a stellar morphology are shown in gray. X-ray QSOs from Bielby et al. (2012) are shown as blue circles and QSOs found by DESI are shown as green circles. The ugr+$grW1$ ATLAS QSO selections are shown as black points. The red dashed lines denote the ATLAS selection in this colour space. All selections are magnitude limited to $g < 22.5$.

sources are shown as green circles. Note that none of the 8 extra UVX+$grW1$ candidates (black points) are detected to the $S_X(0.5-10\text{keV}) > 1 \times 10^{-15}$ ergs cm^{-2}s^{-1} 3σ limit of the Chandra X-ray data. The two X-ray sources and two additional DESI sources that do not overlap with a gray point are morphologically classified as galaxies.

We show the results of these stellar cuts in Table 2.1. We see that the grW is highly successful, selecting 11/12 stellar quasars implying a completeness of 92% with only 42% contamination i.e. an efficiency of 58%. This compares favourably to the other stellar selections eg UVX and X-ray at the brighter 'eROSITA' limit both at 67% completeness. This lower completeness is partly due to both UVX and X-ray being biased against selecting $z > 2.2$ quasars, e.g. 2 out of the 4 stellar WHDF quasars missed by UVX have $z > 2.2$. One of the other 2 missing in UVX is the X-ray absorbed, $z = 0.79$ quasar, WHDFCH0044, which may explain its red $u - g = 0.89$ colour. The other is WHDFCH055 at $z = 0.74$ which is much redder

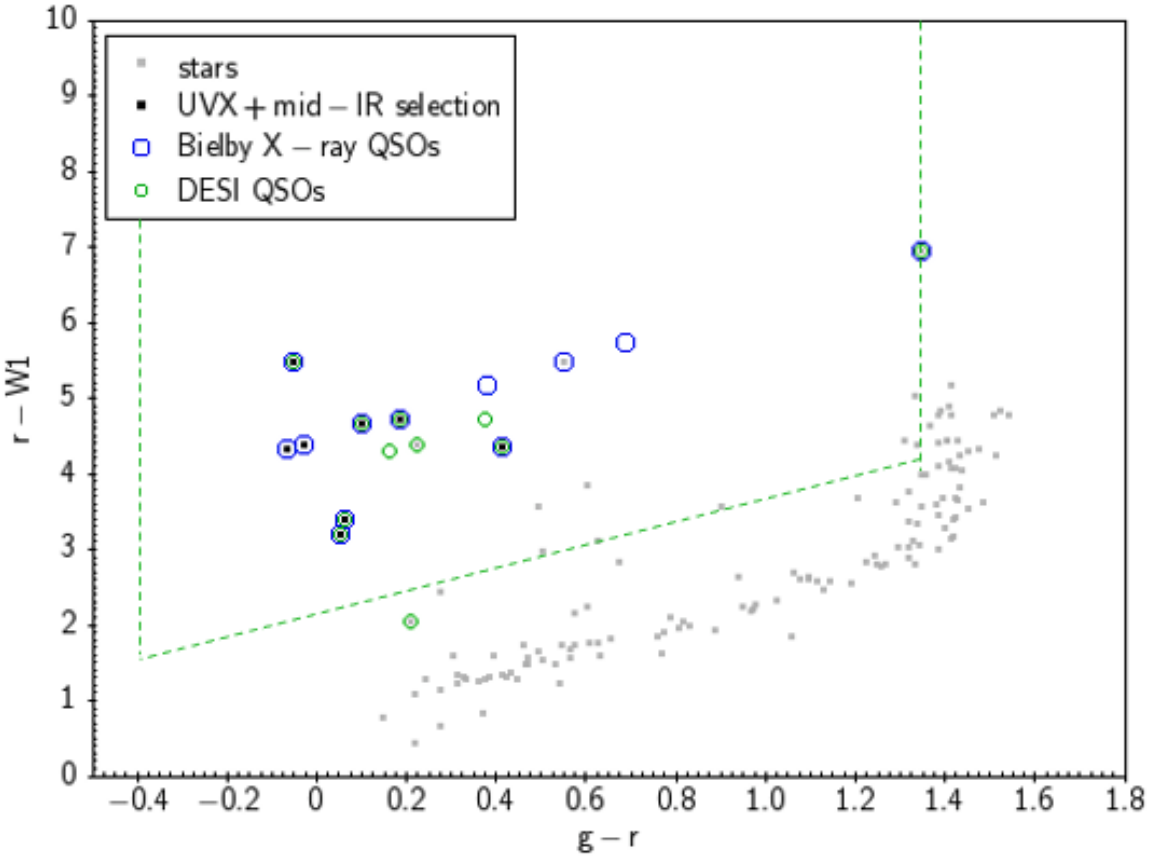

Figure 2.3: Colour selections performed on stellar sources in the extended WHDF in the $grW1$ colour space. WHDF objects with a stellar morphology are shown in gray. X-ray QSOs from Bielby et al. (2012) are shown as blue circles and QSOs found by DESI are shown as green circles. The ugr+$grW1$ ATLAS QSO selections are shown as black points. The green dashed lines denote the ATLAS selections in this colour space. All selections are magnitude limited to $g < 22.5$.

at $u - g = 1.37$ but shows little evidence of X-ray absorption. However, UVX still has a competitively low contamination rate for stellar quasars at 50% compared to 42% for grW and we shall see that UVX still has a role to play when the imaging data is less deep and the star-galaxy separation is less accurate.

Extended Source Cuts

As 5 of the 15 confirmed QSOs from Bielby et al. (2012) and a further 3 DESI QSOs (or 7 in total accounting for one overlap) are morphologically classified as extended sources (galaxies) in the WHDF catalogue, we perform our colour selections on extended sources as well. Down to $g < 22.5$, even the star/galaxy separation in the WHDF data is not entirely reliable, so our decision to include this selection will be further justified when looking at images with lower S/N as in the VST ATLAS survey. At this $g < 22.5$ limit, 2 extended QSOs are found by Bielby et al. (2012) and 2 by DESI.

The suggested cuts, shown in Figs. 2.4 and 2.5, are aimed at minimising galaxy contamination while retaining possible QSOs that have been classified as galaxies.[4]. In these figures, the X-ray sources and DESI sources which are *not* overlapping with gray points are morphologically classified as stellar.

These restricted ugr cuts for extended sources are as follows:

$$\begin{aligned} -0.5 \leq (u-g) \leq 0.9 \\ -0.4 \leq (g-r) \leq 0.4 \end{aligned} \tag{2.3.5}$$

The restricted mid-IR grW cuts are:

$$(r - W1) \geq 1.6 * (g - r) + 3.3 \tag{2.3.6}$$

The two X-ray QSOs with $g < 22.5$ from Bielby et al. (2012) that are morphologically classified as extended sources (WHDFCH20 and WHDFCH110) have redshifts of $z = 0.95$ and $z = 0.82$. Visual inspection suggests that WHDFCH110 might be slightly elongated and that WHDFCH020 might overlap a faint galaxy in the r-band. The two DESI QSOs classified as galaxies with $g < 22.5$ are WHDF 8222 at $z = 2.68$ and WHDF 3081 at $z = 1.31$. WHDF 3081 is also found to be a relatively bright X-ray source, WHDFCH052, listed by

[4]Note that the $z = 2.68$ DESI QSO (ID 8222 in Table A.2) is found to be a double object in deep WHDF H-band imaging with $0.''9$ seeing.

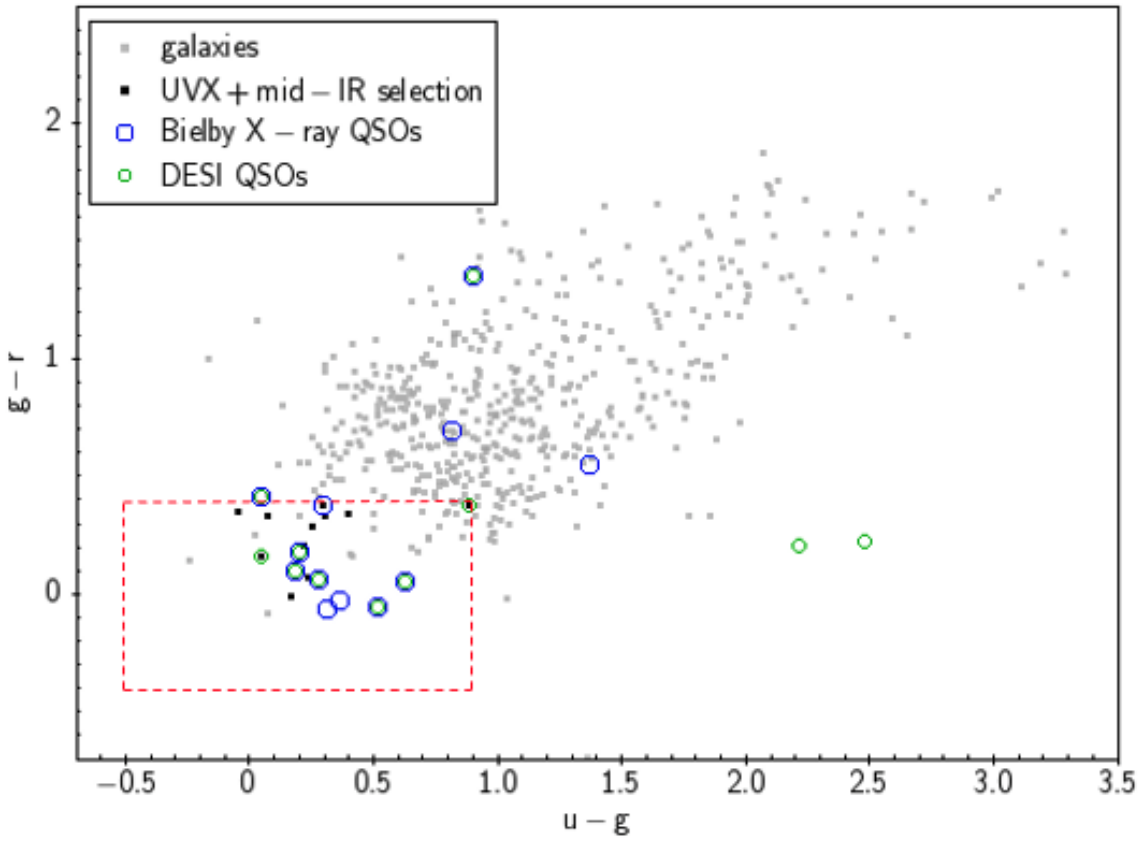

Figure 2.4: Colour selections performed on extended sources in the WHDF in the *ugr* colour space. WHDF extended sources (galaxies) are shown in gray. X-ray QSOs from Bielby et al. (2012) are shown in blue and QSOs found by DESI are shown in green. There are 2 extended QSOs from (Bielby et al., 2012) and 2 extended QSOs from DESI which can be seen to have extended counterparts. The ugr+$grW1$ ATLAS QSO selections for extended sources are shown as black points. The red dashed lines denote the ATLAS selection in this colour space. All selections are magnitude limited to $g < 22.5$. Note that, although difficult to see on the plot, the QSO at u-g=1.37 does not have an extended counterpart.

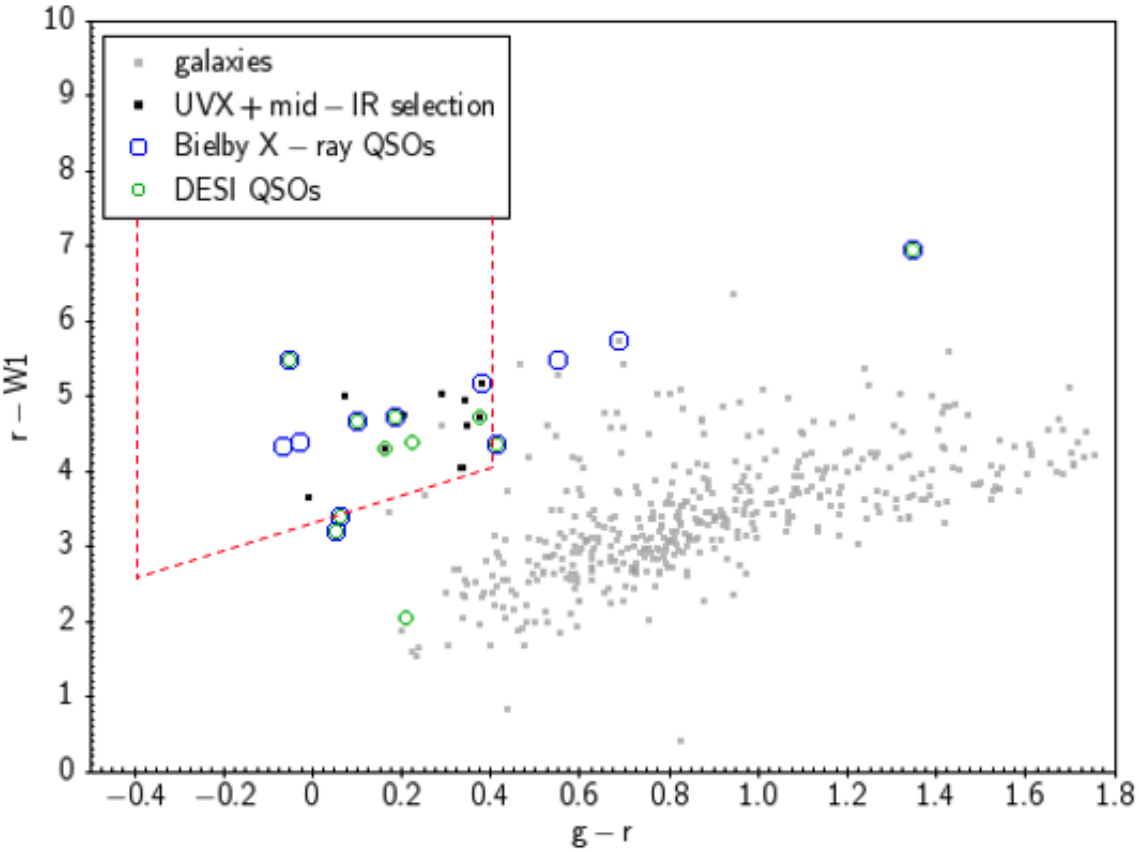

Figure 2.5: Colour selections performed on extended sources in the WHDF in the $grW1$ colour space. WHDF extended sources (galaxies) are shown in gray. X-ray QSOs from Bielby et al. (2012) are shown in blue and QSOs found by DESI are shown in green. There are therefore 2 extended QSOs from Bielby et al. (2012) and 2 extended QSOs from DESI. The ugr+$grW1$ ATLAS QSO selections for extended sources are shown as black points. The red dashed lines denote the ATLAS selection in this colour space. All selections are magnitude limited to $g < 22.5$.

Vallbé Mumbrú (2004) but not by Bielby et al. (2012). WHDF 8222 is similarly listed as a fainter X-ray source by Vallbé Mumbrú (2004) - see Table A.2. We have already noted that the $z = 2.68$ QSO is a double object (in H-band) and probably lensed. The $z = 1.31$ QSO appears to be interacting with a pair of very red compact sources at $\approx 3''$ distance. We conclude on the basis of these 4 extended QSOs that they are mostly not mis-classifications and should be included in our QSO sample. This is supported by other, fainter, $g > 22.5$ QSOs, WHDFCH007, WHDFCH008 that are also classed as galaxies on an WHDF HST i image (Shanks et al., 2021). Finally, WHDFCH048 that also has $g > 22.5$ and is classed as a galaxy, although outside the HST i frame, appears to be interacting with 2 other objects within $\approx 3''$, again justifying its extended classification.

2.3.3 WHDF Selection Summary and Conclusions

To summarise, we have tested our photometric selections in the extended WHDF Chandra X-ray overlap area of 214 arcmin^2 or 0.0594 deg^2. The main results from the WHDF analysis as tabulated in Table 2.1 are :

1) A complete census of the broad lined QSO population in the WHDF to $g < 22.5$ using X-ray, ugr, grW and also DESI results reveals a total confirmed QSO sky density of 269 ± 67 deg^{-2} at $16 < g < 22.5$. From their Luminosity Function (LF) model, Palanque-Delabrouille et al. (2016) estimate 196 deg^{-2} at this limit, again in good statistical agreement with the 269 ± 67 deg^{-2} found in the WHDF. These authors also predict 143 deg^{-2} at $z < 2.2$, within $\approx 1\sigma$ of the 202 ± 58 deg^{-2} found on the WHDF. They also predict 53 deg^{-2} at $z > 2.2$, again in good agreement with the 67 ± 17 deg^{-2} found in the WHDF. We also note that 25% of all WHDF QSOs to $g < 22.5$ were morphologically classed as galaxies/extended in the R-band, a sky density of 67 ± 34 deg^{-2}.

2) The X-ray QSOs have a sky density of 253 ± 65 deg^{-2} with $g < 22.5$ to the faint Chandra limit and 185 ± 56 deg^{-2} with $g < 22.5$ to $S_X(0.5 - 10\,\mathrm{keV}) > 1 \times 10^{-14}$ ergs cm^{-2} s^{-1}, approximately the eROSITA limit. Of these $g < 22.5$ X-ray QSOs, $\approx 20\%$ were classed as extended.

3) From the DESI optical-MIR selection a total sky density of 185 ± 56 deg^{-2} $g < 22.5$ QSOs were found, of which 101 ± 41 deg^{-2} were detected as X-ray QSOs at the eROSITA X-ray limit and 84 ± 38 deg^{-2} were undetected at this limit. Again 20% were classed as extended and 80% were stellar.

4) We conclude that neither X-ray (at the brighter 'eROSITA' limit) nor the preliminary DESI data produce complete stellar QSO samples, both missing $\approx 30\%$ of stellar QSOs to $g < 22.5$. Similarly X-ray and DESI miss $\approx 50-60\%$ of extended QSOs. So, they give a stellar QSO sky density of 135-152 deg^{-2} and extended QSO sky densities of 34-51 deg^{-2}, leading to a sky density for both of 185 deg^{-2}. Given the total WHDF QSO sky density of 269 ± 67 deg^{-2} this means that both have a similar overall completeness of $\approx 70\%$, implying that an eROSITA X-ray survey will add $\approx 40-45\%$ to a $g < 22.5$ optical/MIR QSO sky density. We also note that X-ray selected, stellar sub-samples have essentially zero contamination, much less than any other selection method.

5) For DESI QSOs with $g < 22.5$, 4/11 have $z > 2.2$, implying a sky density of $\approx$67 deg^{-2} and 7/11 having $z < 2.2$ for a sky density of $\approx$118 deg^{-2}. X-ray selection is always more skewed towards lower redshifts (e.g. Boyle et al. 1994), with none here at the brighter 'eROSITA' limit having $z > 2.2$. But note that at the fainter $S_X(0.5-10\,\mathrm{keV}) > 1 \times 10^{-15}$ ergs cm^{-2}s^{-1} limit, three of these four $z > 2.2$ QSOs are ultimately also detected in X-rays.

6) In principle, a stellar grW cut should select $\approx 90\%$ of the QSOs for a sky density of ≈ 185 deg^{-2} while suffering $\approx 38\%$ contamination. The stellar X-ray selection to the eROSITA limit produces 67% completeness, for a sky density of $\approx$135 deg^{-2} with zero contamination, at least when matched to a $g < 22.5$ star sample. The UVX technique produces similar $\approx 67\%$ completeness with only slightly lower $\approx 33\%$ contamination. For extended sources, the grW, UVX and eROSITA X-ray selections all achieve 75% completeness which is only bettered by the 100% completeness of the faint Chandra X-ray selection. The X-ray selections have the lowest contamination and the UVX selection the highest.

7) Thus focusing first on optimising QSO selection in the stellar samples, and assuming no X-ray data is available, grW seems the most promising base for selection giving higher completeness and lower contamination than ugr. For the 20-25% of QSOs classed as extended, although the grW and ugr completenesses are the same, the contamination is lower for $grW1$ than ugr.

So the MIRX cuts generally perform better than UVX when the optical photometry is as deep as in the WHDF and when the MIR photometry is as deep as in the SpIES survey. But we again emphasise that these results apply only in the best quality data as is available in the WHDF. In particular, we shall see below that at SDSS or ATLAS depths with no X-ray data yet available, the ugr selection still has an important role to play alongside grW in selecting $z < 2.2$ and $z > 2.2$ QSO samples at $g < 22.5$.

2.4 VST-ATLAS QSO Selection

Based on the analysis above we now describe our QSO selection using the current VST ATLAS data. As stated in Section 2.2.1, our VST-ATLAS data set was updated from previous work. Therefore, we begin by noting that we have improved the star/galaxy separation by adding to the standard separation in g an additional selection in the $g_{\rm Kron} - g_{A3} : g$ plane[5] to account for seeing variation in interchip gaps covered by only one of the two stacked images (Shanks et al., 2015). Here we used the relations $g_{\rm Kron} - g_{A3} > (0.5 g_{A3} - 0.864)$ for $g < 19.78$ and $g_{\rm Kron} - g_{A3} > 0.125$ for $g > 19.78$ to select extra stars from amongst the objects initially classified as galaxies. To increase the depth of our survey, we also introduce a seeing weighted combination of the ATLAS $u-$band magnitude and the Chilean $u-$band extension program.

As the ATLAS data is noisier than the data available in the WHDF, we have to adjust slightly the selections used there to decrease contamination. This can be seen in the ATLAS $u-g : g-r$ selection in Eq. 5.2.2 which more closely follows the wider ATLAS stellar locus. We shall see that basic grW cuts in ATLAS give a high contamination, leading to candidate densities of up to $\approx$400 deg^{-2} caused by galaxy contamination. As we do not yet have full X-ray coverage of VST-ATLAS, we therefore pursue joint MIRX and UVX selections which seemed to reduce contamination by $\approx 10\%$ even in the high quality WHDF data (see Section 2.3.3). Therefore, instead of selecting either only the grW MIRX candidates OR the ugr UVX candidates, we shall combine these with the aim of providing a high priority (called Priority 1 for the rest of this paper) $16 < g < 22.5$ QSO candidate catalogue, dominated by $z < 2.2$ QSOs because of the inclusion of the UVX cuts.

But first, following Croom et al. (2009) and further motivated by experience with deeper KiDS $ugri$ data in the GAMA G09 field (see Eltvedt et al 2022, in prep.), we apply a cut to remove White Dwarf stars that would otherwise contaminate our UVX selection.

Base selection with White Dwarf cut:

$$\begin{aligned} & 16 < g \leq 22.5 \ \& \ -0.4 \leq (g-r) \leq 1.1 \ \& \\ & not \ [0.44(g-r) - 0.17 < (r-i) < 0.44(g-r) - 0.02 \\ & \& \ (g-r) < -0.05)] \end{aligned} \tag{2.4.1}$$

The selections using our UVX and our mid-IR colour cuts are then defined as follows:

[5] g_{A3} is the g magnitude measured within a $1''$ radius aperture.

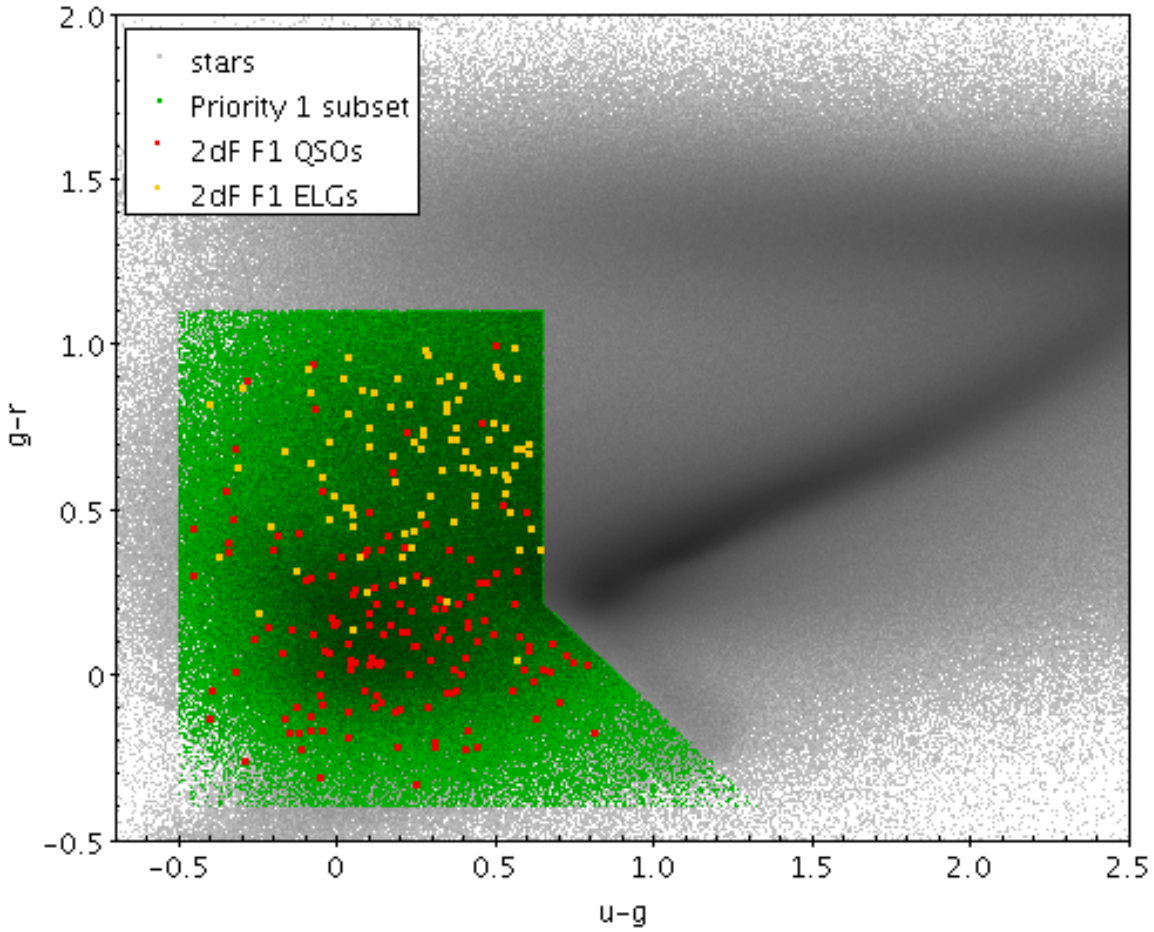

Figure 2.6: The final $u-g:g-r$ selection for VST-ATLAS Priority 1 QSO candidates. We also show the placement of the 2dF F1 objects which were observed in this ugr colour space. Objects which have been spectroscopically identified as QSOs are shown in red, NELGs are shown in yellow. ATLAS stars are shown in gray and the Priority 1 sample is shown in green.

ATLAS UVX selections:

$$\begin{aligned} -0.5 \leq (u-g) \leq 0.65 \;||\; \\ (u-g) < 0.65 \;\&\; (g-r) \leq -0.9(u-g) + 0.8 \end{aligned} \tag{2.4.2}$$

Mid-IR, known hereafter as grW, selections:

$$(r-W1) > 0.75(g-r) + 2.1 \;\&\; (W1-W2) > 0.4 \tag{2.4.3}$$

The last $W1-W2$ cut is only performed on objects which are found using the mid-IR selections with a detection in $W2$. If they have no detection in $W2$, only the mid-IR selections featuring W1 are applied.

The main grW and UVX selections can be seen in Figs. 2.6 and 2.7. Here we show the ATLAS stellar objects in gray, with the stellar loci clearly visible. The candidates selected through

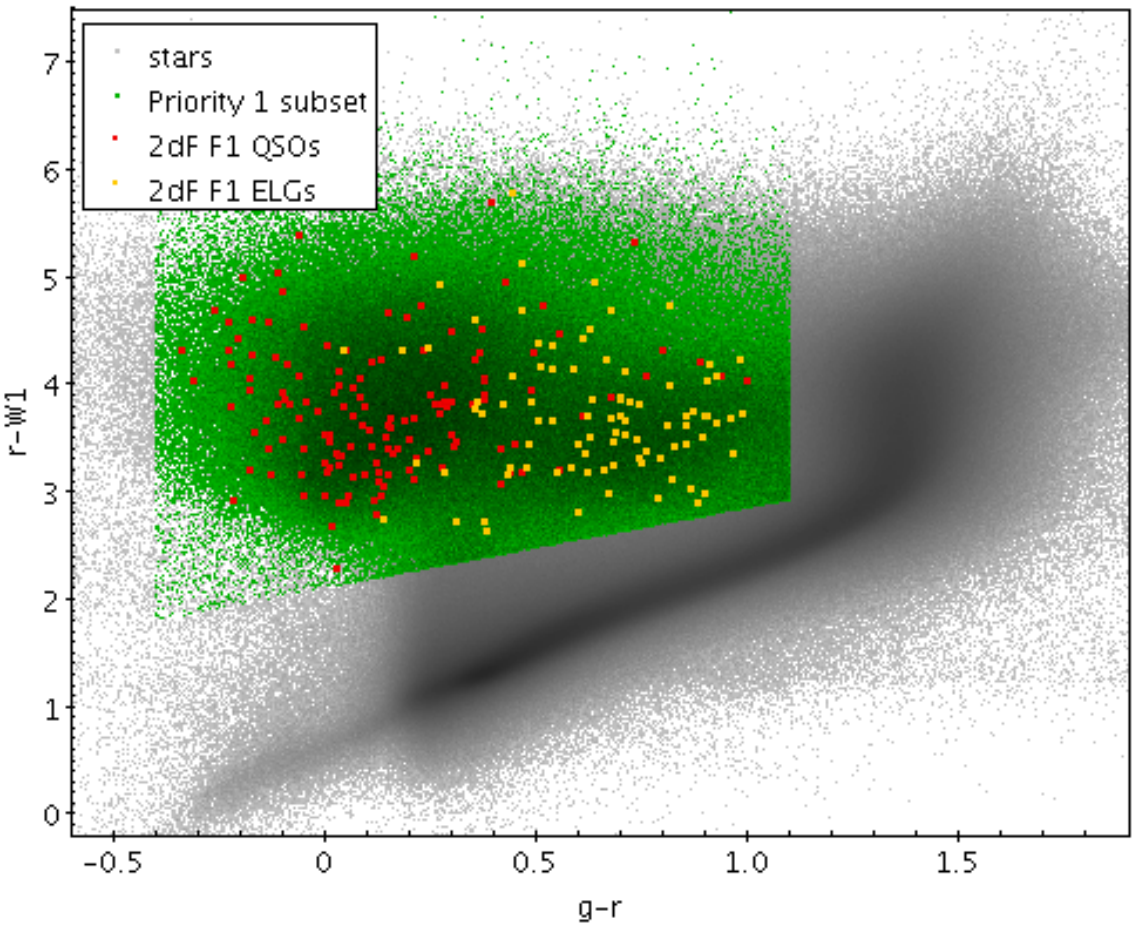

Figure 2.7: The final $g-r : r-W1$ selection for VST-ATLAS priority 1 QSO candidates. We also show the placement of the 2dF F1 objects which were observed in this $grW1$ colour space. Objects which have been spectroscopically identified as QSOs are shown in red, NELGs are shown in yellow. ATLAS stars are shown in gray and the Priority 1 sample is shown in green.

our Priority 1 sample are shown in green. The resulting tile density of QSO candidates targeted through the Priority 1 selections can be seen in Fig. 2.8 for the NGC and SGC.

After the first star-galaxy separation step of QSO selection, we noticed significant gradients in the sky density of objects classified as stellar, particularly in the NGC and, to a lesser extent, in the SGC and these persisted into the final QSO samples such as the Priority 1 selection shown in the Fig. 2.8. The fluctuations within tile concatenations are of order of $\sim \pm 18\%$ (full range) in the NGC and $\sim \pm 9\%$ in the SGC, bigger than expected from Poisson fluctuations. The extra contributions mainly come from increased galaxy contamination in fields with poorer g-band seeing, residual $\sim 20\%$ tile incompleteness in Chilean u-band data where only ATLAS u-band data is available and stellar features like the Sagittarius stream which covers the NW corner of the ATLAS SGC area. This feature also caused a similar gradient in the DESI target catalogue and this had to be removed prior to the QSO angular clustering analysis of Chaussidon et al. (2022a).

After a first round of observing on the 2dF instrument at AAT (see Section 2.5.2), we found that the main contaminants of the Priority 1 selection are compact Narrow Emission Line Galaxies (NELGs), with these source accounting for about 25% of the contamination. Figs. 2.6 and 2.7 show spectroscopically confirmed QSOs in red and NELGs in yellow. The latter seem to cluster in a cloud centred at $g - r \approx 0.7$ and $r - W1 \approx 3.5$ Therefore, we define a further cut to be optionally excluded from this Priority 1 subset in order to reduce this galaxy contamination. This NELG 'exclusion zone' is defined as:

$$g > 22 \ \& \ (r - W1) < 2.5(g - r) + 2.5 \tag{2.4.4}$$

This cuts down the QSO candidate sky densities by 41 and 31 deg^{-2} in the NGC and SGC. The resulting QSO tile density across the sky from this selection which reduces the NELG contamination can be seen in Fig. 2.9 for the NGC and SGC.

We also define a selection to target higher redshift, $z > 2.2$ objects. For this selection, we target objects found in the MIRX selections that are not detected through our UVX selection, also requiring a detection in W2. The tile density of candidates for this selection are seen in Figure 2.10. This selection, defined below in Eq. 2.4.5, is referred to as 'grW non-UVX' throughout the rest of the paper.

$$
\begin{aligned}
&16 < g \leq 22.5 \ \& \ -0.4 \leq (g-r) \leq 1.1 \ \& \\
&(r-W1) > 0.75(g-r) + 2.1 \ \& \ (W1-W2) > 0.4 \ \& \\
&not \ [0.44(g-r) - 0.17 < (r-i) < 0.44(g-r) - 0.02 \\
&\& \ (g-r) < -0.05)] \ \& \\
&not \ (-0.5 \leq (u-g) \leq 0.65 \ || \\
&(u-g) < 0.65 \ \& \ (g-r) \leq -0.9(u-g) + 0.8)
\end{aligned}
\tag{2.4.5}
$$

Finally, we define a selection for QSOs that we believe have been (mis-)classified as galaxies, based on our WHDF analysis. For this selection, we start with the previously defined extended source cuts (as outlined in Section 2.3.2). We adjust the $u-g$ cut in the same way as the stellar selection. We also introduce the $W1-W2$ requirement to decrease contamination. The final extended source selection is shown below in Eq.2.4.6. The tile density of QSO candidates targeted with this selection is seen in Fig. 2.11.

$$
\begin{aligned}
&-0.5 \leq (u-g) \leq 0.65 \ \& \\
&-0.4 \leq (g-r) \leq 0.4 \ \& \\
&(r-W1) \geq 1.6 * (g-r) + 3.3 \ \& \\
&(W1-W2) > 0.4
\end{aligned}
\tag{2.4.6}
$$

The overall sky densities of these selections are shown in Table 2.2. The NGC has an $\approx 24\%$ higher candidate density than the SGC in the Priority 1, grW non-UVX and total cases, the only exception being the galaxy cut. Since the NGC is at lower galactic latitudes than the SGC it is likely that this is caused by higher stellar contamination. However, since the main contaminants have been found to be NELGs a more complicated explanation might be needed such as the higher stellar density causing more galaxy-star overlaps that disrupt the grW stellar rejection via colour contamination. Otherwise the candidate densities are reasonably homogeneous in Figs. 2.8 - 2.11 with the main exception being the NGC high redshift selection where an increasing candidate density toward lower galactic latitudes is seen in Fig. 2.10. We shall see that similar results apply once we split into $z > 2.2$ and $z < 2.2$ samples using photometric redshifts in Section 2.7.

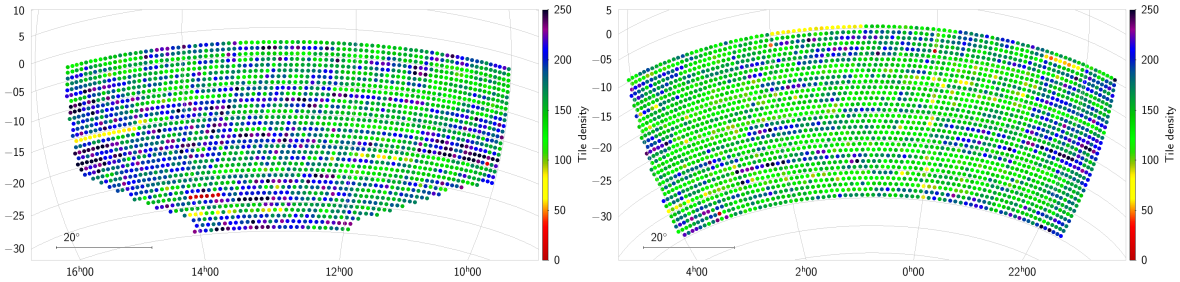

Figure 2.8: VST-ATLAS NGC and SGC tile density (deg^{-2}) of *ugr* & *grW* Priority 1 QSO candidates.

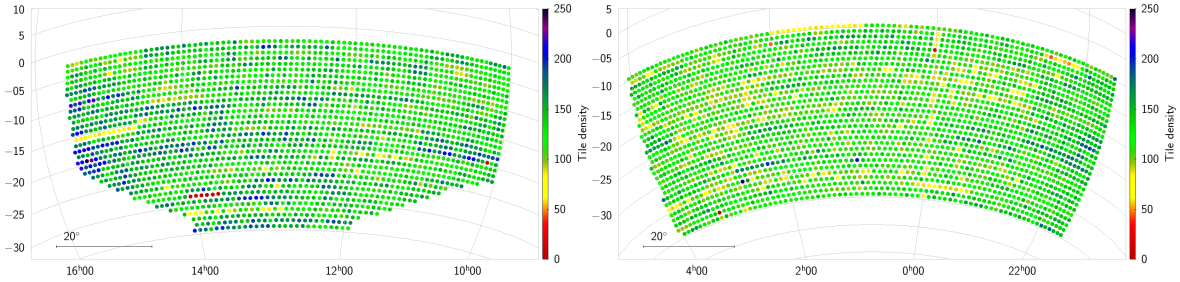

Figure 2.9: VST-ATLAS NGC and SGC tile density (deg^{-2}) of *ugr* & *grW*1*W*2 QSO candidates with an additional selection to remove NELGs.

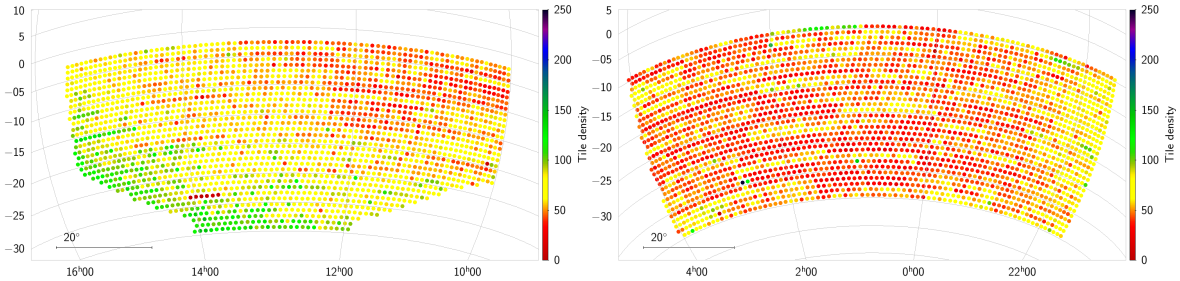

Figure 2.10: VST-ATLAS NGC and SGC tile density (deg^{-2}) of MIRX & non-UVX candidates to target higher redshift objects. Note the significant gradient to higher sky densities towards lower Galactic latitudes (i.e. RA≈ 15h, Dec=-20 deg).

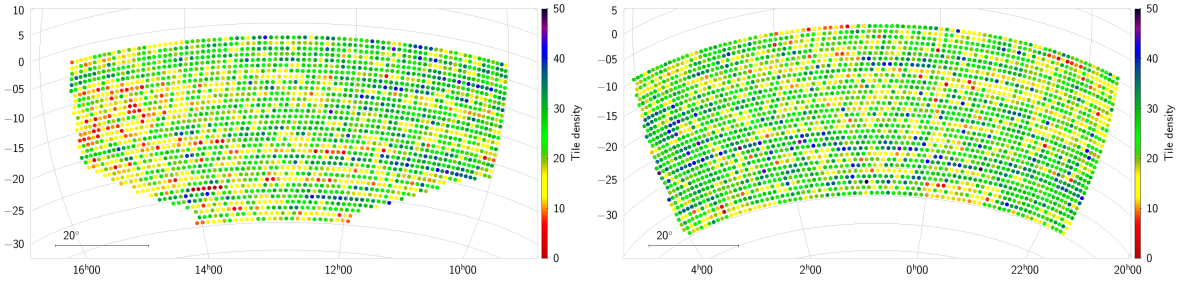

Figure 2.11: VST-ATLAS NGC and SGC tile density (deg^{-2}) of QSO candidates that are classified as galaxies in the g-band.

Table 2.2: Number counts and sky densities for the colour selections applied to the VST-ATLAS footprint. Totals in column 8 are the sum of columns 4, 6, and 7.

Sky Area	UVX selection	*grW* selection	UVX & *grW* "Priority 1"	UVX & *grW* with NELG cut	*grW* & non-UVX	extended cuts	total candidates
NGC (2034 deg^2)	1,128,470	985,294	395,459	312,296	154,723	49,556	599,738
NGC (deg^{-2})	554.8	484.4	194.4	153.5	76	24.4	294.9 deg^{-2}
SGC (2706 deg^2)	910,719	834,994	422,731	339,194	142,204	64,315	629,250
SGC (deg^{-2})	336.6	308.6	156.2	125.3	52.6	23.77	232.5 deg^{-2}
Total (4740 deg^2)	2,039,189	1,820,288	818,190	651,490	296,927	113,871	1,228,988
Total (deg^{-2})	430.2	384.0	172.6	137.4	62.6	24.0	259.3 deg^{-2}

2.5 Spectroscopic Completeness and Efficiency of the VST-ATLAS QSO Selection

We utilise photometric DESI QSO candidate target catalogues along with spectroscopic results which will be released in DESI DR1 (see Chaussidon et al. (2022b), Alexander et al. (2022), Myers et al. (2022) for information on DESI target selection and data quality validation), as well as our own spectroscopic results from 2dF, in order to test the completeness and efficiency of our ATLAS QSO candidate selection to our faint $g < 22.5$ limit. We also similarly utilise 2QZ, 2QDES, and eBOSS, which are published spectroscopic surveys and also have large areas of overlap with VST ATLAS, to test our final ATLAS QSO catalogue down to their respective $g < 20.8$, $g < 22$, and $g < 21.9$ magnitude limits. Taken together, these analyses provide a reasonably complete picture of the completenes and efficiency of our full ATLAS QSO catalogue.

2.5.1 DESI Comparison

The latest DESI internal data release, Guadalupe, covers a large area of the DESI footprint which includes some ≈144 deg^2 overlap with VST ATLAS (see Fig. 2.1). In addition to the Guadalupe release, we also utilize the DESI quasar candidate catalogue/quasar targets in this area, which were chosen photometrically using DECaLS Legacy Survey DR9 data (Yèche et al., 2020), to form a more complete comparison of our quasar candidate selections. In order to test first the accuracy of the ATLAS photometry down to $g < 22.5$, we look initially at an ≈8.5 deg^2 sub-area of the larger ≈144 deg^2 overlap with DESI targets in the NGC centred around RA=$14^{\rm h}08^{\rm m}00.0^{\rm s}$, Dec= $-4°$. This area encompasses approximately one DESI rosette, which has 5000 fibre positions, including sky fibres.

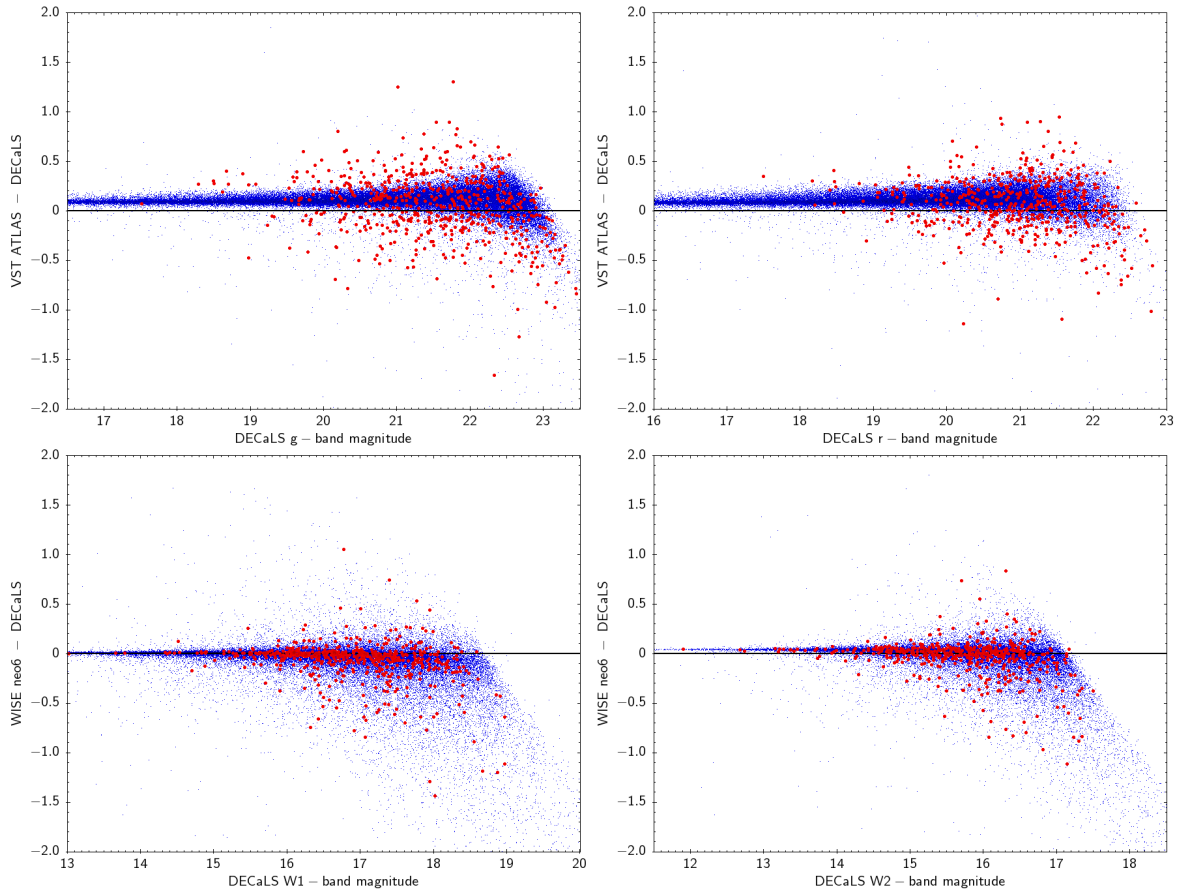

Figure 2.12: DESI DECaLS DR9 vs. VST ATLAS in the $g-$, $r-$bands and DESI DECaLS DR9 v WISE (neo6) in the W1- and W2-bands, in a sample ~ 8.5 deg^2 area. The red points represent known QSOs and the blue points represent objects classified as stars.

DESI-ATLAS photometric comparison

We first check the photometric quality of our VST ATLAS data by matching the raw g-band, r-band, and $W1$-band data to the DECaLS photometry of the DESI targets in the 8.5 deg^2 sub-area of Fig. 2.1. The results can be seen in Fig. 2.12. Generally we see good agreement between the depth of the ATLAS aperture 3 g and r stellar photometry compared to DECaLS, as well as the unWISE neo6 data vs. DECaLS. However, we see that the QSO candidates, indicated in red, show a larger scatter than the general stars, especially in g and r, and particularly at brighter magnitudes.

Comparisons between both SDSS and ATLAS data and SDSS and DESI candidates show a similarly large scatter for quasar candidates. This suggests that this excess scatter, particularly at bright magnitudes, is dominated by quasar variability caused by the significant epoch difference between these 3 datasets. Indeed, even at $21.5 < g < 22.5$, the scatter in stars remains at only the $\pm$0.05mag level implying that our ATLAS photometry remains accurate at and perhaps even beyond our $g = 22.5$ limit. The result in r is similar with a scatter of only $\pm$0.05 mag measured in the range $22 < r < 23$ mag.[6]

DESI - ATLAS Target Overlap

Now we have determined that our data quality is comparable down to our limit of $g < 22.5$, we check target overlap in the $\approx$144 deg^2 area of overlap between DESI observations and the NGC of VST-ATLAS, seen in Fig. 2.1. There are 37,306 ATLAS quasar candidates in this area, giving a 259 deg^{-2} sky density. In the same area there are 50,016 DESI QSO candidates. These were selected through a combination of photometric colour cuts and a Random Forest code (see e.g. Yèche et al. 2020), and are limited to $r < 23$. Of these, 34,106 lie within our $16 < g < 22.5$ range, giving a 237 deg^{-2} target density. When we match these DESI targets to our full VST ATLAS catalogue (prior to making any QSO selections), we get a match of 29,897 objects, with 4,209 (=34,106-29,897 or 12%) being unmatched in ATLAS. If we now perform a match between the DESI targets and our total ATLAS QSO candidate selection, using a 1″ matching radius, we find 17,673 overlapping objects. This includes our full $ugr + grW$ selection, the grW non-UVX selection, as well as our 'galaxy' selection. Therefore, our ATLAS quasar selections are missing 12,224 (=29,897-17,673=41%)

[6] We also note the presence of small offsets in both g and r - these are of order a few hundredths of a magnitude, and are due in part to small colour terms between the DECaLS and ATLAS passbands.

Table 2.3: NGC ATLAS-DESI overlap test of the various ATLAS QSO selections. The selections in column 1 are described in Section 2.4. 'Priority 1' is comprised of objects found in both 'star *grW*' and 'star UVX'. 'Star total' includes the 'priority 1' objects in addition to the 'star *grW* non-UVX' candidates. Column 2 shows the sky density of QSO candidates based on each selection. Column 3 shows the completeness of the ATLAS selections with regards to the DESI spectroscopically confirmed QSOs across the full redshift range. This is then split between the $z < 2.2$ and $z > 2.2$ completeness in columns 4 and 5.

ATLAS Subset	Sky density (deg^{-2})	Completeness (%)	$z < 2.2$ (%)	$z > 2.2$ (%)
Stars $16 < g < 22.5$				
star *grW*	56656/144=393	8735/10107=86.4	6803/7656=88.9	1932/2451=78.8
star *grW* (W2 required)	23534/144=163	7870/10107=77.9	6373/7656=83.2	1497/2451=51.1
star UVX	71844/144=499	7071/10107=70.0	6051/7656=79.0	1020/2451=41.6
Priority 1	24676/144=171	6708/10107=66.4	5818/7656=76.0	890/2451=36.3
star *grW* non-UVX	9296/144=65	1707/10107=16.9	918/7656=12.0	789/2451=32.2
star total	33972/144=236	8415/10107=83.3	6736/7656=88.0	1679/2451=68.5
Galaxies $16 < g < 21.9$				
extended cuts	3334/144=23	912/3267=27.9	858/2675=32.1	54/592=9.12
Total				
	37306/144=259	9327/13374=69.7	7594/10331=73.5	1733/3043=57.0

of the 29,897 QSO candidates selected by DESI and that are available in ATLAS, giving an ATLAS 'target completeness' relative to DESI of 59%. Of these 12,224 objects, 58% are morphologically classified as stars, 41% are classified as galaxies, 48% do not have a detection in $W1$, and 41% were removed due to the base *gri* White Dwarf cut. Comparing our VST ATLAS selections individually, the $ugr + grW$, Priority 1, cut gives us 24,676 candidates in this area, of which 12,765 are in common with DESI QSO candidates. The non-UVX selection has 9,296 candidates, with 3,703 in common. Finally, the extended source selection has 3,334 candidates, with 1,652 in common.

DESI-ATLAS spectroscopic comparison

The DESI collaboration started commissioning their main spectroscopic survey at the start of 2021. We shall be using spectra from the Guadalupe internal data release and we emphasise that all results reported here must be regarded as preliminary because they were taken from a snapshot of the DESI spectroscopic catalogue that may be incomplete in terms of exposure time, area coverage, etc. We use the QSO catalogues described by Chaussidon et al. (2022b) and Alexander et al (2022), constraining our sample to 'dark' and 'bright' main programs, and again focusing on the $\approx$144 deg^2 overlap with VST ATLAS as indicated in Fig. 2.1. This provides at least an initial estimate of DESI completeness and efficiency for the purpose of evaluating the same parameters for VST ATLAS. We emphasise that at this stage not all

the DESI candidates have been spectroscopically targeted, and the DESI results may change when their full coverage and exposure times are achieved.

There are a total of 17,716 spectroscopically confirmed DESI QSOs in the 144 deg^2 area, although only 14,302 lie in the range $16 < g < 22.5$, and not all of these were originally targeted as QSO candidates. Overall, only 17,553 of the 34,106 DESI $g < 22.5$ QSO candidates have so far been observed, with 13,128 of these confirmed to be QSOs, so 14,302-13,128=1,174 were presumably selected through other targeting programs, such as ELGs (Raichoor et al. 2022), LRGs (Zhou et al. 2022) or bright galaxies (Hahn et al. 2022). The 13,128/17,553=74.7% DESI QSO fraction is higher than the 70-71% success rate suggested by Chaussidon et al. (2022b) and Alexander et al. (2022), probably due our application of a $g < 22.5$ limit rather than the full $r < 23$ DESI limit.

The full VST-ATLAS data overlaps with 13,374 of the 17,716 quasars. Out of these 13,374 possible quasars that were available to $g_{\rm ATLAS} < 22.5$, our QSO selections picked up 9,327 objects, composed of 7,594 out of the 10,331 DESI QSOs at $z < 2.2$ and 1,733 out of the 3,043 DESI QSOs at $z > 2.2$ (see Table 2.3). Thus the overall ATLAS completeness at $g < 22.5$ relative to DESI is 70% in this field, with 74% at $z < 2.2$ and 57% at $z > 2.2$.

We note that there remains advantage to be gained from including the ATLAS u-band in our selection as well as grW. Using the stellar grW selection in Eq. 5.2.3 would result in an overall sky density of 393 deg^{-2} and this reduces to 171 deg^{-2} by combining with stellar UVX selection to give Priority 1 in Table 2.3. Although including grW non-UVX increases this by 65 deg^{-2} to 236 deg^{-2}, this represents an $\approx 40\%$ reduction in candidate density. However, if we use grW (which already requires $W1 - W2 > 0.4$ for those objects with $W2$) with the added demand that only objects with a measured $W2$ are included then the density reduces to 163 deg^{-2}. But the total stellar selection with the u band still achieves a completeness with respect to DESI of 83% compared to 78% with grW (W2 required). The completeness advantage is slightly bigger for the $z > 2.2$ sample than for the $z < 2.2$ sample (see Table 2.3).

There remains $393 - 236 \approx 157$ deg^{-2} grW candidates that are not included in either the UVX or non-UVX samples. These could still be treated as lower priority candidates in a spectroscopic survey.

We finally recall from Chehade et al. (2016) that at the depth of the AllWISE W1 and W2 data used by these authors, the MIRX candidates only reached $g \approx 20.5$ mag whereas with neo6 the depth reached is $g \approx 22$ mag in W1 and $g \approx 21.5$ mag in W2. With further

NEOWISE exposure time the W1, W2 depth reached will be highly competitive with UVX so that in the cases at least where deep, high resolution *griz* photometry is available then the u data may not be required. The *griz* photometry that is available in the DES area satisfies these conditions and so the 4MOST Cosmology Redshift Survey (de Jong et al., 2019) may not require the availability of u data to reach the same depths as in VST ATLAS.

DESI comparison conclusions

To summarize, the DESI QSO candidate sky density at $g < 22.5$, over the full redshift range is 237 deg^{-2}. Using a success rate of 74.7%, based on the 13128/17553 spectroscopically confirmed objects, and assuming the observed objects are a random selection from the candidate list, we can estimate that the DESI Guadalupe release currently has a $g < 22.5$ quasar sky density of 178 deg^{-2}. We again emphasise that this result may ultimately change due to the preliminary nature of the DESI internal data release used here. The DESI QSO density over their full magnitude and redshift range is quoted in Chaussidon et al. (2022b) as > 200 deg^{-2} with an efficiency of $\sim 71\%$ based on their main selection.

If we extrapolate these results to $r < 23$ using a canonical $N \propto 10^{0.3m}$ we find that the sky density rises from 237 deg^{-2} to 335 deg^{-2} compared to 310 deg^{-2} quoted by Chaussidon et al. (2022b) (see also Alexander et al. 2022). Similarly, the 178 deg^{-2} QSO sky density we find at $g < 22.5$ increases to 251 deg^{-2} compared to the > 200 deg^{-2} indicated by Chaussidon et al. (2022b). Given that the DESI numbers are restricted to $z > 0.9$ whereas ours apply to $z > 0.5$, we regard these numbers as being in reasonable agreement.

Our VST ATLAS QSO candidate sky density in the DESI overlap area at $g < 22.5$ is 259 deg^{-2}. Based on the spectroscopic completeness relative to DESI (see above), we can extrapolate that the ATLAS confirmed $g < 22.5$ quasar sky density is $0.7 \times 178 = 125$ deg^{-2}. Therefore, the ATLAS efficiency at $g < 22.5$ and all z is $125/259 = 48.2\%$. However, when we look at the efficiency of our targets that were observed by DESI, 10595 of the ATLAS targets in the overlap area were observed, of which 9327 were confirmed to be QSOs. Therefore, we have a $9327/10595 = 88\%$ efficiency of observed targets. This higher efficiency than the 75% and 48% DESI and ATLAS efficiencies noted above, is likely due to jointly selected targets naturally having lower contamination rates than either individual selection.

Finally, we can determine that if we assume DESI Guadalupe is already complete in the area we have used and that Guadalupe samples $z < 2.2$ and $z > 2.2$ targets fairly, then the DESI sky density at $z < 2.2$ will be $178 \times 10331/13374 = 137$ deg^{-2} and at $z > 2.2$

it will be $178 \times 3043/13374 = 41$ deg^{-2}. The ATLAS sky density at $z < 2.2$ will then be $0.74 \times 137 = 102$ deg^{-2} and $0.57 \times 41 = 24$ deg^{-2} for $z > 2.2$.

At $g < 22.5$, for all redshifts, our ATLAS selection is missing confirmed DESI QSOs. The ATLAS $grW1$ bands all seem comparatively deep enough. In the specific case of $W1$, we tested this by swapping the DECaLS DR9 $W1$ for the neo6 $W1$ band and finding that this resulted in little change to the selected candidates. Additionally, the missing QSOs are located in same place in the gri, $grW1$ and ugr colour spaces as the confirmed quasars. The main problem seems to be in $W2$ with 2058/13374= 15% of DESI-ATLAS confirmed quasars missing in neo6 $W2$.

Improved ATLAS morphological star/galaxy separation might reduce our galaxy contamination but, as we have seen, quasars can be correctly classed as extended and NELGs exist that are compact and stellar like. Thus until deeper $W2$ data becomes available we require to use the joint MIRX and UVX selection to limit galaxy contamination while maintaining a high completeness.

We also note that the VST ATLAS 125 deg^{-2} quasar sky density at $g < 22.5$ is a lower limit because there are likely to be extra quasars in the ATLAS candidate list that did not appear in the DESI list. These extra ATLAS quasars could be those that had varied to be brighter than $g < 22.5$ at the ATLAS epoch while being dimmer than the DESI limit ($r < 23$) at the DESI epoch. We shall see there is some evidence for this effect in the 2dF tests of ATLAS cuts in Section 2.5.2 below.

2.5.2 2dF Comparison

We were further able to test our selection through observing runs using the 2dF instrument with the AAOmega spectrograph (Sharp et al., 2006) at the Anglo-Australian Telescope (AAT) in February-April, 2021 (see Table 2.4). Two fields were observed, NGC-F1 and NGC-F2/NGC-F2A. The 580V and 385R gratings were used with the 5700Å dichroic. Both fields were run first with targets from our standard ATLAS quasar UVX+grW selection. The NGC-F2A observation then prioritised the grW non-UVX and the extended source selections. Most data was obtained for NGC-F1 with 4.75 hrs of observations and it is clear that such an exposure time is needed to get as high as $\approx 67\%$ spectroscopic identifications, given the average observing conditions that were experienced, with an average seeing of 2."6 FWHM, leading to an average of $\sim$51% of identifications being made across the two fields, as shown

Table 2.4: ATLAS Fields observed by 2dF. For the NGC-F2A data in the bottom row, the blue and red arm of the spectra were reduced and analyzed separately. Here we show what fields were observed, for how long, the seeing on each field, and what percentage of the data we were able to make spectroscopic QSO IDs on.

Field	RA(deg)	Dec(deg)	Date	Exposure	Seeing	IDs	Total Exp.	Comments
NGC-F1	196.9	-16.0	18/2/2021	1×30mins+4×20mins	2.″1		––	
NGC-F1	196.9	-16.0	09/3/2021	1×25mins+2×30mins	1.″4		––	
NGC-F1	196.9	-16.0	15/3/2021	3×30mins	4.″0	66.8%	4.75hr	
NGC-F2	211.6	-16.0	09/3/2021	18.3+25+15.3mins	1.″5	60.2%	––	
NGC-F2	211.6	-16.0	15/3/2021	3×25mins	4.″0	35 (54)%	2.25hr	
NGC-F2A	211.6	-16.0	07/4/2021	4×20mins	2.″5	43%	1.33hr	Moon

Table 2.5: 2dF NGC-F1 and NGC-F2/F2A 2dF+AAOmega spectroscopic identifications. The $z < 2.2$ and $z > 2.2$ columns describe spectroscopically confirmed QSOs. The percentages in columns 4 and 6 show the efficiency of our selection at both redshift ranges. † implies that an extra NELG cut was used.

Field	Candidates (#)	Fibred (#)	$z < 2.2$ QSOs (N/Percent)	$z < 2.2$ QSOs (deg^{-2})	$z > 2.2$ QSOs (N/Percent)	$z > 2.2$ QSOs (deg^{-2})	NELGs (deg^{-2})	Stars (deg^{-2})	No ID (deg^{-2})
NGC-F1 UVX	561	352	203/57.7%	107.8	28/8.0%	14.9	52.5	2.4	17.3
NGC-F2 UVX†	486	347	154/44.4%	71.9	24/4.9%	11.2	19.6	4.7	54.6
NGC-F2A non-UVX	187(g<21.1)	182	5/2.7%	1.7	36/19.8%	12.0	4.8	5.1	33.3
NGC-F2A galaxies	102	65	2/0.0%	0.7	9/11.2%	3.0	4.9	1.2	15.2
NGC-F2A NELG cut	127	102	0/0.0%	0.0	19/11.2%	7.9	5.8	0.8	16.2
Total	187+62+34=283deg^{-2}	599	208	>110.2	64	>29.9	>62.2	>8.7	50.6

in Table 2.4. The exposure time for the NGC-F2 observation was less than half that of NGC-F1 resulting in only 54% spectral identifications achieved.

After the first 2dF run on NGC-F1 we noted that there was significant contamination by NELGs with a sky density of ≈50 deg^{-2}. So for the F2 observation we applied a further *gri* stellar cut to reduce this contamination (see Section 2.4, Eq. 2.4.4). This did reduce the NELG contamination but also contributed to the lower F2 quasar sky densities (see Table 2.4) and so this further NELG cut is not advised when trying to maximise quasar sky densities.

In what follows, we therefore focus on the combination of the NGC-F1 UVX+grW, priority 1, selection and the F2A non-UVX and extended source selection. In NGC-F1, we have 561 priority 1 QSO candidates. Of these 561 candidates, 352 were fibred. After analyzing the resulting spectra in MARZ (Hinton et al., 2016), we find that 231 of these are identified as having $QOP = 3$ or 4 redshfts (where QOP is the MARZ spectral quality parameter with $QOP = 3, 4$ implying redshift qualities 'good' and 'excellent'). This is 65.6% of our target

Table 2.6: Completeness and efficiency of the VST ATLAS QSO candidates based on DESI and 2dF, from Tables 2.3 and 2.5.

Survey	ATLAS candidates	ATLAS QSOs	ATLAS Comp.	ATLAS Eff.	Pri 1 Comp.	Pri 1 Eff.	Non-UVX Comp.	Non-UVX Eff.	Ext. Comp.	Ext. Eff.
DESI	259 deg^{-2}	125 deg^{-2}	70%	48.3%	66%	52%	17%	35%	28%	53%
2dF	283 deg^{-2}	140 deg^{-2}	N/A	50%	N/A	66%	N/A	22%	N/A	11%

Table 2.7: VST-ATLAS completeness in the SGC based on spectroscopically confirmed QSOs from 2QZ, 2QDES, and eBOSS. Confirmed QSOs-stellar and Confirmed QSOs-exten. refer to the number of confirmed QSOs that are classed as stellar and extended, respectively, in the VST-ATLAS catalogue prior to making any QSO selection.

Survey	Confirmed QSOs-stellar	Overlap Priority 1	Overlap grW non-UVX	Completeness (Star total)	Confirmed QSOs-exten.	Overlap gal cut	Completeness (Stellar+Extended)
2QZ ($g < 20.8$)	10179	9372	544	97.4%	1672	939	91.6%
2QDES ($g < 22$)	2258	1962	130	92.6%	232	105	88.2%
eBOSS($g < 21.8$)	1495	1148	270	94.8%	221	78	87.2%

list, which gives us 122.7 deg^{-2} QSOs when normalized to the full number of targets at the same priority level in the field. We find 88 NELGs, giving us a galaxy contamination of 25%, or 52.5 deg^{-2}. There are 4 stars, which results in an 1.1% stellar contamination, or 2.4 deg^{-2}. Finally, there are 29 objects which have no clear ID, a rate of 8.2%, or the equivalent of 17.3 deg^{-2} in our priority candidate subset. Furthermore, of the 231 spectroscopically identified QSOs, we find 203 at $z < 2.2$, giving a sky density of 107.8 deg^{-2} in our target redshift range, and 28 QSOs at $z > 2.2$ giving a sky density of 14.9 deg^{-2}.

In NGC-F2 lower QSO ($QOP = 3$ or 4) sky densities were found with only 71.9 deg^{-2} at $z < 2.2$ and 11.2 deg^{-2} at $z > 2.2$ identified in the $ugr + grW$ selection, compared to 107.8 and 14.9 deg^{-2} with the the same selection in the NGC-F1 field.

So, as summarised in Table 2.5, the AAT 2dF observations of NGC-F1 and NGC-F2A suggest that by combining the F1 priority 1 and the F2A non-UVX and extended source selections, achieves a $z < 2.2$ QSO sky density of 110 deg^{-2} and a $z > 2.2$ sky density of 30 deg^{-2} for a total sky density of 140 deg^{-2}. With a combined candidate density of 283 deg^{-2}, this implies an ATLAS efficiency of 140/283=50%. These and the other ATLAS efficiencies are summarised in Tables 2.5 and 2.6. We see there is reasonable agreement between the results found in the DESI area and the 2dF field. These two tests complement each other with the DESI area giving lower limits on confirmed quasar sky densities from ATLAS because DESI itself may not be complete. The 2dF efficiencies will be upper limits especially at $z < 2.2$ because of the $g < 21.1$ limit that had to be used due to a lack of 2dF fibres for the NGC-F2A grW & non-UVX sample (termed 'NGC F2A non-UVX' in Table 2.5).

2.5.3 2QZ, 2QDES, eBOSS Comparison

We also utilize previously completed spectroscopic surveys to assess further the completeness and efficiency of our VST-ATLAS quasar selections. The completeness for each selection, compared to spectroscopically confirmed QSOs from 2QZ, 2QDES, and eBOSS, can be seen

Table 2.8: VST-ATLAS completeness in the NGC based on spectroscopically confirmed QSOs from 2QZ, 2QDES, and eBOSS. Confirmed QSOs-stellar and Confirmed QSOs-exten. refer to the number of confirmed QSOs that are classed as stellar and extended, respectively, in the VST-ATLAS catalogue prior to making any QSO selection.

Survey	Confirmed QSOs-stellar	Overlap Priority 1	Overlap grW non-UVX	Completeness (Star total)	Confirmed QSOs-exten.	Overlap gal cut	Completeness (Stellar+Extended)
2QZ ($g < 20.8$)	1337	1216	88	97.5%	188	106	92.5%
2QDES ($g < 22$)	4175	3417	204	86.7%	134	64	85.5%
eBOSS($g< 21.8$)	1855	1230	399	87.8%	282	86	80.3%

in Table 2.7 for the SGC and Table 2.8 for the NGC through the individual 'Overlap' columns as well as the final 'star total' and 'stellar+extended' completeness columns. The confirmed QSOs-stellar column refers to the total number of confirmed QSOs in each respective survey that, when matched to the full VST ATLAS survey, are classified as stars through our star/galaxy classifications. The confirmed QSOs-exten. column is the number of confirmed QSOs that are classified as a galaxy in our classifications.

The main result here is that in the brightest 2QZ sample the ATLAS stellar (star total) selections are producing $\approx 97\%$ completeness. These completenesses reduce for objects classed as extended but only to $\approx 92\%$. It is not clear why this is the case but the poorer completeness for extended objects might be explained if they contained more lensed double quasars that were prone to higher variability, for example. We note that $1672/11851 = 14\%$ of 2QZ SGC quasars are classed as extended, with a similar fraction in the NGC, which further justifies our inclusion of extended sources in our selections. The lower completenesses in 2QDES and eBOSS are mainly due to their fainter magnitude limits, possibly allied to higher variability if they are gravitationally lensed. The eBOSS sample is mainly a sub-sample of the DESI quasars in areas near the Dec≈ 0 deg Equatorial regions.

2.5.4 Spectroscopic analysis conclusions

Through our comparisons of DESI and ATLAS, our own observations from 2dF, and comparisons with 2QZ, 2QDESp, and eBOSS, we are able to estimate the completeness and efficiency of our VST ATLAS QSO candidates. The main results of these analyses, as shown in Tables 2.5, 2.6, 2.7, and 2.8 are:

1. From DESI comparisons, we estimate the overall VST ATLAS QSO completeness at 70%. At brighter magnitudes we see higher completenesses in the range 88-97% from comparisons with 2QZ, 2QDESp, and eBOSS.

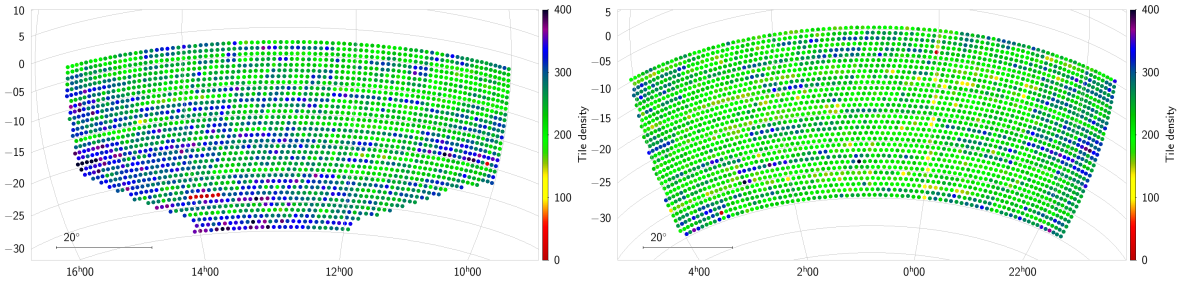

Figure 2.13: VST-ATLAS tile density (deg^{-2}) of the total number of QSO candidates in the NGC and SGC using our full Priority 1 + grW&non-UVX + extended selections.

2. From DESI and 2dF comparisons, we estimate the VST ATLAS QSO efficiency in the range 48-50%. We thus estimate the ATLAS true QSO sky density to be in the range of 125-140 deg^{-2} for our full redshift range, with 102-110 deg^{-2} at $z < 2.2$ and 24-30 deg^{-2} at $z > 2.2$.

2.6 Final ATLAS QSO Catalogue

As summarised in Table 2.2, our final Priority 1 quasar candidate counts give us a sky density of 194 deg^{-2} in the NGC, and a sky density of 156 deg^{-2} in the SGC. The colour selections performed on galaxies give an additional candidate sky density of 24 deg^{-2} in both the NGC and SGC. The mid-IR, grW non-UVX candidates give us a sky density of 76 deg^{-2}, and a sky density of 53 deg^{-2} in the SGC.

Combining the NGC and SGC gives a sky density of 173 deg^{-2} Priority 1 candidates, plus 63 deg^{-2} non-UVX candidates, plus 24 deg^{-2} with the additional extended source selections. The 65% higher candidate sky densities seen in the NGC for the UVX selection is probably due to the lower Galactic latitudes covered by the NGC, causing higher amounts of star contamination. In the Priority 1 sample the NGC is only 24% higher because of the intrinsically low stellar contamination in combining the UVX and grW selections, which allows the more isotropic quasar distribution to dominate. As can be seen in Fig. 2.13, the quasar candidate sky density across the NGC and SGC is relatively uniform, barring some striping most likely due to sky conditions such as seeing and sky brightness. The catalogue of QSO candidates is described in Table 2.9 and can be accessed at: `https://astro.dur.ac.uk/cea/vstatlas/qso_catalogue/`.

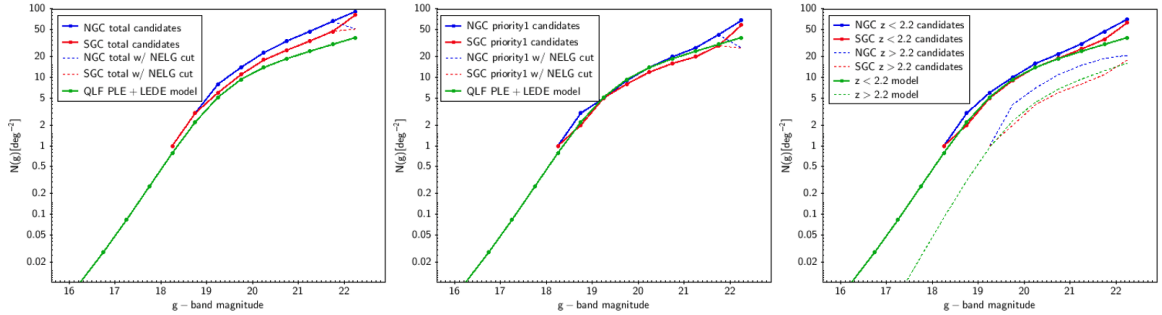

Figure 2.14: The observed VST ATLAS QSO candidate NGC and SGC number-magnitude counts compared to the PLE+LEDE QLF model predictions of Palanque-Delabrouille et al. (2016). (a) The full NGC+SGC VST-ATLAS QSO candidate sky densities as a function of $g-$band magnitude are shown in blue and red. The predicted QSO number counts from the QLF PLE+LEDE model in the $0 < z < 4$ redshift range are shown in green. (b) Same as (a) for the Priority 1 counts compared to the $0 < z < 2.2$ model. (c) Same as (a) for $z_{\rm photo} < 2.2$ (blue and red solid lines) and $z_{\rm photo} > 2.2$ (blue and red dashed lines). The effect of the NELG cut is also shown in (a) and (b).

2.6.1 n(g)

In Fig. 2.14, we now compare our candidate QSO number counts to the pure luminosity function plus luminosity and density evolution (PLE+LEDE) model Palanque-Delabrouille et al. (2016), based on the quasar luminosity function (QLF) measured in eBOSS in the redshift range $0.68 < z < 4.0$. This QLF data is fit by a double power-law model, with a linear pure luminosity-function for redshifts of $z < 2.2$ combined with a luminosity and density evolution model at $z > 2.2$. This new QLF is then used to predict the expected quasar number counts in order to optimize the fibre targeting for DESI to their limit of $r \approx 23$. They updated their selection algorithm based on the time variability of quasar fluxes in SDSS Stripe 82. From Table 6 of Palanque-Delabrouille et al. (2016), we take the expected quasar number counts, which are presented in bins of $\Delta g = 0.5$ mag and $\Delta z = 1$ for the magnitude range of $16 < g < 22.5$ and the redshift range of $0 < z < 4$.

These expected number counts are shown in Fig. 2.14, first for their full $0 < z < 4$ redshift range. They predict a quasar candidate sky density of 196 deg^{-2} over this redshift range at $g < 22.5$, consistent with the 269 ± 67 deg^{-2} we estimated from the deep WHDF data in Section 2.3.2. This predicted sky density can be compared to our full Priority 1+'grW+non-UVX'+extended quasar selection which gives a candidate sky density of 259 deg^{-2} at $g < 22.5$, 32% higher than the Palanque-Delabrouille et al. (2016) QLF PLE+LEDE $0 < z < 3$ model, due mostly to contamination which is highest in the non-UVX and extended source cuts. Using their Table 6, we also estimate a rough quasar candidate sky density in the $0 < z < 2.2$

range, more appropriate for comparison with our Priority 1 sample. Therefore, compared to the 195 deg^{-2} candidates at $0 < z < 3$, we find ≈143 deg^{-2} in the redshift range of $0 < z < 2.2$ compared to 173 deg^{-2} in our Priority 1 sample and 137 deg^{-2} if the NELG cut is also made (see Table 2.2). This agreement to within ≈ 4% of model (143 deg^{-2}) vs. Priority 1 with NELG cut (137 deg^{-2}) is reasonably consistent with the low contamination rate for the Priority 1 sample found in the NGC-F1 2dF data when the NELG cut is applied (see Table 2.5).

As in Section 2.4, we note that the NGC sky density at 295 deg^{-2} is significantly (≈ 26.7%) higher than the SGC at 232.8 deg^{-2}. Now it is likely that this is simply due to higher contamination in the NGC, especially with the known NELG contamination of the raw Priority 1 sample and the increased contamination of the non-UVX and extended source cuts. However, the NGC count remaining high relative to the SGC over the large $18 < g < 22$ range seen in Fig. 2.14 (a) is somewhat surprising given the high efficiency/low contamination of QSO selection at bright, $g < 21$, magnitudes.

To investigate this effect further, we again restrict ourselves to just the Priority 1 candidates, that in the main have $z < 2.2$ due to the inclusion of the UVX criterion. They are therefore also more comparable to counts to brighter limits selected only by UVX, such as 2QZ, 2SLAQ and SDSS. For example, at the 2QZ limit of $g < 20.8$ the sky density at $z < 2.2$ is known to be ≈ 35 deg^{-2}, rising to ≈ 40 deg^{-2} after 2QZ completeness correction (e.g. Croom et al. 2009). But the main reason we focus on the Priority 1 candidates is their high efficiency/low contamination which facilitates model and NGC vs SGC count comparison. So in Fig. 2.14 (b) the Priority 1 NGC and SGC $n(g)$ counts are compared to the QLF PLE+LEDE model, now over the redshift range of $0.5 < z < 2.2$. Here, again we see that the NGC sky density at $g < 22.5$ remains higher than the SGC count, now by 24.4% (194.4 vs 156.2 deg^{-2} - see Table 2.2). We also note that the NGC count remains consistently higher than the SGC count over the $18 < g < 22$ range. So we now limit the Priority 1 sample at $g < 20.8$ where we expect a true QSO sky density of ≈ 40 deg^{-2}. We find that the NGC sky density is 46.8 deg^{-2} whereas the SGC sky density is 40.2 deg^{-2}, so the NGC Priority 1 count is 16.3% higher than the SGC. To find what is causing this excess contamination in the NGC, we can look back at the NGC-F1 2dF observations at this same limit. In this field the Priority 1 candidate density to $g < 20.8$ was 44.1 deg^{-2}, so similar to the NGC average of 46.8 deg^{-2}, within error. At $g < 20.8$, NGC F1 sky densities were QSO 39.3 deg^{-2}, NELG 1.6 deg^{-2}, Stars/WD 0.5 deg^{-2} and non-IDs 2.6 deg^{-2}. So assuming that the non-IDs are not QSOs this implies only ≈11% contamination in this typical NGC field. So this contamination barely

Table 2.9: The columns of the VST ATLAS QSO Catalogue, which can be found at: `https://astro.dur.ac.uk/cea/vstatlas/qso_catalogue/`

Column	Units	Description
RA	Degrees J2000	Right ascension of the object
DEC	Degrees J2000	Declination of the object
selection	-	the selection, i.e. Priority 1, non-UVX, or extended that the object belongs in
u-mag	AB	VST ATLAS u-band Aperture 3 magnitude in the AB system
u-err	-	error on the VST ATLAS u-band Aperture 3 magnitude
g-mag	AB	VST ATLAS g-band Aperture 3 magnitude in the AB system
g-err	-	error on the VST ATLAS g-band Aperture 3 magnitude
r-mag	AB	VST ATLAS r-band Aperture 3 magnitude in the AB system
r-err	-	error on the VST ATLAS r-band Aperture 3 magnitude
i-mag	AB	VST ATLAS i-band Aperture 3 magnitude in the AB system
i-err	-	error on the VST ATLAS i-band Aperture 3 magnitude
z-mag	AB	VST ATLAS z-band Aperture 3 magnitude in the AB system
z-err	-	error on the VST ATLAS z-band Aperture 3 magnitude
W1-mag	Vega	neo6 W1-band magnitude in the Vega system
W1-err	-	error on the neo6 W1-band magnitude
W2-mag	Vega	neo6 W2-band magnitude in the Vega system
W2-err	-	error on the neo6 W2-band magnitude
photo-z	-	photometric redshift calculated using the ANNz2 algorithm

takes us to the level of the SGC which would require $\approx 16\%$ contamination in the Priority 1 NGC sample. Since it is likely that an SGC field observed for as long as NGC-F1 would also have similar contamination, it is not clear that increased contamination in the NGC does explain its increased sky density relative to the SGC. Deeper 2dF data in an SGC field to determine the amount of contamination there is required to resolve this question of this apparent NGC-SGC anisotropy. We return to these issues at the end of Section 2.7.

2.7 ANNz2 Photometric Redshift Estimation

Finally, we wish to split our three candidate selections into two catalogues, a $z < 2.2$ 'tracer sample' and a $z > 2.2$ LyA sample using photometric redshifts for use by the 4MOST Cosmology Redshift Survey. These photometric redshifts will also be useful for projects to be discussed in Chapter 3. To determine the photometric redshifts we utilize the ANNz2 software (Sadeh et al., 2016). This code uses artificial neural networks and boosted decision/regression

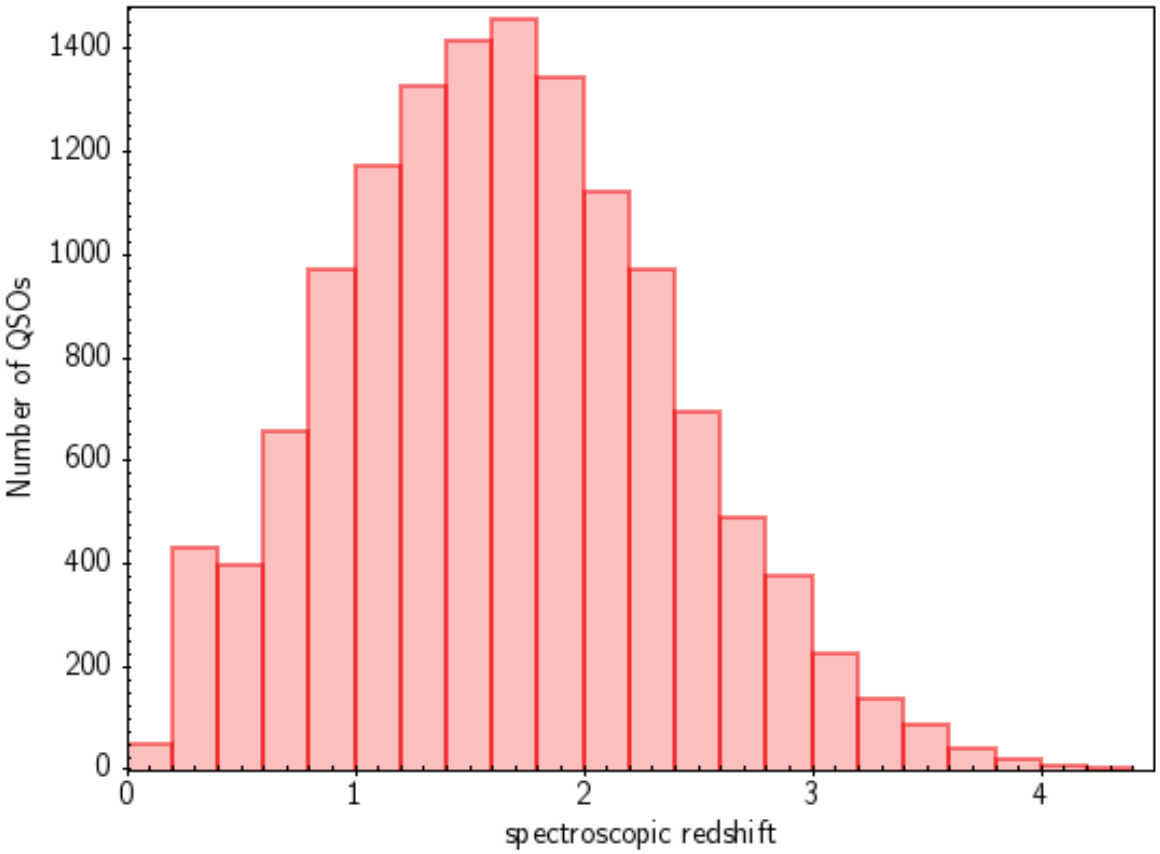

Figure 2.15: Spectroscopic redshift distribution of the full ANNz2 training and evaluation sample, using the DESI Guadalupe QSO Catalogue which will be released in DR1.

trees to optimize the photo-z estimation and has already been implemented as part of the analysis in DES (Sánchez et al., 2014). ANNz2 utilizes training based machine learning methods to derive the relationship between photometric observables and redshift.

2.7.1 ANNz2 Training

To use ANNz2, we must train the algorithm with existing data which has similar properties to our candidates. We generate a training catalogue with the DESI Guadalupe data over the ≈144 deg^2 overlap area discussed in Section 2.5.1. From this, we use the 13374 QSOs in the overlapping area with the ATLAS NGC area, matched to the VST-ATLAS data in order to train on photometry which we will be using for our dataset. The spectroscopic redshift distribution of the sample is shown in Fig. 2.15. We use the ATLAS+unWISE $ugrizW1W2$ magnitudes, errors, and the DESI spectroscopic redshifts to train the algorithm as these spectroscopically confirmed quasars were targeted through similar colour selections and cover the required redshift range.

To test the efficiency of the algorithm as well as our training sample, we divide the sample

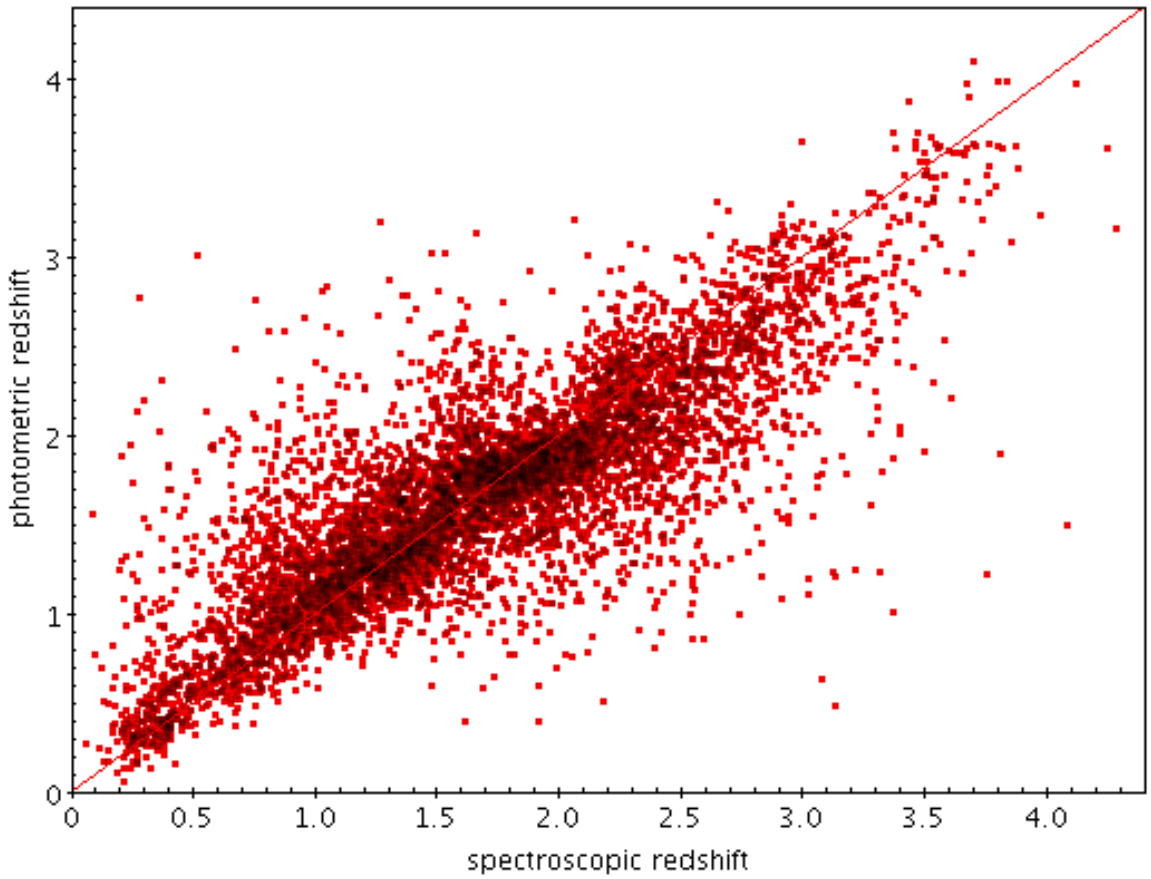

Figure 2.16: Photometric redshift compared to spectroscopic redshift for a random half of our DESI DR1 QSO sample used to test the training of the ANNz2 algorithm.

randomly in half, training on one half and testing the code on the other half. The result of that testing is seen in Fig. 2.16. Here we plot the photometric redshift estimated by ANNz2 vs. the spectroscopic redshift of the testing half of the training sample. We can compare our results with Fig. 4 of Yang et al. (2017), which shows their photo-z vs. spec-z results using optical only as well as optical + mid-infrared photometry. The top right panel of their Fig. 4 uses SDSS *ugriz* and AllWISE W1, W2 to generate photometric redshifts, similar to our *ugriz* and neo6 W1 and W2 data. Comparing our Fig. 2.16 to this top right panel in Figure 4 of Yang et al. (2017), we see a similar relative degeneracy in the $0.8 < z < 3$ range. However, our version, which has the benefit of deeper W1 and W2 data, seems to represent an improvement due to the removal of the outlying clumps of photo-z degeneracies.

We estimate the photometric redshift error by measuring the standard deviation of $\Delta z = (z_{\rm photo} - z_{\rm spec})$ to be $\sigma_z = 0.4$. We also find the standard deviation on the quantity $\frac{\Delta z}{1+z_{\rm spec}}$ to be ± 0.16. At $0.5 < z_{\rm photo} < 2.2$ this error is minimised and is reasonably constant at $\sigma_z \approx 0.33$.

2.7.2 Photometric redshift samples

Fig. 2.17 shows the resulting ANNz2 photometric redshift distributions of all ATLAS quasar candidates in the NGC and SGC. With ANNz2, we are able to create $z_{\rm photo} < 2.2$ and $z_{\rm photo} > 2.2$ quasar candidate targets. The candidate sky densities for both samples are shown in Table 2.10, where they are further split into NGC and SGC sky densities. We see that the overall $z_{\rm photo} < 2.2$ sky density is 193.5 deg^{-2} with the NGC now being 18% larger than the SGC (212.2 vs. 179.5 deg^{-2}), similar to the Priority 1 case. The $z_{\rm photo} > 2.2$ sky density is 65.8 deg^{-2} with the NGC now being 55% higher than the SGC (82.3 vs. 53.1 deg^{-2}). In Fig. 2.14 (c) we show the number-magnitude relations for these two redshift ranges with the NGC-SGC-model comparison for $z_{\rm photo} < 2.2$ being similar to the results previously found in Figs. 2.14 (a,b). The 55% higher NGC sky density for $z_{\rm photo} > 2.2$ is due to artefacts, or contamination, in the non-UVX selection (as we can see in Table 2.2) and is seen over a wide magnitude range ($19 < g < 22.5$).

From the candidate sky densities for these $z_{\rm photo} < 2.2$ and $z_{\rm photo} > 2.2$ catalogues, we can estimate their true QSO sky densities. From Table 2.5, our ATLAS efficiency decreases to 53% at $z < 2.2$ and 59% at $z > 2.2$ when we correct for ATLAS completeness using DESI, and our AAT 2dF observations suggest an efficiency of $\approx 50\%$. Then, since DESI completeness corrected ATLAS contaminations are 47% at $z < 2.2$ and 41% at $z < 2.2$, averaging gives

efficiencies of 51.5% at $z < 2.2$ and 54.5% at $z > 2.2$, implying true sky densities of 100 deg^{-2} at $z < 2.2$ and 36 deg^{-2} at $z > 2.2$. Assuming at $z < 2.2$ a 51.5% efficiency and a candidate density from Table 9 of 193.5 deg^{-2} also gives a QSO density of ≈ 100 deg^{-2} (coincidentally).

Adding eROSITA X-ray data then will give an increased stellar+extended sky density of $\approx 45\%$ over DESI and $\approx 23\%$ over a nominal grW cut. Assuming an average increase of $\approx 33\%$ will then raise our $z < 2.2$ sky density to ≈ 130 deg^{-2}. Our $z > 2.2$ sky density is unaffected by the X-ray data and so will remain at ≈ 36 deg^{-2}.

Now it should be noted that these estimates are approximate because they do not take into account inaccuracies in the photometric redshifts. This is particularly true for the $z > 2.2$ sample as can be seen in Fig. 2.18 where the fractional completeness with respect to the 1733 DESI QSOs detected by ATLAS (see Table 2.3) and candidate sky density are shown as a function of the $z_{\rm photo}$ cut. We find that the best trade-off between these two is with a cut at $z_{\rm photo} > 1.9$ where the $z > 2.2$ fractional completeness is 90% and the sky density is ≈ 100 deg^{-2}. We find that this adjustment of the $z_{\rm photo}$ cut is less of a consideration when the aim is to target a $z < 2.2$ sample. Otherwise, we note that the highest overall completeness allied to the lowest overall candidate sky density at $z > 2.2$ will always be achieved by making a combined redshift survey of the two photo-z samples simultaneously, because this avoids target duplication in the $1.9 < z_{\rm photo} < 2.2$ range.

Finally, in Figs. 2.19 (a,b) we show the tile density maps for the $z < 2.2$ sample in the NGC and SGC and in Figs. 2.20 (a,b) we similarly show the tile density maps for the $z > 2.2$ sample. While the $z < 2.2$ maps look reasonably uniform across the sky as does the $z > 2.2$ map in the SGC, the $z > 2.2$ NGC map shows evidence of a gradient indicating that the high sky densities seen in Table 2.2 and Fig. 2.14 (c) are coming from the NGC at lower galactic latitudes. This could be due to extra star contamination, despite the fact that the main QSO contaminant is expected to be compact galaxies. Otherwise, the gradient might be due to some inaccuracy in our dust extinction correction. Additionally, some striping can be seen throughout the NGC and SGC, most likely due to inconsistencies in the depth of the $g-$ and $r-$bands.

2.8 Conclusions

The main aim of this chapter was to present the VST-ATLAS QSO catalogue. We initially followed the photometric QSO selection work of Chehade et al. (2016) who used early VST

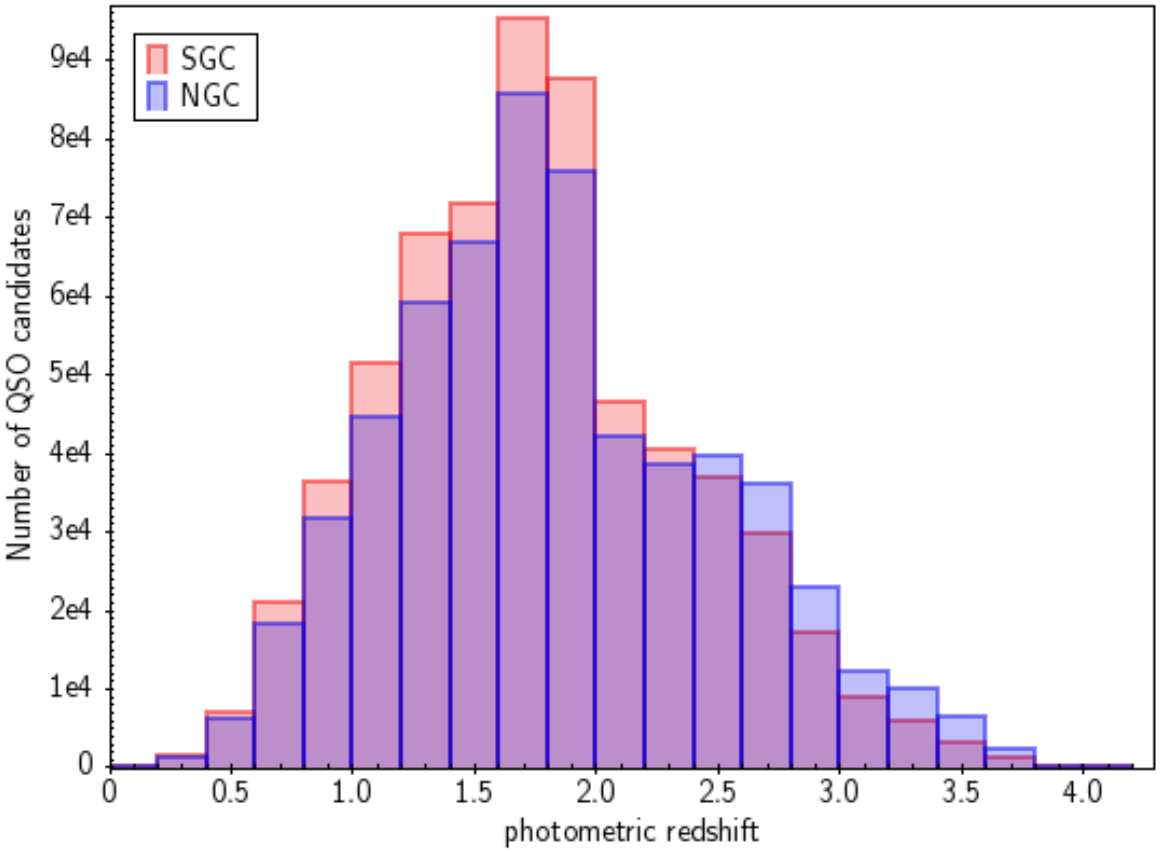

Figure 2.17: Photo-z distribution of our total QSO candidate catalogue over the full VST-ATLAS footprint, split into NGC and SGC sub-samples. Note that this is not weighted by area and that the NGC covers 2034 deg^2 and the SGC covers 2706 deg^2. The place where that makes the discrepancy the greatest between the NGC and SGC is at z>2.2, which is due to artefacts, or contamination, in the non-UVX selection.

Table 2.10: QSO number counts and sky densities from our three selections (Priority 1, star *grW* non-UVX, extended) applied to the full VST-ATLAS footprint, divided into $z_{\rm photo} < 2.2$ and $z_{\rm photo} > 2.2$ candidates based on ANNz2.

Sky Area	total candidates $z_{\rm photo} < 2.2$	total candidates $z_{\rm photo} > 2.2$
NGC (2034 deg^2)	431587	168151
NGC (deg^{-2})	212.2 deg^{-2}	82.3 deg^{-2}
SGC (2706 deg^2)	485670	143580
SGC (deg^{-2})	179.5 deg^{-2}	53.1 deg^{-2}
total sky (4740 deg^2)	917257	311731
total sky (deg^{-2})	193.5 deg^{-2}	65.8 deg^{-2}

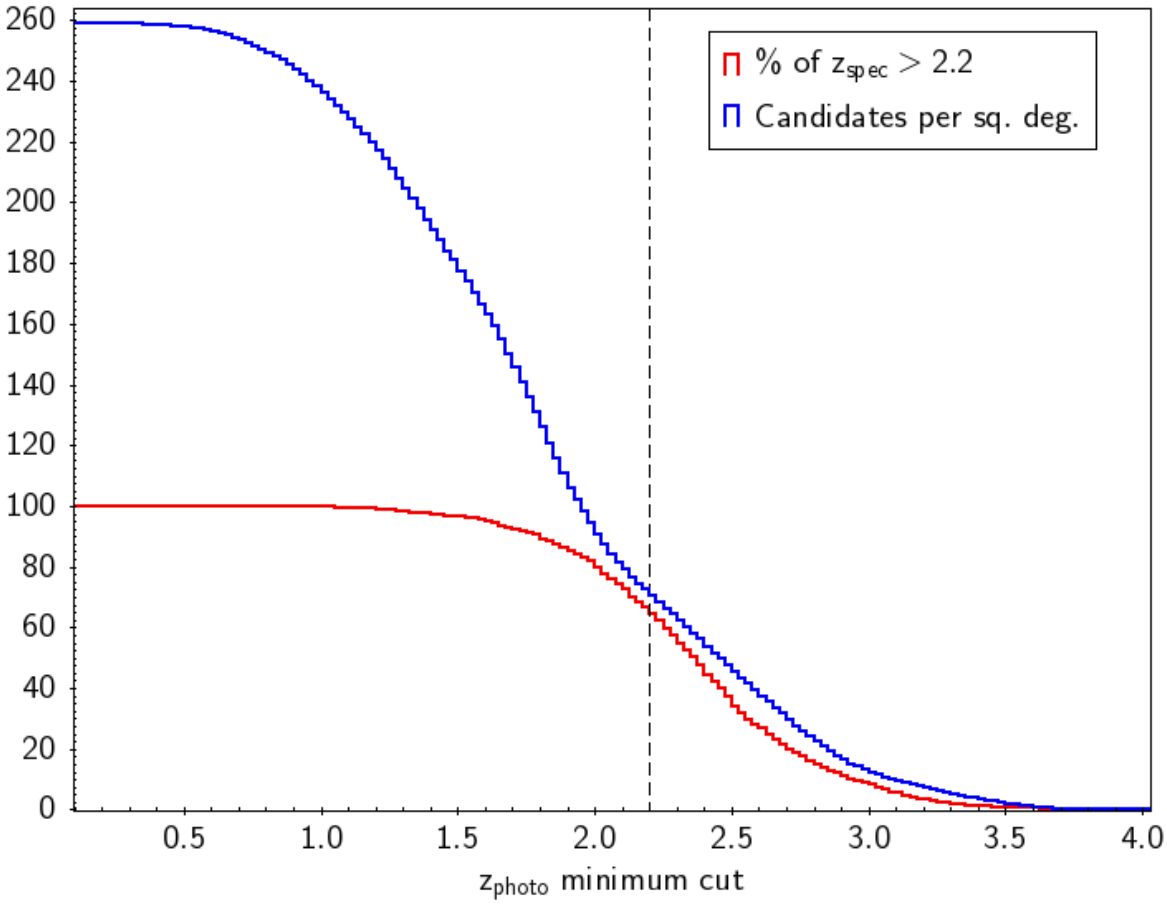

Figure 2.18: Dependence of QSO fractional completeness (as a percentage) with respect to the 1733 $z > 2.2$ QSOs detected by ATLAS (red line) and sky density of candidates per deg^{-2} (blue line) on $z_{\rm photo}$ minimum cut. Dashed line marks the nominal $z_{\rm photo} > 2.2$ cut.

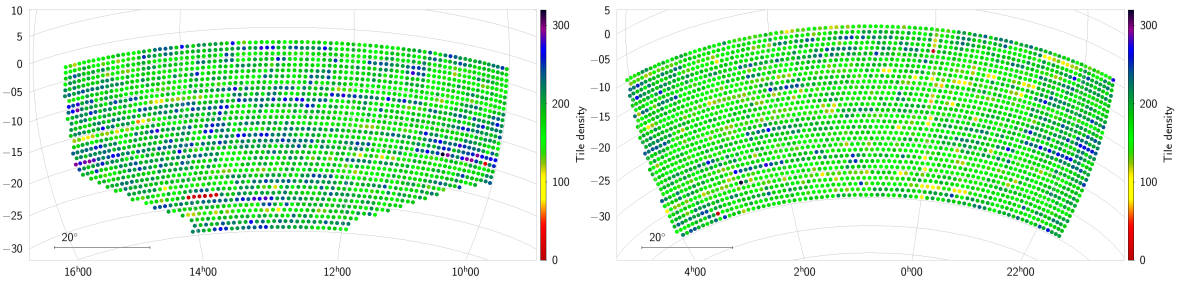

Figure 2.19: (a) VST-ATLAS tile density (deg^{-2}) for $z_{\rm photo} < 2.2$ QSO candidates in the NGC. (b) VST-ATLAS tile density (deg^{-2}) for $z_{\rm photo} < 2.2$ QSO candidates in the SGC. The slight gradient seen in the NGC (a) and the striping seen in both the NGC (a) and SGC (b) are discussed in the text.

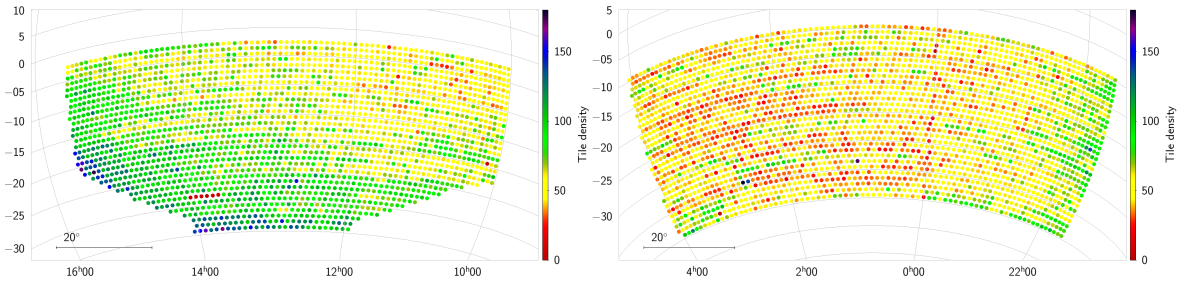

Figure 2.20: (a) VST-ATLAS tile density (deg^{-2}) for $z_{\rm photo} > 2.2$ QSO candidates in the NGC. (b) VST-ATLAS tile density (deg^{-2}) for $z_{\rm photo} > 2.2$ QSO candidates in the SGC. The slight gradient seen in the NGC (a) and the striping seen in both the NGC (a) and SGC (b) are discussed in the text.

ATLAS *ugriz* data, combining it with AllWISE W1 and W2 survey data. These datasets differ from those of Chehade et al. (2016) in that the sky coverage of ATLAS is now complete over its ≈4700 deg^2 and also in the depth of the *u*-band which generally has 240s exposure, 2× more than Chehade et al. (2016) mainly by virtue of the ATLAS Chilean Survey (ACE, Barrientos et al in prep.). In addition to the VST ATLAS *ugriz* photometry we have also replaced AllWISE with the WISE 6 year neo6 $W1$ and $W2$ MIR data (Meisner et al., 2021) that has 6× the 1 year exposure time of AllWISE. The neo6 W1 and W2 bands thus reach ≈ 1 mag fainter than the AllWISE survey data used by Chehade et al. (2016). We have also almost completed the DES *u* Chile Extension (DEUCE) which provides *u*-band coverage to similar depth over a further 2800 deg^2 of the DES survey, which will allow full $ugrizW1W2$ photometry over the full ≈7500 deg^2 of the 4MOST Cosmology Redshift Survey.

Here, we first used higher signal-noise William Herschel Deep Field (WHDF) *ugri* and SpiES W1, W2 data (Timlin et al., 2016) to establish the potential QSO sky density available to $g = 22.5$. WHDF has the benefit of a 75ksec Chandra exposure to help us assess what the eROSITA X-ray data might add to the 4CRS survey, in terms of further increasing the QSO sky density. We also determined that the inclusion of objects that have been morphologically classed as extended sources and with QSO $ugriW1W2$ colours provided the most complete QSO catalogue. Some of these sources are confirmed as extended sources even at HST 0.″1 resolution due to host galaxy contributions and gravitational lensing. Overall, WHDF data suggested that to $g < 22.5$ a QSO sky density of $\approx 269 \pm 67$ deg^{-2} was in principle available when X-ray and optically extended sources were included.

2.8.1 QSO statistics in the full ATLAS catalogue

Armed with the lessons learned from these analyses, we applied our selections to VST ATLAS *ugri* data, complemented by the W1 and W2 bands from the unWISE neo6 data release. We then suitably adjusted the cuts for ATLAS's less accurate photometry. This resulted in the full VST ATLAS QSO catalogue containing ≈ 1.2 million QSO candidates with a sky density of $\approx$259 deg^{-2}.

Despite the WHDF results suggesting that *grW* selections were the most complete, for VST ATLAS we still found improved efficiency and completeness when *u* band selections were included. The reason is that at VST ATLAS depth, despite ATLAS's excellent sub-arcsecond seeing in *g* and *r*, star-galaxy separation gets increasingly unreliable as we approach our $g = 22.5$ limit. Although the *grW* selection removes the main Galactic star populations with high efficiency, QSOs occupy the same $grW1$ locus as late-type galaxies and the more compact of these (NELGs) comprise our main contamination. We note that a $W1-W2 > 0.4$ criterion can also reduce galaxy contamination but the neo6 W2 data runs out ≈ 0.7 mag before our $g = 22.5$ limit. DESI take advantage of their deeper 'forced' W1 and W2 data to eliminate more galaxies. Here, we instead exploit our relatively deep 'forced' *u* data. We demand our candidates pass our joint UVX + *grW* cuts and similarly our joint *grW* + non-UVX cuts. This reduces our selected stellar QSO candidate density by $\approx 60\%$. If, instead of including the *u* data, we apply the strict $W1 - W2 > 0.4$ cut to the *grW* selection, effectively now demanding a $W2$ detection for all candidates, the sky density shows a bigger reduction to 147 deg^{-2}. However, in the latter case the completeness compared to DESI also drops from 83% to 78% including a 17% drop in the $z > 2.2$ range. We therefore utilize our *u* data as a more efficient way to reduce contamination while maintaining higher levels of completeness rather than imposing a strict $W1 - W2$ cut, in the absence of deeper $W2$ data.

We then used spectroscopically confirmed 2QZ, 2QDESp, SDSS eBOSS, DESI QSOs and also new, specially commissioned, 2dF observations of ATLAS QSO candidates to test our selections. The latter 2dF results suggest that we shall reach at least > 110 deg^{-2} at $z < 2.2$ and > 30 deg^{-2} at $z > 2.2$. But note these results assume we apply UVX + *grW* and non-UVX cuts simultaneously; if only the non-UVX cut was made a significantly lower $z > 2.2$ density would be found.

We find a completeness of 70% with respect to confirmed DESI QSOs for our total candidate sample, with an efficiency of 48%. Through comparing with 2QZ, 2QDESp, and eBOSS, we are able to see good completeness of $\approx 88\%$, with the brightest, stellar, ATLAS selections

giving $\approx 97\%$ completeness.

We performed a $g-$band number count comparison with the work done by Palanque-Delabrouille et al. (2016). These models are also used by DESI to determine their expected QSO number counts. We find that our observed number counts of 259 deg^{-2} at $g < 22.5$ are somewhat higher than the QSO sky density of 195 deg^{-2} predicted by their PLE+LEDE QSO luminosity function model. However, when the estimated efficiency and incompleteness of our sample is taken into account, the ATLAS QSO counts are expected to be in reasonable agreement with the model, although still lower than the WHDF QSO sky density of $\approx 269 \pm 67$ deg^{-2}, given the WHDF's advantage of having much deeper Chandra X-ray, Spitzer SpiES W1 and W2 and optical data available.

2.8.2 QSO statistics in ATLAS catalogues split at $z_{\rm photo} = 2.2$

Applying the ANNz2 algorithm of Sadeh et al. (2016) to our final QSO candidate catalogue provided photometric redshift estimates for all catalogue members. The resulting QSO candidate sky density over our full $\approx$4740 deg^2 is 194 deg^{-2} for the $z < 2.2$ 'tracer' QSO candidate catalogue and 66 deg^{-2} for the $z > 2.2$ LyA QSO candidate catalogue.

We then estimated the true QSO sky densities for the ATLAS catalogues split at $z_{\rm photo} < 2.2$ and $z_{\rm photo} > 2.2$, finding true sky densities of 100 deg^{-2} at $z < 2.2$ and 36 deg^{-2} at $z > 2.2$. Adding eROSITA X-ray data should then increase our $z < 2.2$ sky density to ≈ 130 deg^{-2} with our $z_{\rm photo} > 2.2$ sky density remaining at ≈ 36 deg^{-2}. These estimates ignore the ± 0.4 photo-z error, and from Fig. 2.18 we found that the best trade-off between completeness and efficiency in our high redshift sample is with a cut at $z_{\rm photo} > 1.9$. Otherwise, we note that the highest overall completeness coupled with the lowest overall candidate sky density at $z > 2.2$ is best achieved via a combined redshift survey of the two photo-z samples simultaneously where there is no need to incur duplication of targets e.g. in the $1.9 < z_{\rm photo} < 2.2$ range.

2.8.3 Future applications of the VST ATLAS QSO catalogues

Further improvements to VST ATLAS QSO selection, including deeper unWISE data and also upcoming eROSITA X-ray data, mean that we are well positioned to exceed our target QSO sky densities of 130 deg^{-2} at $z < 2.2$ and 30 deg^{-2} at $z > 2.2$. Although the ATLAS QSO catalogues already include photometric redshifts that are accurate to $\sigma_z = 0.4$, more accurate spectroscopic redshifts will be needed to measure Redshift Space Distortions (RSD)

and Baryon Acoustic Oscillation (BAO) scales from QSO and Lyman α forest clustering to make the most accurate measurements of cosmological parameters.

This ATLAS QSO catalogue will be used as a basis for the QSO component of the 4CRS. With the addition of the DES area, this 4CRS QSO redshift survey will cover 7500 deg^2 of sky with a QSO target sky density of 240deg^{-2}. The 4MOST eROSITA AGN survey will also cover most of this area and contribute $\approx$55 deg^{-2} or $\approx$40% of the target $z < 2.2$ 'tracer' QSO sky density of $\approx$130 deg^{-2}. Thus by combining the ATLAS optical/MIR and eROSITA X-ray QSO surveys, we can produce a QSO redshift survey that is highly competitive for cosmology at a much reduced cost. As well as providing high-quality BAO and RSD measurements out to $z \approx 3.5$, the 4MOST QSO redshift survey will also give vital support to DES and LSST galaxy weak lensing analyses at lower redshift ($z < 1$) by constraining the crucial redshift distribution of the lensed galaxies via QSO-galaxy cross-clustering.

Meanwhile, in advance of 4CRS, in Chapter 3 we shall exploit the current ATLAS QSO photo-z catalogue to measure QSO lensing magnification caused by foreground galaxies, as well as by galaxy clusters from the VST ATLAS Galaxy Cluster Catalogue I (Ansarinejad et al. 2022), using the cross-correlation technique. We shall also similarly report, in Chapter 4, on measuring the lensing of Cosmic Microwave Background fluctuations by the QSOs themselves and combine all of these results to fit QSO Halo Occupation Distributions (HOD) and measure host halo masses.

Chapter 3

Weak Lensing Analyses

3.1 Introduction

In terms of understanding the nature of dark matter, gravitational lensing analyses are clearly of prime interest (e.g. Kaiser & Squires (1993), Kaiser (1998), Myers et al. (2003)). Here we are interested in exploiting weak lensing but more in terms of 'magnification bias' (e.g. Narayan & Nityananda 1985) rather than the usual weak shear which is based on distortion of background galaxies. This "magnification bias" causes the background objects to appear brighter than they actually are while reducing the apparent solid angle behind the foreground objects, causing an increase in QSO density at bright QSO magnitudes where the slope of their number count is steeper and a decrease at fainter magnitudes where their number counts are flatter. These studies of magnification bias have generally been done using a 2-D cross-correlation analysis on the sky of foreground galaxies and background lensed QSO sources.

Galaxy-quasar cross-correlation studies have been conducted since Seldner & Peebles (1979) detected a possible quasar excess around Lick catalogue galaxies. More recently, works by Boyle et al. (1988a), Williams & Irwin (1998), Myers et al. (2003), Myers et al. (2005) and Mountrichas & Shanks (2007) have used background 2QZ (Croom et al., 2005) quasars to detect the effect of galaxy and galaxy cluster lensing, and Scranton et al. (2005) have performed such lensing analyses using photo-z selected quasars from the Sloan Digital Sky Survey (SDSS). Myers et al. (2003) and Mountrichas & Shanks (2007) found a higher than expected amplitude of lensing magnification bias based on simple $\Omega_m = 0.3$ models that assumed galaxies traced the mass, and suggested there may be inconsistency with the standard ΛCDM model. However, Scranton et al. (2005) argued conversely that their SDSS results

were compatible with the standard ΛCDM model. Here, we perform a weak gravitational lensing analysis through a cross-correlation of background quasars and foreground galaxies and galaxy clusters using the VST ATLAS Quasar Catalogue defined in Chapter 2 to provide independent new data to further address the reasons for this apparent discrepancy. Here we present our results, their interpretation, and whether our results indicate the need for a high Ω_M model or if the currently accepted standard cosmological model is sufficient. We show that an anti-correlation is detected at faint quasar magnitudes and a positive correlation at detected at bright magnitudes as predicted by lensing. Through this cross-correlation we will be able to test halo occupation distribution (HOD) models and their assumed mass profiles over a wide range of halo masses.

We further apply these quasar lensing analyses to galaxy cluster and LRG samples. We also measure the lensing of the Cosmic Microwave Background (CMB) (Planck Collaboration et al., 2018) by our galaxy, LRG and cluster surveys through cross-correlations with the Planck CMB lensing map (e.g. Geach et al. 2019, Han et al. 2019), allowing us to directly compare results for the galaxy/LRG/cluster bias and halo masses with the quasar lensing results.

The outline of this chapter is as follows. The data used in this Chapter are described in Section 3.2. Section 3.3 describes the cross-correlation of foreground galaxy clusters with our quasar catalogue. Section 3.4 describes the cross-correlation of foreground galaxies with our quasar catalogue. We analyse HOD models in Section 3.5 and 3.6, where we also perform a cross-correlation of foreground LRGs with our quasar catalogue. We discuss our results in Section 3.7.

3.2 Data

3.2.1 Quasar Sample

The VST-ATLAS quasar catalogue described in Section 2 has a certain amount of stellar and galaxy contamination, an inevitable consequence of requiring high quasar completeness. To perform these weak lensing analyses we use a more conservative, point-source only selection of our quasar catalogue to reduce galaxy contamination as well as possible overlap in the galaxy and quasar catalogues. We use the quasar candidate catalogue with the $ugri + giW1W2$ cuts

described in Ch. 2.4. We then further restrict this stellar candidate selection to $17 < g < 22$.

Following an analysis of preliminary spectroscopically confirmed QSOs (see Sec. 2.5.2), we also restrict this sample to $-0.25 < (g - r) < 0.4$, $(u - g) < 0.55$, $(r - W1) < 5$, and require $(W1 - W2) > 0.4$, again to reduce the possibility of galaxy contamination in our sample. Of this more conservative selection, we only consider quasar candidates with photometric redshifts $z > 1$ to prevent overlap in real space of quasar and galaxy samples, using results from the ANNz2 photometric redshift estimation (see Sec. 2.7). We also mask areas around Tycho stars to $V_T < 12.5$ following the method of Ansarinejad et al. (2023). Also masked are globular clusters and dwarf galaxies as well as a few areas with poor photometry. These selections result in a total of 204264 objects giving us a quasar candidate sky density of 44deg^{-2}, shown in Fig. 3.1.

3.2.2 Galaxy Cluster Sample

We use the VST ATLAS Southern Galaxy Cluster Catalogue (Ansarinejad et al., 2023) to perform the angular cross-correlations between foreground galaxy clusters and background quasars. The galaxy groups and clusters in this catalogue were selected using VST ATLAS optical photometry in the *griz* bands using the ORCA cluster detection algorithm (Murphy et al., 2012). The ORCA cluster detection algorithm finds similarities in galaxy colors and regions with a high projected surface density and then uses the friends-of-friends technique to determine galaxy clusters groups. The selection criteria is described in full by Ansarinejad et al. (2023). This cluster catalogue overlaps the full ~ 4700 deg^2 area of our VST-ATLAS quasar survey to a depth of $r_{Kron} < 21$.

We introduce the same Tycho stars and globular cluster mask as in our QSO catalogue. This galaxy cluster catalogue is then divided into clusters with 5 or more members ($n > 5$) and clusters with 40 or more members ($n > 40$). The resulting $n \geq 5$ catalogue has $N_g = 386268$ galaxies, with a galaxy cluster member sky density of 82.18deg^{-2} and a cluster sky density of 6.54deg^{-2}. The $n \geq 40$ catalogue has $N_g = 60210$, with a galaxy cluster member sky density of 12.81deg^{-2} and a cluster sky density of 0.19deg^{-2}.

Fig. 3.2 shows a patch of sky in the SGC from our $n \geq 40$ galaxy group sample. The cross-correlations between the galaxy cluster and quasar catalogues are performed between quasars

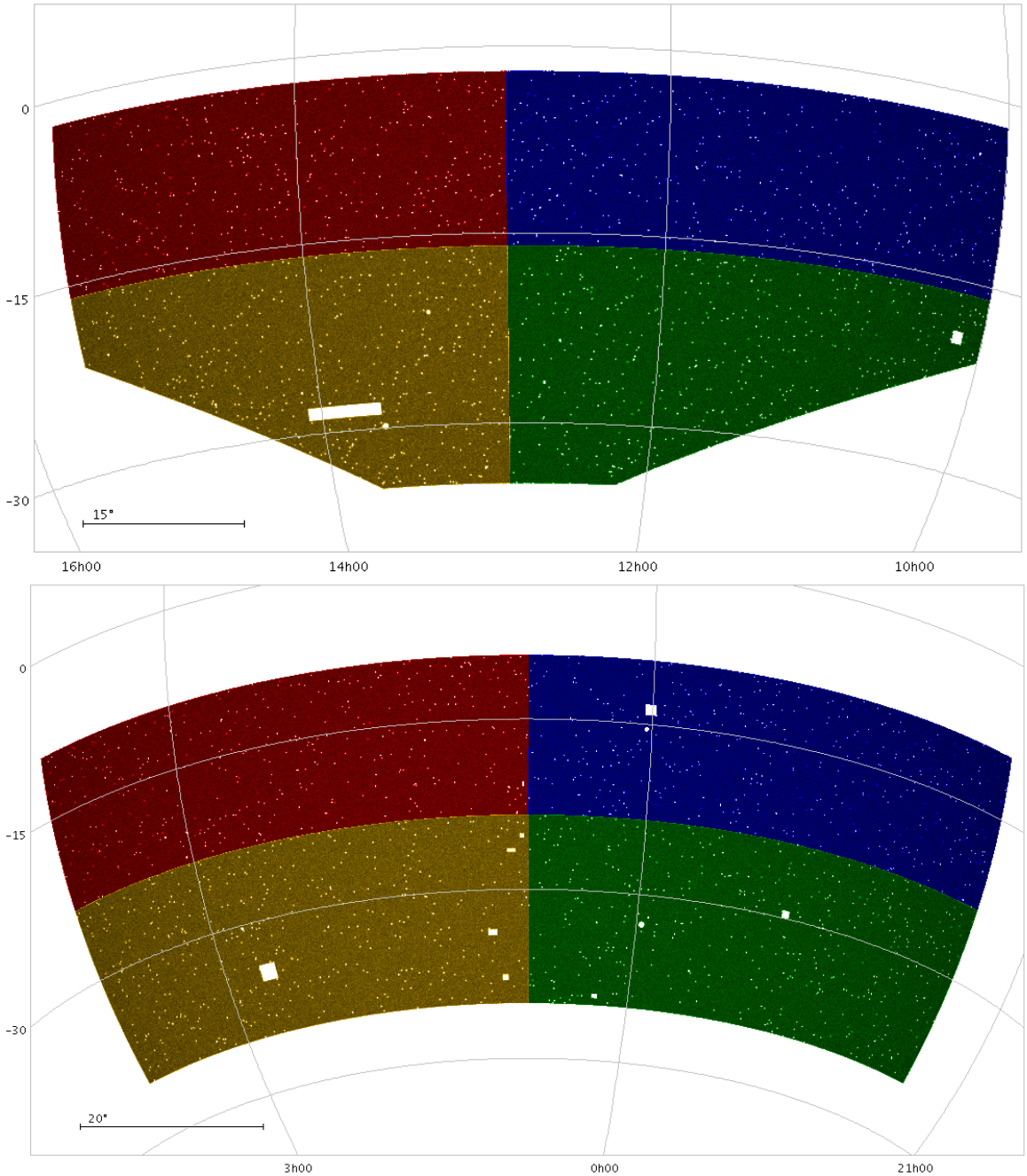

Figure 3.1: Map of our quasar candidates in the NGC and SGC, split into 8 equal area regions to calculate the error from field-to-field variations. We have masked out Tycho stars, globular clusters, nearby dwarf galaxies and areas that are underdense due to poor observing conditions. These are left as white areas in the map.

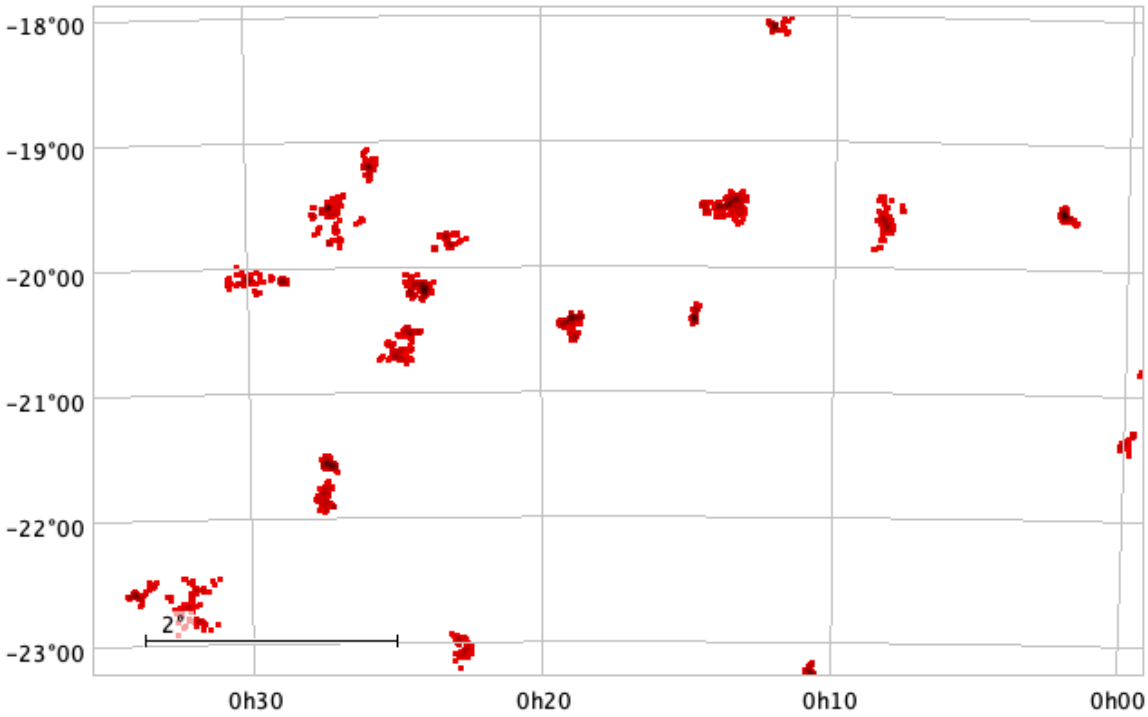

Figure 3.2: Sky map of defined $n \geq 40$ galaxy clusters in a section of the SGC with each point corresponding to a galaxy.

and individual members of each galaxy cluster rather than the center of the clusters. Therefore, the larger clusters are weighted more heavily.

3.2.3 Galaxy Sample

To perform the cross-correlation analyses of our quasar candidate catalogue and individual galaxies, we also generate galaxy catalogues from the VST ATLAS data using the same star/galaxy separation as for our QSO sample. To provide an accurate comparison to the work done on SDSS data by Scranton et al. (2005), we require the galaxies to have detections to $r_{sdss} < 21$, using a 0.15 mag offset (Shanks et al., 2015) to convert to the total r-band SDSS magnitudes, ie $r_{sdss} = r_{Kron} - 0.15$. We use the same Tycho stars and globular cluster mask for all of our catalogues.

3.2.4 Luminous Red Galaxy Sample

We perform cross correlation with LRGs to test HOD models in Section 3.6. To do this, we create a catalogue of LRGs based on the "Cut 1" $z < 0.4$ selection shown in Figure 3 of

Eisenstein et al. (2001), who get an LRG sky density of 14.3 deg^{-2}. Applying their selections on our galaxy catalogue as described in 3.2.3, we get a sample with a sky density of 9.3 deg^{-2}. As this is lower than the 14.3 deg^{-2} sky density, we adjust the selection slightly from $r_{KRON} < 19.2$ and $r_{KRON} < 12.38 + 2.33 * (g - r) + 4 * (r - i)$ to $r_{KRON} < 19.5$ and $r_{KRON} < 12.68 + 2.33 * (g - r) + 4 * (r - i)$ to increase the density of LRGs we are getting to 16 deg^{-2}.

3.2.5 Star Control Sample

We create a subset of stars to check potential star contamination in the signal of our cross-correlations between galaxy clusters and quasars, galaxies and quasars, and finally LRGs and quasars. We select stars away from the W1 limit as we noticed that stars were being lost due to potential systematic effects, such as sky subtraction, near the W1 limit. We also go to the brighter limit of $g < 21$, than the $g < 22$ limit of our VST ATLAS catalogue to decrease potential contamination, creating a control sample that is as well positioned as possible to check our work.

As noted above, prior to selecting stars away from the W1 limit, we found anomalies where cross-correlation of galaxies and stars showed unexpected anti-correlation. This anti-correlation appeared to increase with galaxy apparent brightness. We also found that this anti-correlation was more evident in star samples that relied on stars selected at the faintest W1 and W2 neo6 magnitudes. The effect was reduced, but still not eliminated, when DECALS DR10 "forced" W1 and W2 photometry was used instead of neo6. We hypothesize that there may be a sky subtraction bias in W1 in the vicinity of bright galaxies where the sky brightness may be over-estimated. The effect was particularly evident in stars selected in $grW1$ to lie at $r - W1 < 2$. This selection is otherwise optimal in avoiding galaxy contamination (see Sec. 2.4) but since our QSO samples reach $g \approx r \sim 22$ this means the equivalent star sample reaches $W1 \sim 21$ compared to a neo6 limit of $W1 \sim 20$ so these samples suffer high incompleteness and will be more prone to the sky subtraction issue postulated above. When a control star sample with an $r - W1$ distribution more similar to the QSOs was used (i.e. $g - r > 3$ and $3 < r - W1 < 8$), this anti-correlation reduced significantly. We considered the possibility that galaxy contamination in this star sample might also contribute to this reduction. However, simple $g < 22.5$ star samples with no colour selection also gave no evidence of anti-correlation so we concluded that the star-galaxy anti-correlation is only serious in star

samples too close to the $W1$ limit. In this case the effect on our QSO samples will be small. But we shall show the star-galaxy correlation results alongside the quasar-galaxy correlation results so that the size of any possible systematic effect can be judged.

3.2.6 CMB Lensing Data

We use the 2018 release of the Planck lensing convergence baseline map, using the CMB-only minimum variance estimates of the lensing signal to scales of $l = 4096$ (Planck Collaboration et al. (2018)), to perform cross-correlations with our galaxy, galaxy cluster, and LRG samples. Small angular scales correspond to a high l value as $\theta \sim \frac{180\,\mathrm{deg}}{l}$. The Healpix a_{lm} are first smoothed with a Gaussian filter with a FWHM of 15 arcmin. We then convert this baseline Minimum Variance lensing map from the stored convergence spherical harmonics a_{lm} to a Healpix map (as done by Geach et al. (2019)) with nside= 2048 and an $l_{max} = 4096$. This then gives us a list of RA and DEC coordinates of the healpix pixel centers. We apply the lensing mask provided by the Planck Collaboration et al. (2018) to the CMB data and select two areas that overlap our $\sim 4700\mathrm{deg}^2$ QSO sample. The lensing convergence maps we use in our work are shown in Fig. 3.3.

3.2.7 Possible systematic effects

Contamination of the QSO sample by stars or galaxies will show different effects on our cross-correlation results. Star contamination will dilute bright and faint cross-correlations by the fraction of stars in the QSO sample. However, the $grW1$ cut we make is very efficient at removing stars at the $g < 22$ magnitude range of our QSO sample. So the main QSO contaminant is likely to be galaxies in the same redshift range as the $r < 21$ galaxy sample and this will reduce galaxy QSO anti-correlation at faint magnitudes while increasing galaxy-QSO cross-correlation at bright QSO magnitudes. However, the restricted version of our quasar sample which we are using reduces this contamination (see Section 4.2.1). We shall see that the level of agreement between the positive and negative cross-correlations seen at bright and faint QSO magnitudes with a lensing model can be taken as confirming this low level of galaxy contamination.

A similar argument applies to any dust obscuration associated with the foreground galaxy population, since this would increase the anti-correlation at faint QSO magnitudes while decreasing the positive signal at bright magnitudes, producing disagreement with the lensing

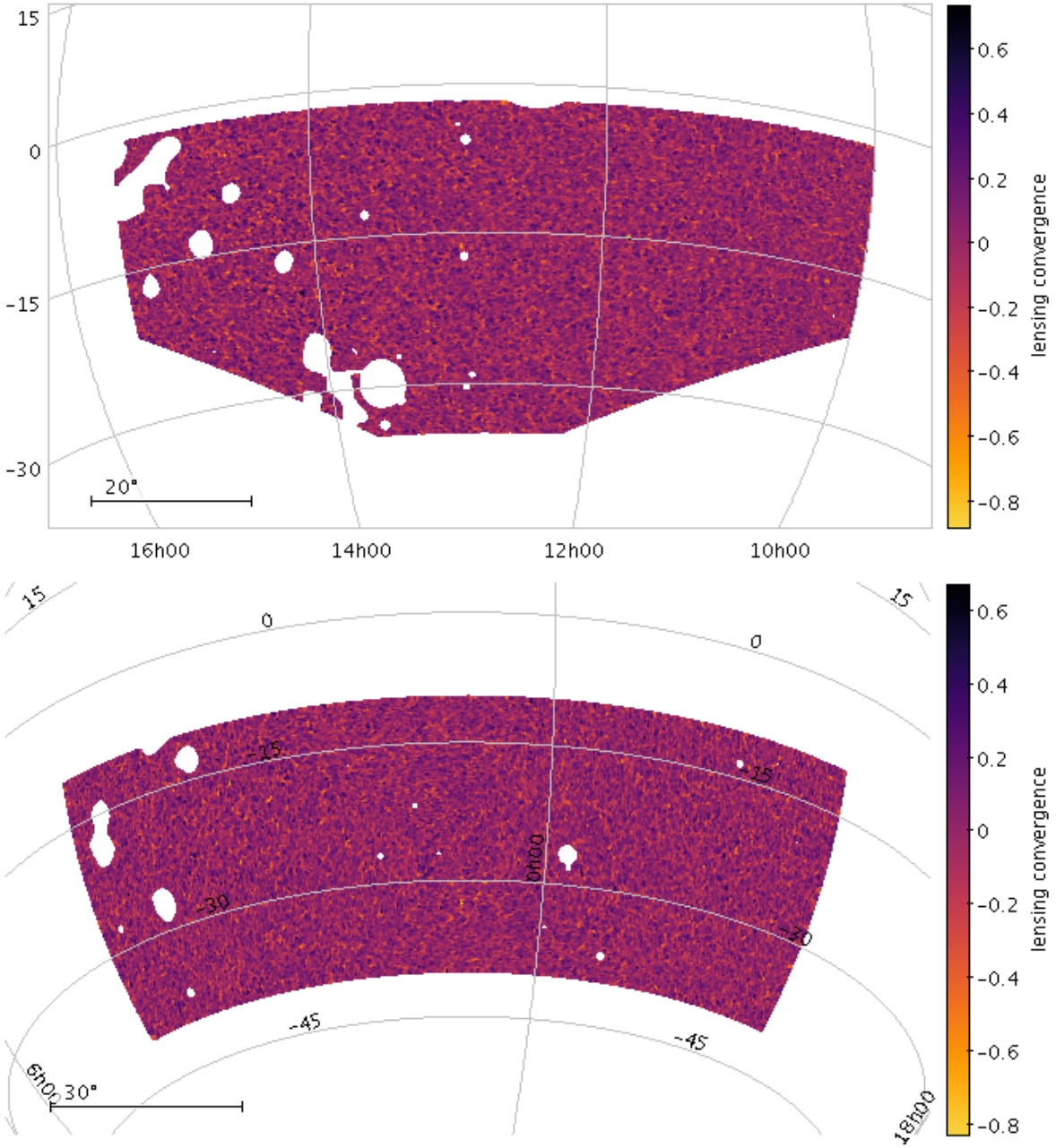

Figure 3.3: The CMB lensing convergence map in the NGC and SGC, with RA in hms on the x-axis and DEC in degrees on the y-axis. The masked areas are left in white.

model. Ménard et al. (2011) did find evidence for dust effects in the SDSS galaxy-QSO cross-correlations but they were highly sub-dominant with respect to the lensing effect. We tested limiting our QSO sample in the W1 band and compared the galaxy-QSO cross-correlations to those found in the g-limited QSO samples and again found little difference between the two, implying that lensing dominates our cross-correlation results.

The other major systematic was the possible sky subtraction issue in W1,W2 in the vicinity of bright galaxies, as mentioned in Sec. 3.2.5. This evidenced itself in a strong anti-correlation between bright galaxies and stars. However, the effect reduced when the star control sample was selected to have r-W1 colours more similar to the QSOs (see Section 3.2.5) and we show these galaxy-star cross-correlations alongside the galaxy-QSO versions in Figs. 3.4, 3.9, and 3.13, for comparison purposes.

3.3 QSO - Galaxy Cluster Lensing

3.3.1 Cross-Correlation Method

We use the data samples described in Section 3.2 to make a weak gravitational lensing analysis via a cross-correlation of background quasars and foreground galaxies and galaxy clusters. Following Limber's equation (Limber, 1953), we can express the 3-D correlation function (and power spectrum) as 2-D angular correlations. To calculate the angular cross-correlation, we need random data sets with the same input parameters as our quasar + galaxy/galaxy cluster samples. Therefore, we generate catalogues of uniformly distributed random points covering the same area as our survey with typically > 10 times as many sources as the observable data sets. These random catalogues are then also masked in the same manner as our data catalogues.

We use the publicly available Correlation Utilities and Two-point Estimates (CUTE) code Alonso (2012) to determine the angular cross-correlation of our samples. CUTE calculates the cross-correlation by using the normalized Landy-Szalay estimator for a two-point correlation function, defined as:

$$\omega_{GQ}(\theta) = \frac{D_G D_Q - D_G R_Q - R_G D_Q - R_G R_Q}{R_G R_Q}, \tag{3.3.1}$$

We check the output generated by the Landy-Szalay estimator by manually checking the D_GD_Q, D_GR_Q, R_GD_Q, and R_GR_Q outputs which we need to calculate the angular cross-correlation. Here D_GD_Q denotes the number of data-point pairs drawn from the galaxy sample and quasar sample with separation θ. For D_GR_Q the quasar sample is replaced with the sample of randomly distributed quasar points with the same angular selection function as the data. Similarly, for R_GD_Q the galaxy sample is replaced with our random galaxy sample. The R_GR_Q output is the number of data-point pairs drawn from the two random quasar and galaxy samples.

To generate error estimates from field-field variations, we divide the quasar and galaxy samples into 8 similarly sized $\approx 600deg^2$ regions, 4 in the NGC and 4 in the SGC. These fields are shown in Fig. 3.1. Then we estimate the standard errors of the cross-correlation by using the field-field error, with N being the number of fields:

$$\sigma_{\bar{\omega}(\theta)} = \frac{\sigma_{N_s-1}}{\sqrt{N_s}} = \sqrt{\frac{\sum(\omega_i(\theta) - \bar{\omega_i}(\theta))^2}{N_s^2 - N_s}}, \tag{3.3.2}$$

3.3.2 Quasar-Galaxy Cluster Lensing SIS Model

The lensing of the background objects depends on the mass profiles of the foreground objects. For galaxy clusters, we initially assume the simplest mass profile of a singular isothermal sphere (SIS). The deflection angle of sources by such foreground lenses is given by:

$$\alpha = \frac{4GM(<b)}{bc^2} = \frac{D_s}{D_{ls}}(\theta - \theta_q), \tag{3.3.3}$$

(e.g. Myers et al. 2003) where b is the impact parameter, $M(<b)$ is the mass contained within the radius of the lens, D_s is the angular diameter distance from the observer to the source, D_{ls} is the angular diameter distance from the source to the lens, θ is the angle from the observer's line of sight to the image, and θ_q is the angle from the observer's line of sight

to the source quasar.

We see an increase in apparent brightness/magnitude of the background object as the surface brightness of the object is conserved, but spread across a larger surface area. Therefore the flux received from the object is increased. The magnification, A, of the object due to a foreground lens can be described as:

$$A = |\frac{\theta}{\theta_q}\frac{d\theta}{d\theta_q}| \tag{3.3.4}$$

On the assumption of lensing by a SIS, the mass surface density is:

$$\Sigma_{SIS} = \frac{\sigma^2}{2Gr} \tag{3.3.5}$$

where σ is the velocity dispersion of the SIS and the density goes as $\rho(r) = \frac{\sigma^2}{2\pi G r^2}$. This can be integrated over a radius of $r = 0$ to $r = b$ and combined with Eq. 3.3.3 to give the amplification due to a SIS of a background source at radius θ:

$$A = |\frac{\theta}{\theta - 4\pi(\frac{D_{ls}}{D_s})(\frac{\sigma}{c})^2}| \tag{3.3.6}$$

This amplification factor can also be described as the ratio of the lensed flux and the unlensed flux (Croom (1997)). As the amplification affects the relative distribution of background and foreground objects, we can relate the angular cross-correlation to the amplification factor through:

$$\omega(\theta) = A^{2.5\alpha-1} - 1 \tag{3.3.7}$$

where α is the slope of the cumulative source number count, $dlog(N)/dm$. Zero correlation is predicted at $\alpha = 0.4$ with an anti-correlation at $\alpha < 0.4$, and a positive correlation at $\alpha > 0.4$.

In our model, we use the flat ΛCDM cosmology, with $\Omega_M = 0.3$ and $\Omega_\Lambda = 0.7$. We assume an average foreground galaxy sample and galaxy cluster redshift of $z = 0.15$ and an average

quasar sample redshift of $z = 1.5$. This gives us an angular diameter distance of the quasar sample $D_S = 1780$ Mpc and $D_{LS} = 1235$ Mpc. We also use a lensing coefficient of $2.5\alpha - 1 = -0.37$ for the faint QSOs with $20 < g < 21$ and $2.5\alpha - 1 = 0.95$ for the bright QSOs with $17 < g < 19$ taking these and other values from Table 1 of Scranton et al. (2005) for consistency with their assumptions.

3.3.3 Quasar-Galaxy Cluster Lensing NFW Model

Similar to modelling the cluster lensing via SIS we next model the clusters using an (Navarro et al., 1996) NFW model. We follow this route here because the HOD approach for clusters is less developed than for galaxies. Nevertheless, for computational convenience we use the Cosmology and HalO Model Python code (CHOMP), which is a halo modelling package written by Morrison, Scranton, and Schneider to produce the projected, lensed NFW mass profile which in 3-D takes the form:

$$\rho(r) = \frac{\rho_s}{(r/r_s)(1 + r/r_s)^2}, \tag{3.3.8}$$

with a characteristic density, ρ_s and scale radius, r_s. CHOMP also assumes that halo concentration is a function of halo mass with the functional form $c(m) \approx 9(m/m^*)^{-0.13}$ taken from Bullock et al. (2001). We then compute these projected, lensed NFW mass profiles by simply isolating the NFW part of the 1-halo term produced by CHOMP. Full details of the 1- and 2-halo terms and their projection and magnification as implemented in CHOMP are given by Jain et al. (2003) and will be further summarised in Section 3.5.

3.3.4 Quasar-Galaxy Cluster Cross-Correlation Results

We perform the cross-correlation of our $n > 5$ and $n > 40$ galaxy cluster catalogues with our $17 < g < 19$ and $20 < g < 21$ quasar samples. We test the robustness of our detections by performing the cross-correlations with star samples in the same magnitude ranges. We can see in Fig. 3.4 a clear anti-correlation with the faint, $20 < g < 21$, quasar samples for both the $n > 5$ and $n > 40$ galaxy clusters. The cross-correlations with both the bright and faint star samples show virtually zero correlation in comparison, making a strong argument for the reality of our detected cluster-quasar cross correlation signals at both bright and faint QSO

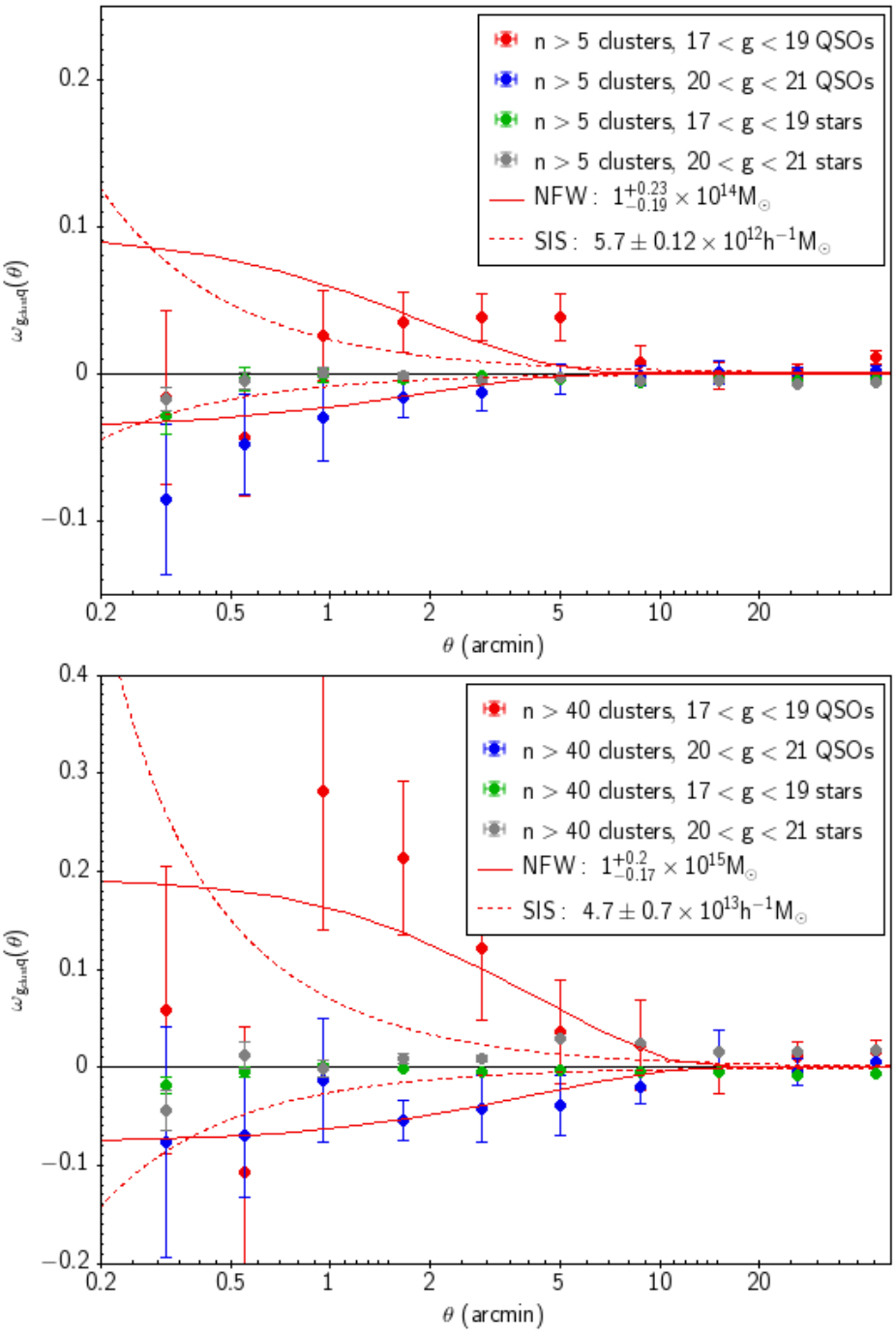

Figure 3.4: Results of the cross-correlation of both our bright and faint quasar candidate catalogues in the $g-$band and the VST ATLAS galaxy cluster catalogue for clusters comprised of n>5 and n>40 galaxies, using the CUTE code for angular cross-correlation. The SIS model here has a velocity dispersion of $270 kms^{-1}$ and $460 kms^{-1}$ and the HOD models are using a halo mass of 10^{14} solar masses for the the $n > 5$ galaxy clusters, and a halo mass of 10^{15} solar masses for the $n > 40$ galaxy clusters. The positive models are for the bright QSO-galaxy cluster cross correlation results and the negative models are for the faint QSO-gal clust cross correlation results.

Table 3.1: Summary of results for galaxy cluster masses. w_{cq} denotes the cluster-QSO cross-correlation, shown for the SIS and NFW cases, and $w_{c\kappa}$ is the cluster-CMB cross-correlation. A2023 cluster masses are estimated by Ansarinejad et al. (2023).

Method	n>5 Mass ($10^{13}\mathrm{h}^{-1}M_\odot$)	n>5 (χ^2_{red})	n>40 Mass ($10^{13}\mathrm{h}^{-1}M_\odot$)	n>40 (χ^2_{red})
w_{cq} SIS	0.57 ± 0.12	1.8	4.7 ± 0.7	2.0
w_{cq} NFW	10.0 ± 2.1	1.6	100 ± 20	0.5
$w_{c\kappa}$ NFW	3.2 ± 0.7	3.2	32 ± 12	1.1
A2023	23 ± 8	–	43 ± 27	–

magnitudes in Fig. 3.4.

We perform a χ^2 test for both the SIS model and the NFW based HOD model on the cross-correlation results in order to determine which model describes our data best. To do this, we use the inverse variance weighted mean of the bright and faint QSO cross-correlation results for both the $n > 5$ and $n > 40$ galaxy cluster cases. For the SIS model, we find that the $n > 5$ galaxy cluster - QSO cross-correlation has a best fit velocity dispersion of $\sigma = 270^{+50}_{-65}\mathrm{kms}^{-1}$ with a reduced χ^2 of 1.8 and the $n > 40$ galaxy cluster - QSO cross-correlation has a best fit velocity dispersion of $\sigma = 460^{+60}_{-80}\mathrm{kms}^{-1}$ with a reduced χ^2 of 2.0. Using the $M = \frac{2\sigma^2 r}{G}$ relation appropriate for an SIS model and taking $r = 0.17\mathrm{h}^{-1}\mathrm{Mpc}$ and $r = 0.48\mathrm{h}^{-1}\mathrm{Mpc}$ for $n > 5$ and $n > 40$ clusters respectively as empirically estimated from the cluster data themselves, these velocity dispersions correspond to masses of $5.7 \times 10^{12}\mathrm{h}^{-1}M_\odot$ for $n > 5$ clusters and $4.7 \times 10^{13}\mathrm{h}^{-1}M_\odot$ for $n > 40$ (see Table 3.1).

As for the SIS case, we perform a χ^2 fit to the w_{cq} with NFW profiles, finding that the $n > 5$ clusters are best fit by $10^{14.0\pm0.09}\mathrm{h}^{-1}M_\odot$ with a reduced χ^2 of 1.6 and the $n > 40$ cluster cross-correlations are best fit by $10^{15.0\pm0.08}\mathrm{h}^{-1}M_\odot$ with a reduced χ^2 of 0.5. Therefore, the NFW is a better fit for the galaxy cluster-QSO cross-correlation as the SIS generally appears to be too steep at small scales, while the NFW is better able to fit the dampening of the signal at small scales. The implied NFW mass for $n > 40$ clusters also is more in agreement with mass estimates presented by Ansarinejad et al. (2023), with a mean mass of our $n > 40$ galaxy cluster sample of $4.3 \pm 2.7 \times 10^{14}\mathrm{h}^{-1}\mathrm{M}_\odot$.

3.3.5 Galaxy Cluster - CMB Lensing Map Cross-Correlation

Galaxy cluster-QSO cross-correlation mainly probes the 1-halo term, whereas cross-correlation of the Planck CMB lensing convergence map with the galaxy clusters only constrains the 2-halo term due to the $\approx 6'$ Planck resolution. Nevertheless, we can check if the NFW profiles found to fit our QSO-galaxy cluster cross-correlations give halo masses consistent with the CMB lensing method. We model the CMB lensing by foreground galaxy clusters using the 5-parameter HOD methodology of Zheng & Weinberg (2007). We again employ the CHOMP halo modelling package and here use it more conventionally, to make 1-halo + 2-halo predictions, with the latter dominant. We assume the following HOD parameters $\log(M_0) = \log(M_{min})$, $\log(M_{1'}) = \log(M_{min}) + 1.08$, $\sigma_M = 0.4$ and $\alpha = 0.7$ with masses in solar mass units assuming $h = 0.7$. These parameters are used for values of $\log(M_{min}) = 12.0, 12.5, 13, 13.5, 14, 14.5, 15$ to probe a similar range of masses studied previously for both the SIS and NFW QSO lensing models. We assume a flat redshift distribution between $z = 0.01$ and $z = 0.36$ as an approximation for our cluster samples and a flat redshift distribution is also assumed for the CMB between $z = 1050$ and $z = 1150$.

Shown in Fig. 3.5, we see the result of cross-correlating the $n > 5$ and $n > 40$ galaxy clusters with the CMB lensing convergence map, along with the various HOD results. There is a potential smoothing at the smallest scales here due to the $6'$ resolution of the Planck CMB lensing convergence data. Therefore, the results in the bin at the smallest scale may be more systematically uncertain than indicated by the field-field error bars.

Performing a χ^2 fit of the models to the data we find that the cross-correlation of the $n > 5$ clusters with the CMB lensing convergence map is best fit by a HOD with $\log_{10}(M_{min}) = 13.5$ with a reduced χ^2 of 3.2, which is not a good fit. For cross-correlation of $n > 40$ clusters, we get a best fit model with $\log_{10}(M_{min}) = 14.5^{+0.03}_{-0.5}$ with a reduced χ^2 of 1.1, with the corresponding NFW 1-halo term from QSO lensing giving $\log(M_h) = 15$. In general, the cross-correlation of galaxy clusters with the Planck CMB lensing convergence map seem to agree with the NFW model results from QSO lensing in the previous section, although the $n > 40$ fit has a slightly lower 2-halo mass than the NFW fit for the 1-halo term. We see a more significant departure in the halo mass predictions of the SIS model with the SIS masses being $\approx 10\times$ smaller than the NFW masses, as summarised in Table 3.1. The average masses of the $n > 5$ and $n > 40$ clusters as estimated by Ansarinejad et al. (2023) are also given in

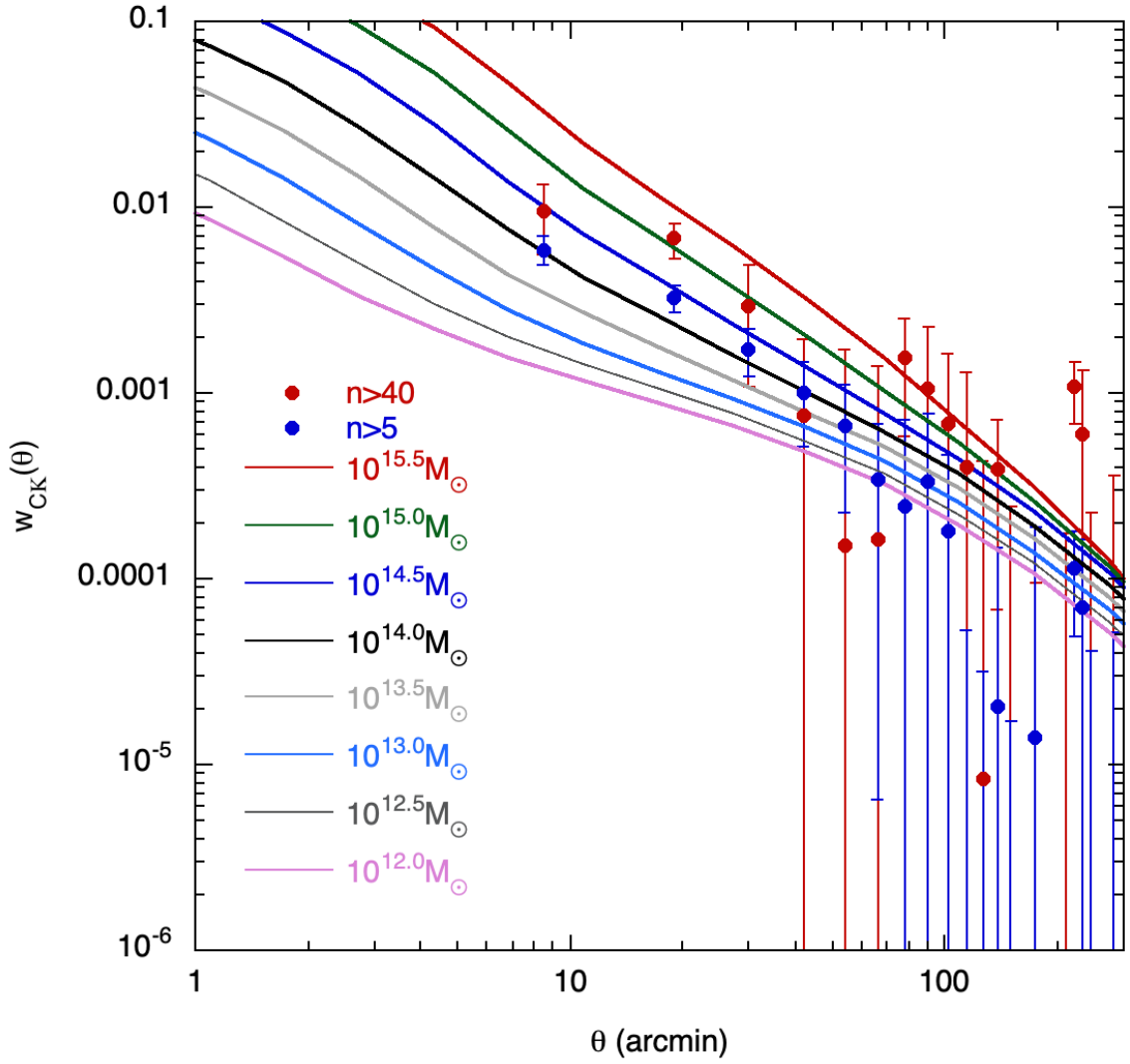

Figure 3.5: $w_{c\kappa}$ cluster-CMB cross-correlation functions for $n > 5$ and $n > 40$ clusters compared to $w_{c\kappa}$ predicted by supplying CHOMP with the Zheng & Weinberg (2007) HOD parameters of $\log(M_{min}) = 12.0, 12.5, 13, 13.5, 14, 14.5, 15$, $\log(M_0) = \log(M_{min})$, $\log(M_{1'}) = \log(M_{min}) + 1.08$, $\sigma_M = 0.4$ and $\alpha = 0.7$ with masses in solar mass units assuming $h = 0.7$. The models were integrated over the redshift range $0.01 < z < 0.36$ and $\sigma_8 = 0.8$ was assumed throughout.

Table 3.1. We see that for $n > 40$ clusters, our NFW lensing masses bracket the estimate of Ansarinejad et al. (2023) and so are in good agreement. For $n > 5$ clusters the QSO and CMB lensing masses are a factor of $\approx 2\times$ smaller than that of Ansarinejad et al. (2023) and so the agreement is less good here.

We conclude that for the richer, $n > 40$, galaxy clusters, the NFW density profile fits significantly better than the SIS profile at the small, 1-halo, scales probed by our QSO lensing results. Generally the SIS profiles are too centrally peaked compared to the QSO lensing data. At larger scales, the CMB lensing results for these richer clusters also suggest that they are well-fitted by a HOD model with a 2-halo term based on a ΛCDM cosmology. The estimated average mass for these richer clusters, assuming NFW/ΛCDM 1+2-halo terms, is in the range $3\times10^{14}-1\times10^{15}\mathrm{h}^{-1}\mathrm{M}_{\odot}$, in good agreement with mass estimates from Ansarinejad et al. (2023) and other authors.

For the less rich $n > 5$ groups and clusters, the QSO lensing statistics are poorer and here both the 1-halo NFW and the SIS models provide acceptable fits to these data. The best-fitting NFW model implies a mass of $\approx 1 \times 10^{14}\mathrm{h}^{-1}\mathrm{M}_{\odot}$ for this $n > 5$ sample, a factor of $\approx 2\times$ lower than the estimate of Ansarinejad et al. (2023) but in agreement within the errors. At larger scales, the CMB lensing signal for this $n > 5$ sample is strongly detected at a level almost as high as for the $n > 40$ sample. However, in this case, a HOD model based on a ΛCDM cosmology and where the minimum halo mass was allowed to vary in the range $1 \times 10^{12} < M_{\mathrm{min}} < 3 \times 10^{15}\mathrm{h}^{-1}\mathrm{M}_{\odot}$ could not be found to fit the CMB lensing data when fitted over the full $\theta < 300'$ range. The reason for this disagreement is currently unclear but will be further investigated in the work on galaxy lensing following in Sections 3.4 and 3.5.

3.4 QSO-Galaxy Cross-Correlation

We now turn to estimating foreground galaxy halo masses via the lensing of background QSOs, complemented by constraints from the angular autocorrelation function of the same galaxies. For the galaxy-QSO cross-correlations, we shall first use a model where galaxies trace the mass to connect with the previous studies of, e.g. Myers et al. (2003), before dropping this assumption and fitting HOD models (such as Scranton et al. (2005), Jain et al. (2003), Zheng & Weinberg (2007), etc).

3.4.1 Quasar-Galaxy Cross-Correlation Model

We first use the Williams & Irwin (1998) model, as outlined by Myers et al. (2005), to describe the correlation between our quasar sample and foreground galaxies. Although Myers et al. (2005) uses a galaxy sample to $g < 20.5$, we use a galaxy sample of $r < 21$ in order to match the magnitude limit of the SDSS galaxy sample of Scranton et al. (2005). This Williams & Irwin (1998) model (from here referred to as the WI model) bases predictions for w_{gq} on the auto-correlation, w_{gg}, of the galaxy sample and on the assumption that galaxies trace the mass. The lensing convergence κ is defined as:

$$\kappa = \frac{\Sigma(D_l, \theta)}{\Sigma_{cr}(D_l, D_s)}, \tag{3.4.1}$$

where D_l is again the angular diameter distance of the lens, $\Sigma(D_l, \theta)$ is the surface mass density of the lens, and $\Sigma_{cr}(D_l, D_s)$ is the critical mass surface density, defined in Myers et al. (2005) as $\Sigma_{cr}(D_l, D_s) = \frac{c^2}{4\pi G}\frac{D_s}{D_l D_{ls}}$.

We can estimate the effective convergence using the relation :

$$\kappa_{eff}(\theta) = \frac{3H_0^2 c}{8\pi G}\Omega_m(\delta_G - 1)\int_0^{z_{max}} \frac{(1+z)^3 \frac{dt}{dz} dz}{\Sigma_{cr}(z, z_s)}, \tag{3.4.2}$$

(see Myers et al. (2005), Williams & Irwin (1998)). Here, we take $z = 1.5$ as the median redshift of our quasar sample and the galaxy sample peaks at ~ 0.2, so we integrate to a redshift of $z_{max} = 0.3$ where the distribution drops to $\sim 20\%$. From this calculation, we find $\bar{\kappa} = 0.025$. The quasar-galaxy cross-correlation can then be modelled using the ω_{gg} and a Taylor expansion of Eq. 3.3.7. Therefore we predict the galaxy-quasar cross-correlation using:

$$\omega_{gq}(\theta) = (2.5\alpha - 1)\frac{2\bar{\kappa}}{b}\omega_{gg}(\theta), \tag{3.4.3}$$

where $\frac{\bar{\kappa}}{b} = \frac{\kappa_{eff}(\theta)}{(\delta_G - 1)}$. Here b represents the linear galaxy bias $b = \langle \delta_G - 1 \rangle / \langle \delta_M - 1 \rangle$. The r.m.s. galaxy fluctuation $\langle \delta_G \rangle$ will be estimated via ωgg, here represented by a power law

fit to our galaxy sample auto-correlation function (acf) which gives $\omega_{gg} = 0.142\theta^{-0.70}$ in the range $\theta < 120'$, as shown in Sec. 3.5.

In passing, we note the excellent agreement of the ATLAS $17 < r < 21$ galaxy w_{gg} with the equivalent SDSS w_{gg} of Wang et al. (2013) also shown in Fig. 3.9 (a). Given this SDSS-ATLAS acf agreement extends to $\theta = 8$deg. or $r_{com} \approx 90\mathrm{h}^{-1}$Mpc at the average galaxy redshift of $z \approx 0.22$, this represents a strong argument for the accuracy of these two independent results and also for the reliability of their parent datasets.

3.4.2 Quasar-galaxy cross-correlation results

The results of cross-correlating our ATLAS QSO catalogue in various magnitude ranges with our $17 < r < 21$ mag galaxy catalogue is shown in Fig. 3.6. Also shown is the HOD model from the SDSS results of Scranton et al. (2005) in blue, and the WI model described in the previous section is shown in red. At angular scales of $\theta < 5'$, we see a negative cross-correlation between ATLAS quasars and foreground galaxies at quasar g-band magnitudes of $g > 20$ whereas at brighter QSO limits we see a positive correlation. These are the same trends as seen by Scranton et al. (2005) and by Myers et al. (2003, 2005) previously and they are as expected from the basic theoretical lensing model described in Section 3.4.1.

To ease model comparisons between Scranton et al. (2005) (S05) and ourselves, we use the values for $\langle\alpha_{S05} - 1\rangle$=$\langle 2.5\alpha - 1\rangle$[1] listed in Table 1 and Fig. 2 of Scranton et al. (2005). Then, using our $w_{gg} = 0.142\theta^{-0.70}$ fit, with $\bar{\kappa} = 0.025$ and $(2.5\alpha - 1)$=-0.37, we see from Fig. 3.7 that the best fit for the galaxy bias is $b = 0.5^{+0.13}_{-0.09}$ for the ATLAS cross-correlation at $20 < g < 21$. In this χ^2 fit, the covariance between the ω_{gq} points is ignored since it is usually sub-dominant (Boyle et al., 1988a). As previously noted, these cross-correlation amplitudes are high as measured by the simple WI model since $b = 0.5$ corresponds to $\sigma_8 \approx 2$[2] when the usual range is $0.7 < \sigma_8 < 0.8$ (e.g. Planck Collaboration et al. (2020), Heymans et al. (2021)) i.e. $1.25 < b < 1.4$.[3] Certainly, the $b = 1.25$ (i.e. $\sigma_8 \approx 0.8$) model appears to give a poor fit

[1] Note that α_{S05} refers to a flux limited power law QSO number count, $N(> f)$ in the notation of Scranton et al. (2005), whereas in our notation α refers to a magnitude limited power law number count, $N(< m)$.

[2] If we assume $\sigma_{gg,8} \approx 1$ then $b = 1.25$ corresponds to $\sigma_8 = \sigma_{gg,8}/b \approx 0.8$ whereas $b = 0.5$ corresponds to $\sigma_8 \approx 2$.

[3] We note that assuming $\Omega_m = 1$ in eq 3.4.2 would also increase the cross-correlation amplitude and imply a fitted bias value of $b \approx 1.7$. Although this value is close to the expected $b = 2$ for this cosmology, this $\Omega_m = 1$ model is excluded by CMB + H_0 constraints and so we restrict our attention here to the standard cosmological model with $\Omega_m = 0.3$.

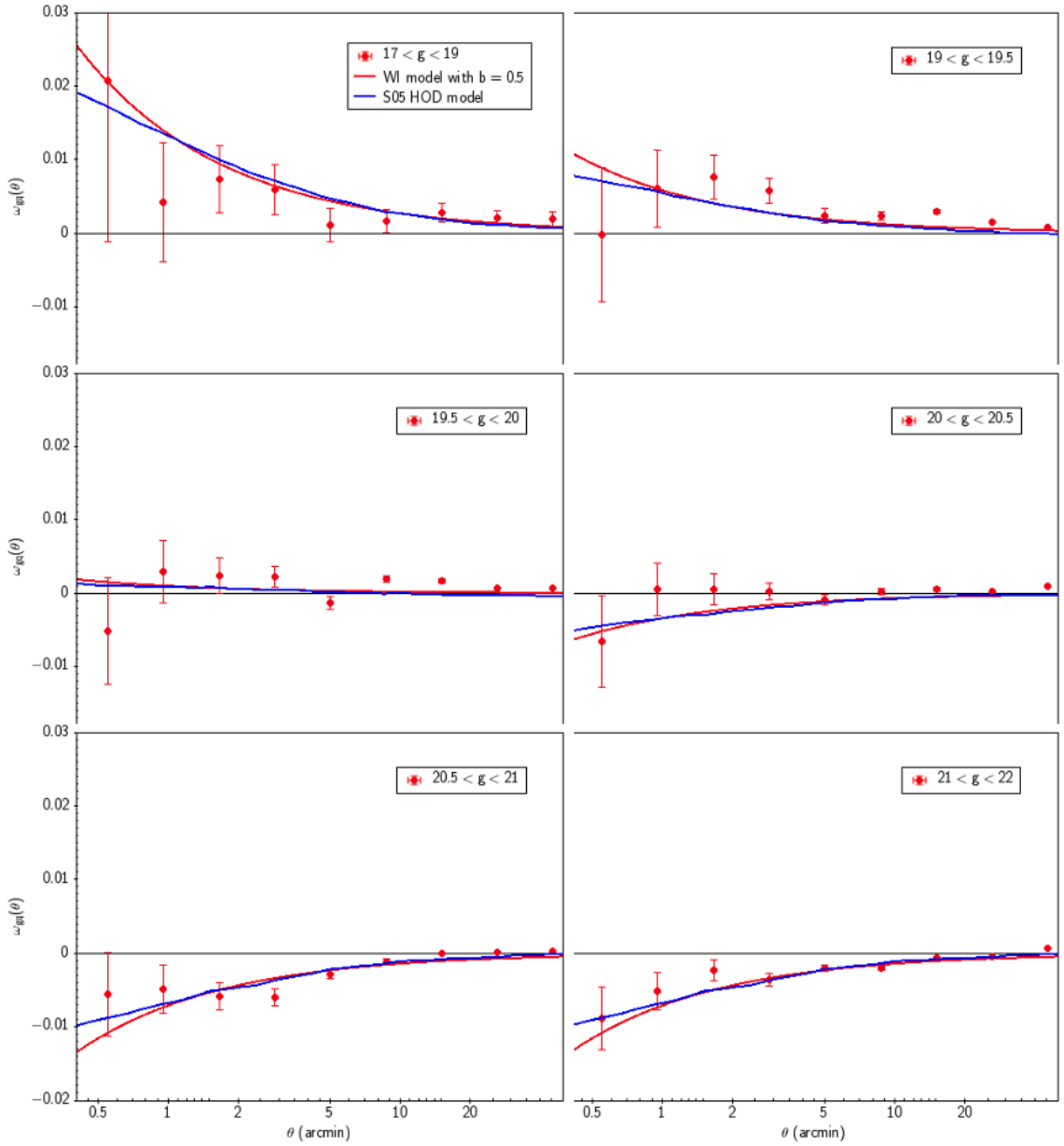

Figure 3.6: Cross-correlations of our quasar candidate catalogue at $17 < g < 19$, $19 < g < 19.5$, $19.5 < z < 20$, $20.5 < g < 21$, and $21 < g < 22$ and our VST ATLAS galaxy catalogue at $r < 21$, using the CUTE code for angular cross-correlation across the full sky. We also add the Scranton et al. (2005) HOD model for each of the quasar $g-$band magnitude bins. A bias value of $b = 0.5$ is consistently assumed for our WI model in red. The $\langle 2.5\alpha - 1 \rangle$ values for each QSO magnitude range for both our model and the Scranton et al. (2005) model are as follows: 0.95 for QSOs in the $17 < g < 19$ range, 0.41 for $19 < g < 19.5$, 0.07 for $19.5 < g < 20$, -0.24 for $20 < g < 20.5$, and -0.5 for $20.5 < g < 21$. We also assume this -0.5 value for the $21 < g < 22$ range.

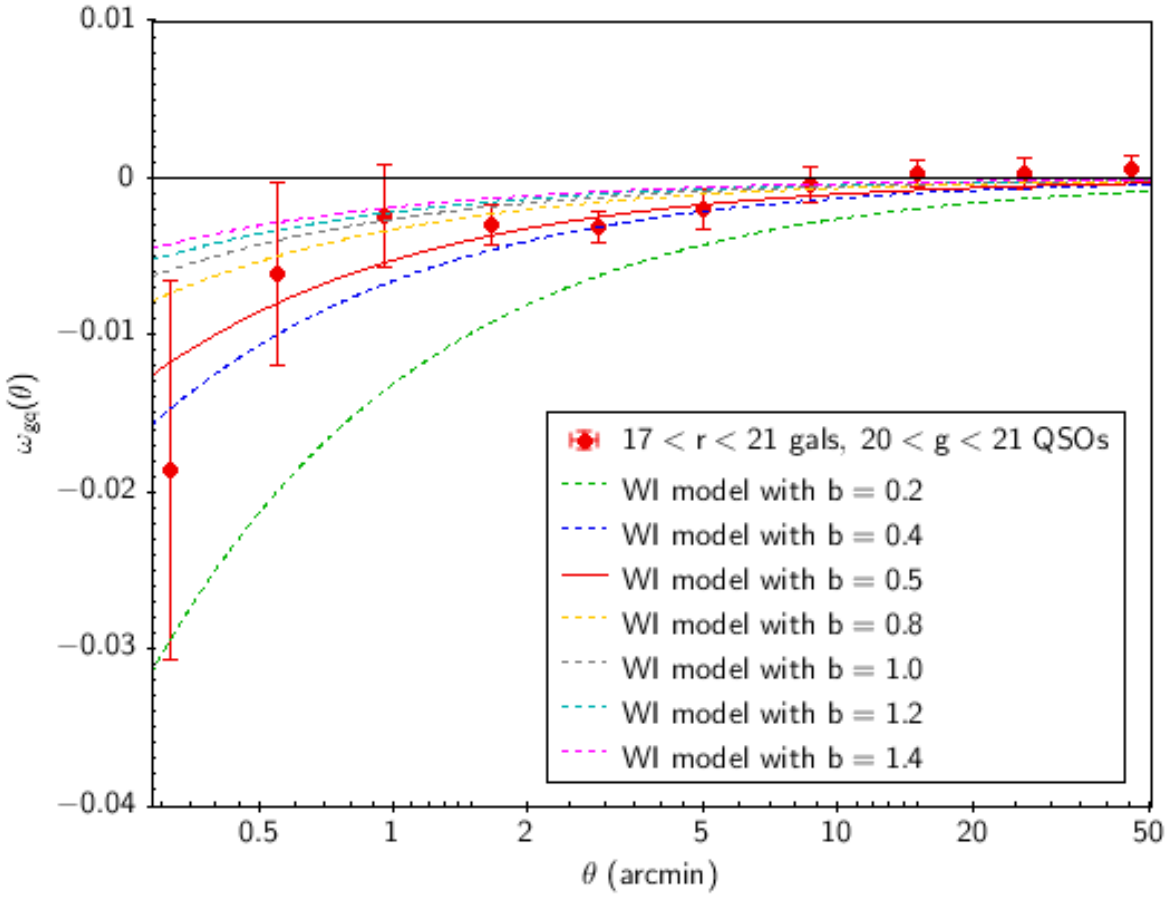

Figure 3.7: Our $\omega_{gg} = 0.142\theta^{-0.70}$ model fit, with $\bar{\kappa} = 0.025$ and $\langle\alpha - 1\rangle$=-0.37, with bias values of $b = 0.2$, $b = 0.4$, $b = 0.5$, $b = 0.8$, $b = 1.0$, $b = 1.2$, and $b = 1.4$ for our cross-correlation at $20 < g < 21$.

in Fig. 3.9(b). However, dropping the assumption that galaxies trace mass may mean that models can be found that are more consistent with ΛCDM.

So as previously suggested by Mountrichas et al. (2009), we first conclude that there is little disagreement in terms of the observed data between SDSS and our ATLAS results and that the main disagreement is between these two models. We further conclude that the Williams & Irwin (1998) assumption that galaxies trace the mass is unlikely to be correct, given that would imply $b = 0.5$ i.e. $\sigma_8 = 2$ in contradiction with all observed CMB power spectra. So models that drop this assumption, like the S05 HOD model, are likely to be required. However, the S05 HOD model may still underestimate the lensing signal, particularly at small $\theta < 0.'5$ scales. So in Section 3.5 we shall look for a HOD model that improves the w_{gq} fit while also simultaneously fitting the w_{gg} of our $17 < r < 21$ galaxy sample.

3.5 HOD models via quasar-galaxy lensing and galaxy-galaxy clustering

3.5.1 Modelling galaxy-galaxy angular correlations

We now make a further check of the Scranton et al. (2005) HOD model using their publicly available code from the CHOMP GitHub site written by Morrison, Scranton, and Schneider. The code follows Jain et al. (2003) in making predictions for both the angular auto-correlation function w_{gg} and the galaxy-mass cross-correlation function $w_{g\kappa}$ based on a mass power-spectrum, $P(k)$, and a HOD, with the average number of galaxies per halo of mass M being denoted by $< N(M) >$.

First, we have assumed the simple HOD model $< N(M) >= 1 + (M/10^{12.15})^{1.0}$ for $M > 10^{11.15} M_\odot$ (with $h = 0.7$) used by Scranton et al. (2005) and we use this to predict w_{gg} for the $17 < r < 21$ galaxy sample used here (see Fig. 3.8). We note in passing that Scranton et al. (2005) did not compare their observed and predicted w_{gg}. We find that this model with $\sigma_8 = 0.8$ over-predicts w_{gg} at $\theta < 5'$ and under-predicts it at larger, $\theta > 5'$, scales. This under-prediction of the 2-halo term relative to the 1-halo term seems a common characteristic of HOD models. Essentially, the observed w_{gg} seems to show a more exact power-law behaviour than the HOD models. Mead & Verde (2021) and references therein suggest that halo models generally underpredict the ΛCDM power-spectrum in the region between the 1-

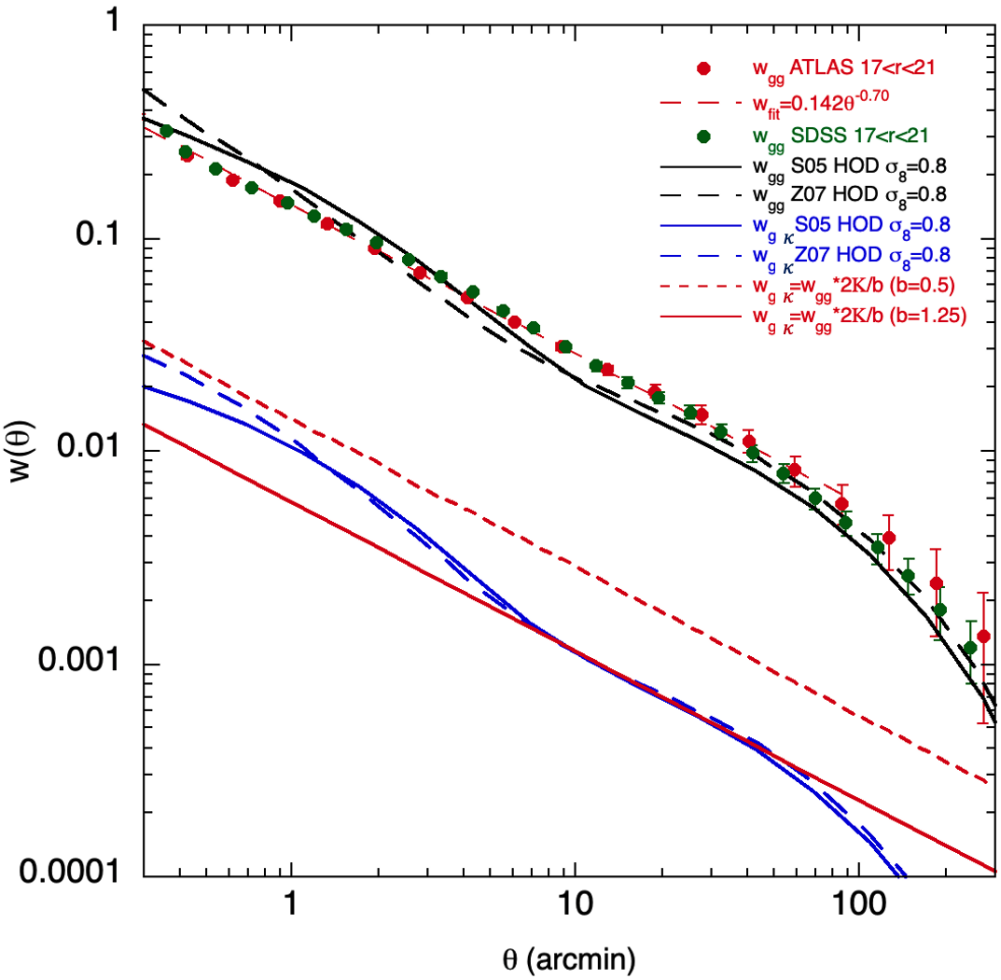

Figure 3.8: w_{gg} and $w_{g\kappa}$ auto- and cross-correlation functions predicted by the HOD models of Scranton et al. (2005) (S05) and Zheng et al. (2007) (Z07) (with $M_r < -20$). Both models assume $h = 0.7$ and $\sigma_8 = 0.8$. The w_{gg} model fitted for the $17 < r < 21$ galaxies is $w_{gg}(\theta) = 0.142\theta^{-0.70}$ (red, long dashes).

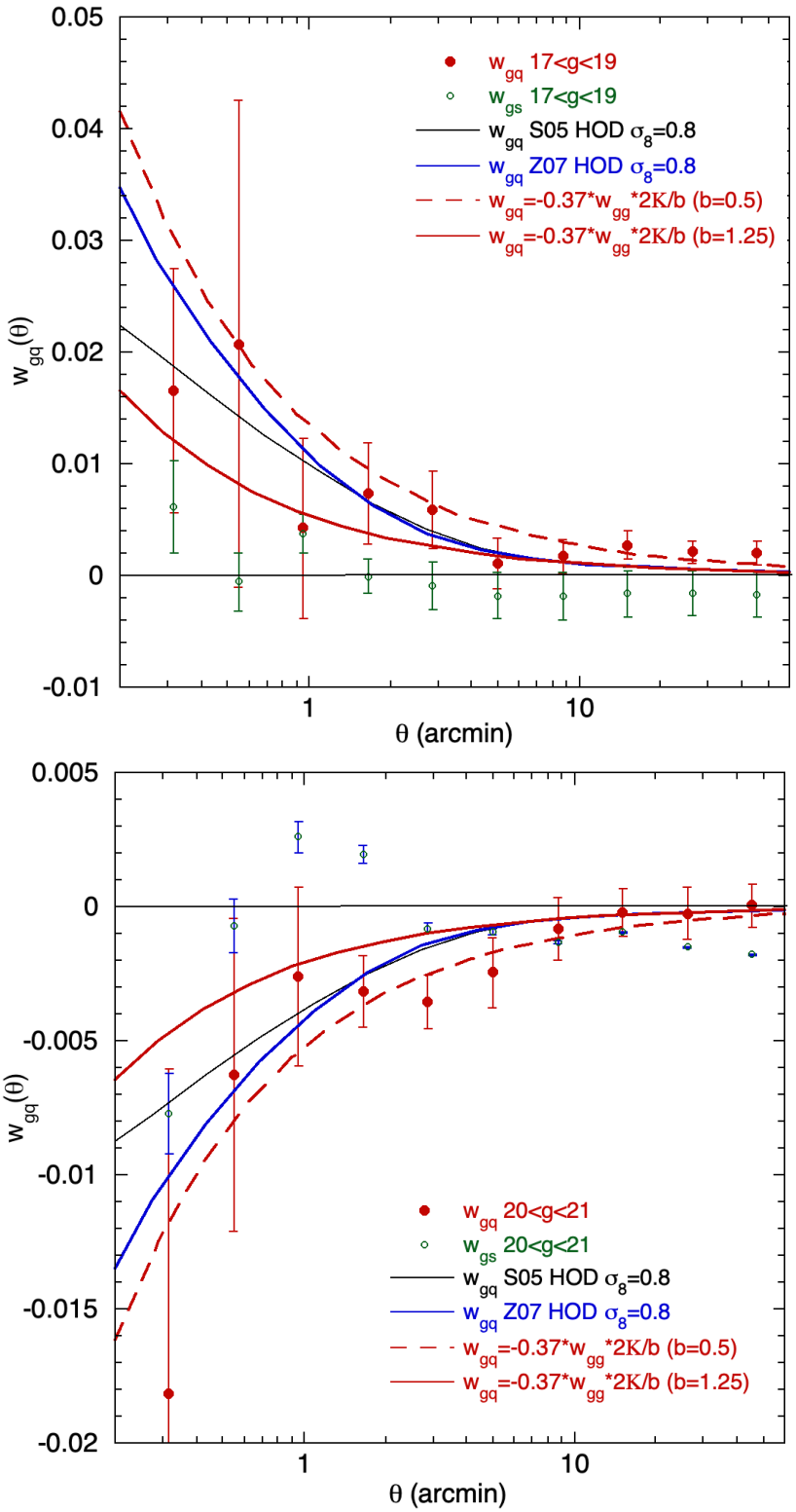

Figure 3.9: (a)The cross-correlation function, $w_{gq}(\theta)$, for $17 < g < 19$ QSO candidates and $17 < r < 21$ galaxies, compared to the two HOD models (S05 and Z07) and the two models of Williams & Irwin (1998) with $b = 1.25$ and $b = 0.75$. (b) The same as (a) for the $20 < g < 21$ limited QSO case.

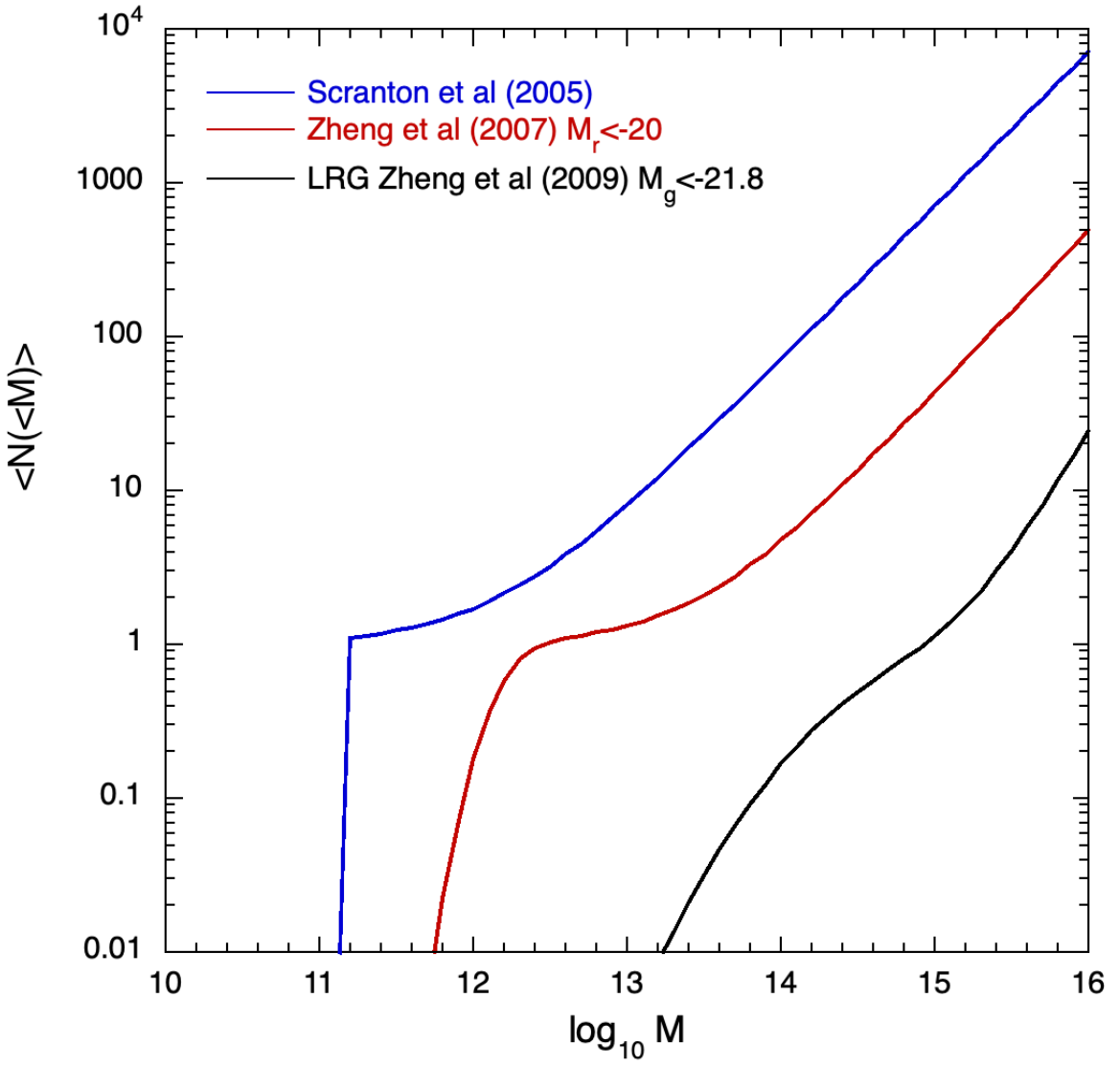

Figure 3.10: HOD models of Scranton et al. (2005) (with $\log(\mathrm{M_{min}}) = 11.15(11.0)$, $\sigma_M = 0.01$, $\log(\mathrm{M_0}) = 0.0$, $\log(\mathrm{M_1'}) = 12.15(12.0)$, $\alpha = 1.0$) and Zheng & Weinberg (2007) $M_r < -20$ model (with $\log(\mathrm{M_{min}}) = 12.17(12.02)$, $\sigma_M = 0.26$, $\log(\mathrm{M_0}) = 11.53(11.38)$, $\log(\mathrm{M_1'}) = 13.46(13.31)$, $\alpha = 1.06$). The LRG model is from Zheng et al. (2009) (with $\log(\mathrm{M_{min}}) = 14.45(14.30)$, $\sigma_M = 0.71$, $\log(\mathrm{M_0}) = 12.64(12.49)$, $\log(M_1') = 15.10(14.95)$, $\alpha = 1.35$). All masses assume $h = 0.7$ ($h = 1$).

and 2-halo terms. Indeed, Peebles (1974, 1980) expressed doubts as to whether a preferred (halo) scale could ever be produced by the smooth $1/r^2$ power-law behaviour of Newtonian gravity.

In searching for an improved HOD model, we then consider the HOD recommended for SDSS galaxies with $M_r < -20$ by Zheng et al. (2007) as an alternative to the simple S05 HOD. The parameters of this model are given in the caption of Fig. 3.10. This model produces slightly improved agreement with the ATLAS w_{gg} at both small and large scales. We also consider the range of HOD models fitted to SDSS semi-projected correlation functions $w_p(\sigma)$ by Zehavi et al. (2011) (see their Fig. 10 and Table 3) corresponding to galaxies with absolute magnitudes from $M_r < -18.0$ to $M_r < -22.0$ but no better fit to our $17 < r < 21$ w_{gg} is found.

In more general searches within the 5-parameter HOD scheme of Zheng et al. (2007), we still find it difficult to improve on the above SDSS $M_r < -20$ HOD as a description of the ATLAS w_{gg}. Given the excellent agreement of the ATLAS w_{gg} and the SDSS w_{gg} of Wang et al. (2013), also shown in Fig. 3.8, we have no reason to believe that this HOD fitting issue stems from the ATLAS data. So, bearing in mind these residuals at small and large scales, we shall consider the above two HOD models as reasonable fits and proceed to test them further using our weak lensing analyses.[4]

3.5.2 HOD modelling from galaxy-quasar lensing

We then continue to follow the method of Jain et al. (2003) to predict the $w_{g\kappa}$ cross-correlations, first assuming the Scranton et al. (2005) HOD. Having multiplied the model $w_{g\kappa}$'s in Fig. 3.8 by $(2.5\alpha - 1) = 0.95, -0.37$ for the bright $17 < g < 19$ and faint $20 < g < 21$ QSO samples respectively, we compare the Scranton et al. (2005) and Zheng & Weinberg (2007) HOD predictions to our w_{gq} results in Figs. 3.9(a, b). In turn, we compare these to the $w_{g\kappa} = w_{gg} \times 2\bar{\kappa}/b$ WI models with $b = 0.5$ and $b = 1.25$. The Zheng et al. (2007) HOD model seems to give a better fit than the Scranton et al. (2005) model in Figs. 3.9(a, b). with both models fitting these data better than the standard $b = 1.25$ ($\sigma_8 = 0.8$) WI model. Indeed, in Figs. 3.9 (a),(b) we see that the HOD model of Zheng et al. (2007) gives almost as good a fit as the best fit, $b = 0.5$, WI model. However, the errors are still large in Figs. 3.9(a,

[4]Fitting a -0.8 power law to our w_{gg} at $\theta < 60'$ and then applying Limber's formula gives a 3-D correlation function scale-length of $r_0 = 5\mathrm{h}^{-1}$ Mpc.

b) and we remain wary about the size of the small-scale ($\theta < 0.'5$) anti-correlation of the stellar control sample in Fig. 3.9(b). Another issue is that looking back at Fig. 3.8 we note that, at $\theta > 1'$, the predicted $w_{g\kappa}$ for the two HOD models with $\sigma_8 = 0.8$ lies significantly below the best fit, $b = 0.5$ (or $\sigma_8 = 2$), Williams & Irwin (1998) model implying that both sets of models cannot fit the data equally well on these larger scales. This motivates a more detailed study of the 1-halo term using LRGs in Section 3.6 below, while a further test of the 2-halo fit of the HOD models is available from the CMB lensing test in Section 3.5.3 below. However, our main conclusion at this point is that we confirm that HOD models can be found that simultaneously give reasonable fits to w_{gg} and w_{gq} at small scales and that these fit w_{gq} significantly better than simpler models that assume galaxies trace the mass with bias in the standard ΛCDM $b \approx 1.2 - 1.4$ (or $\sigma_8 \approx 0.7 - 0.8$) range.

3.5.3 Further Galaxy-CMB lensing test of HOD models

In Fig. 3.11 we show the $17 < r < 21$ galaxy - Planck CMB Lensing Map cross-correlation function compared to the predictions of the HOD models of Scranton et al. (2005) and Zheng et al. (2007). Here we see that the data is in reasonable agreement with the Scranton et al. (2005) model at all scales (with a reduced χ^2 of 2.67) and fits particularly well in the range $10' < \theta < 60'$ with a reduced χ^2 of 1.15, whereas the Zheng et al. (2007) model appears to over-predict the data at all scales (with a reduced $\chi^2 > 10$), despite its good fit to w_{gg} at $\theta > 20'$. We also note that the scales probed with the *Planck* map are mostly at the scales of the 2-halo term with $r_{com} \approx 1\mathrm{h}^{-1}$ Mpc corresponding to $\theta \approx 8'$ at the average galaxy redshift of $z = 0.15$. So CMB lensing at *Planck* resolution is clearly the test of choice for the 2-halo term while the galaxy QSO cross-correlation function in Fig. 3.9 (a),(b), with its scale extending down to $\approx 1'$, provides a better test of the 1 halo-term. Here we have seen that both Scranton et al. (2005) and Zheng et al. (2007) models give reasonable fits to w_{gq} but the Scranton et al. (2005) HOD fits the CMB lensing data better than the Zheng et al. (2007) HOD galaxy at larger scales, despite both HOD models fitting the w_{gg} equally well in this range dominated by the 2-halo term. But higher signal-noise data for QSO lensing and higher resolution data for CMB lensing should give further interesting tests of both the 1- and 2-halo terms of these galaxy halo occupation models independently over the full range of scales.

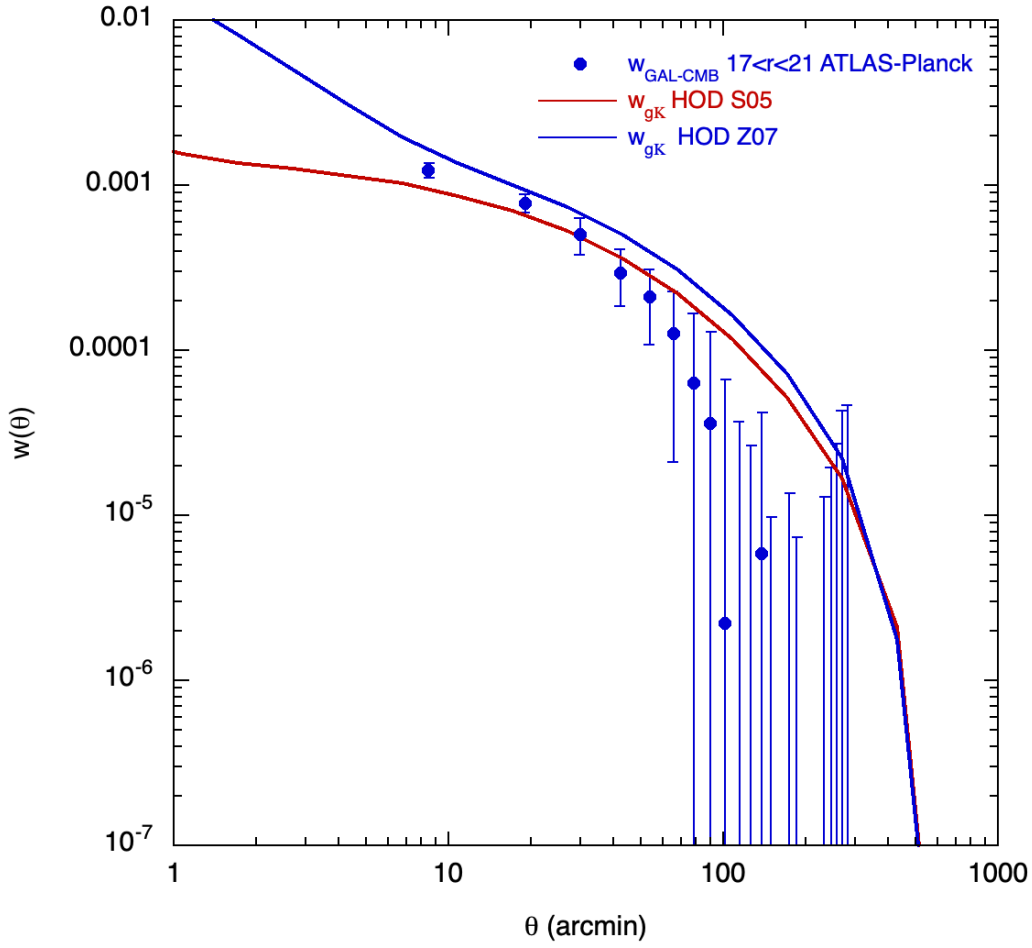

Figure 3.11: w_{g-CMB} cross-correlation function for $17 < r < 21$ galaxies and the Planck (2018) Lensing Map with field-field errors, compared to the HOD models of Scranton et al. (2005) and Zheng et al. (2007) (with $M_r < -20$). Both models assume $h = 0.7$ and $\sigma_8 = 0.8$. The first bin centre at $8'$ corresponds to ≈ 1 h^{-1}Mpc at the galaxy mean z of $z = 0.15$.

3.6 LRG HOD modelling

We next attempt to model the VST ATLAS LRG sample that are assumed to occupy the $0.16 < z < 0.36$ range with an approximately flat $n(z)$ (see Fig. 1 of Eisenstein et al. (2001)). From Fig. 3.12 we see that the LRG auto-correlation function $w_{LRG-LRG}$ is $\approx 10\times$ higher than the $17 < r < 21$ galaxy w_{gg} in Fig. 3.8. The higher amplitude clustering of the LRGs will allow more powerful weak lensing tests of the 1- and 2-halo terms for HODs claimed to be appropriate for LRGs. So we shall now test the LRG HOD model advocated by Zheng et al. (2009) with $M_g < -21.8$ (see Fig. 3.10) and first compare it to our LRG $w_{gg}(\theta)$ in Fig. 3.12. While reaching the amplitude of the observed LRG $w_{gg}(\theta)$ at $\theta \approx 1'$, we see that the HOD predicted w_{gg} again underestimates the observations at scales of $\approx 10'$, similar to what was found for the $17 < r < 21$ galaxy HOD model of Zheng et al. (2007) in Fig. 3.9 (a). The fit also appears somewhat worse at large scales than found for the SDSS LRG $w_p(\sigma)$ by Zheng et al. (2009). Nevertheless, since the HOD model fits w_{gg} in the range $\theta < 5'$ we again suggest that it is a useful basis to test the HOD model of Zheng et al. (2009) against the simpler Williams & Irwin (1998) model using the LRG-QSO cross-correlations as considered in Section 3.6.1 below.

3.6.1 LRG-QSO lensing

As before for galaxies, we investigate the mass distribution around LRGs by analysing their cross-correlation with $17 < g < 19$ and $20 < g < 21$ ATLAS QSO samples, but based here first on the Zheng et al. (2009) HOD model for w_{gm} as shown by the dashed line in Fig. 3.12. We see that for the $20 < g < 21$ QSO case in Fig. 3.13 (b), a significant anti-correlation signal is seen at $\theta < 5'$ and particularly at $\theta \approx 0.'3$ where $w_{gq} \approx -0.17$, even taking into account that the control star sample also shows an anti-correlation (albeit much less significant) at $\theta \approx 0.'3$. However, a less strong signal is seen in the $17 < g < 19$ case in Fig. 3.13 (a) where w_{gq} is consistent with zero at all scales; we note that the errors are larger here. We then checked for the presence of dust by re-doing the cross-correlations with the QSO samples limited at bright and faint W1 magnitudes. The bright cross-correlation is expected to increase more than the faint cross-correlation in the case of dust due to the steeper QSO $n(g)$. However, both the bright and faint W1 cross-correlations were consistent with the g-limited results in Figs. 3.13 (a, b). Inspection of the w_{gq} results in the 8 sub-areas used for the field-field errors also showed that the anti-correlation existed in almost all sub-areas.

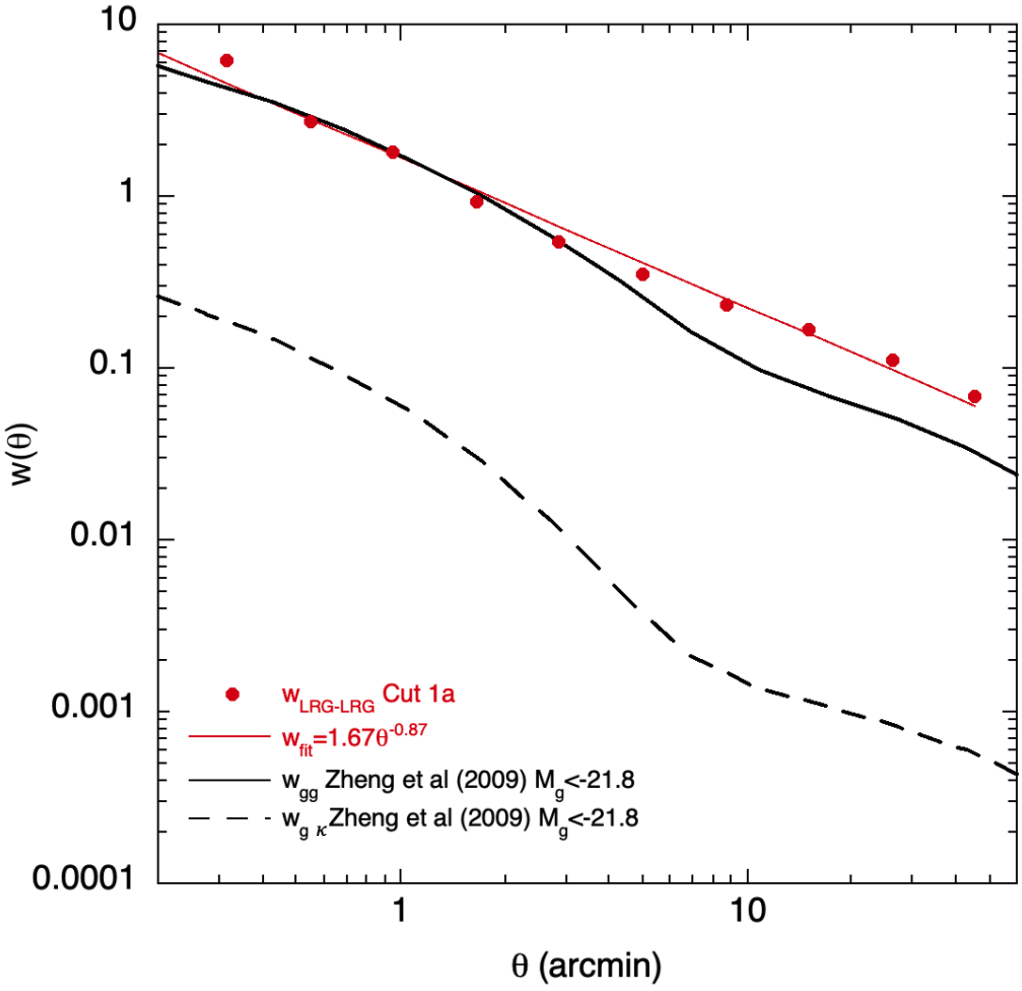

Figure 3.12: w_{gg} and $w_{g\kappa}$ auto- and cross-correlation functions predicted by the HOD model of Zheng et al. (2009) for $M_g < -21.8$ SDSS LRGs (with $\sigma_8 = 0.8$ and $h = 0.7$), compared to $w_{gg}(\theta)$ for our LRGs.

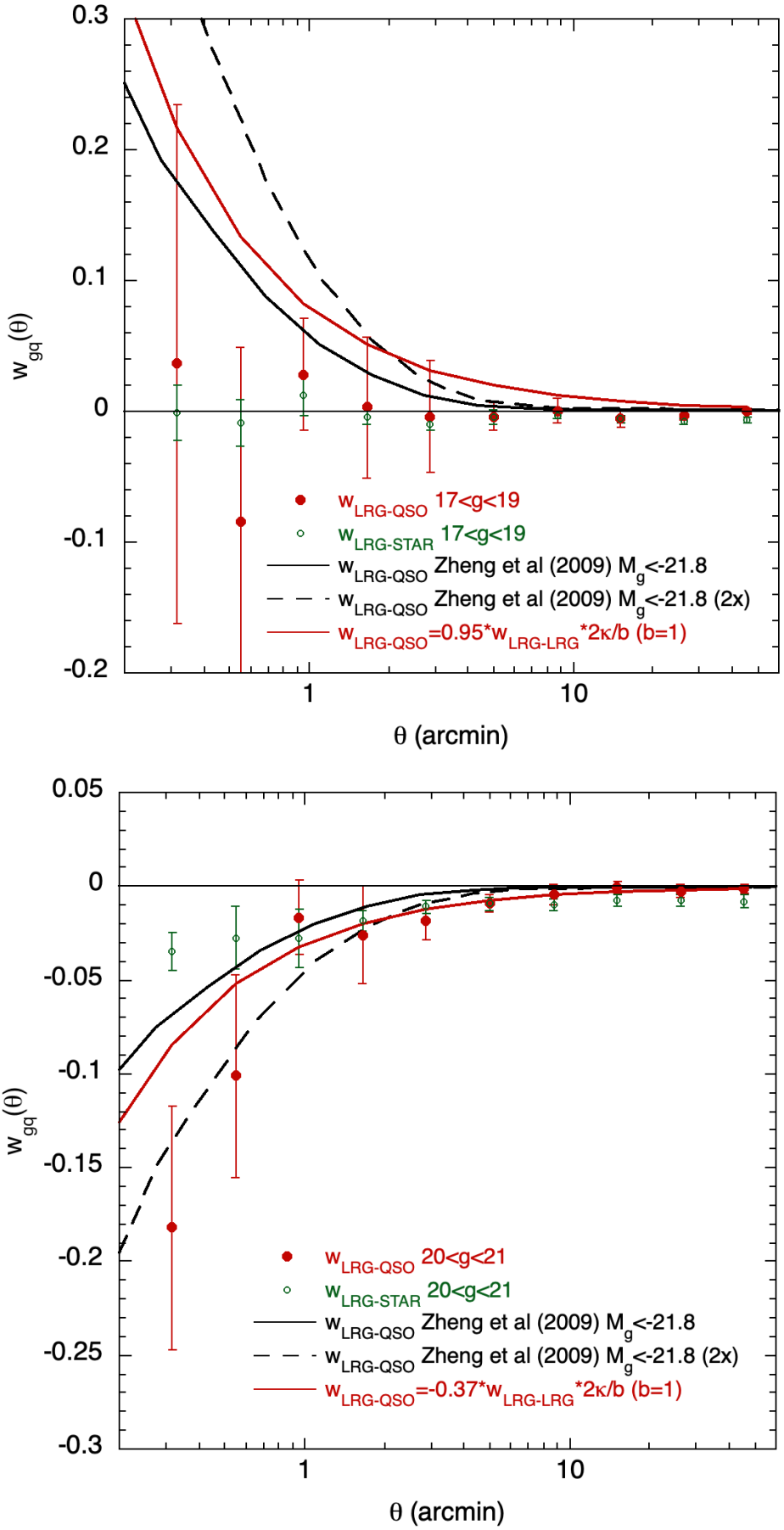

Figure 3.13: (a) The cross-correlation function, $w_{gq}(\theta)$, for $17 < g < 19$ QSO's and our LRG sample, compared to the HOD model of Zheng et al. (2009) and the 2 models of Williams & Irwin (1998) with $b = 1$ and $b = 0.6$. (b) Same as (a) for the QSO magnitude range $20 < g < 21$.

We compare to the model of Zheng et al. (2009) for $M_g < -21.8$ LRG's (solid black line) and see that although it is consistent with the bright QSO cross-correlation in Fig. 3.13 (a) it remains significantly above the less noisy faint QSO result at most scales below $\theta \approx 5'$ in Fig. 3.13 (b). As in Section 3.6 above, we have assumed a flat $n(z)$ in the range $0.16 < z < 0.36$ for the LRGs, following Eisenstein et al. (2001). A Williams & Irwin (1998) model with $b = 1$ based on the LRG-LRG autocorrelation function in Fig. 3.13 is also shown in Figs. 3.13 (a, b) assuming the same optical depth ($\kappa = 0.025$) used previously for the $r < 21$ galaxy sample in Section 3.4. This model assumes that the LRGs trace the mass and this model does get closer to the w_{gq} results than the above HOD model. However, the low point at $\theta = 0.'3$ remains over-estimated by both. To check if it's the form or the amplitude of the halo mass profile that is causing the problem we show the HOD model multiplied by a factor of 2 as the dashed line in Fig. 3.13 (a, b); the improved fit for the faint cross-correlation suggests that it may be the amplitude rather than the form of the NFW mass profile that is at fault.

We conclude that the Zheng et al. (2009) LRG HOD that gives a reasonable fit to the ATLAS LRG w_{gg} at least at small, $\theta < 2'$ scales may be rejected by w_{gq} in the same angular range. The problem seems to be that the effective bias produced by the HOD appears too small and a higher amplitude mass profile may be needed to improve the fit. We also note that the LRG HOD also underestimates the LRG w_{gg} at larger scales and this might only be addressed by using a higher value of $\sigma_8 >\approx 1$ which seems another problem for the LRG HOD approach at larger scales to put alongside the lensing magnification problem at smaller scales.

3.6.2 Further LRG-CMB lensing test of HOD model

In Fig. 3.14 we show the $0.16 < z < 0.36$ LRG cross-correlation with the Planck CMB lensing convergence map compared to the prediction of the Zheng et al. (2009) HOD model. We see reasonable agreement between the data and model here for the 2-halo term at $\theta > 10'$ although this is the range where the model significantly underpredicts the LRG w_{gg}. At smaller scales where the Z09 model fits the LRG w_{gg} very well, the CMB lensing prediction is too low compared to the observed result, in agreement with the LRG-QSO cross-correlation result seen in Fig. 3.13(b). Thus the LRG HOD model either fits the LRG w_{gg} while underestimating the QSO and CMB lensing results at small scales or underpredicts the LRG wgg while fitting the CMB lensing result at large scales. This is reasonably consistent with the galaxy lensing results in Section 3.5.3, where at small scales the HOD underestimates the

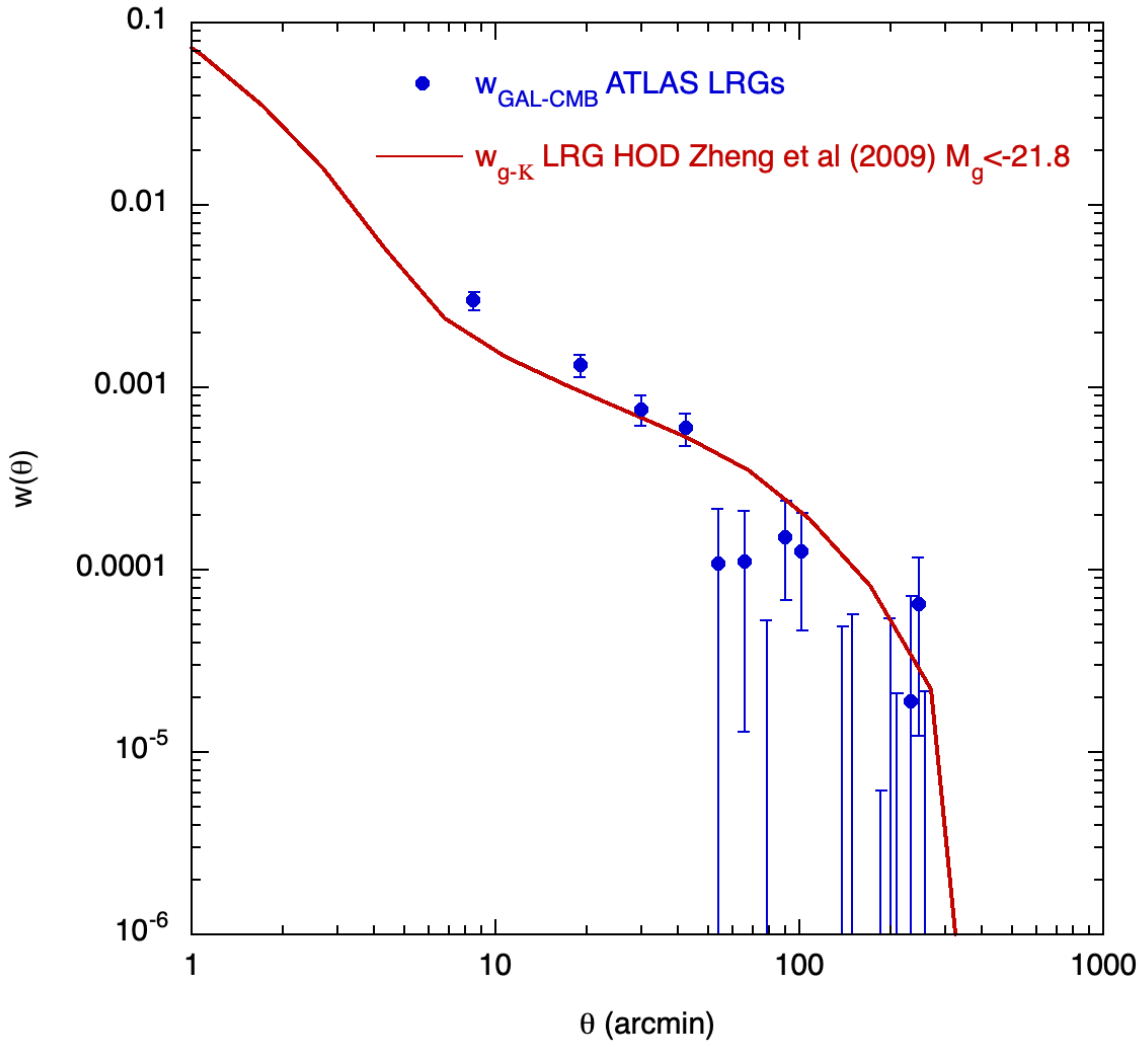

Figure 3.14: w_{g-CMB} cross-correlation function for our LRG sample with $0.16 < z < 0.26$ and the Planck (2018) Lensing Map with field-field errors, compared to the HOD model of Zheng et al. (2009) with parameters $log(M_{min}) = 14.45$, $\sigma_M = 0.80$, $log(M_0) = 12.64$, $log(M_{1'}) = 15.10$, $\alpha = 1.72$. The model assumes $h = 0.7$ and $\sigma_8 = 0.8$. The first bin centre at $8'$ corresponds to ≈ 1.7 h^{-1}Mpc at the LRG mean redshift of $z = 0.26$.

galaxy-QSO cross-correlation w_{gq} relative to the galaxy w_{gg} whereas at large scales the Z07 HOD, at least, fits w_{gg} while over-predicting the galaxy CMB lensing result. However, the LRG results are stronger because of their high amplitude and signal-noise. Similar large scale behaviour may also be seen in the CMB lensing results for the $n > 5$ groups and clusters sample in Fig. 3.5 and Table 3.1 of Section 3.3.5.

3.7 Conclusions

We have detected lensing magnification of background quasars by foreground clusters, galaxies and LRGs. We have used stars as control samples and these have suggested there may be a sky-subtraction problem for the neo6 and DECALS DR10 W1 and W2 magnitudes when measured in the vicinity of bright galaxies. We have also investigated lensing of the CMB by these VST ATLAS cluster and galaxy samples and detected strong effects in each case.

From the lensing of ATLAS quasars by galaxy clusters in the ATLAS catalogue of Ansarinejad et al. (2023) we find that NFW profiles with halo masses of $\approx 1 \times 10^{15}\mathrm{M}_{\odot}$ fit clusters with $n > 40$ members with $\approx 1 \times 10^{14}\mathrm{M}_{\odot}$ fitting groups/clusters of $n > 5$ members. The $n > 40$ clusters show the greatest signal but both cluster samples show a preference for an NFW profile over a SIS profile at the small scales probed by quasar lensing. The larger scales dominated by the 2-halo terms are much better investigated using CMB lensing. Cross-correlation of the *Planck* CMB lensing convergence map with the galaxy clusters shows very strong signals for both cluster samples and we find cluster masses of $\approx 1 \times 10^{14}\mathrm{M}_{\odot}$ for the $n > 5$ clusters and $\approx 3 \times 10^{14}\mathrm{M}_{\odot}$ for the $n > 40$ clusters. Overall, the quasar and CMB lensing mass estimates are in good agreement for both samples. However, the CMB lensing cross-correlation is less well fitted by the $n > 5$ sample than is the $n > 40$ sample. Also, while the quasar and CMB lensing masses bracket the average masses quoted for the $n > 40$ clusters, the lensing mass estimates for the $n > 5$ sample are generally lower than those quoted by Ansarinejad et al. (2023) by a factor of $\approx 3 - 5$.

For the VST ATLAS $17 < r < 21$ galaxy sample, we find that galaxy-galaxy angular auto-correlation and the quasar-galaxy cross-correlation results are consistent with those for SDSS galaxies by respectively Wang et al. (2013) and Scranton et al. (2005) and both are at similar levels of significance. We then addressed the question of how e.g. Myers et al. (2005) found

too high a level of QSO magnification for compatibility with standard ΛCDM cosmology compared to Scranton et al. (2005), who found that the SDSS QSO magnification studies were consistent with standard cosmology predictions. Generally we agree with the previous conclusions of Mountrichas & Shanks (2007) that the actual observations are very consistent with each other and that the difference lies in the models used to interpret these quasar-galaxy cross-correlations. Previously, Myers et al. (2005) assumed that galaxies traced the mass up to a linear bias factor and we have again shown using this assumption that values of the galaxy bias much smaller than unity or equivalently values of σ_8 higher than unity are needed for such models to fit. If instead the HOD approach of Scranton et al. (2005) is followed, then models such as the SDSS $M_r < -20.8$ model of Zheng & Weinberg (2007) can be found that at least approximately fit our measured galaxy angular auto-correlation function while simultaneously reasonably fitting the QSO-galaxy cross-correlation function at the same scales. However, there is a hint that the Zheng & Weinberg (2007) model that fits w_{gg} is still slightly too low in lensing magnification amplitude at the smallest scales of w_{gq}. Our strong detection of the ATLAS galaxy- *Planck* CMB lensing signal was also slightly over-predicted by the Zheng & Weinberg (2007) HOD model at a similar level as the 2-halo term's over-prediction of the group/cluster $n > 5$ sample. But both these deficiencies were only marginally detected and this motivated us to look at the lensing results for the more extreme case of highly clustered LRGs to see if any such problems persisted there.

We therefore select a sample of ATLAS $r < 19.5$ LRG's, using similar criteria to the SDSS Cut 1 of Eisenstein et al. (2001) with a $0.16 < z < 0.36$ redshift range and find an LRG auto-correlation function amplitude $\approx 10\times$ that of the above $17 < r < 21$ galaxy sample. We find that the LRG HOD of Zheng et al. (2009) again fits $w_{gg}(\theta)$ well at small scales but underestimates w_{gg} at larger scales, similar to the galaxy HOD. We then compare the LRG HOD prediction to the QSO-LRG cross-correlation function and find that it under-predicts the amplitude of the LRG anti-correlation with $20 < g < 21$ ATLAS quasars, at a level stronger than the hint in the $17 < r < 21$ galaxy w_{gq}. Multiplying the LRG HOD prediction by a factor of 2 significantly improves the fit, demonstrating the size of the effect. The $17 < g < 19$ QSO-LRG cross-correlation shows less discrepancy with the HOD prediction but here the errors are much larger.

Overall, we conclude that our QSO-galaxy cross-correlation results are in good agreement with previous authors for clusters and $17 < r < 21$ galaxies and that HOD models improve

standard ΛCDM cosmology fits, in particular in the $17 < r < 21$ galaxy case, compared to models where galaxies trace the mass. In the case of clusters, NFW mass profiles are preferred over SIS profiles, with NFW mass estimates compatible with previous results for both clusters and groups. CMB lensing results for groups tends to be under-predicted by standard 2-halo models and this is also seen marginally in the CMB lensing of the $17 < r < 21$ galaxies. LRGs show the biggest discrepancies with a standard HOD model, where they under-predict w_{gq} by a factor of $\approx 2\times$ in the fainter QSO samples, while over-predicting the LRG-CMB lensing result by a smaller factor. Further investigation is required to see if improved HOD models can be found to address these anomalies at large and small scales in the galaxy, group and particularly LRG samples.

Chapter 4

QSO halo and BH masses via clustering and CMB lensing

4.1 Introduction

The overall aim of this Chapter is to determine the QSO host halo mass function at $z \approx 1.7$. Previously, the main route to finding QSO halo masses has been by estimating the bias of QSOs through the comparison of the QSO 3-D redshift-space correlation function with an assumed ΛCDM clustering correlation function, and then using the bias-halo mass relation to estimate average halo masses. This then leads to studies investigating, for example, any QSO halo mass dependence with QSO luminosity (Chehade et al., 2016). Here, we first measure the 2-D angular auto-correlation function of our QSO sample defined in Chapters 2 and 3. This function is independent of redshift space distortions and only one or two authors have previously been able to go this route (e.g. Petter et al. 2023). The high quality of the VST ATLAS QSO samples have allowed us to measure the QSO 2-D angular correlation function and make a new bias and average halo mass estimates in this way. We then proceed to make a more detailed estimate of the QSO halo mass function by fitting QSO HOD models to the QSO auto-correlation function data.

We then go on to use QSO lensing of the CMB to make further tests of the above results. Here, we cross-correlate the ATLAS QSO sample with the *Planck* CMB lensing convergence map. This first allows us to test directly the bias estimated from QSO clustering, free from the assumption of the ΛCDM model, and to make an independent estimate of the QSO average host halo mass via the above bias-halo mass relation. Then, we make a direct measurement

of the full QSO host halo mass function by fitting a HOD model to our QSO-Planck cross-correlations. Here, we follow recent works of Geach et al. (2019), Petter et al. (2022), and Petter et al. (2023), who argue that the cross-correlation of a CMB lensing convergence map and a quasar sample offers a more precise way of measuring the quasar bias than the more commonly used 2-point auto-correlation function (e.g. Chehade et al. 2016) for quasar samples as they are less likely to be affected by quasar survey systematics. Measuring the deflection of CMB photons also allows us to utilize weak lensing at higher redshifts than possible with quasar-galaxy cross-correlation. Finally, we are able to determine the QSO halo mass function by multiplying the derived QSO HOD with the ΛCDM halo mass function.

The structure of this Chapter is as follows. In Section 4.2 we describe the two data catalogues we will be using throughout the chapter. In Section 4.3 we start our analysis by performing an autocorrelation of our QSO sample to measure the clustering amplitude and compare our sample to that of Petter et al. (2023), whose HOD parameters we will be using for our analysis in Section 4.5, before deriving both the QSO bias and host halo mass via this ω_{qq}. We then detect the deflection (lensing) of the CMB (Planck Collaboration et al., 2018) by our quasar candidates through a cross-correlation of our QSO survey and the Planck CMB lensing map (e.g. Geach et al. (2019), Han et al. (2019), Petter et al. (2022)) in Section 4.4 to also derive a host halo mass via the measurement of the QSO bias. Finally, in Section 4.5 we fit both our ω_{qq} and ω_{Q-CMB} results with a HOD model to find the best fitting average halo mass of our QSO sample. We present our conclusions in Section 4.6.

4.2 Data

4.2.1 Quasar Sample

We use a non-photometric redshift restricted version of the QSO sample described in Chapter 3, which introduces restricted $ugriW1W2$ selections to the Priority 1 QSO sample from Chapter 2, as well as a mask to remove Tycho stars and globular clusters. These selections result in a total of 230914 ATLAS quasar candidates giving us a sky density of $49\mathrm{deg}^{-2}$. The photometric redshift distribution of our final QSO sample is shown in Fig. 4.1. Also shown in Fig. 4.1, is the $n(z)$ distribution for SDSS quasars to a similar limit in the form of:

$$(\frac{dN}{dz})_Q \sim z^{2.56} exp[-(\frac{z}{2.02})^{12.76}], \tag{4.2.1}$$

(Scranton et al., 2005) which, although the model is rejected by the data, it still represents a reasonable fit to the shape of our distribution. We therefore use this relation to describe our QSO sample in Section 4.5.

We visually inspect the QSO candidate distribution in the sky to see a relatively flat distribution of candidates across the sky as well as confirming that we have masked out bright stars and globular clusters (the mask is described in Appendix B). This density of candidates is shown in Figure 4.2.

4.2.2 Planck CMB Lensing Convergence Map

To perform our cross-correlation, we use the 2018 release of the Planck lensing convergence baseline map (Planck Collaboration et al. (2018)), described in Chapter 3 and shown in Fig. 3.3.

4.3 QSO Angular Correlation Function, w_{qq}

The QSO angular correlation function, $w_{qq}(\theta)$, measures the strength of quasar clustering as a function of the angular separation, θ, of quasars on the sky. The large width of the QSO $n(z)$, typically spanning the range $1 \lesssim z \lesssim 2$, tends strongly to dilute the QSO clustering in 3-D, making w_{qq} hard to detect against the random noise and low-level systematics. Therefore QSO clustering has traditionally only been measured using QSO redshift surveys like 2dF (Croom et al. (2005)) which do not suffer from projection effects. Only recently have QSO angular correlation functions been measured (e.g. Petter et al. 2023) since they demand large sky areas to remove statistical noise and careful treatment of QSO survey systematics. So a significant detection of w_{qq} also represents a challenging test of the reliability of a quasar survey.

Once detected, w_{qq} offers an alternative route to the quasar spatial correlation function, $\xi(r)$, uncontaminated by redshift space distortion effects (Kaiser, 1987). The first aim then is usually to compare the clustering amplitudes of the QSO and underlying matter to determine the QSO linear bias, defined by $b_Q = \sqrt{(}\xi_{qq}/\xi_{mm})$ where ξ_{mm} is the spatial correlation

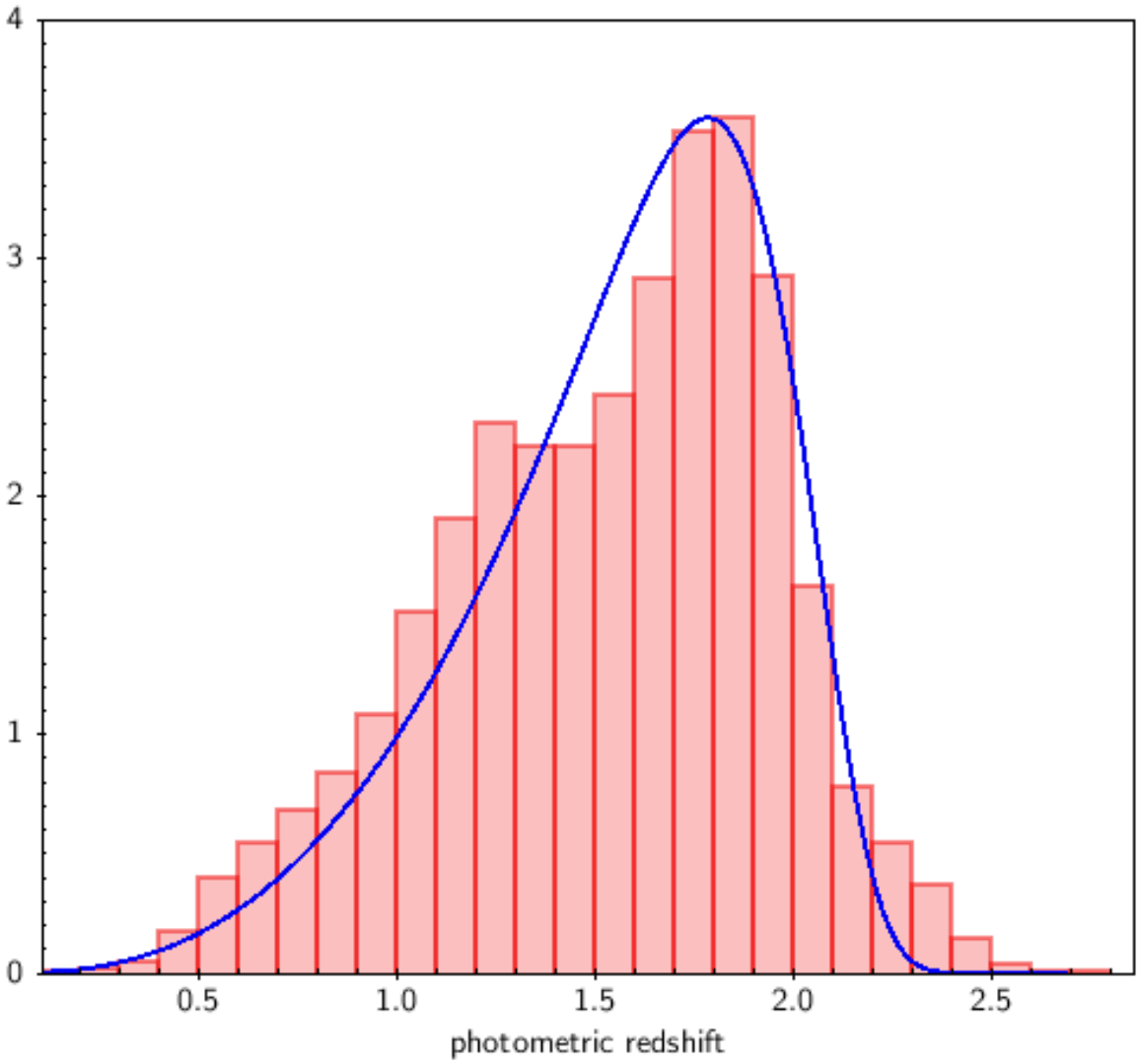

Figure 4.1: Our VST ATLAS+unWISE QSO sample redshift distribution, dN/dz, along with the SDSS n(z) redshift distribution from Scranton et al. (2005) described by Equation 4.2.1, with the y-axis showing the total number of QSOs in the NGC+SGC divided by 7049.4 in order to scale it to the model.

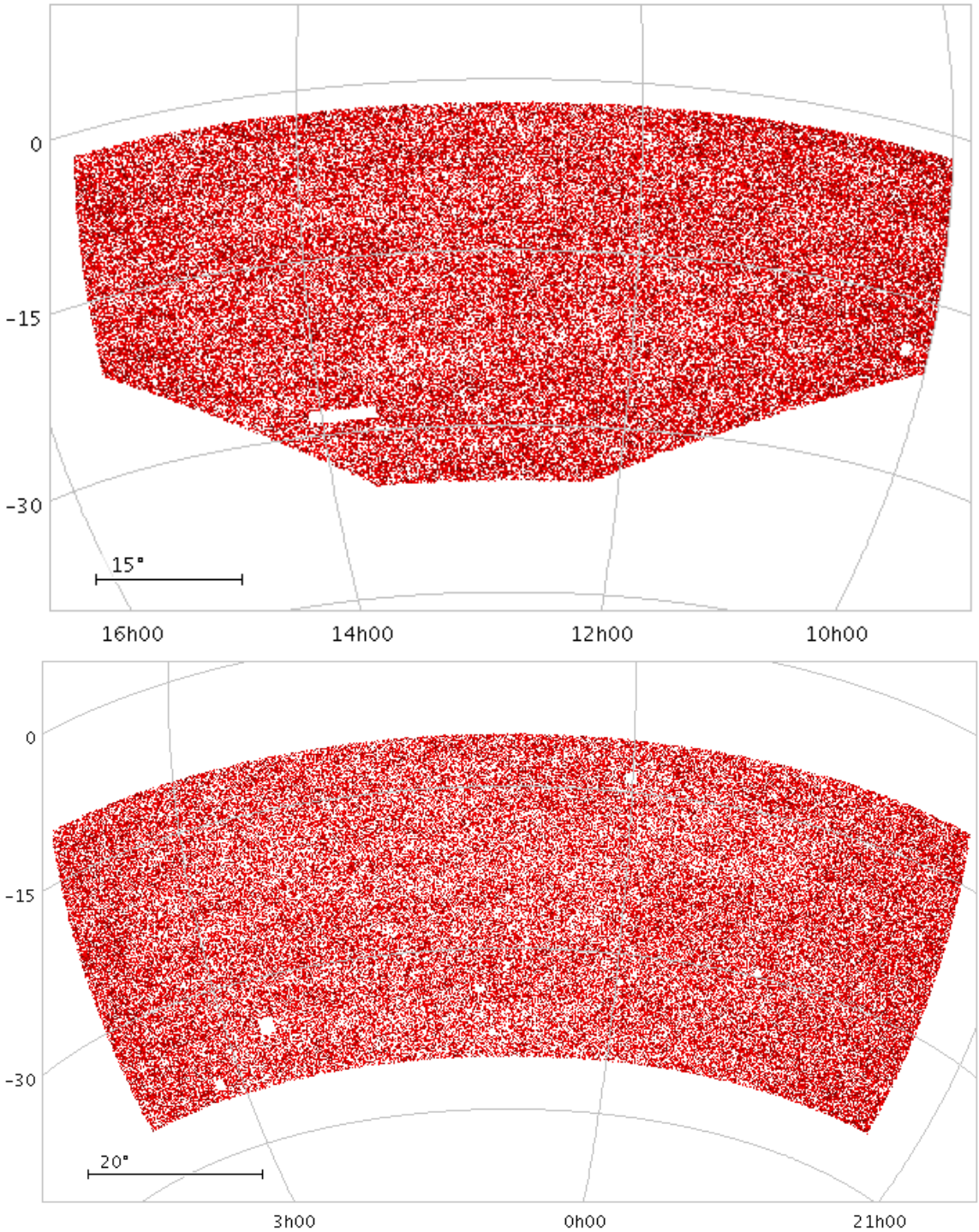

Figure 4.2: Sky density maps of the VST ATLAS QSO candidates in the NGC (above) and the SGC (below) used in this paper. Areas of higher density are shaded in a darker red whereas lower density areas are lighter.

function of the matter distribution. The halo mass of the QSO host galaxy can then be estimated via the QSO bias - halo mass relation. Thus the quasar angular correlation function, w_{qq}, provides a viable alternative to the redshift survey route to determining quasar halo masses.

4.3.1 Method

We perform the autocorrelation of our QSO sample using the Correlation Utilities and Two-point Estimates (CUTE) code Alonso (2012), utilizing the mask described in Appendix B and a randoms catalogue masked in the same way, with 10x the amount of objects than in the QSO catalogue. As described in Ch. 3, CUTE calculates the autocorrelation by using the normalized Landy & Szalay (1993) estimator, defined as:

$$\omega_{QQ}(\theta) = \frac{D_Q D_Q - D_Q R_Q - R_Q R_Q}{R_Q R_Q}, \tag{4.3.1}$$

We check the output generated by the Landy-Szalay estimator by manually checking the individual outputs needed to calculate the angular cross-correlation. The standard errors of the cross-correlation are estimated by using the field-field error defined as:

$$\sigma_{\bar{\omega}(\theta)} = \frac{\sigma_{N_s-1}}{\sqrt{N_s}} = \sqrt{\frac{\sum(\omega_i(\theta) - \bar{\omega_i}(\theta))^2}{N_s^2 - N_s}}, \tag{4.3.2}$$

The result of our QSO autocorrelation is shown in Figure 4.3 alongside the angular auto-correlation measurements obtained by Petter et al. (2023), who split their sample up into unobscured and obscured QSOs. Here we see that both of the Petter et al. (2023) samples display a steeper angular autocorrelation, especially at small $\theta < 0.5'$ scales, where the 1-halo term dominates. The sample used by Petter et al. (2023) is a WISE selected QSO sample, which is then matched to the DESI DR9 r-band (Dey et al., 2019b). This has a magnitude limit of $r \sim 24$. The $r - W2$ cut made in their sample to define the obscured and unobscured samples is shown in their Figure 1, and the redshift distributions of the resulting samples are shown in their Figure 2 (with distributions ranging from $0 \lesssim z \lesssim 3.5$). The n(z) distribution

of obscured QSOs can be seen to be broader with a less distinct peak than our QSO n(z) distribution in Fig.4.1.

4.3.2 Limber's approximation

We fit all three autocorrelations via Limber's approximate projection formula (Limber, 1953) to translate the 2-D angular correlation function, $\omega(\theta)$ to the 3-D spatial correlation function, $\xi(r)$. If $\xi(r)$ is a power-law, $\xi(r) = (r/r_0)^{-\gamma}$, then $w(\theta)$ is also a power law of the form, $w(\theta) = (\theta/\theta_0)^{1-\gamma}$. Then, knowing the amplitude (θ_0) and slope ($1-\gamma$) of the 2-D correlation function, the 3-D clustering amplitude (r_0) can be obtained via Limber's formula for each of the QSO samples. Previous studies, such as Phillipps et al. (1978) and Peebles (1980) have shown this approximation to be accurate at small angular scales below a few degrees separation if the power law is an accurate descriptor of $\xi(r)$. We see in Figure 4.3 that our QSO correlation function gives a clustering amplitude of $r_0 = 5.2$ h^{-1} Mpc, with $\gamma = -1.8$, similar to the clustering amplitude of galaxies. The unobscured and obscured QSOs from Petter et al. (2023) give $r_0 = 6.0$ and 7.9 h^{-1}Mpc respectively. We are able to use this clustering amplitude in the following section in order to estimate the QSO bias, and therefore derive the halo mass.

Although our QSO sample seems to have a higher angular clustering amplitude in Fig. 4.3, this best-fit 3-D clustering amplitudes, r_0, would indicate the opposite. This occurs because the ATLAS QSO $n(z)$ has a smaller width than the $n(z)$'s of the Petter et al. (2023) QSO samples, shown in their Figure 3. If a QSO sample genuinely has a higher 3-D clustering amplitude, this would imply a higher QSO halo bias. But it could also indicate that the QSO samples of Petter et al. (2023) have lower star contamination or they have assumed a QSO $n(z)$ that is too wide for their actual $n(z)$. In addition, the samples of Petter et al. (2023) show a steeper correlation function at small scales which may indicate a contribution from a 1-halo term than if the correlation function followed a pure power-law. So to understand the form of the ATLAS QSO correlation function in more detail, including the relative contributions of the 1- and 2-halo terms, in Section 4.5 we shall fit more sophisticated HOD models to our results.

4.3.3 QSO bias and halo mass via w_{qq}

We now compare our measurement of w_{qq} (deprojected via Limber's formula) to the ΛCDM matter clustering correlation function at $z \approx 1.7$ to estimate the QSO bias at this redshift.

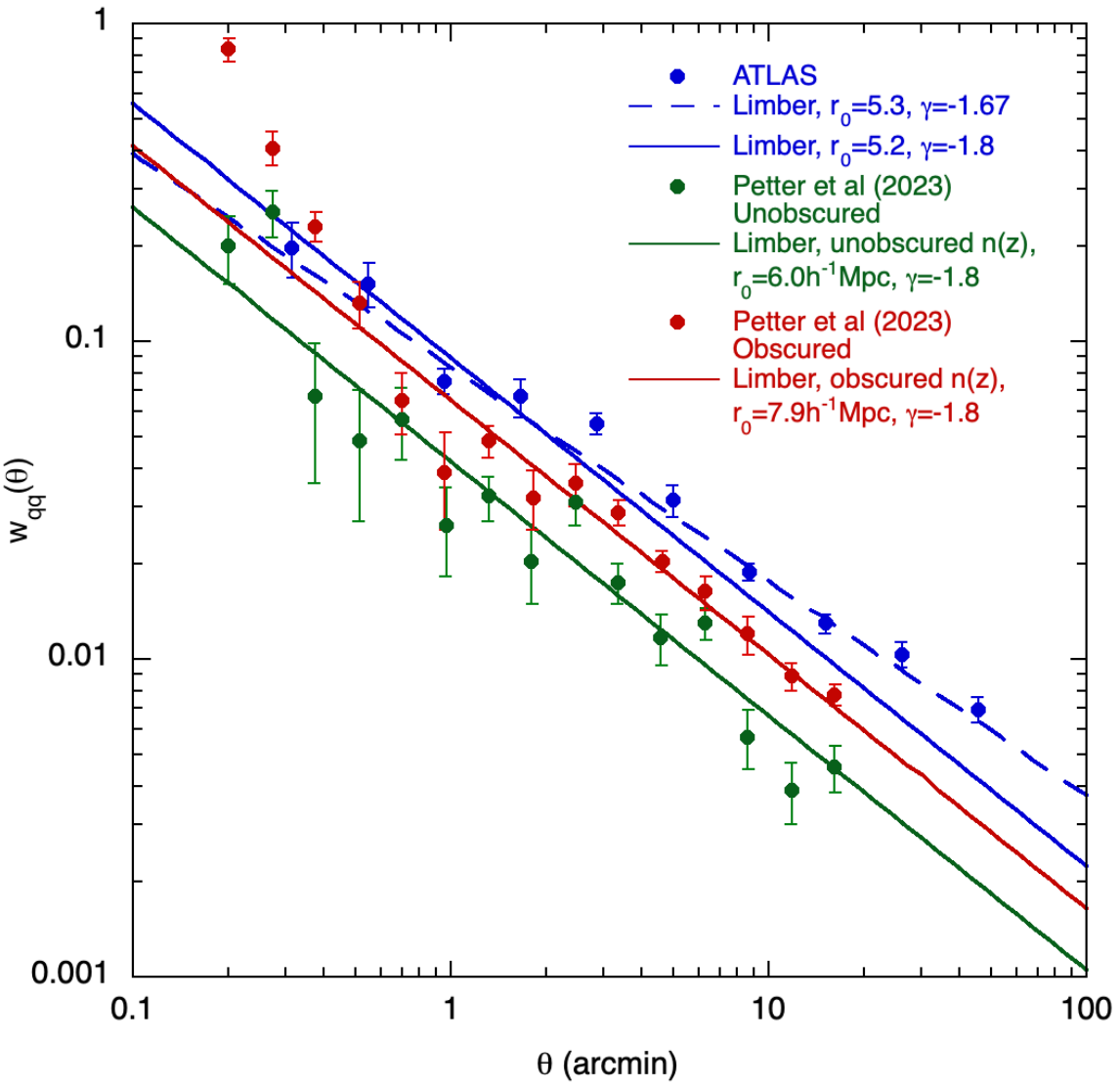

Figure 4.3: We show the autocorrelation function of our ATLAS QSO sample along with the unobscured and obscured QSO samples of Petter et al. (2023). Limber's formula over full redshift range of our ATLAS QSO sample gives $r_0 = 5.2$ h^{-1} Mpc. The Limber formula predictions of $r_0 = 6.0, 7.9$ h^{-1}Mpc for the unobscured and obscured Petter et al. (2023) samples are also shown, based on their self-consistent redshift distributions. All w_{qq} models assume power-laws for the 3-D $\xi(r)$ with slope $\gamma = -1.8$, along with one better fit model with $r_0 = 5.3$ h^{-1} Mpc and slope $\gamma = -1.67$ for our QSO w_{qq}.

Following Croom et al. (2005) we make this comparison by integrating over $\xi(r)$ out to r=20h^{-1}Mpc to form ξ_{20}. This $0 < r < 20\mathrm{h}^{-1}$Mpc range is chosen so that it is dominated by the linear regime at $r > 5\mathrm{h}^{-1}$Mpc and where $\xi(r)$ can be approximated by a power-law:

$$\xi_{20} = 3/20^3 \int_0^{20} \xi(r) r^2 dr = 3/20^3 \int_0^{20} (r/r_0)^{-\gamma} r^2 dr \tag{4.3.3}$$

Here we have already assumed a power law form for $\xi(r)$ with power-law slope, $-\gamma$, and scale length, r_0. We note that $r_{\mathrm{comoving}} = 20\mathrm{h}^{-1}$Mpc at $z = 1.7$ corresponds to $\theta = 20.'8$ (see Figs. 4.3 and 4.7).

Now, approximating w_{qq} by a power-law of slope $1 - \gamma = -0.67$ and applying Limber's formula, we find $r_0 = 5.3 \pm 0.1\mathrm{h}^{-1}$Mpc which from eq (4.3.3) gives $\xi_{20} = 0.25 \pm 0.01$ for our QSOs. A ΛCDM matter power spectrum implies $\xi_{20} = 0.235$ for the matter at $z = 0$. Assuming a linear gravitational growth factor of $D(z = 1.7) = 2.033$ between $z = 1.7$ and $z = 0$ then gives $\xi_{20} = 0.235/2.033^2 = 0.057$ for the matter at $z = 1.7$. The QSO bias at $z = 1.7$ is $b_Q = \sqrt{(}0.25/0.057) = 2.09 \pm 0.09$. Then, following eqs. (13-17) of Chehade et al. (2016) we derive the bias-mass relation for QSOs at our average QSO redshift, $z = 1.7$, as shown in Fig. 4.4. From that, we estimate a mean QSO halo mass of $M_{\mathrm{halo}} = 8.5 \pm 3 \times 10^{11}$ h^{-1} $\mathrm{M}_\odot$ at this redshift.

4.4 QSO-CMB Lensing Cross-Correlation

The cross correlation of our QSO catalogue with the Planck CMB lensing convergence map (Planck Collaboration et al. (2018) is an independent method towards determining the QSO bias and the QSO halo mass.

4.4.1 Quasar-CMB Lensing Cross-Correlation Model

We first perform our analysis using the model described in the studies of Geach & Peacock (2017), Geach et al. (2019), and Petter et al. (2022). The model includes a lensing convergence contribution made by a 1−halo and a 2−halo term. Similarly to the equation used in the Williams & Irwin (1998) model from Ch. 3, the convergence due to the 1-halo term is defined as:

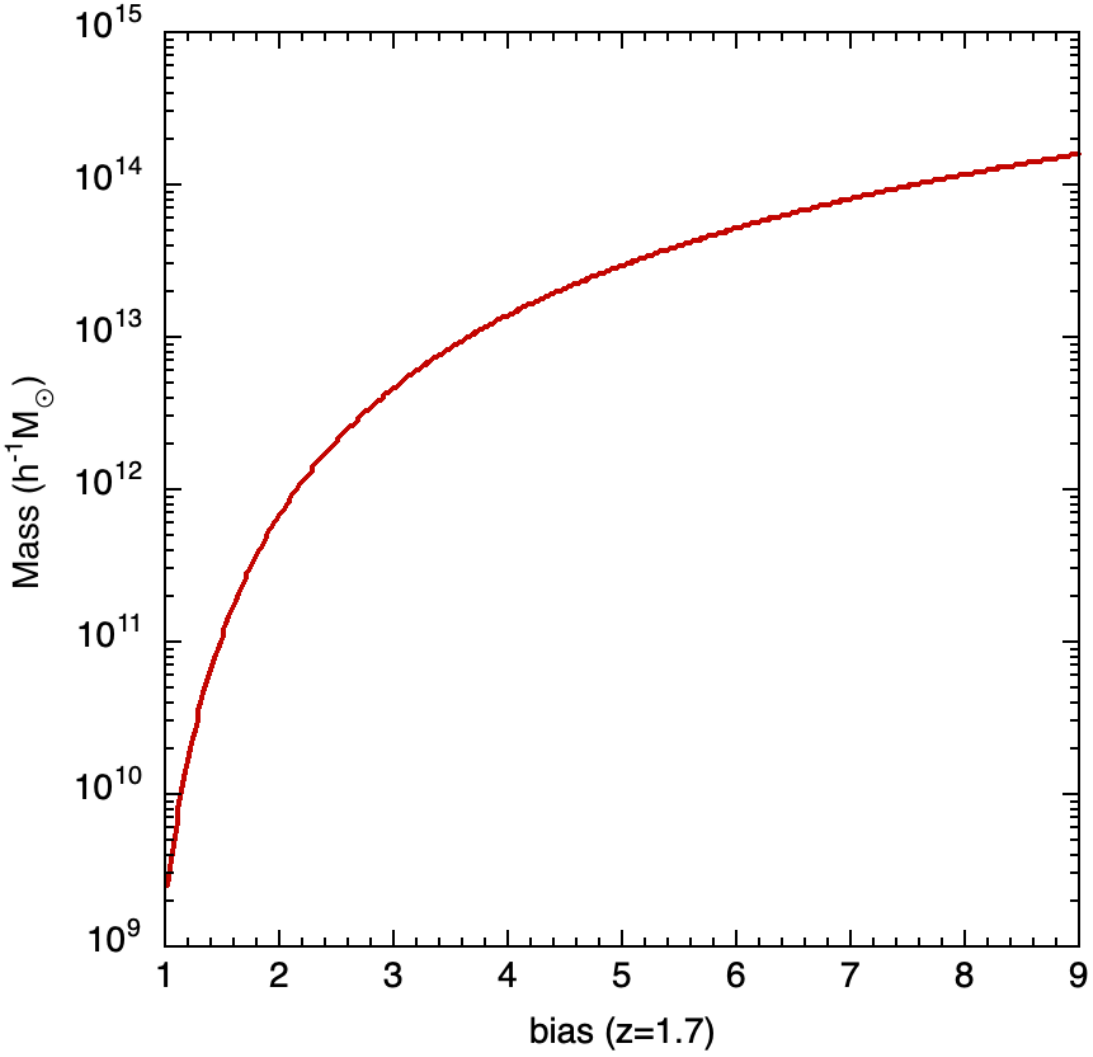

Figure 4.4: The calculated bias-mass relation for QSOs at redshift z=1.7 based on equations 13-17 of Chehade et al. (2016).

$$\kappa_1(R) = \frac{\Sigma(R)}{\Sigma_{crit}} \tag{4.4.1}$$

where $\Sigma(R)$ is the projected mass surface density given an NFW density profile, and Σ_{crit} is the critical surface density. Here, the projected mass surface density is:

$$\Sigma(R) = 2\int_R^{\inf} \frac{r\rho r}{\sqrt{(r^2 - R^2)}} dr \tag{4.4.2}$$

The 2−halo term is described by:

$$\kappa_2(\theta) = \frac{\bar{\rho}(z)}{(1+z)^3 \Sigma_{crit} D^2(z)} \int \frac{ldl}{2\pi} J_0(l\theta) b_h \triangle(k, z) \tag{4.4.3}$$

where J_0 is a Bessel function of the zeroth order, $D(z)$ is the angular diameter distance, $\triangle(k, z)$ is the linear matter power spectrum, $\bar{\rho}(z)$ is the average density of the Universe at z and b_h is the quasar bias for a halo of mass M_h. Then, the final model for the lensing convergence is:

$$< \kappa >= \int dz(\kappa_1 + \kappa_2) dn/dz \tag{4.4.4}$$

The lensing convergence results obtained by Geach et al. (2019) are shown in their Figure 3. There we see the radial profile of the quasar stacked convergence along with the best fitting lensing model as a solid line. The model includes the 1- and 2-halo contribution to the lensing signal, although at scales of $\theta > 5'$, the 1−halo term is mostly filtered out. A similar approach is taken by Petter et al. (2022), where their Figure 5 shows a comparable model. Both Geach et al. (2019) and Petter et al. (2022) filter and stack their model (based on Equation 4.4.4) in order to mimic the filtering done on the CMB and QSO data. Therefore, the final model does fall below zero at $\sim \theta = 40$arcmin (see Fig. 4.5), even though neither the 1- or 2-halo term

components do so. Below, we shall be simply scaling the 2-halo term of the model presented in both Geach et al. (2019) and Petter et al. (2022) for a first order calculation of our QSO bias.

The CMB lensing convergence denoted by κ is a projection of a 3D density field. The quasar density is also a projection of a 3D density field. We convert these 3D projections into angular comoving distances in order to perform angular correlations. In our analysis we assume that we have the same absolute magnitude range as Chehade et al. (2016). We also use a comparable quasar sample to Geach et al. (2019) and Petter et al. (2022). However, our photometric redshifts are less accurate and therefore it may not be worth splitting up in to redshift and/or magnitude bins to perform further analysis.

4.4.2 Quasar-CMB Lensing Cross-Correlation Results

Results of the cross-correlation we perform between our quasar sample and the Planck CMB Lensing map can be seen in Fig. 4.5. We show our results along with the results found by Geach et al. (2019) and Petter et al. (2022). We note that the errors on our results are reasonably comparable to both Geach et al. (2019) and Petter et al. (2022). The main difference between the two results is between 30-60 arcmin where our results are higher; the reason for this discrepancy is unclear.

We determine the QSO bias found with our results by scaling the total filtered model determined by Geach et al. (2019), indicated on Figure 3 of their paper, as well as the filtered total model from Petter et al. (2022), indicated on Figure 5 of their paper, to our data. Both models include the 1- and 2-halo term described in the previous section and are filtered in the same way as their data. We look at the $0' < \theta < 60'$ range as our data falls below $\kappa = 0$ at larger scales. The negative cross-correlations predicted at large scales by this model may arise as we smoothed the spherical harmonics (the a_{lm}) before converting this to a Healpix map with the healpy alm2map routine. Additionally, there are most likely more systematics at larger scales, despite the errors being smaller. We also note that this χ^2 fit and associated errors are only approximate as they do not take into account covariance between data points. Upon scaling the models, we find that the total model from Geach et al. (2019) has a best χ^2 fit for a scale of 0.8. Therefore, scaling the measured quasar halo bias of $b_h = 2.7 \pm 0.3$ at $z = 1.7$ found by Geach et al. (2019) by 0.8, gives us a QSO halo bias of $b_h = 2.16 \pm 0.43$ at $z = 1.7$. For the total model of Petter et al. (2022), we find a best fit scaling factor of 0.85.

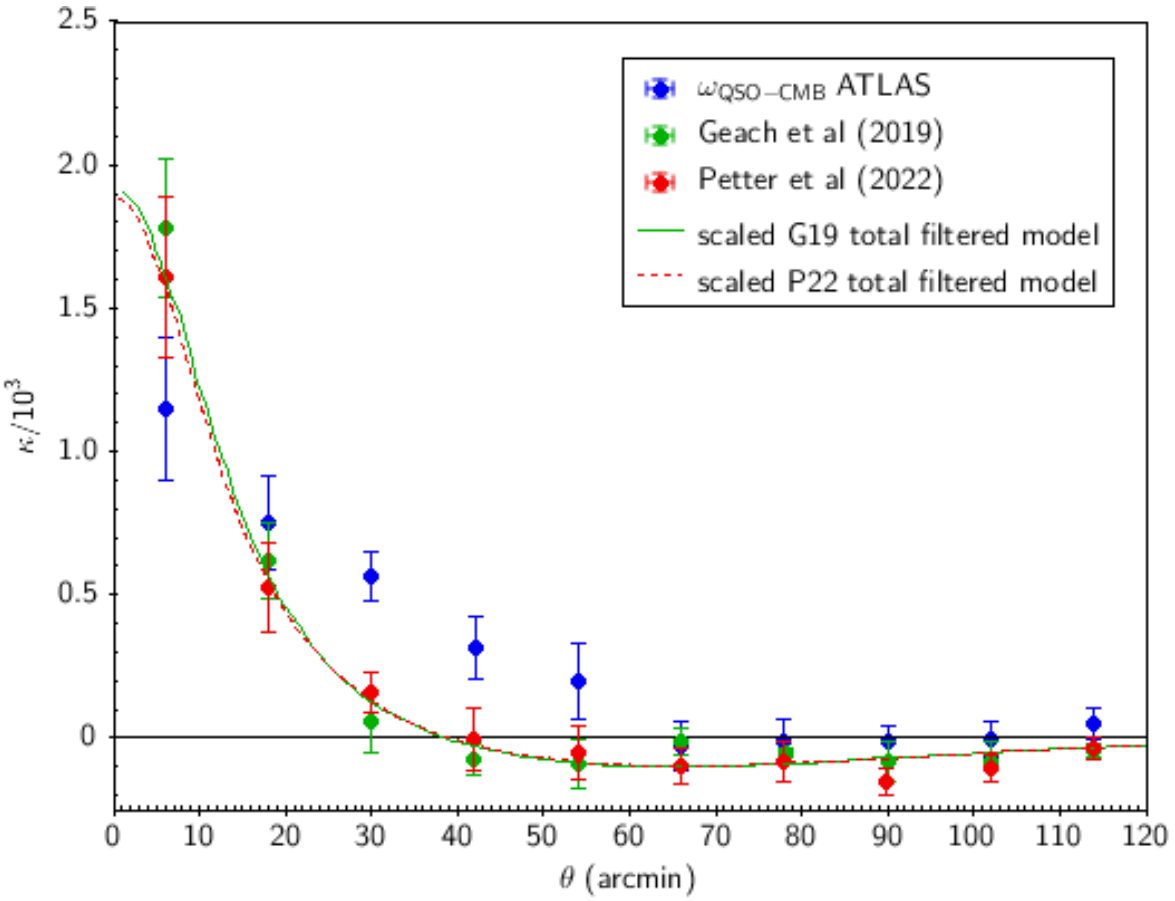

Figure 4.5: We show our QSO-CMB Lensing cross-correlation result in blue along with the result obtained by Geach et al. (2019) and Petter et al. (2022), in green and red respectively. The total filtered model, scaled by a factor of 0.8, from Geach et al. (2019) is shown as a green line. The total filtered model, scaled by a factor of 0.85, from Petter et al. (2022) is shown as a dashed red line.

Through scaling their QSO halo bias of $b_h = 2.35 \pm 0.02$ by 0.85 we can infer a QSO bias value of $b_h = 2.0 \pm 0.17$ for our data. The bias to mass relation described in Section 4.3.3 then indicates a host halo mass of $9.17\text{x}10^{11}h^{-1}\text{M}_\odot$ for $b_h = 2.16$ and $6.71\text{x}10^{11}h^{-1}\text{M}_\odot$ for $b_h = 2.0$. We therefore average these two bias measurements determined via scaling the total models of Geach et al. (2019) and Petter et al. (2022) to get $b_h = 2.08 \pm 0.3$, with a host halo mass of $8.3 \pm 3 \times 10^{11}h^{-1}\text{M}_\odot$.

In Figure 14 of Chehade et al. (2016), they show the bias they determined as a function of redshift and absolute magnitude. In Fig. 4.6, we add to Fig. 14 of Chehade et al. (2016) our bias measurement of $b_h = 2.08 \pm 0.3$, shown as a red point, and the $b_h = 2.35 \pm 0.02$ value found by Petter et al. (2022) in green. The bias result of of $b_h = 2.7 \pm 0.3$ at $z = 1.7$ found by Geach et al. (2019) is shown as a blue point. We also show the bias value of $b_h = 2.09$ determined via the QSO auto-correlation in Section 4.3.3 in yellow. The dotted black line represents the bias result determined by Chehade et al. (2016) and the bias result from 2QZ (Croom et al., 2005) is shown as a dashed black line. Also in the figure is the measurement of the quasar halo bias from the BOSS survey (Dawson et al., 2013) determined by Eftekharzadeh et al. (2015). The solid grey line represents the evolution for a halo of mass $2 \times 10^{12}\text{h}^{-1}\text{M}_\odot$. From this figure, we see that the quasar halo bias measured by Geach et al. (2019) is in line with the bias measured 2QZ, but falls above the bias found by Chehade et al. (2016) (the black dotted line). The bias found by Petter et al. (2022) is in line with the result found by Chehade et al. (2016). We see that our bias measurements fall slightly below all of these results but are still within reasonable agreement. We note that we have assumed a uniform redshift distribution and peak for ourselves, Petter et al. (2022), and Geach et al. (2019). Uncertainties in photometric redshifts and the ranges used for the analyses may account for some discrepancies between these results.

Overall there seems to be good agreement between the quasar-CMB lensing results of Geach et al. (2019), Petter et al. (2022), and the results from Chehade et al. (2016) which are derived from QSO clustering. The bias, and associated host halo mass results we find via QSO-CMB lensing are also in good agreement when scaling to the total model. We use this as a first order estimate of our data and continue forward by fitting a separate HOD model to our results. These QSO bias and host halo mass measurements, along with the measurements found in Section 4.5, are summarized in Table 4.1.

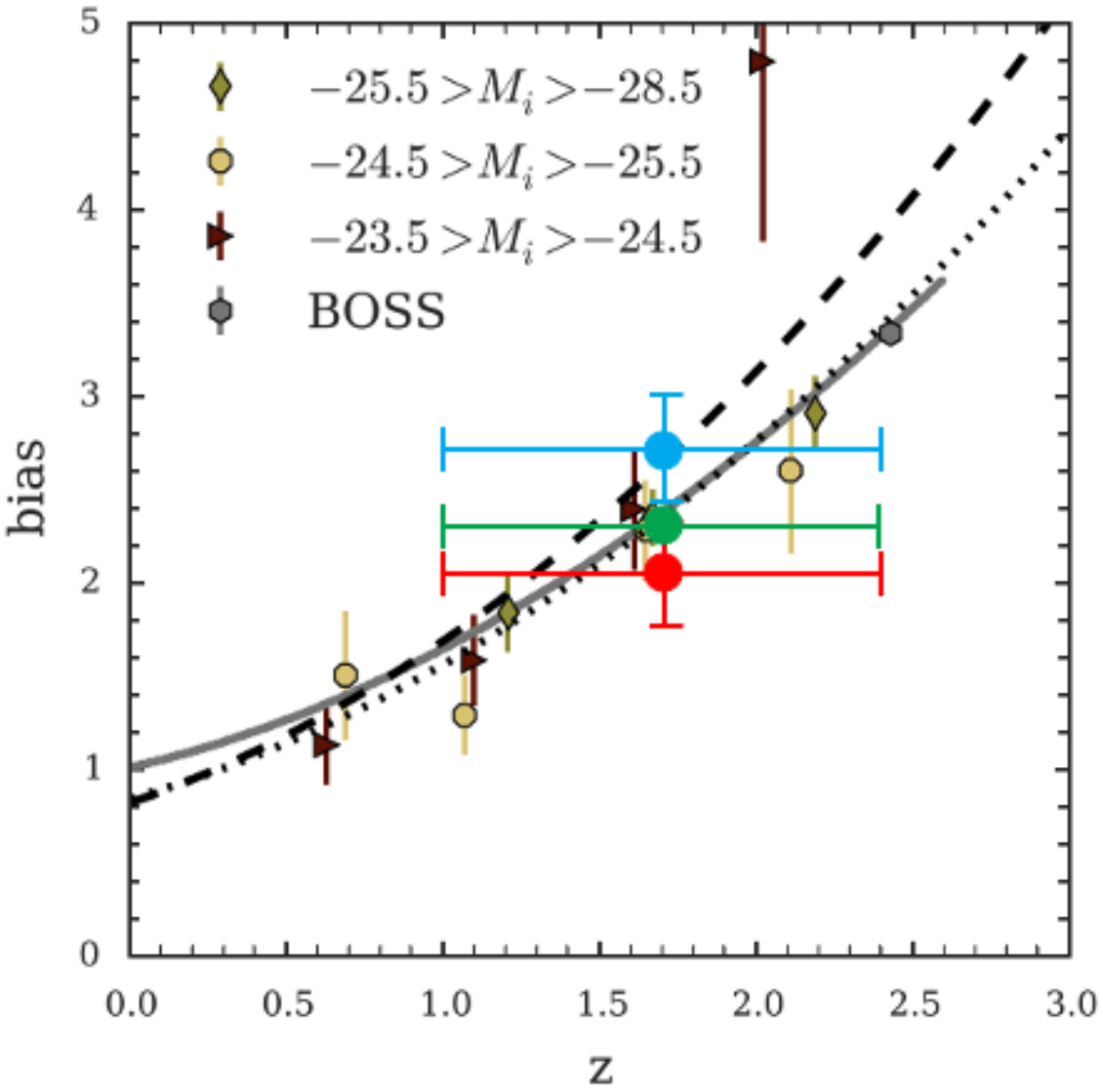

Figure 4.6: The quasar halo bias as a function of redshift, taken from Figure 14 of Chehade et al. (2016). We show the b_h value of 2.7 ± 0.3 at $z = 1.7$ found by Geach et al. (2019) in blue and the $b_h = 2.35 \pm 0.02$ value found by Petter et al. (2022) in green. Our bias value of $b_h = 2.08 \pm 0.3$ estimated via scaling of the 2-halo model is shown together with our bias value of $b_h = 2.09$ determined via ω_{qq} in Section 4.3.3 in red. The dotted black line represents the bias result determined by Chehade et al. (2016) and the bias result from 2QZ (Croom et al., 2005) is shown as a dashed black line. The solid grey line represents the evolution for a halo of mass $2 \times 10^{12} \mathrm{h}^{-1} \mathrm{M}_{\odot}$.

Table 4.1: Summary of results for QSO bias b_Q and halo mass M_{halo}. Rows 1-3 contain our VST ATLAS results via (1) the bias from the QSO angular autocorrelation function, (2) the bias fitted to the QSO-CMB lensing cross-correlation function and (3) a HOD model fitted jointly to the above two. Also shown are previous results from Croom et al. (2005), Chehade et al. (2016), Geach et al. (2019), Petter et al. (2022) and Petter et al. (2023).

$z = 1.7$ QSO Sample + Method	bias (b_h)	Mass ($10^{12}h^{-1}M_\odot$)	log Mass ($h^{-1}M_\odot$)
ATLAS ACF w_{qq}	2.09 ± 0.09	0.85 ± 0.3	11.9 ± 0.04
ATLAS CMB Lensing $w_{q\kappa}$	2.08 ± 0.3	$0.83^{+0.8}_{-0.5}$	11.9 ± 0.4
ATLAS HOD w_{qq}+$w_{q\kappa}$	$2.60^{+0.30}_{-0.23}$	$2.5^{+1.5}_{-0.9}$	12.4 ± 0.2
Croom05 z-space ACF	2.17 ± 0.09	1.2 ± 0.2	12.1 ± 0.08
Chehade16 z-space ACF	2.34 ± 0.35	2.0 ± 1.0	12.3 ± 0.4
Geach19 CMB Lensing	2.7 ± 0.3	$4.0^{+2.3}_{-1.5}$	12.6 ± 0.2
Petter22 CMB Lensing	2.35 ± 0.02	3.0 ± 0.4	12.5 ± 0.05
Petter23 HOD w_{qq}+$w_{q\kappa}$	2.3 ± 0.5	4.0 ± 1.4	12.6 ± 0.2

4.5 HOD Model via QSO auto-correlation and QSO-CMB lensing cross-correlation

4.5.1 HOD model

We utilize the CHOMP package, introduced in Sec. 3.5, to fit HOD models to both the auto-correlation, w_{qq}, of our QSO sample as well as the QSO-CMB lensing convergence map cross-correlation, $w_{g\kappa}$. To check the CHOMP methodology, we first supplied CHOMP with the HOD model parameters of Petter et al. (2023). However, in the case of the QSO correlation function, we found that CHOMP could not reproduce the w_{qq} results of Petter et al. (2023), assuming their HOD parameters. In this case, we used the alternative HaloMod package (Murray et al., 2021) to predict the Petter et al. (2023) 3-D $\xi(r)$ and then input this into Limber's formula using Eq.(13) of Phillipps et al. (1978). The resulting w_{qq} was found to agree with Petter et al. (2023) and the same procedure was then used to fit our ATLAS w_{qq}.

For the 1-halo term of QSO and matter clustering, we assume a Navarro et al. (1996) NFW model, to predict the projected, lensed mass profile, w_{qm} and then $w_{q\kappa}$. CHOMP also assumes that halo concentration is a function of halo mass with the functional form $c(m) \approx 9(m/m^*)^{-0.13}$ taken from Bullock et al. (2001). For the 2-halo term, CHOMP assumes the form given in eq. (6) of Jain et al. (2003) with a bias model from Tinker et al. (2010), etc. CHOMP and HaloMod both allow use of the 5-parameter HOD model of Zheng & Weinberg (2007) to fit the 2-point auto-correlation function. For all HOD models, we assume a ΛCDM cosmological model with the matter density $\Omega_M = 0.3 - 0.046$, baryon density

$\Omega_b = 0.046$ and $\Omega_\Lambda = 0.7$. We assume adiabatic Gaussian primordial density fluctuations with a power-law index of the spectrum $n_s = 0.96$. The r.m.s. matter density fluctuation is assumed to be $\sigma_8 = 0.8$. The Hubble constant we use throughout is $h = 0.7$. Finally, we define the QSO halo redshift to be at $z = 1.7$ and the CMB at redshift $z = 1100$. Then we fit the HOD parameters: the minimum halo mass scale, $\log M_{min}$, the minimum mass scale softening width, $\sigma_{\log M}$, for the central galaxies, the satellite cut-off mass scale, $\log M_0$, the satellite HOD power-law normalization, $\log M_{1'}$ and its slope, α, at high halo masses.

4.5.2 QSO autocorrelation

In Fig. 4.7, we compare our observed QSO correlation function, w_{qq}, to our fitted HOD (solid blue line), with parameters, $\log M_{min} = \log M_0 = 12.2$, $\log M_1 = 13.28$, $\sigma_{\log M} = 0.4$ and $\alpha = 0.7$. Also shown as the solid red line is the HOD fit from Petter et al. (2023) for their unobscured QSO sample, with parameters $\log M_{min} = \log M_0 = 12.4$, $\log M_1 = 13.5$, $\sigma_{\log M} = 0.4$ and $\alpha = 0.7$. This model is rejected by our data to $\theta < 15$ arcmin with a reduced χ^2 of 7.2. We see that our HOD model has slightly reduced mass parameters due to the ATLAS w_{qq} having a lower amplitude ($r_0 = 5.2$ h^{-1} Mpc) than the unobscured QSO w_{qq} of Petter et al. (2023) that has $r_0 = 6.0$ h^{-1} Mpc, assuming a $\gamma = -1.8$ power-law form for $\xi(r)$ in both cases (as noted in Sec. 4.3.2). Our HOD fits the data to $\theta < 15$ arcmin with a reduced χ^2 of 1.79.

4.5.3 QSO-CMB cross-correlation

We next test these two HOD models for internal and external consistency using the QSO-CMB lensing convergence map cross-correlation function. As we see some discrepancy with regards to various parameter fits for the QSO autocorrelation, we use the QSO-CMB cross-correlation as an independent method to measure the host halo masses. Here, we expand upon the results described in Section 4.4.2 to compare the predictions of the above two HOD models to our QSO-CMB cross correlation results. We note that at the $6'$ resolution of the Planck lensing map, our cross-correlation analysis will mainly be sensitive to the 2-halo term of QSO clustering.

We see in Fig. 4.8 that our observed CMB lensing cross-correlation function is in good agreement with our HOD model. As previously noted in Section 4.4.2 our observational results are also in good agreement with the results of Geach et al. (2019) and Petter et al.

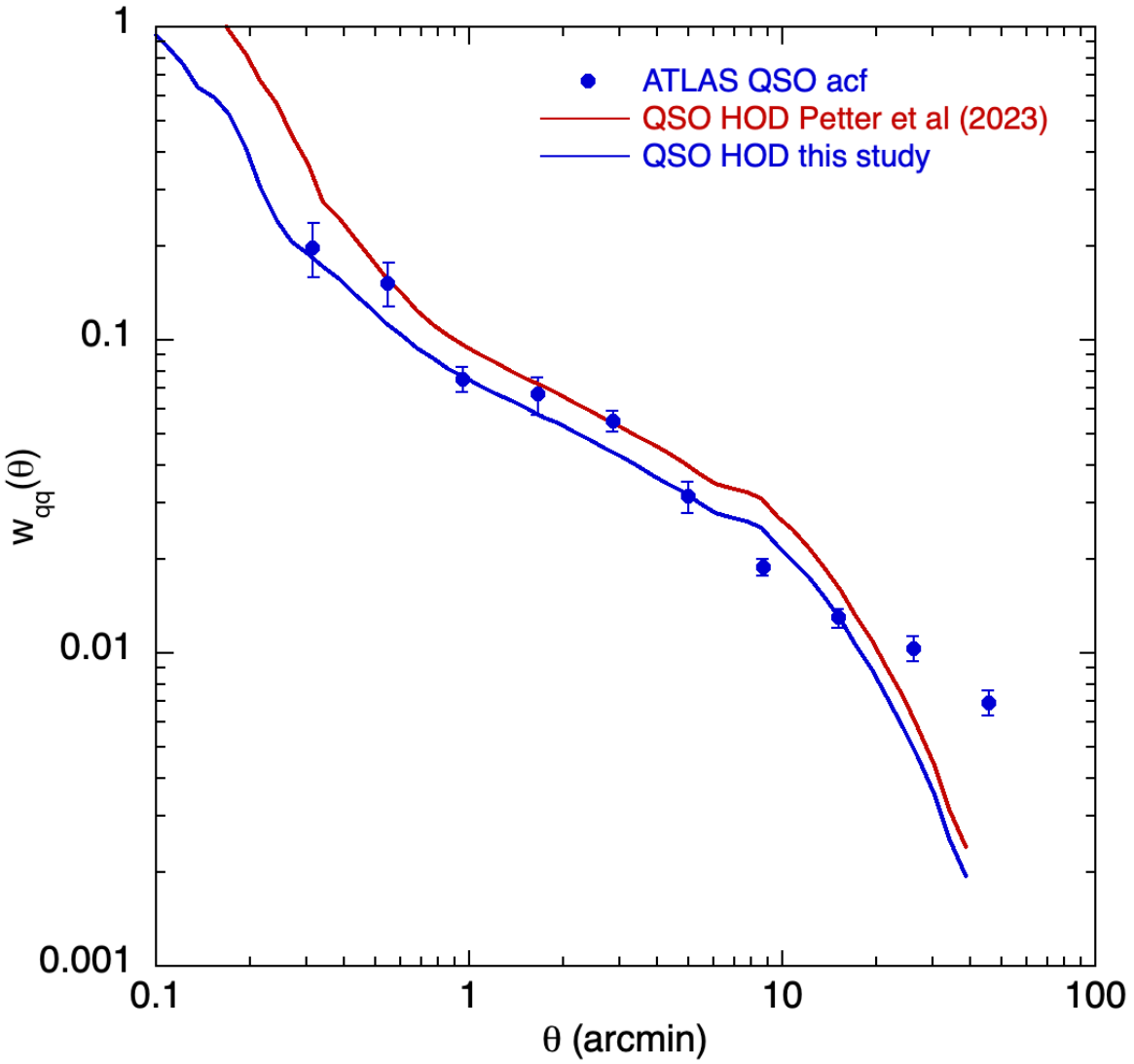

Figure 4.7: The ATLAS $17 < g < 22$ QSO angular auto-correlation function, w_{qq}, compared to our $1 < z < 2.2$ HOD model (solid blue line) with parameters: $\log(M_{min}) = 12.2$, $\sigma_{\log M} = 0.4$, $\log(M_0) = 12.2$, $\log(M_{1'}) = 13.28$ and $\alpha = 0.7$. The red line shows the unobscured QSO HOD model of Petter et al. (2023) with parameters: $\log(M_{min}) = 12.42$, $\sigma_M = 0.4$, $\log(M_0) = 12.42$, $\log(M_{1'}) = 13.28$ and $\alpha = 0.7$. Both HOD models assume standard ΛCDM parameters with $h = 0.7$ and $\sigma_8 = 0.8$.

(2022), although our cross-correlation data points are higher than the other two at $10 < \theta < 60'$ and this appears to be reflected in the HODs derived from the ATLAS and Petter et al. (2023) w_{qq} results, as discussed in Section 4.5.4 below.

4.5.4 Halo mass of QSOs

In Fig. 4.9(a) we show our QSO HOD in blue, using the same parameters as in Fig. 4.7, alongside the Petter et al. (2023) HOD in red, as a function of halo mass, i.e. the halo mass function. In Fig. 4.9(b) we show the QSO space density as a function of halo mass formed by multiplying the halo mass function by our HOD model and that of Petter et al. (2023). Averaging over these two distributions we find that the average QSO halo mass is $\log M_{eff} = 12.39$ $(h^{-1}M_{\odot})$ for our HOD and $\log M_{eff} = 12.90$ $(h^{-1}M_{\odot})$ for the HOD of Petter et al. (2023). We note that this latter value calculated by ourselves is somewhat higher than the $\log M_{eff} = 12.6(h^{-1}M_{\odot})$ found by Petter et al. (2023) based on their $b_{eff} = 2.25$. Otherwise we note that our lower ($\approx 3\times$) average QSO halo masses are in line with our w_{qq} having a lower scale length of $r_0 = 5.2$ h^{-1} Mpc compared to the $r_0 = 6.0$ h^{-1} Mpc measured by Petter et al. (2023) for their unobscured QSO sample. Also the results we obtain from the HOD analyses are generally slightly larger than when estimating halo masses directly from w_{qq} and b_Q. However, in terms of the QSO-CMB lensing results in Fig. 4.8, we do find a larger observed amplitude at $\theta > 10'$ than Geach et al. (2019) for this cross-correlation which is well fitted by our HOD model. The lower cross-correlation at $\theta > 10'$ observed by Petter et al. (2023) is also well fitted by their HOD model. So the HOD models seem internally consistent between w_{qq} and $w_{QSO-CMB}$. The HODs also seem externally consistent, given the similarities in halo mass function and average halo masses between Petter et al. (2023) and ourselves.

Working directly from our QSO halo mass function in Fig. 4.9 (b), we find that the average halo mass at $z = 1.7$ is $\log M_{eff} = 12.4$. We further note that our $\log M_{eff} = 12.4$ QSO HOD estimate for the average QSO halo mass is higher than the $\log M = 11.9$ QSO halo mass found from the $b_Q = 2.09$ bias implied by the ratio of the QSO and matter auto-correlation functions (see Section 4.3.3). It is also larger than the halo mass estimated at $M = 2.58 \pm^{0.39}_{0.36} \times 10^{12}\mathrm{h}^{-1}\mathrm{M}_{\odot}$ i.e. $\log M = 11.9$ from the bias of $b_Q = 2.08 \pm 0.3$ we found by scaling the QSO CMB lensing result of Geach et al. (2019) in Section 4.4.2, shown in Table 4.1.

From our HOD model in Fig. 4.9 (b) we see that the QSO mass function shows a steep

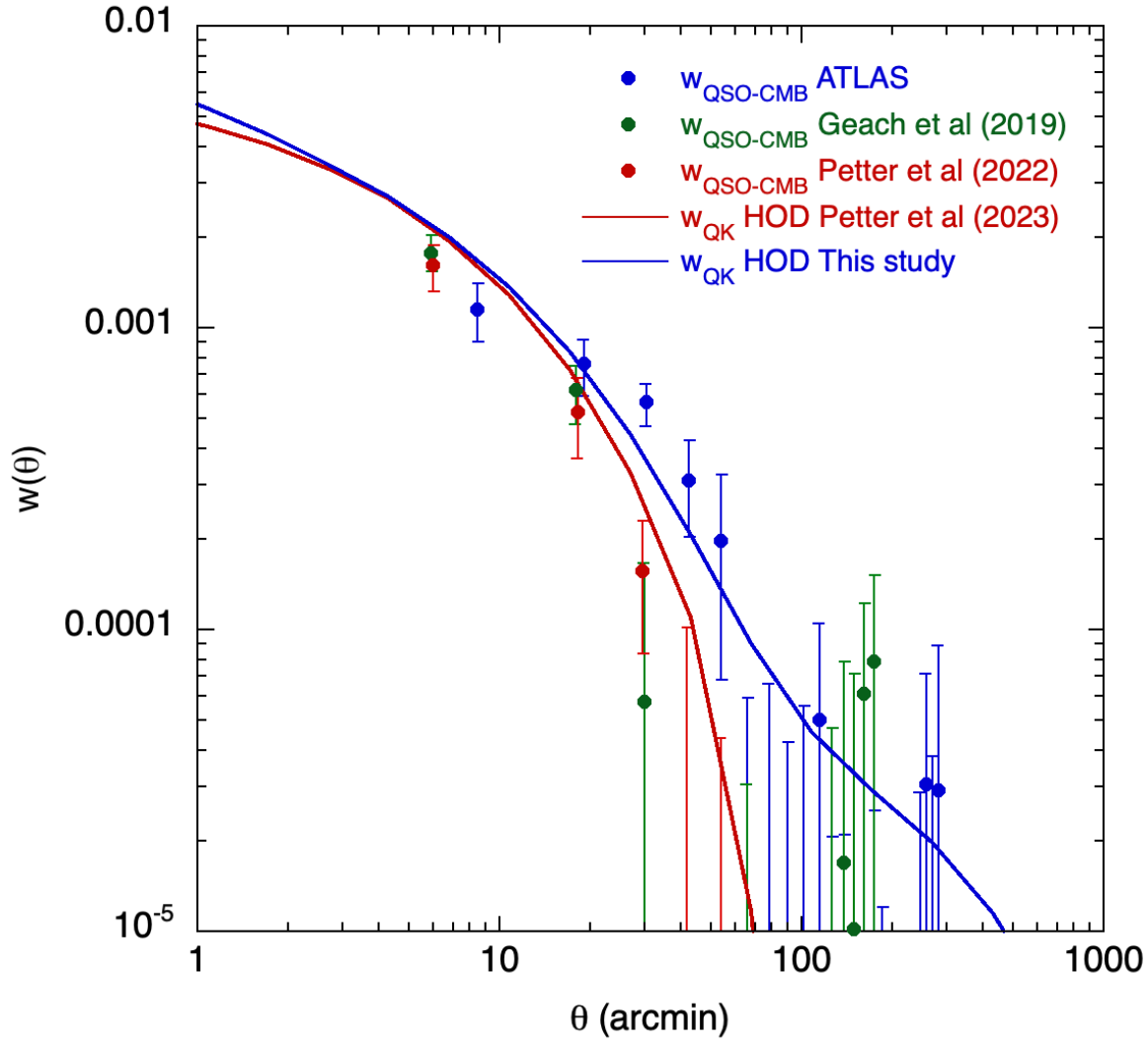

Figure 4.8: The ATLAS QSO-Planck CMB Lensing Map angular cross-correlation function, $w_{QSO-CMB}$, compared to the results of Geach et al. (2019) and Petter et al. (2022). The solid blue line represents our $1 < z < 2.2$ QSO HOD model previously shown in Fig. 4.7 with the same HOD parameters as detailed there. The solid red model represents the HOD model of Petter et al (2023) again as shown in Fig. 4.7. Both models again assume standard ΛCDM parameters with $h = 0.7$ and $\sigma_8 = 0.8$.

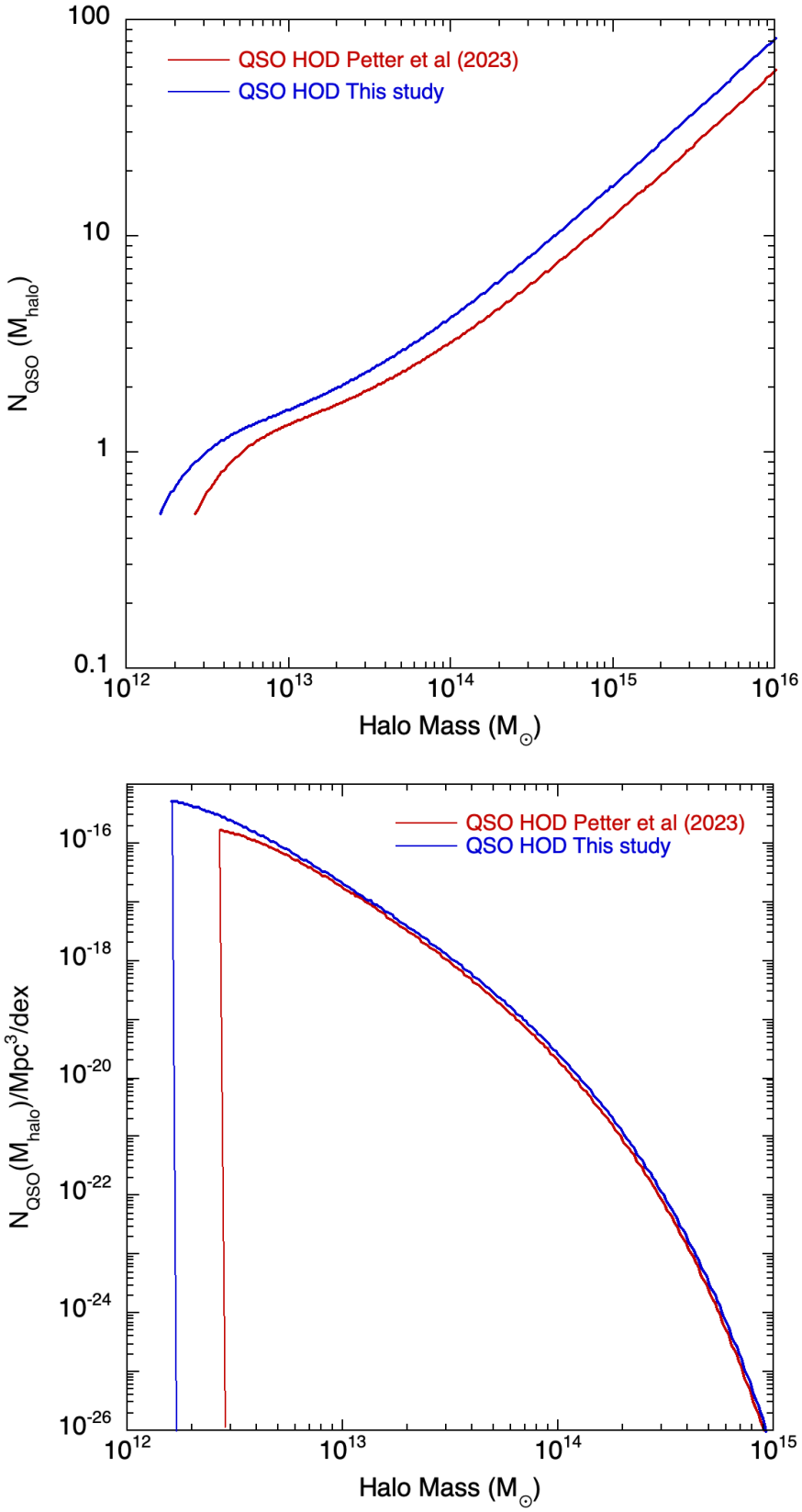

Figure 4.9: (a) The QSO HOD as a function of halo mass. The solid blue line represents our $1 < z < 2.2$ QSO HOD model previously shown in Fig. 4.7 with the same HOD parameters as detailed there. The solid red model represents the HOD model of Petter et al. (2023) again as shown in Fig. 4.7. (b) The QSO space density as a function of halo mass formed by multiplying the halo mass function by a HOD model. The solid blue line represents our $1 < z < 2.2$ QSO HOD model previously shown in Fig. 4.7 with the same HOD parameters as detailed there. The solid red model represents the HOD model of Petter et al. (2023) again as shown in Fig. 4.7.

fall away from $\log M_{min} = 12.2$. Indeed, we calculate that 67% of these $z = 1.7$ QSOs lie in the small halo mass range $12.2 < \log M < 13.2$. Thus it is not unreasonable to say that most QSOs have roughly the same halo mass. This result has been noted before by Shanks et al. (2011) who compared the increasingly faint SDSS, 2QZ and 2SLAQ measurements of the redshift-space correlation $\xi(s)$ and found no dependence of the QSO clustering amplitude on QSO luminosity. Chehade et al. (2016) in the 2QDES pilot survey reached even fainter magnitudes and confirmed this luminosity independence over an order of magnitude (i.e. $\approx 10\times$) in luminosity and over the full $0 < z < 2.5$ redshift range. Since QSO clustering is luminosity independent the implication may be that QSO halo mass and then QSO black hole mass are also luminosity and redshift independent. Here our HOD model now shows that despite the large luminosity range shown by QSOs at fixed redshift (e.g. $z \approx 1.7$), the range of halo and hence black hole masses covered is actually very small. This supports the idea that most QSOs have the same black hole mass.

4.5.5 QSO Halo mass and stellar mass functions compared

Further supporting evidence for this hypothesis comes from the X-ray survey in the PRIMUS field, analysed by Aird et al. (2012). Their Figure 4 (top left panel) shows the probability, $p(L_X|M_*, z)$ for a galaxy of given stellar mass, M_*, and redshift, z, to host an AGN of X-ray luminosity, L_X found for X-ray emitting AGN in this survey. Although it is clear that there do exist X-ray AGN in low stellar mass galaxies, their numbers are quite small compared to the numbers in high stellar mass galaxies.

From the top left panel of their Fig. 4 with $0.2 < z < 0.6$, we sum over the four L_X bins to find the probability, $p_{AGN}(M^*, z)$, of a galaxy of stellar mass, M_*, hosting an X-ray AGN. Since the relations in the four L_X bins appear approximately parallel, we are justified here in adopting an average slope giving $p_{AGN} \approx M_*^{0.75}$. From Ilbert et al. (2013), their $0.2 < z < 0.5$ stellar mass function in their Fig. 5 is given by their eq (2) with $\log(M*) = 10.88$, $\phi*_1 = 1.68 \times 10^{-3}$ h^{3}Mpc$^-$3, $\alpha_1 = -0.69$, $\phi*_2 = 0.77 \times 10^{-3}$ and $\alpha_2 = -1.42$. Multiplying this stellar mass function by the probability, $p_{AGN} \sim M_*^{0.75}$, then gives the number density of AGN as a function of stellar mass as shown in Fig. 4.10. So for the form of the AGN-stellar mass function we find a peaked distribution, centred on $M_* \approx 6 \times 10^{10} M_\odot$. Essentially the low stellar mass end is cut off by the steep correlation with X-ray luminosity while the AGN space density at high stellar masses is naturally suppressed by the decrease in the galaxy

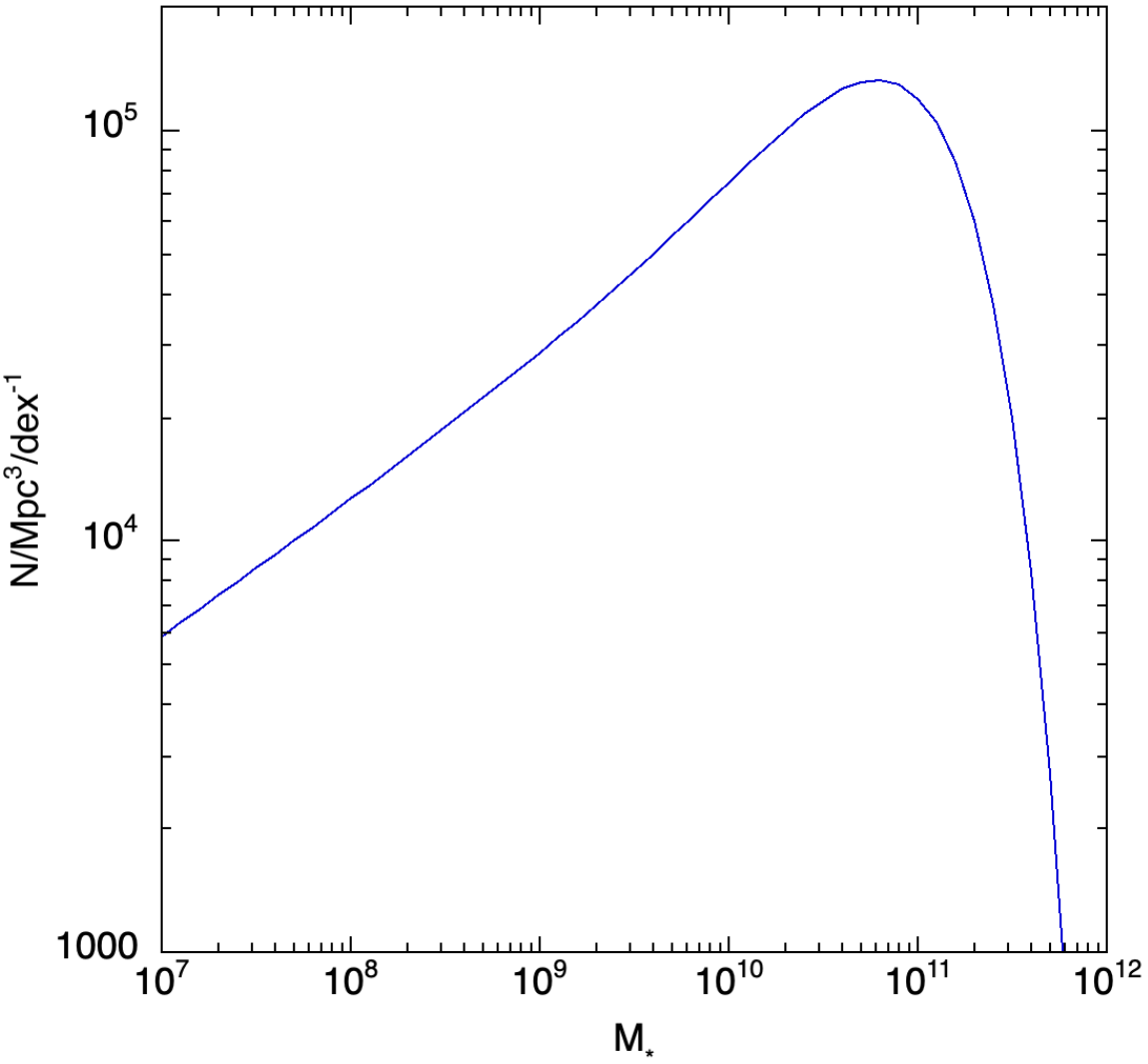

Figure 4.10: The QSO space density as a function of galaxy stellar mass formed by multiplying the galaxy stellar mass function by essentially the X-ray luminosity-stellar mass relation of Aird et al. (2012). Note the similarity to the QSO space density as a function of halo mass in Fig. 4.9.

stellar mass function at high masses. We find 67% of the AGN lie in the stellar mass range $10.0 < \log M_*(M_\odot) < 11.5$. Given a halo mass-stellar mass ratio of ≈ 40 at the peak we see that there is reasonable consistency between the QSO halo and stellar mass functions with both implying a relatively small mass range preferred for QSO hosts.

4.5.6 Evolution of QSO halo mass and luminosity functions

Finally, we consider the question of the physical interpretation of the evolution of the QSO Luminosity Function (LF) which takes a Pure Luminosity Evolution (PLE) form over the range $0 < z < 2.2$ (e.g. Longair 1966; Marshall 1985). Here, QSO luminosity at L^* increases

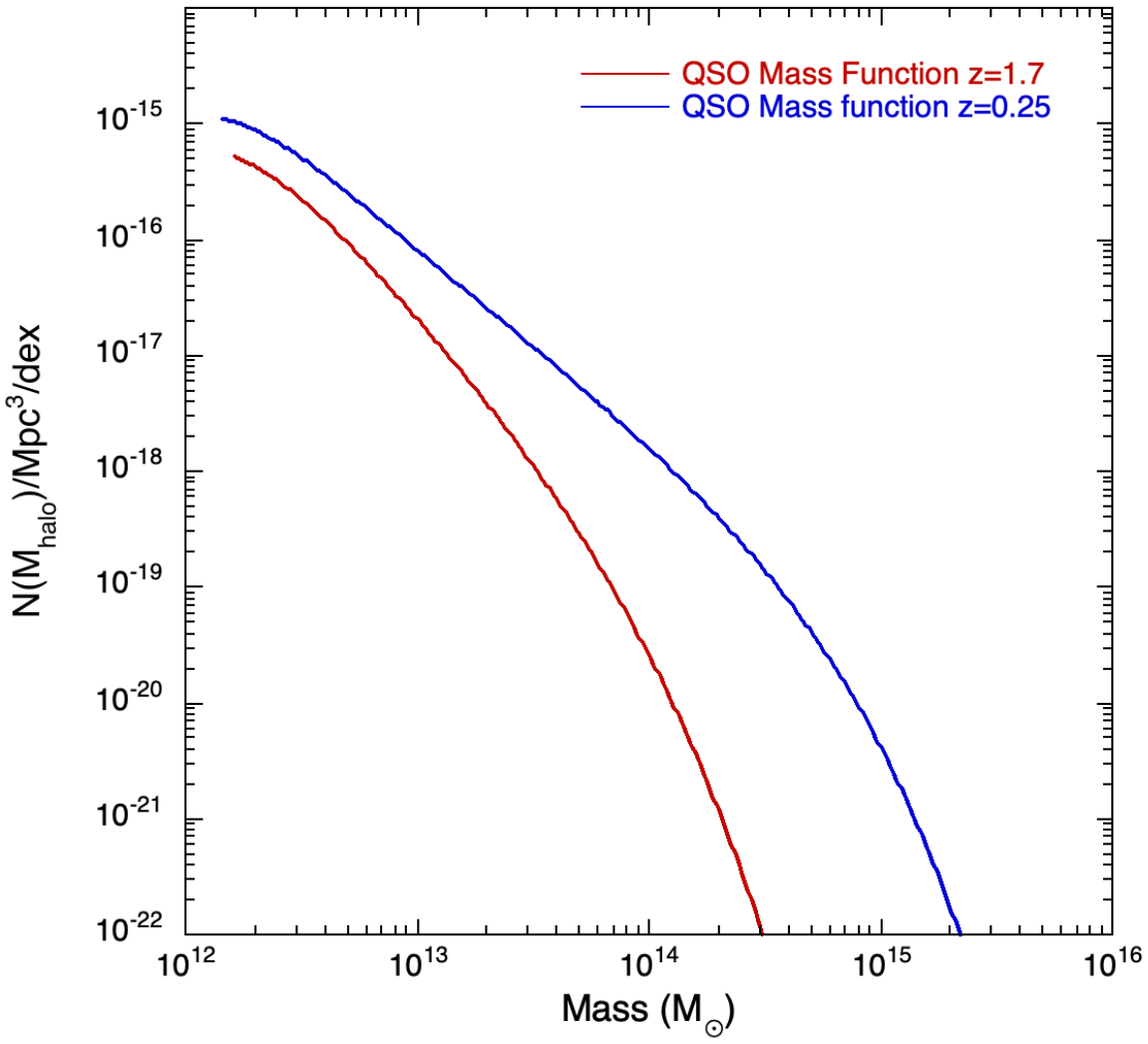

Figure 4.11: The QSO space density at $z = 1.7$ and $z = 0.25$ as a function of halo mass for our QSO HOD model previously shown in Fig. 4.7 and with the same HOD parameters as detailed there. The difference between the two models represents the evolution of the halo mass function between these two redshifts which may appear not dis-similar to the Pure Luminosity Evolution shown by the QSO Luminosity Function.

by $\approx (1+z)^3$ or a factor of ≈ 30 by $z = 2.2$. Shanks et al. (2011) (see also Marshall (1985); Boyle et al. (1988b); Croom et al. (2004), Croom et al. (2009)) have speculated that this coherence of the amplitude of the QSO LF over $\approx 10^{10}$ years might demand a coincidence if QSOs only had lifetimes of $10^6 - 10^9$ years, implying that they may be longer-lived. The PLE model also predicts only a slow rise in BH mass between $z = 2.2$ and $z = 0$ despite the sharp decrease in QSO luminosity and again this could be in agreement with the luminosity independence of QSO clustering. However, these authors also noted that the evolution of the QSO correlation function and its implied bias with redshift were not consistent with such a long-lived model (see e.g. Fry (1996)). The evolution of the QSO mass function shown in Fig. 4.11 highlights this issue. Here, taking $b_Q(z = 0.25) = 1.0$ from the $b_Q - z$ fit shown in eq. 15 of Croom et al. (2005), and fitting a HOD to the resulting $\xi_{20}(z = 0.25)$ with $\log(M_{min}) = \log(M_0) = 12.15$, $\sigma_{\log M} = 0.4$, $\log(M_{1'}) = 13.23$ and $\alpha = 0.7$ gives the QSO mass function for $z = 0.25$. This has moved to higher masses compared to the $z = 1.7$ case, taken from Fig. 4.9(b), as might be expected after gravitational growth, whereas the LF moves to lower luminosities at lower redshift (see e.g. Fig. 6 of Croom et al. (2009)). This behaviour of the LF under PLE is sometimes called "downsizing". With lower luminosities and higher masses at low redshifts the Eddington ratios are clearly lower at low redshift. Now despite the opposite direction of the evolution of the mass and luminosity functions, both appear consistent with evolution in the horizontal (mass) direction with the mass function showing roughly constant space densities with redshift, similar to the LF. Since this constant QSO density with redshift seems to appear naturally out of gravitational growth in the ΛCDM model, then no appeal to a long-lived QSO model may be needed to explain the non-evolution of the QSO LF in the density direction. In this case the dimming of the QSO LF with decreasing redshift could be ascribed to depletion of the supply of gas+stars to fuel QSO accretion. The analogy here would be with galaxy evolution if the reason for the observed dimming of the galaxy LF is depletion of the gas supply, in this case inhibiting star-formation. Although in both cases there would need to be a mechanism invoked to restrict fuel supply while gravitational growth was on-going, this interpretation for QSO PLE seems worth further study, including testing its prediction of QSO M_{BH} independence of redshift and luminosity via (stacked) reverberation mapping analyses.

4.6 Conclusions

The aim of this chapter was to make new estimates of QSO host halo masses via QSO clustering and QSO-CMB lensing cross-correlation analyses. The QSO catalogues came from the VST-ATLAS quasar survey of Chapters 2 and 3. The depth and reliability of the ATLAS QSO catalogue meant that we could measure the QSO 2-point angular correlation function directly from the data. We found that it was well modelled in 3-D by a correlation function with a power law form, $\xi(r) = (r/r_0)^{\gamma}$ with $r_0 = 5.2\mathrm{h}^{-1}$ Mpc and $\gamma = -1.8$. Then assuming a linear regime mass power spectrum in a ΛCDM model, we compared galaxy and mass auto-correlation functions within a $20\mathrm{h}^{-1}$ Mpc radius sphere (i.e. ξ_{20}) to find $b_Q = 2.09 \pm 0.09$ implying a QSO halo mass of $M_{halo} = 8.5 \pm 0.3 \times 10^{11} M_{\odot}$.

We then cross-correlated the QSO sample described in Sec. 4.2.1 with the CMB lensing maps of Planck Collaboration et al. (2018). We first used methods similar to those outlined by Geach et al. (2019) to measure the bias and halo mass via the lensing of the CMB by foreground quasars. Here we find good agreement between our data and that of Geach et al. (2019) as well as that of Petter et al. (2022). We are then able to fit the model determined by Geach et al. (2019) to our data with a scaling factor of 0.8 and a scaling factor of 0.85 to the model determined by Petter et al. (2022). Therefore, we are able to measure a quasar halo bias of $b_h = 2.08 \pm 0.3$ at an average redshift of $z = 1.7$, corresponding to a halo mass of $0.83 \times 10^{12} h^{-1}\mathrm{M}_{\odot}$. Our bias value is in excellent agreement with the quasar bias from quasar clustering in Chehade et al. (2016) as well as the QSO-CMB cross-correlation study of Petter et al. (2022).

We then combined these two methods and fitted a HOD model to w_{qq} which could be tested for consistency using QSO-CMB lensing. The HOD parameters that we obtained from w_{qq} were similar to those measured for unobscured QSOs by Petter et al. (2023) with the only difference being that $\log(M_{min}$, $\log(M_0)$, and $\log(M_{1'})$ were $\log(M) = 0.2$ smaller than measured by Petter et al. (2023). From the resulting QSO mass function produced by multiplying the ΛCDM halo mass function by the QSO HOD, we found an average QSO halo mass at $z = 1.7$ of $\log M_{eff} = 12.4$, again about $\log(M) = 0.2$ smaller than measured by Petter et al. (2023) and also slightly higher than measured from b_h inferred directly from w_{qq} and via CMB lensing cross-correlation, $w_{q\kappa}$. However, this HOD model from our w_{qq} was also found to be a good fit to our CMB lensing results, confirming consistency between these

two independent observations. From the QSO mass function we also found that 67% of the $z = 1.7$ QSOs had halo masses that lie in the small halo mass range $12.2 < \log M < 13.15$ suggesting that most QSOs have similar halo and hence black hole masses. A similar result can be found by combining the galaxy stellar mass function of Ilbert et al. (2013) and the probability of a galaxy hosting an X-ray AGN as a function of stellar mass as estimated by Aird et al. (2012). Here, 67% of $z = 1.7$ AGN are found to lie in the stellar mass range $10.0 < \log M_*(M_\odot) < 11.5$.

Finally, we inter-compared the QSO halo mass functions at $z = 0.25$ and $z = 1.7$ and showed that they appear to evolve to higher masses as redshift decreases as would be expected from gravitational growth. Although the QSO LF evolves in the opposite direction to lower luminosities at low redshift, the two functions otherwise appear similar with the halo mass function evolving mostly in the mass rather than the space density direction. This is reminiscent of the PLE shown by the QSO Luminosity Function. Thus it may be that this constant QSO space density with redshift may be naturally explained by gravitational growth in a ΛCDM Universe with no need to invoke long lived QSO models as discussed by Shanks et al. (2011). In this case the decreasing brightness of QSOs towards the present day may be explained by the increasing lack of material available for accretion to fuel the QSO, despite the gravitational growth of the QSO halo mass. This would then amount to a analogous explanation to the PLE seen in galaxies where the low luminosity of galaxies at low redshift may be due to the reduction in the gas supply needed to fuel star-formation, causing the galaxies to dim in the rest optical bands by the present day (see e.g. Metcalfe et al. (2001)).

Chapter 5

Stacked Reverberation Mapping

5.1 Introduction

Remarkably few QSOs have well-measured black hole (BH) masses, which are crucial for understanding AGN BH and accretion disc physics. The evolution of the active BH mass function also maps out the cosmic history of BH accretion which is important for theories of galaxy formation given the role of AGN in providing 'feedback' to suppress star-formation in massive halos at early times. Unfortunately, it is at higher redshifts where the lack of reliably measured BH masses is most acute. So, at $z < 0.3$, ≈ 35 AGN have had their BH mass estimated dynamically via H_β broad-line region (BLR) 'reverberation mapping' (RM) (e.g. Peterson 2004, Kaspi et al. 2000). But at higher z, MgII and CIV lags have still been measured for only < 100 QSOs, from SDSS IV (e.g. Shen et al. 2015, 2019) and OzDES (Hoormann et al., 2019). Here, we aim to improve knowledge of the active BH mass function and the BH-accretion disc connection at $0.5<z<3$ using reverberation mapping applied in a new, observationally highly efficient, form.

Reverberation mapping (RM) of QSOs, which utilizes the intrinsic variation of QSOs in order to determine black hole masses is currently the only method with which we are able to determine larger samples of black hole masses at higher redshifts. This is done by tracing variations in the continuum emission, after a time lag, to variations in the broad-line luminosity. The time lag can be mapped to the light crossing time of the broad line region. Given this 'reverberation-mapped' radius, R_{BLR}, and an estimate of the r.m.s. velocity of broad line region gas clouds $< v^2 >^{1/2}$ from the FWHM of an emission line, the black hole mass can be estimated from the virial relation ($M_{BH} \approx R_{BLR} < v^2 > /G$).

Aside from this traditional RM technique, a stacking method was developed by Fine et al. (2012, 2013) in order to probe a wider range of timescales through stacked cross-correlations, providing a more observationally efficient way of determining black hole mass estimates in lower luminosity and higher redshift samples. The Fine et al. (2013) results show that the stacked RM method works and this has now been confirmed by the OzDES project (Malik et al. 2023, Sommer N. et al., in prep.) who find that while only a few out of several hundred quasars give individually significant lag detections, many others give consistent lags when 'stacked' at similar quasar luminosities and redshifts.

We now apply this stacking technique to $\geq 10\times$ more QSOs than Fine et al. (2013), by targetting the GAMA G09 field (Baldry et al. 2010). G09 itself is almost fully contained within the eROSITA eFEDS PV field (Liu et al. 2022, see also Predehl et al. 2021) thus providing multi-wavelength coverage including X-ray, optical, NIR and MIR photometry to enable efficient QSO selection. We then use the Anglo-Australian Telescope to measure 2-3 2dF+AAOmega (Sharp et al., 2006) epochs of emission line strength for the QSOs, with a further spectroscopic epoch supplied by DESI. Combined with a larger number (≥ 50) of CTIO DECam (Flaugher et al., 2015) r-band continuum epochs, these data allow us to make stacked continuum-broad line lag estimates of mean QSO BLR radii. Meanwhile, eROSITA is contributing up to 5 epochs of X-ray flux for the same QSOs in the same time period and combining these with the DECam r-band continuum light curves, enables us for the first time to stack continuum-X-ray cross-correlations to estimate the size of the accretion disk. Thus, ultimately, these data may allow us to measure the ratio of QSO BLR and accretion disk radii and establish its dependence on black hole mass (M_{BH}).

5.2 QSO Target Catalogue

For stacked RM, we require a large number of r-band photometric epochs coupled with ≥ 2 spectroscopic epochs and ≥ 2 X-ray epochs. The more QSOs that can be observed in each of these ways, the more efficient our observations will be. So the multiplex advantages of observing up to 360 QSOs simultaneously with 2dF (and eROSITA) is where the gain in stacked RM lies. We aim to create a QSO target catalogue with a QSO sky density of ≈ 90 deg^{-2} that can be reached at $g \approx 22$mag, high enough to be suitable for stacked RM while accepting that in average conditions with typical 2dF exposure times of 1.5hr, the limit for measuring broad line strengths may be $g < 21$ mag where the sky density is ≈ 40 deg^{-2}.

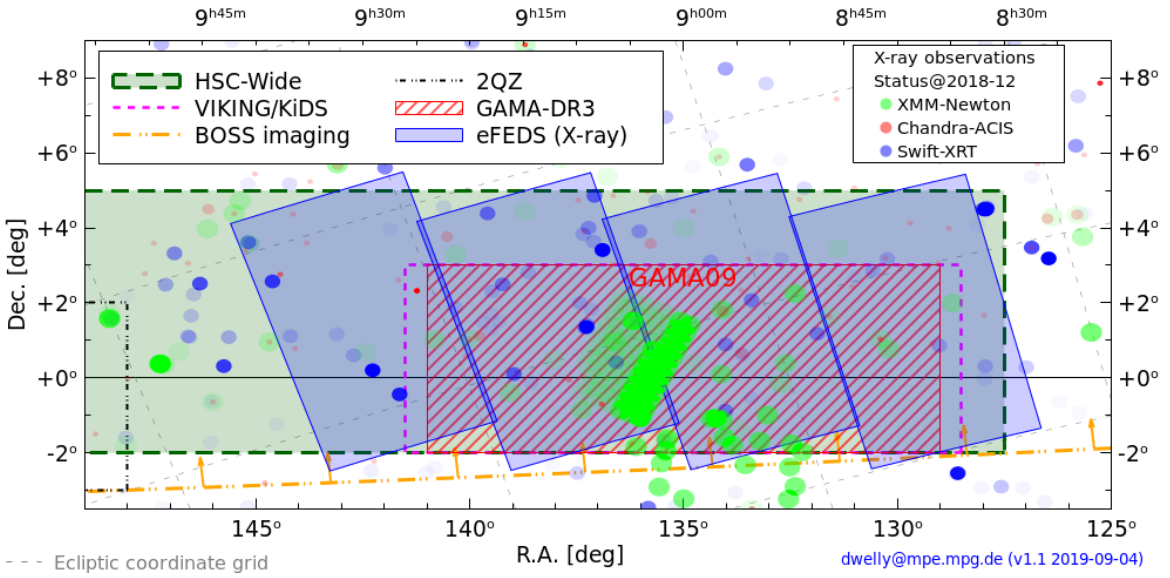

Figure 5.1: Survey locations. The four gray rectangles represent the ≈ 140 deg^2 of the eROSITA eFEDS field and the red shaded rectangle represents the ≈ 70 deg^2 of the GAMA G09 field. The red dashed rectangle represents the KIDS-N-W2 area. Our aim was to cover as much of the eFEDS X-ray field as possible and the positions of our 23 target fields can be seen in Fig. 5.2.

We therefore aim to make a target QSO catalogue of 2500-6000 QSOs in an ≈ 69 deg^2 survey region centred on the GAMA G09 field. This comprises up to 72 optical photometry epochs from DECam, for which observations commenced in February 2020, and 2 to 3 epochs of 2dF spectroscopic measurements. We use KiDS+NEOWISE to create a photometrically selected QSO candidate catalogue for these optical and spectroscopic observing programs. The KiDS+NEOWISE QSO candidates are supplemented with DESI QSO candidates (and spectroscopically confirmed QSOs as available via internal data releases) as well as eROSITA X-ray QSOs and any publicly available overlapping spectroscopic surveys in the area, such as 2SLAQ, eBOSS, SDSS IV. The area of sky surveyed is shown in Fig. 5.1. These data allow us to measure continuum-emission line time lags for the H_β, MgII and CIV lines over wide redshift and luminosity ranges as well as the X-ray-continuum lag.

5.2.1 Data

eROSITA

The extended ROentgen Survey with an Imaging Telescope Array (eROSITA) launched in 2019 on the Spectrum-Roentgen-Gamma (SRG) mission (Predehl et al., 2021). It was planned to conduct a four year long survey collecting eight passes of X-ray observations, lasting six

months each. Performance verification (PV) of the instrument was conducted in the ≈ 140 deg^2 eROSITA Final Equatorial Depth Survey field (eFEDS) at a slightly greater depth than expected over the whole sky at the end of eROSITA All-Sky Survey (Brunner et al., 2022). The GAMA G09 field overlaps with $\approx 50\%$ of this eFEDS field (see Fig. 5.1). Therefore, we chose to perform our stacked RM project in this eFEDS/G09 field and use the positions of QSOs in the eROSITA PV data and subsequently the full eROSITA eFEDS AGN catalogue (Liu et al., 2022) to provide our highest priority targets for 2dF Broad Line monitoring. eROSITA would thus provide us with up to 9 epochs of X-ray data, ideally timed to fit in with our optical and spectroscopic observing program.

KiDS

We utilize the Kilo-Degree Survey (KiDS) DR4 (KiDS: Kuijken 2011; de Jong et al. 2013) to create a photometrically selected candidate catalogue to increase QSO numbers for our BL and X-ray RM survey. This data release contains *ugri*-band photometry over 1350 deg^2 of sky, observed with the OmegaCAM camera at the VLT Survey Telescope (Capaccioli & Schipani 2011; Kuijken 2011; Kuijken et al. 2002, also described in Chapter 2). The 1350 deg^2 area includes NGC equatorial and SGC polar strips, plus two smaller NGC areas. One of these smaller areas, KiDS-N-W2, covers the 70 deg^2 area of the GAMA G09 survey field (Driver et al., 2011), although not the whole eFEDS X-ray field. KiDS was observed in the *ugri* bands with r-band seeing of $\approx 0.''7$ seeing and reaching an AB magnitude limit of $r < 25.0$, with comparable limits in the other bands. The images are processed using the Astro-WISE pipeline (McFarland et al., 2013) and calibrated using Gaia DR2 (Gaia Collaboration et al., 2018) and SDSS (Alam et al., 2015). We utilize the KiDS aperture fluxes and star/galaxy classification to create our QSO candidate catalogues.

DECaLS DR9

Referenced in Ch. 2, we use data from the DECaLS Legacy Survey DR9 release (Dey et al., 2019b) for the W1- and W2-band data necessary for our candidate selection. The WISE fluxes in DECaLS DR9 come from the year 6 release of the NEOWISE-Reactivation mission (Schlafly et al., 2019), also called neo6 previously in this work. However, these fluxes are measured using 'forced-photometry' at the location of the DR9 optical sources in the unWISE images in order to detect fainter sources than the standard neo6 catalogues that are cut at a $>3\sigma$ detection limit. These data cover the entire eFEDS X-ray field.

DESI

We utilize various DESI (DESI Collaboration et al., 2016) data to supplement our KiDS+ NEOWISE QSO candidate selection, especially at the edges of the eFEDS fields where we don't have full coverage from KiDS (see Figs. 5.1,5.2). Therefore, in these eFEDS areas, we include DESI QSO candidates as 2dF targets to our $g < 22.0$ limit. Described by Yèche et al. (2020), these candidates are selected based on DECaLS DR9 $grz + W1 + W2$ photometry as described above, with the additional application of the Random Forest ML algorithm to achieve their $r < 22.7$ limit.

In addition to the DESI QSO candidate catalogue, at a later stage we also added DESI spectroscopically confirmed QSOs to our target catalogues as internal DESI data releases were published.

eBOSS + 2SLAQ + SDSS IV SPIDERS

To our QSO RM catalogue, we add spectroscopically confirmed QSOs overlapping our area from the eBOSS DR16 survey (Ahumada et al., 2020). The eBOSS observations were made using the BOSS spectograph (Smee et al., 2013) with target classes including the main 'tracer' ($z < 2.2$) QSO sample and also Lyα QSOs at $z > 2.2$ to provide BAO measurements. The eBOSS target selections (Myers et al., 2015) for these samples probe QSOs to $g < 22 - 22.5$ in the $0.9 < z < 3$ redshift range.

We also add overlapping QSOs from the 2dF-SDSS LRG and QSO Survey (2SLAQ) described by Croom et al. (2009) to provide additional spectroscopically confirmed QSOs to our target catalogue.

Similarly, we also included 1656 eROSITA eFEDS X-ray QSOs that were spectroscopically confirmed and redshifted in the SDSS IV SPIDERS survey (Liu et al., 2022).

5.2.2 KiDS+WISE QSO Selection

Using the KiDS+WISE data in the G09 field, we select additional candidate QSOs to add to our 2dF target list using the mid-IR and UVX cuts outlined in Ch. 2 as a starting point. We optimise these for completeness and contamination in KIDS data using the spectroscopically confirmed 2SLAQ, eBOSS, etc QSOs that overlap the G09 field. In our photometric QSO selection we only include the sample described as Priority 1 in Ch. 2 in order to reduce contamination by galaxies (and stars).

This comprises the $ugr + griW1$ selection combined with the KiDS stellar classification and a base selection with a white dwarf cut, a UVX selection, and a mid-IR selection. These are defined as follows.

The base selection + white dwarf cut:

$$\begin{aligned} &16 < g \leq 22.5 \ \& \ -0.4 \leq (g-r) \leq 1.1 \ \& \\ &not \ ((r-i) > 0.4385 * (g-r) - 0.1681) \\ &\& \ not \ ((r-i) < 0.4385 * (g-r) - 0.0181 \& (g-r) < -0.05) \end{aligned} \tag{5.2.1}$$

The UVX selection:

$$\begin{aligned} &-0.5 \leq (u-g) \leq 0.6 \ || \\ &(u-g) < 0.6 \ \& \ (g-r) \leq -0.9(u-g) + 0.8 \end{aligned} \tag{5.2.2}$$

The mid-IR selection:

$$\begin{aligned} &(i-W1) \geq (g-i) + 2.2 \ \& \\ &-1 \leq (g-i) \leq 2.35 \ \& \\ &(i-W1) < 8 \end{aligned} \tag{5.2.3}$$

5.2.3 Final 2dF QSO Target Sample

For 2dF, we observe all of the eROSITA QSOs (Liu et al., 2022) in our sample at the highest priority given our twin aims of applying stacked RM to Broad Lines and X-ray QSOs. Then, all spectroscopically confirmed objects in our catalogue get assigned second highest priority. This consists of all eBOSS QSOs, and all DESI and KiDS candidates spectroscopically confirmed after our first year of observing, as well as the incoming DESI spectroscopic identifications. Then, at third priority we put the rest of the KiDS and DESI QSO candidates.

There is significant overlap in the sample, with a number of DESI candidates and spectra having been eBOSS QSOs as well as KiDS targets, and all of the catalogues having an overlap with eROSITA QSOs. However, we label our QSO targets (shown in Fig. 5.2) in the manner with which we assigned the priority level, first highlighting all of the initial spectroscopic and X-ray identifications. For example, as observations continued, we could confirm a larger number of KiDS targets through both our observing program as well as via the DESI spectra. However, these would still be labeled as KiDS targets in our data, although their priority for spectroscopic follow-up would be adjusted accordingly.

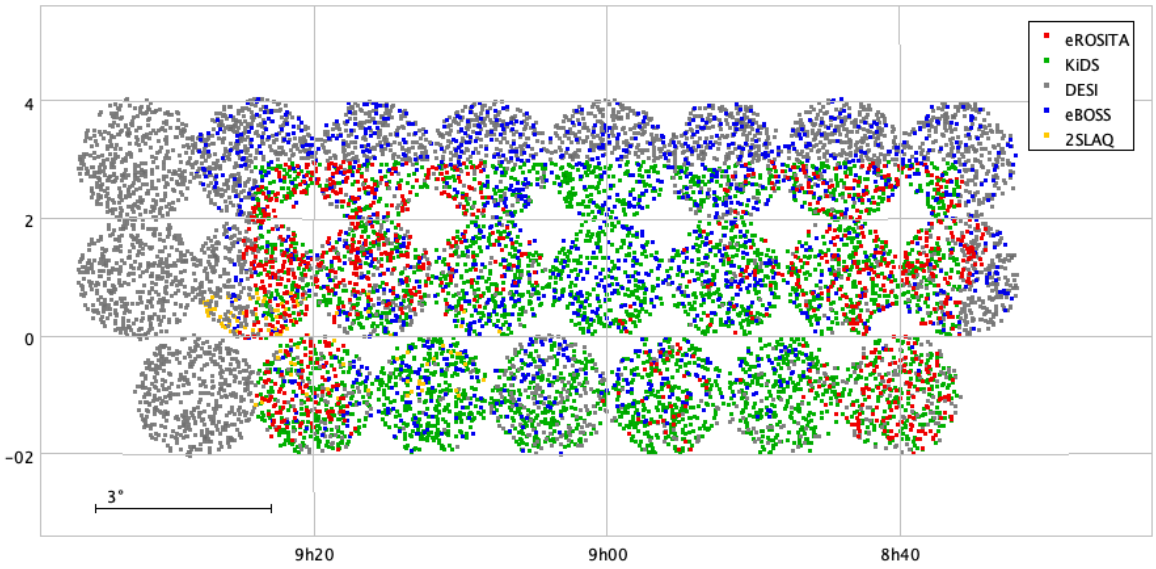

Figure 5.2: Our targets in the eROSITA eFEDS field. We combine eROSITA PV data, KiDS, DESI, eBOSS, and 2SLAQ in order to have the most complete sample of QSO targets for our stacked reverberation mapping project, with RA in hms on the x-axis and DEC in degrees on the y-axis. Here, data originally received from eROSITA is shown in red, candidates from our KiDS target selection are shown in green, DESI targets are shown in gray, eBOSS QSOs are shown in blue, and 2SLAQ QSOs are shown as yellow points. These targets overlap in various ways, especially during the 3.5 years of observations we conducted, with DESI spectroscopy being done in this area, eROSITA X-ray imaging this area, and with us conducting 2dF spectroscopic observations as well.

5.3 Continuum r-band Observing Program

We were awarded near weekly r-band continuum observing covering the full area of our eFEDS fields with the following proposals: NOAO (2020A-0142 and 2020B-0182), CNTAC (CN2020A-34), NOIRLab (2021B-0038), NOIRLab (2022A-880319), and NOIRLab (2022B-122231) as part of the DECAT collaboration. This allowed us to measure r-band continuum variability over a period of > 3 years during the November-June observing season.

5.3.1 CTIO DECam

We carried out r-band observations remotely at the Cerro Tololo Inter-American Observatory (CTIO) in Chile, using the Dark Energy Camera (DECam) on the Victor M. Blanco 4-meter Telescope. DECam (Honscheid & DePoy 2008, Diehl & Dark Energy Survey Collaboration 2012, Flaugher et al. 2015) is an ≈ 520 megapixel optical camera with 62 science CCDs with $0.''26$ pixels, giving a circular field of ≈ 3 deg^2 area, the same as 2dF. We observed only with the DECam-r band filter covering the range 5700-7000 Å , always using a single 60s exposure (with 25s overhead) for each of the 23 fields, reaching $r \approx 23.5/22.0$ at 5σ in $1''/2''$ seeing and dark/bright conditions. We collected all of our data via remote observing, between 4th February, 2020 and 10th March, 2023. Note that data were taken up to June 2023 but were not used due to no further spectroscopic data being taken after February 2023 nor X-ray data after November 2021. There were significant interruptions to our DECam observing with no observing being possible during April-June, 2020 due to CTIO being closed due to the COVID pandemic, nor from early December - mid January, 2020 due to a DECam technical problem. The timeline of our CTIO DECam observations compared to the AAT + DESI spectroscopic (see Section 5.4) and eROSITA X-ray observations (see Section 5.5) is shown in Fig. 5.3.

5.3.2 Data Calibration and Reduction

After the images are processed via the community pipeline (Valdes et al., 2014), our DECam data was reduced and calibrated by N. Metcalfe. The r-band images were processed by SExtractor (Bertin & Arnouts, 1996) with the flat-fielded data downloaded from the NOIRlab Astro Data Archive assuming an arbitrary calibration for the magnitudes. The resulting image catalogues are then matched to SDSS r-band magnitudes and calibrated accordingly.

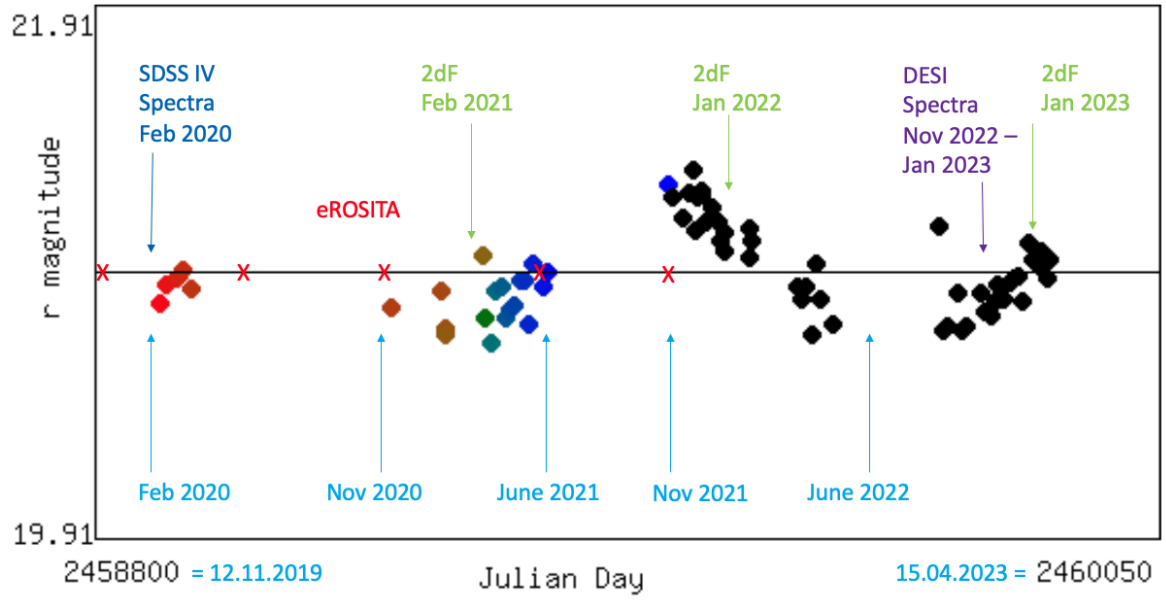

Figure 5.3: The timelines of our DECam imaging, 2dF+DESI spectroscopy and eROSITA X-ray observations are compared from November 2019 to April 2023, demonstrated on a randomly picked QSO light curve. The circular points show the r-band light curve of this object, with no distinction made between the colors of these points. The light blue arrows on the bottom of the figure are a guide for the dates on which observations were taken. The red X marks show when eROSITA X-ray data was collected, the green arrows show the times at which we collected spectroscopy at the AAT 2dF, and the purple text indicates when the DESI spectroscopy was taken that is used in our work.

Now correctly calibrated, the original images are then re-run through SExtractor with magnitudes calibrated to the SDSS system. The Julian dates for each observation are taken from the original images and the mean, median, and rms magnitudes for each object (not just QSOs) are calculated, averaging over the recorded dates. Some data is then rejected using the scatter in these data, for example due to bad observing conditions such as high cloud coverage for a particular epoch.

The final reduced data were then made available at `https://astro.dur.ac.uk/~nm/pubhtml/decam/index.php`. There, we can see the full DECam light curves for each object and can search by target class. For fields 1-23, shown in Figure 5.2, two fields (eFEDS08, 16) were only observed $\approx$ 15 times, with the rest having $\geq$50 observations, up to a maximum of 72 epochs. We can therefore make preliminary tests of the data and select objects of interest that display variations in the r-band. Figure 5.4 shows four examples of such light curves. In Fig. 5.4 a light curve of a star is shown as an example of a non-varying continuum. The light curves shown in Fig. 5.4 (b), (c), and (d) are example QSO lightcurves at various redshifts which show significant variability.

5.4 Spectroscopic Observing Program

In 21A we were awarded 4 2dF nights by OPTICON (O/2021A/13) for 13-16/3/21 and 4 nights by ATAC (A/2021A/6) to perform spectroscopic observations of our QSO candidates in the eROSITA eFEDS fields for our stacked RM project. These were then followed up by nights awarded by Opticon-TAC (21B/022) for 6-9/1/22, ATAC(21B/01) for 26-28/1/22, Opticon-TAC (22A/046)for 25-27/3/22, and finally Opticon-TAC (22B/045) for 28-31/1/23. The 21A runs were reasonably successful but the later runs were increasingly cloud affected. This spectroscopic observing program allowed us to measure broad line strengths for the QSOs in order to perform our optical to BLR reverberation mapping to determine the radius of the BLR and ultimately determine black hole masses.

5.4.1 AAT 2dF observing

To observe multiple spectroscopic epochs of our QSOs in the G09 field, we utilize the 2-degree Field (2dF) fibre coupler feeding 400 fibres over 3 deg^2 into the AAOmega spectrograph (Sharp et al., 2006) at the Anglo Australian Telescope (AAT: Lewis et al. 2002). The AAT-2dF has a robot fibre positioner which places target fibres of 2.″1 diameter to 0.″3

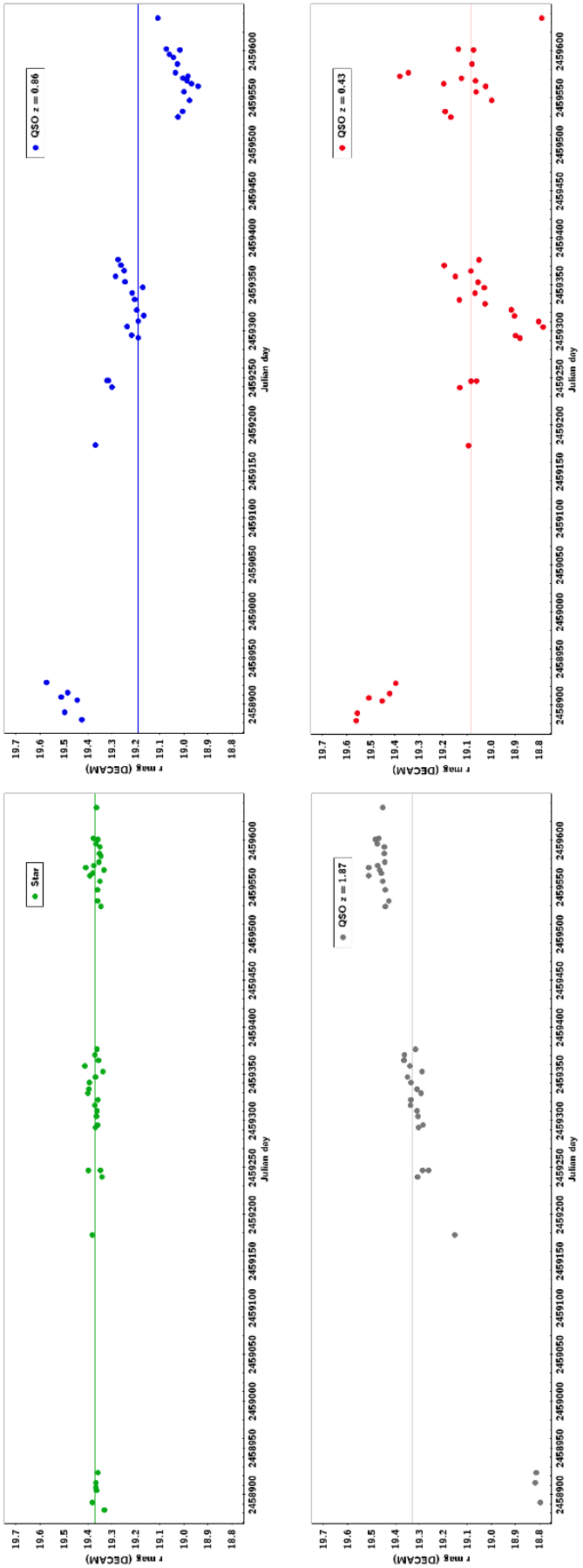

Figure 5.4: Four example lightcurves taken from `https://astro.dur.ac.uk/~nm/pubhtml/decam/index.php`. (a) shows the typical lightcurve of a star. In (b), (c), and (d) we see examples of QSO lightcurves at various redshifts which show variability characteristic of QSOs.

precision. We used the 580V grating (3.6 Å resolution) in the blue arm of AAOmega and the 385R grating(5.5 Å resolution) in the red arm with the dichroic set at 5700 Å , giving a wavelength coverage from 3800-8700 Angstroms. In order to prepare our QSO candidate files for observation, we add GAIA guide stars in every field to calibrate the telescope positioning fibres as well as SDSS Sp Standard Stars and multiple sky fibres.

2dF Spectroscopic Reduction

The spectra are first reduced with the 2dfdr data reduction package (Taylor et al., 1996) so that after de-biasing and flat-fielding, the spectra are extracted into 1-D form and then wavelength calibrated using arc spectra and then sky subtracted. Spectra from the blue and red arms were then spliced together (except in the cases denoted by a dagger in Table 5.1 where this was not possible for technical reasons).

We first tried to flux calibrate our spectra using these standard stars, but found that these were quite limiting as they occasionally lack the full colour/gri-band information and sometimes had poor S/N spectra. Therefore, we found that the best way to flux calibrate the spectra was to match the integrated flux in the appropriate portion of the spectrum to the g, r and i band imaging photometry, with the r-band taken from the closest (in time) DECam observation, and g and i formed from this r-band using SDSS $g-r$ and $r-i$ colours. This assumes that the $g-r$ and $r-i$ colours are constant, at least to first order, even when the r-band varies. Target fibres are allocated via the priority system described in Section 5.2.3. Our full observations are described in Tables 5.1 and 5.2. These spectroscopic epochs allow us to measure broad line strength variability in order to derive average BLR radii and black hole masses.

We then used MarZ (Hinton et al., 2016) to perform QSO line identifications and redshift all of the spectra, helped by eye where necessary. The MarZ software was developed by the OzDES group, to be an open-source web application designed for use on AAOmega spectra. Shown in Fig. 5.5 are some examples of our QSO spectra displayed the MarZ software. The black lines are our spectra, the red line is the MarZ QSO template, and QOP:4 denotes a spectroscopic identification at our highest confidence level. We publish a list of newly identified QSOs, cross referenced with eROSITA, DESI, eBOSS, and other publicly available spectroscopic data to remove all duplicate observations, in the appendix.

2dF QSOs were included in the RM samples if they had spectroscopic quality, QoP = 3 or 4. Because of the high signal-noise of the DESI spectroscopy, in cases where the redshift

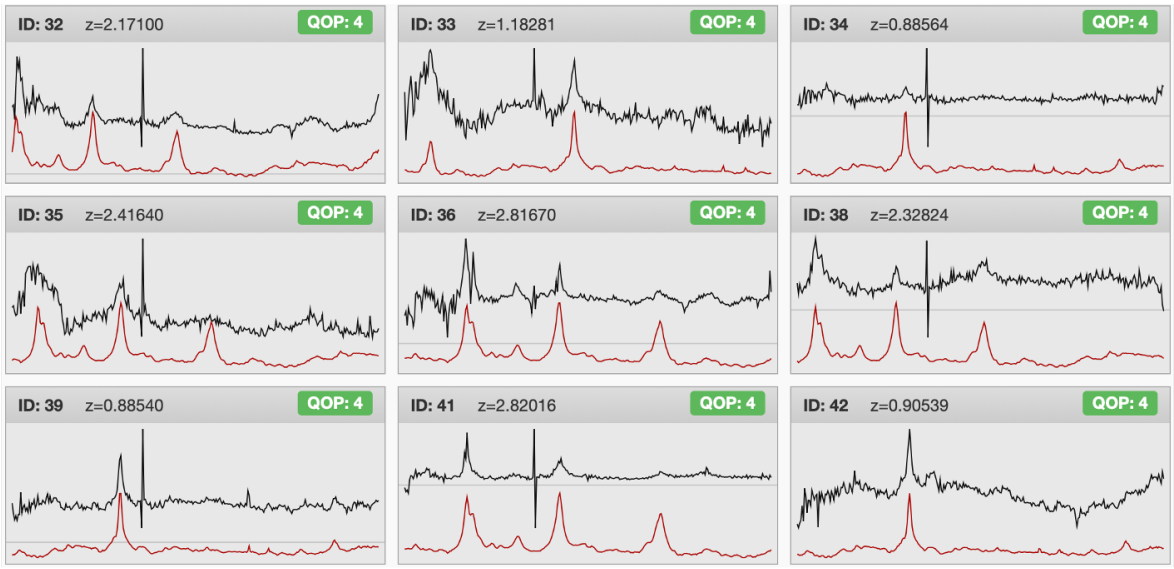

Figure 5.5: Spectra of 9 of our QSOs, calibrated by 2dF, and shown using the MarZ software. The wavelength range covered is 3800-8700 Å .

difference was $\Delta z > 0.01$, we replaced the 2dF redshift with the DESI redshift. Of course, only a minority of these QSOs have emission line strength accurate enough for Broad Line RM analysis or are bright enough for X-ray RM analysis. The 272 new QSO redshifts measured by 2dF, excluding those already measured by DESI or SDSS are listed in Appendix B.

5.4.2 DESI spectroscopy

The DESI collaboration spectroscopically observed many QSOs, including many of the DESI selected QSOs in the eFEDS fields, in the period November 2022-January 2023, with the Guadalupe release being the main source of confirmed QSOs. These were vital in that they made up for poor observing conditions during our AAT runs in the periods January-April 2022, 2023. DESI spectra have both higher ≈ 1Å resolution and higher S/N than typical 2dF spectra, which makes for better measurements of QSO broad emission line strengths.

5.4.3 SDSS IV SPIDERS spectroscopy

These obsevations were made on the SDSS 2.5-m telescope as part of the SDSS IV SPIDERS program (PI A. Merloni). In a 6-night run in February 2020, redshifts for 1656 broad line QSOs were measured for this X-ray selected sample from the eROSITA eFEDS PV program and these were always included in the subsequent 2dF runs as being confirmed QSOs with already measured redshifts. However, line strengths from the SDSS IV spectra of these

Table 5.1: AAT 2dF+AAOmega eFEDS spectroscopic observations, February-April 2021. † means redshifting done in blue and red spectrograph arms separately. Note that fields eFEDS15, 20, 16, 04, 07, 08 are excluded from the BL RM analysis due to 2dF spectroscopy being either poor or lacking.

Field Name	RA (deg)	Dec (deg)	RA (J2000)	Dec	Date Observed	Exposures (mins)	Seeing (″)	QOP>2 (%)	2SLAQ	DESI used?	eROSITA redshifts?	Comments
eFEDS17	130.0	-1.0	08h 40 00	-01 00 00	18/2/21	5×20	2.1	77.1	N	N	Y	
eFEDS10	131.0	1.0	08h 44 00	+01 00 00	18/2/21	3×25	2.1	84.9	N	N	Y	
eFEDS21	132.0	-1.0	08h 48 00	-01 00 00	18/2/21	3×25	2.1	79.2	N	N	Y	
eFEDS11	133.0	1.0	08h 52 00	+01 00 00	09/3/21	3×25	1.3-1.8	85.6	N	N	Y	
eFEDS18	134.0	-1.0	08h 56 00	-01 00 00	09/3/21	3×25	1.8	83.8	N	N	Y	
eFEDS12	135.0	1.0	09h 00 00	+01 00 00	09/3/21	3×25	1.6	93.7	N	N	Y	
eFEDS22	136.0	-1.0	09h 04 00	-01 00 00	09/3/21	2×25+1×17	1.8	16.5	N	N	YN	cloud
eFEDS13	137.0	1.0	09h 08 00	+01 00 00	15/3/21	3×25	2.8	87.9	Y	N	Y	
eFEDS19	138.0	-1.0	09h 12 00	-01 00 00	13/3/21	2×25	1.8	61.2	Y	N	N	
eFEDS14	139.0	1.0	09h 16 00	+01 00 00	15/3/21	3×25	3.5	57.7	Y	N	Y	
eFEDS23	140.0	-1.0	09h 20 00	-01 00 00	15/3/21	3×25	3.3-4.0	77.2	Y	N	Y	
eFEDS15	141.0	1.0	09h 24 00	+01 00 00	15/3/21	3×25	4.2	29.3	Y	Y	Y	
eFEDS20	142.0	-1.0	09h 28 00	-01 00 00	-	-	-	-	Y	Y	Y	low KIDS
eFEDS16	143.0	1.0	09h 32 00	+01 00 00	-	-	-	-	Y	Y	N	no KIDS
eFEDS09	129.0	1.0	08h 36 00	+01 00 00	16/3/21	1×25+1×20	3.0	-	Y	Y	N	cloud
eFEDS01	129.0	3.0	08h 36 00	+03 00 00	16/3/21	3×25	2.0	77.6	N	Y	N	cloud
eFEDS02	131.0	3.0	08h 44 00	+03 00 00	16/3/21	1×19	3.0	2.8	N	Y	N	
eFEDS03	133.0	3.0	08h 52 00	+03 00 00	07/4/21	3×20	1.5	41.3†	N	Y	N	ave. qual z
eFEDS04	135.0	3.0	09h 00 00	+03 00 00	-	-	-	-	N	Y	N	
eFEDS05	137.0	3.0	09h 08 00	+03 00 00	07/4/21	3×20	2.8	44.9†	N	Y	N	cloud, high qual z
eFEDS06	139.0	3.0	09h 16 00	+03 00 00	07/4/21	4×20+12.5	2.8	30.5†	N	Y	N	cloud, high ZD
eFEDS07	141.0	3.0	09h 24 00	+03 00 00	-	-	-	-	N	Y	N	
eFEDS08	143.0	3.0	09h 32 00	+03 00 00	-	-	-	-	N	Y	N	no KIDS

Table 5.2: AAT 2dF+AAOmega eFEDS spectroscopic observations, Jan-Mar 2022+Jan 2023. Note that fields eFEDS15, 20, 16, 04, 07, 08 are excluded from the BL RM analysis due to 2dF spectroscopy being either poor or lacking.

Field Name	RA (deg)	Dec (deg)	RA (J2000)	Dec	Date Observed	Exposures (mins)	Seeing (″)	QOP>2 (%)	2SLAQ	DESI used?	eROSITA redshifts?	Comments
eFEDS17	130.0	-1.0	08h 40 00	-01 00 00	09/1/22	4×25	2.8	40.6	N	N	Y	cloud, high ZD
eFEDS10	131.0	1.0	08h 44 00	+01 00 00	28/1/22	3×25	2.2	57.5	N	N	Y	
eFEDS21	132.0	-1.0	08h 48 00	-01 00 00	28/1/22	3×25	2.2	36.9	N	N	Y	
eFEDS11	133.0	1.0	08h 52 00	+01 00 00	27/1/22	3×20	2.2	68.4	N	N	Y	cloud×1
eFEDS18	134.0	-1.0	08h 56 00	-01 00 00	28/1/22	2×25+1×13	2.2	80.0	N	N	Y	
eFEDS12	135.0	1.0	09h 00 00	+01 00 00	09/1/22	3×25	3.0	39.4	N	N	Y	cloud
eFEDS22	136.0	-1.0	09h 04 00	-01 00 00	-	-	-	-	N	N	YN	
eFEDS13	137.0	1.0	09h 08 00	+01 00 00	28/1/23	3×25	2.2	59.2	Y	N	Y	
eFEDS19	138.0	-1.0	09h 12 00	-01 00 00	-	-	-	-	Y	N	N	
eFEDS14	139.0	1.0	09h 16 00	+01 00 00	28/1/23	3×25	1.7	29.3	Y	N	Y	fibre positioner problem
eFEDS23	140.0	-1.0	09h 20 00	-01 00 00	28/1/23	3×25	2.1	49.7	Y	N	Y	cloud×1
eFEDS15	141.0	1.0	09h 24 00	+01 00 00	-	-	-	-	Y	Y	Y	
eFEDS20	142.0	-1.0	09h 28 00	-01 00 00	-	-	-	-	Y	Y	Y	low KIDS
eFEDS16	143.0	1.0	09h 32 00	+01 00 00	-	-	-	-	Y	Y	N	no KIDS
eFEDS09	129.0	1.0	08h 36 00	+01 00 00	28/1/23	3×25	2.5	54.8	Y	Y	N	high ZD
eFEDS01	129.0	3.0	08h 36 00	+03 00 00	09/1/22	4×25	1.9-3.0	50.1	N	Y	N	cloud×1
eFEDS02	131.0	3.0	08h 44 00	+03 00 00	31/1/23	2×25+1×8	2.2	45.5	N	Y	N	cloud
eFEDS03	133.0	3.0	08h 52 00	+03 00 00	31/1/23	3×25	2.2	54.7	N	Y	N	
eFEDS04	135.0	3.0	09h 00 00	+03 00 00	-	-	-	-	N	Y	N	
eFEDS05	137.0	3.0	09h 08 00	+03 00 00	31/1/23	3×25	1.5	85.9	N	Y	N	
eFEDS06	139.0	3.0	09h 16 00	+03 00 00	31/1/23	4×25	2.2	77.8	N	Y	N	
eFEDS07	141.0	3.0	09h 24 00	+03 00 00	-	-	-	-	N	Y	N	
eFEDS08	143.0	3.0	09h 32 00	+03 00 00	-	-	-	-	N	Y	N	no KIDS

QSOs have still to be measured and so this early spectroscopic epoch was not used for the Broad-Line - continuum cross-correlation function results described in Section 5.6.

5.4.4 Measuring 2dF and DESI Line Strengths

In order to perform stacked RM, we must first measure the line strengths of our spectra, as the light curves comprised of these line strengths will be cross-correlated with the r-band continuum light curves to determine lags. We adapt the a code created by Hoormann et al. (2019), available at `https://github.com/jhoormann/OzDES_makeLC`, for the OzDES group. This code has multiple functionalities, including calculating emission line fluxes after continuum subtraction, which we use here to measure H_β (4861 Å), MgII (2800 Å) and CIV (1549 Å) broad line strengths for each of our spectra. An example of how the of the line strengths are measured is shown in Fig. 5.6 (a), with a spectral emission line observed at 2 epochs being shown as the blue and black spectra. The green highlighted section is identified by the code as the broad line whose strength we want to make measure, then the continuum there is determined by making a simple linear interpolation between the blue lines in Fig. 5.6 and subtracted. The output of such measurements for two epochs of spectra taken of one object are shown in Fig. 5.6 (b). The code is also able to calculate the width of the defined emission lines, from which we calculate the velocity dispersion but this is left for future work.

5.5 X-ray Data

The original plan was to use the eFEDS initial full depth PV observation and add to these the 8 eROSITA 6 monthly eRASS observations from May 2020 to December 2023. But because of the closure of eROSITA due to "geopolitical problems" at the end of February 2022, only the PV observation in December 2019 and 4 other epochs were obtained, in May 2020, November 2020, May 2021 and November 2021. These X-ray imaging observations were reduced, producing a catalogue of 22079 X-ray AGN (Liu et al., 2022). Note that the eFEDS PV 1st epoch X-ray fluxes and errors used here are those of Liu et al. (2022) multiplied by 1.5 and $\sqrt{1}.5$ respectively to approximately convert from these 0.5-2 keV fluxes to the 0.2-2.3 keV fluxes (and errors) of the other four X-ray epochs from eRASS1234. The factor of 1.5 was estimated by direct comparison of QSOs selected in both the PV and eRASS datasets.

The eFEDS PV X-ray flux limit is $S_X(0.5-2\text{keV}) < 1\times10^{-14}\text{ergs cm}^{-2}\text{ s}^{-1}$ (or $S_X(0.2-2.3\text{keV}) < 1.5\times10^{-14}\text{ergs cm}^{-2}\text{ s}^{-1}$) and the eRASS1234 limit for a single pass is $S_X(0.2-$

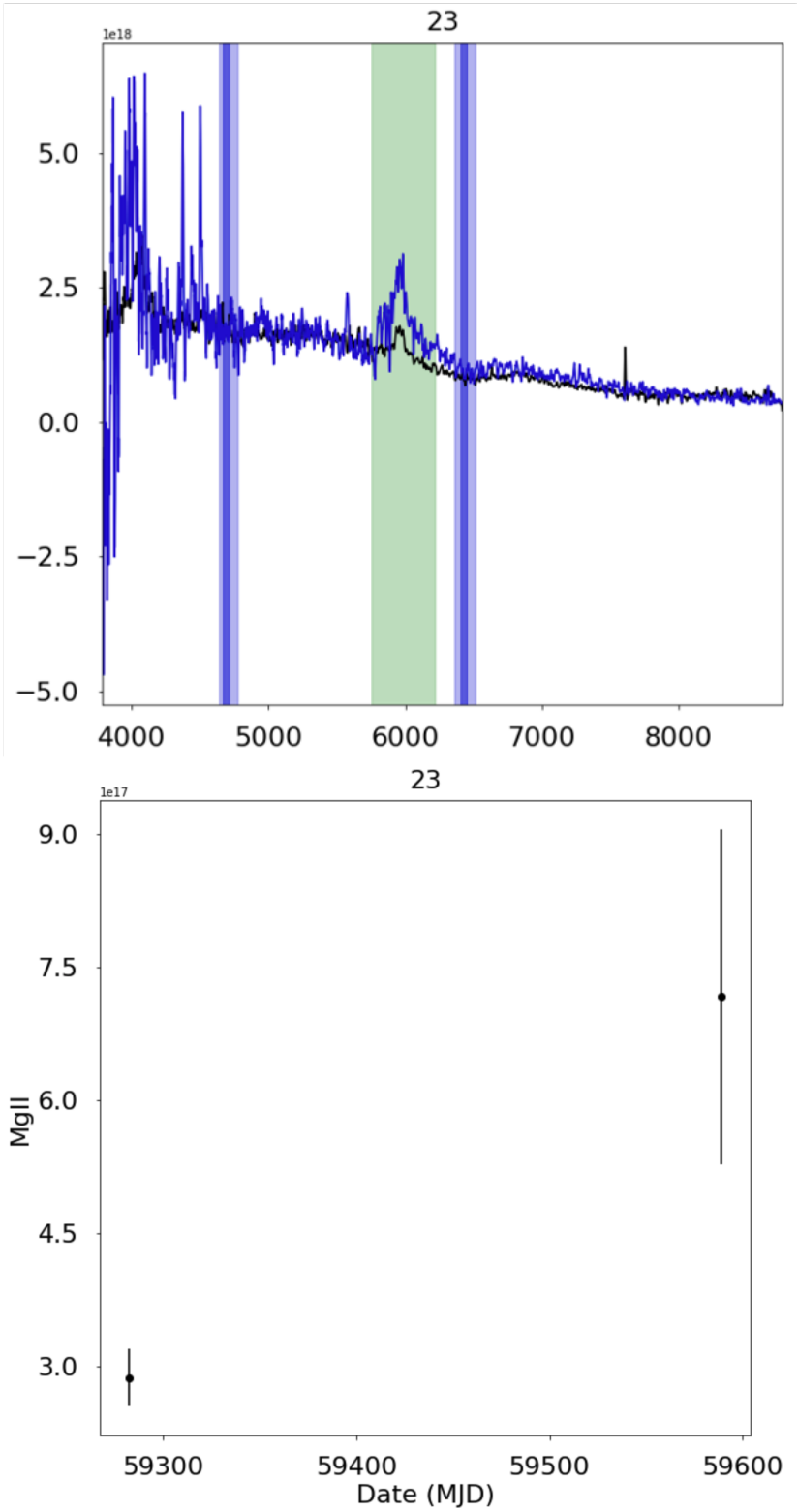

Figure 5.6: Example of the output of the line strength measurements. (a) shows how the emission line strengths are measured and (b) shows the output for 2 spectroscopic observing runs on one object.

2.3keV) $< 4 \times 10^{-14}$ergs cm^{-2} s^{-1}. X-ray sources were selected for 2dF spectroscopic observation to the full eFEDS PV depth while the QSOs included in the RM analysis were limited to the eRASS1234 limit. Of the 22079 X-ray AGN in the eFEDS AGN catalogue, 2993 overlap our $3 \times 23 = 69$ deg^2 survey area. However, many of these are low redshift Sy2 rather than the broad line QSOs/Sy1 we are targetting. When we cut back to our $S_X(0.2 - 2.3\text{keV}) < 4 \times 10^{-14}$ergs cm^{-2} s^{-1} RM limit, 1104 X-ray sources are included. Of these, 593 X-ray QSOs are finally selected to be matched to DECam (and SDSS) images and have 2 or more X-ray epochs with X-ray and optical light curve standard deviations > 0.075mag (see Section 5.7.1).

5.6 Stacked Reverberation Mapping

5.6.1 Reverberation Mapping

First proposed by Blandford & McKee (1982), reverberation mapping provides an indirect method towards determining black hole physics and black hole masses by tracking variations in the continuum flux and broad-line region (BLR). The time lag between flares, or variations, in the accretion disk continuum reaching the BLR is used to estimate the radius of the BLR and then black hole masses via the Virial Theorem. Light curves from Fig. 29 in Peterson (2001) for AGN continuum and Broad Line fluxes are shown in Fig. 5.7, with lines drawn between points to show how variations in the continuum are traced by variations in the BLR. The peak in the cross correlation of the two data sets measures this time lag between variations in the continuum and when the variations are seen in the broad lines. With this time lag, we can determine the radius of the BLR. Note that in this standard RM case only one QSO is considered and the cadence of Broad Line and Continuum observations are the same with both light curves sampled at similar rates. In the stacked RM case described next, for a single QSO, the spectroscopic light curve is sampled at a much lower rate than the continuum.

5.6.2 Stacked reverberation mapping

Introduced by Fine et al. (2012) and confirmed by Fine et al. (2013) and Sommer et al (in prep), we use the process of 'stacked' reverberation mapping which assumes that QSOs for stacking have a constant BLR radius due to their having e.g. a small range in redshift and luminosity. The technique involves stacking the cross-correlation functions of broad

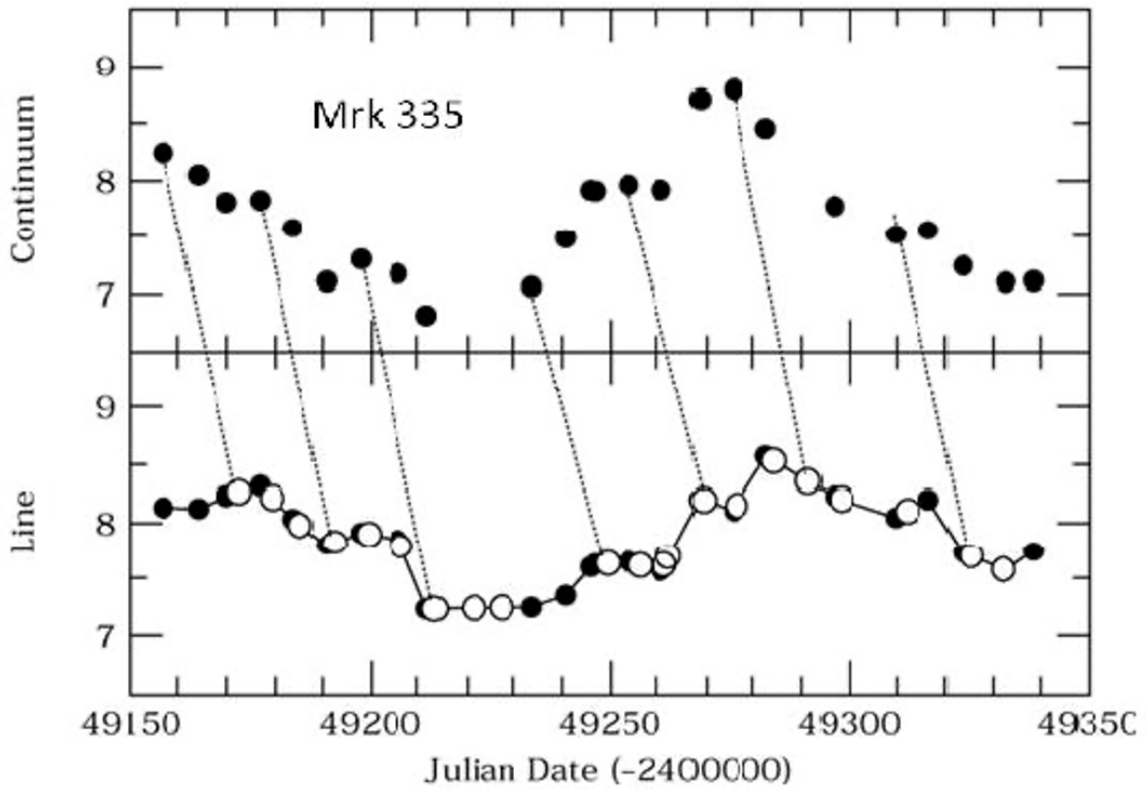

Figure 5.7: Example lightcurve adapted from Figure 29 of Peterson (2001) to show how variations in the continuum are traced by variations in the Broad Line.

line and continuum variations (or X-ray and continuum variations), resulting in a significant improvement in observational efficiency over single object RM if the spectra of many QSOs can be observed simultaneously as with 2dF. This technique may also allow us to probe higher redshifts and a wider range of QSO luminosities. Additionally, as noted by Malik et al. (2023), standard RM applied to higher redshift QSOs typically only give reliable lag measurements for < 10 individual QSOs out of a sample of several hundred. Stacking the cross-correlations will give results at higher efficiency and may increase the S/N of lag detections significantly.

RM was initially restricted to the measurement of the H_β line, providing a significant radius-luminosity relation of $R_{BLR} \propto L^{0.67}$ (e.g. Kaspi et al. 2005). However, subsequent use of MgII and CIV lines to estimate black hole masses for higher redshift QSOs, assume no evolution in their $R_{BLR} - L$ relations (e.g. Vestergaard et al. 2008). Through stacked RM, we hope to be able to probe the higher redshift range necessary to test for evolution in this $R_{BLR} - L$ relationship.

5.6.3 Estimating stacked cross-correlations and cross-covariances

We utilize the method outlined by Fine et al. (2013) to calculate the cross-correlation function, where continuum measurements are denoted by C, emission-line strength measurements are denoted by L, and the pairs of observations for an individual QSO are shown as (C_i, L_j). The correlation coefficient is defined as:

$$r(C,L) = \sum_{i,j} \frac{(C_i - \overline{C})(L_j - \overline{L})}{n_{ij}\sigma_C \sigma_L} \tag{5.6.1}$$

where n_{ij} is the number of C, L pairs in lag bin $(j-i)$ and σ_C and σ_L are the standard deviations of the continuum and emission line light curves for that QSO. The cross-correlations for each QSO are then stacked to create a composite cross-correlation with a higher S/N ratio than would be possible for individual objects at the redshift and luminosity range we are probing. An example of this method for 3 of our objects is shown in Figure 5.8. Here, we see in the left column the continuum light curves for the three individual objects. Then, the middle column illustrates the line strength measurements for two spectroscopic epochs, again for each of the three quasars. Finally, the right hand column shows the individual cross-correlations that will be stacked for our full sample later on.

We find that when σ_C or σ_L are dominated by measurement errors then the cross-correlation is the preferred estimator due to $r(C,L)$ down-weighting the most noisy measurements (see Section 5.6.4). But we also define the cross-covariance as

$$c(C,L) = \sum_{i,j} \frac{(C_i - \overline{C})(L_j - \overline{L})}{n_{ij}} \tag{5.6.2}$$

because in some cases that is found to give smaller field-field errors than the cross-correlation. Here, we shall use the cross-correlation $r(C,L)$ in all cases of BL-continuum analyses whereas we shall use the cross-covariance, $c(C,L)$, for the X-ray-continuum analyses.

In all cases we shall convert BL and X-ray fluxes to magnitudes, consistent with the r-band flux being expressed in magnitudes for the continuum measurements, and use these rather than fluxes in the cross-correlations and cross-covariance estimates. Fine et al. (2013) also discussed estimates of the cross-correlation functions that were either weighted or unweighted by the cross-correlation errors, propagated from the errors on the line strength and the r-band magnitudes. Here, since the error propagation of the cross-correlation functions may be unreliable, we shall use the simplest stacked estimate, unweighted by propagated errors.

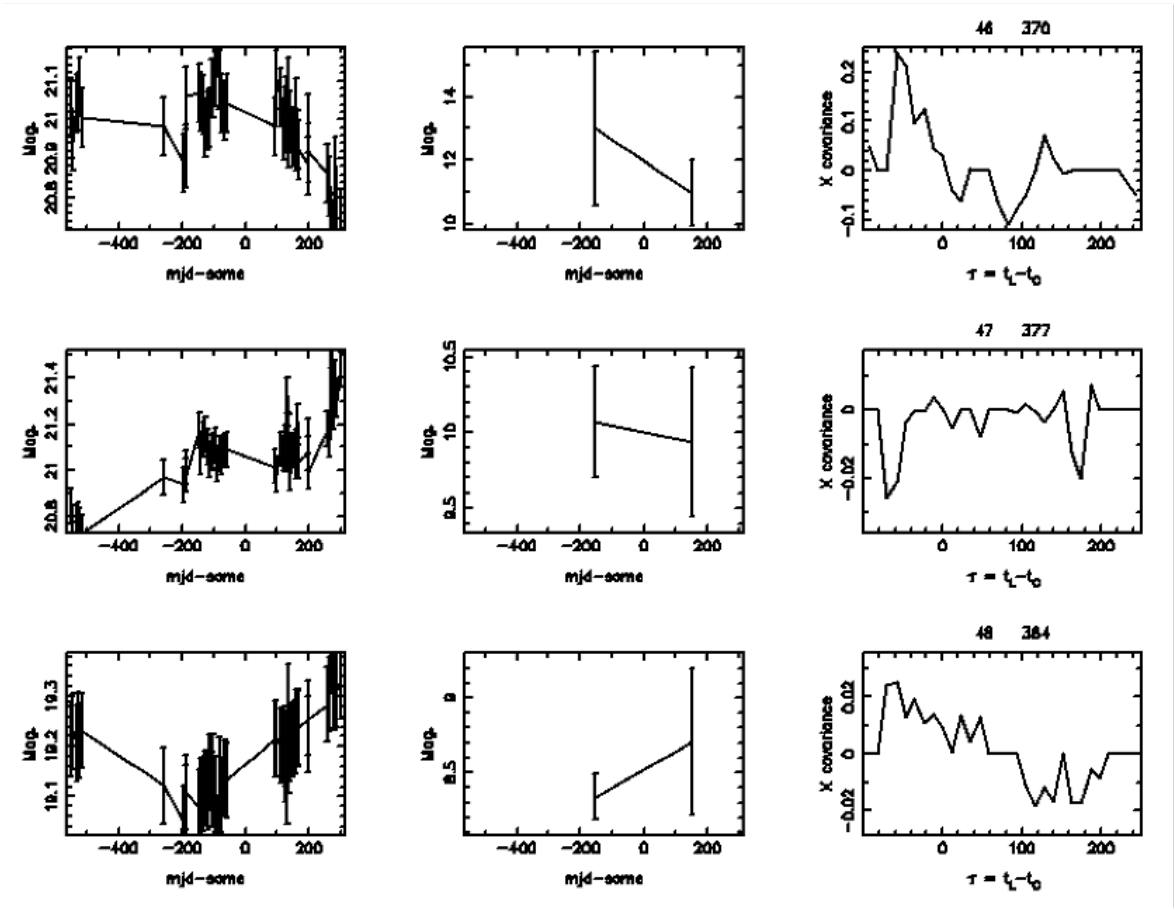

Figure 5.8: Example of the output of the reverberation mapping code. The left-most column of figures show DECam r-band light curves, the middle column shows the Broad Line Light curves, and the right hand column shows the resulting cross-correlations of individual QSOs.

To determine the errors in the final stacked cross-correlation, for simplicity and accuracy we decided to follow Fine et al. (2013) and use field - field errors based on 17 eFEDS fields for our continuum-BL analysis and all 23 fields (see Fig.5.2) for our continuum-X-ray analysis. The 17 field subset for the BL case comprises all the fields with good spectroscopic data as indicated in Tables 5.1 and 5.2 i.e. missing out fields eFEDS 15, 20, 16, 04, 07, 08.

5.6.4 Variability amplitudes and error estimates compared

In Table 5.3 we list the average standard deviations for the r-band continuum ($\overline{\sigma_C}$), BL strengths ($\overline{\sigma_L}$) and X-ray ($\overline{\sigma_X}$) light curves. These are estimated over up to 72 r-band epochs, 3 BL epochs and 5 X-ray epochs. These are given for the full sample used in the L-C and X-C cross-correlation analyses. We see that the BL strength ($\overline{\sigma_L}$) appears significantly larger than the r-band continuum ($\overline{\sigma_C}$) or X-ray ($\overline{\sigma_X}$). However, when we take into account the errors in these bands that are also shown in Table 5.3, we see that the BL errors may dominate the variability of the QSOs. This is particularly true for the first two BL epochs that usually come from 2dF and less true for the higher signal DESI BL strengths. Similarly, the X-ray variability amplitudes for epochs 2-5 even seem larger than the X-ray variability amplitudes with only the first epoch having a variability amplitude that is larger than the quoted error. The lower error of the first X-ray epoch is easily explained by its longer exposure time. However, the only explanation for X-ray epochs 2-5 is that the flux errors may be overestimated. The same explanation may apply to the first 2 BL epochs although at least the errors estimated by the OzDES software are usually only comparable to the variability amplitude and so there is less evidence that errors are overestimated in this case.

5.7 Results

5.7.1 Continuum - Broad Line stacked cross-correlation

Using the H_β, MgII and CIV line strengths described in Section 5.4.4, we cross correlate the optical continuum - BL light curves to measure the lag and hence the radius of the BLR. We first select the best quality data in terms of broad-line strengths by cutting down our eyeball selected QSO BL lists from 2dF (and DESI) still further. We restrict all emission line samples to $S/N > 1$ in the OzDES line strength estimates, having excluded a few lines where the OzDES software had spuriously assigned a line flux error negligibly close to zero. Note that individual lines were excluded here since QSOs that started with lines at 3 epochs would

Table 5.3: The top 3 panels show mean light curve standard deviations averaged over all QSOs in a sample ($\overline{\sigma_C}$, $\overline{\sigma_L}$) and errors for the 3 broad line QSO sub-samples, split into bright and faint by absolute magnitude, M_g, as shown. The bottom panel shows similar data for the X-ray QSO sub-sample. The similarly averaged broad line (L) errors are given for epochs (1), (2) and (3) individually and also for the X-ray epochs from (1)-(5). All sub-samples have the same cuts applied as the data used in Figs. 5.9, 5.10, 5.11 and Fig. 5.12. All units are magnitudes.

BL/X-ray	Bright	Faint	All
H_β	$M_g < -22.5$	$M_g > -22.5$	All
N_{QSO}	52	49	101
σ_C	0.12 ± 0.10	0.12 ± 0.06	0.12 ± 0.08
σ_L	0.22 ± 0.25	0.35 ± 0.40	0.27 ± 0.33
$\mathrm{error}_L(1)$	0.22 ± 0.18	0.31 ± 0.20	0.27 ± 0.20
$\mathrm{error}_L(2)$	0.19 ± 0.22	0.28 ± 0.21	0.26 ± 0.22
$\mathrm{error}_L(3)$	0.25 ± 0.24	0.22 ± 0.21	0.25 ± 0.22
MgII	$M_g < -24.5$	$M_g > -24.5$	All
N_{QSO}	260	335	595
σ_C	0.12 ± 0.10	0.14 ± 0.11	0.13 ± 0.11
σ_L	0.43 ± 0.42	0.37 ± 0.38	0.39 ± 0.40
$\mathrm{error}_L(1)$	0.34 ± 0.24	0.37 ± 0.23	0.36 ± 0.24
$\mathrm{error}_L(2)$	0.37 ± 0.26	0.37 ± 0.24	0.37 ± 0.25
$\mathrm{error}_L(3)$	0.28 ± 0.21	0.45 ± 0.23	0.36 ± 0.23
CIV	$M_g < -25.5$	$M_g > -25.5$	All
N_{QSO}	297	312	609
σ_C	0.11 ± 0.07	0.17 ± 0.11	0.14 ± 0.10
σ_L	0.28 ± 0.23	0.37 ± 0.50	0.34 ± 0.44
$\mathrm{error}_L(1)$	0.27 ± 0.20	0.40 ± 0.22	0.33 ± 0.23
$\mathrm{error}_L(2)$	0.15 ± 0.13	0.29 ± 0.20	0.23 ± 0.20
$\mathrm{error}_L(3)$	0.28 ± 0.26	0.44 ± 0.22	0.31 ± 0.25
X-ray	$M_g < -22.7$	$M_g > -22.7$	All
N_{QSO}	327	266	593
σ_C	0.13 ± 0.08	0.13 ± 0.08	0.13 ± 0.08
σ_X	0.31 ± 0.16	0.33 ± 0.20	0.31 ± 0.18
$\mathrm{error}_X(1)$	0.13 ± 0.04	0.13 ± 0.04	0.13 ± 0.04
$\mathrm{error}_X(2)$	0.48 ± 0.11	0.48 ± 0.12	0.48 ± 0.12
$\mathrm{error}_X(3)$	0.48 ± 0.11	0.47 ± 0.13	0.48 ± 0.12
$\mathrm{error}_X(4)$	0.44 ± 0.13	0.44 ± 0.13	0.44 ± 0.13
$\mathrm{error}_X(5)$	0.41 ± 0.14	0.37 ± 0.14	0.39 ± 0.14

Table 5.4: Measured lags in units of rest frame days. r_{BLR} is the predicted value for H_β from eq. 6 of Kaspi, S. et al (2000), for MgII from eq. 14 of Zhefu Yu et al (2023) MNRAS, 522, 4132 and for CIV from eq. 2 of Kaspi, S. et al (2007, ApJ 659,997) and ApJ, 533, 631. Luminosities (erg s^{-1}) were converted from absolute magnitudes using $L = 10^{-0.4(M_g-71.2)+7}$.

Line/Xray	H_β		MgII			CIV			X-ray	
Abs. Mag.	All	All	M_g<-24.5	M_g>-24.5	All	M_g<-25.5	M_g>-25.5	All	M_g<-22.7	M_g>-22.7
Lag (days)	58±39d	59±28d	60±31d	39±8d	35±25d	167±22d	34±20d	35±12d	35±6d	47±6/170±3d
Stat. Sig.	3.3σ	4.1σ	4.8σ	1.5σ	2.2σ	1.3σ	3.2σ	4.0σ	3.0σ	$2.7\sigma/2.0\sigma$
N_{pairs}	113	345	455	560	719	232	381	1017	590	363/266
$\bar{M}_g$	-22.5±0.9	-24.3±1.0	-25.2±0.6	-23.7± 0.6	-25.5±0.9	-26.2±0.6	-25.0±0.5	-22.9±2.2	-24.3±1.3	-21.4±1.4
$\bar{L}$	3×10^{44}	2×10^{45}	4×10^{45}	9×10^{44}	5×10^{45}	9×10^{45}	3×10^{45}	4×10^{44}	2×10^{45}	1×10^{44}
$\bar{z}$	0.54±0.1	1.24±0.3	1.4±0.3	1.1±0.2	2.14±0.4	2.25±0.4	2.0±0.3	0.81±0.7	1.3±0.7	0.52±0.3
N_{qso}	101	595	260	335	609	297	312	593	327	266
r_{BLR}	71d	154d	202d	113d	42d	59d	33d	-	-	-
Fine (2013)	All	All	M_g<-23.0	M_g>-23.0	All	M_g<-24.0	M_g>-24.0	All	M_g<-21.2	M_g>-21.2
Lag (days)	-	125 ± 50	-	-	70 ± 40	100 ± 50	0 ± 50	-	-	-

still have 2 useable lines if one epoch was excluded. All BL flux strengths and errors are converted to magnitudes. For the continuum r-band, we further excluded any QSO with r-band dispersion less than ± 0.075 mag (i.e. $\sigma_L < 0.075$ mag) which is our average photometric error down to $r \approx 21$. This was done on the grounds that any intrinsic variability would be close to zero and inclusion of this non-varying QSO light curve would only add noise to the cross-correlation result. We also clean the r-band light curve eliminating any epoch where the QSO brightens or dims by more than a magnitude compared to the two epochs on either side. These always result in less than a few percent of the light curve epochs being lost.

We show in Figs. 5.9, 5.10 and 5.11 the stacked reverberation mapping results for the H_β, MgII and CIV QSOs in the 17 eFEDS fields with good spectroscopic data. The stacked cross-correlation functions are shown above a graph showing the number of pairs used to calculate each point of the cross-correlation. The results from the bright half of our broad line samples are then shown in the middle panel and those from the faint half are shown in the bottom panel. The absolute magnitudes that divide bright and faint QSOs are and $M_g = -22.5$ for H_β, $M_g = -24.5$ for MgII and $M_g = -25.5$ for CIV, the M_g threshold is chosen to divide sample into two roughly equal halves while maintaining reasonably round numbers for the M_g thresholds. Full details of the statistical significance of the cross-correlation peaks detected and the result of fitting Gaussians to these peaks to estimate the associated lags and peak widths are given in Table 5.3. The calculate field - field errors for each point, as described in Sec. 5.6.3. We note that there are peaks present in the results where there are a small number of pairs, which is suspicious. We will be looking to check these results with simulations.

The results for the full MgII sample in Fig. 5.10 based on 595 QSOs show a strong peak at 59±28 days detected at 4.1σ (by combining the points in the peak and combining the errors in quadrature). The lower panels show that this peak is detected mainly in the bright half of the sample at 60 ± 31 and 4.8σ and not significantly detected in the faint half of the sample, at 39 ± 8 days and only 1.5σ. For the CIV line, the full QSO sample based on 609 QSOs gives a peak at 35 ± 25 days at a significance of 2.2σ with the hint of another peak at ≈ 160 days but only at the $\approx 1\sigma$ level. The 35 ± 25 peak is absent in the bright half of the QSO sample in the middle panel, although the ≈ 160 day peak may persist at similarly low amplitude and significance as in the full sample. In the faint half of the survey, the peak at 34 ± 5 days appears most significantly at 3.8σ with the low significance ≈ 160 day peak reduced still further in amplitude. Finally, for the $H\beta$ line results in Fig. 5.9, the full sample in the top panel shows a peak at 58 ± 39 days detected at 3.3σ based on only 101 QSOs but no significant detections of any peaks were found in the brighter or fainter halves of this sample

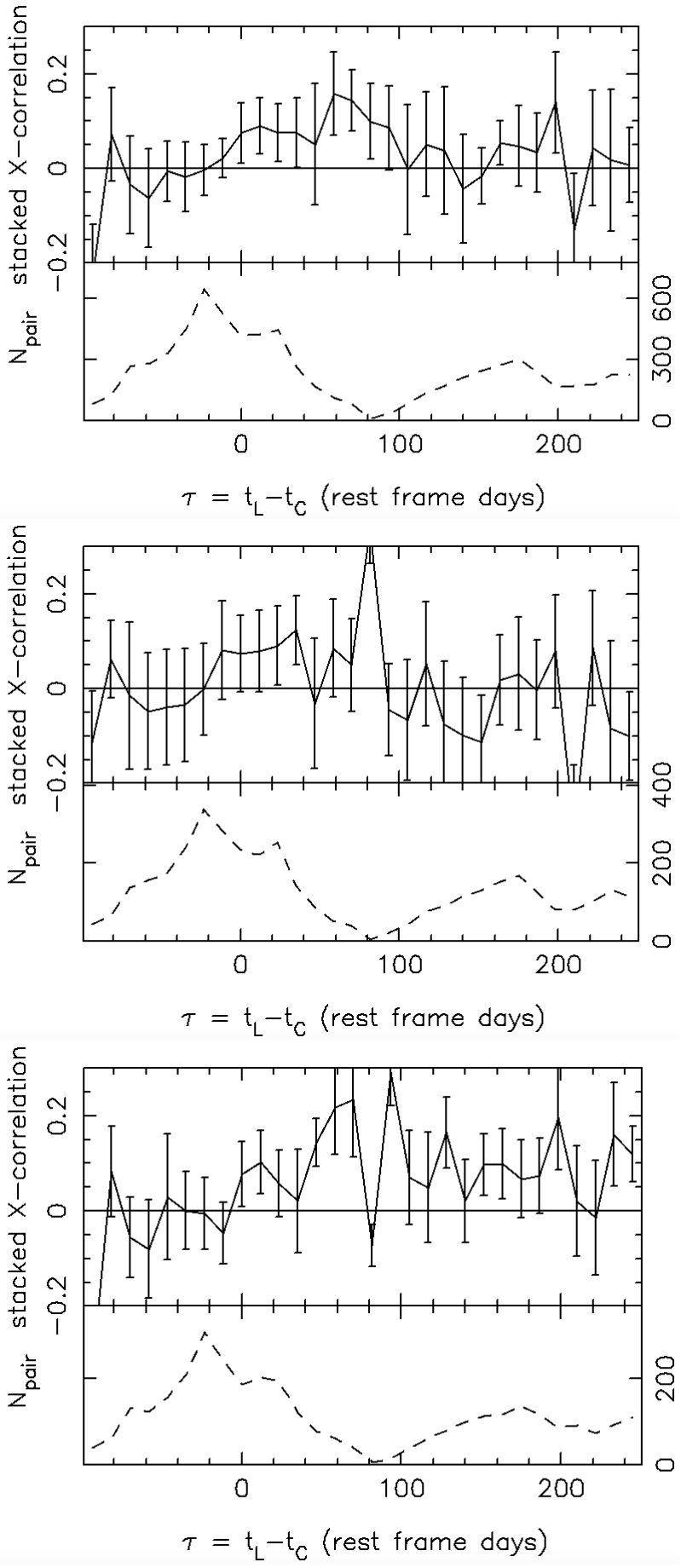

Figure 5.9: The stacked reverberation mapping result for optical to BLR variability, using the H_β broad line strength of QSOs in 17 of our eFEDS fields. Top: Full absolute magnitude range, Middle: Bright QSOs with $M_g < -22.5$, Bottom: Faint QSOs with $M_g > -22.5$.

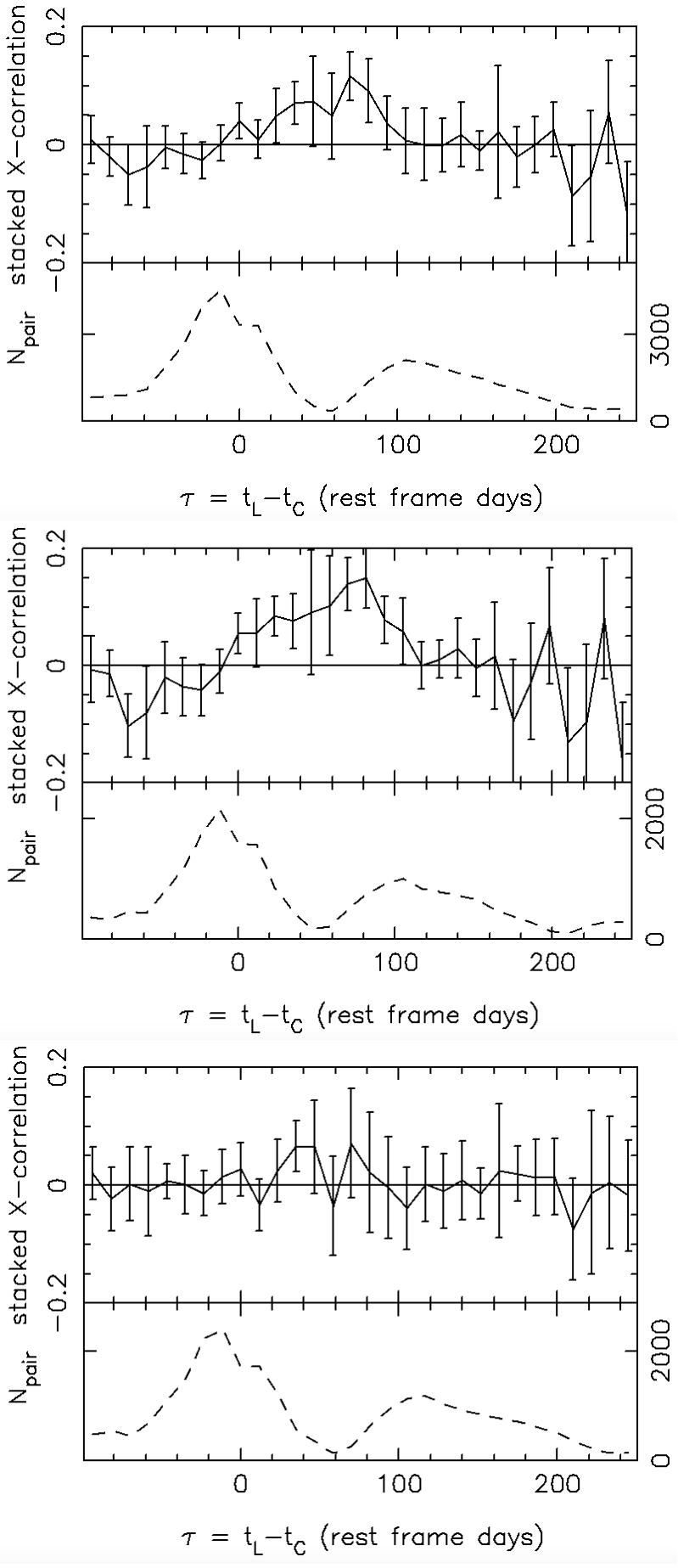

Figure 5.10: The stacked reverberation mapping result for optical to BLR variability, using the MgII broad line strength of QSOs in 17 of our eFEDS fields. Top: Full absolute magnitude range, Middle: Bright QSOs with $M_g < -24.5$, Bottom: Faint QSOs with $M_g > -24.5$.

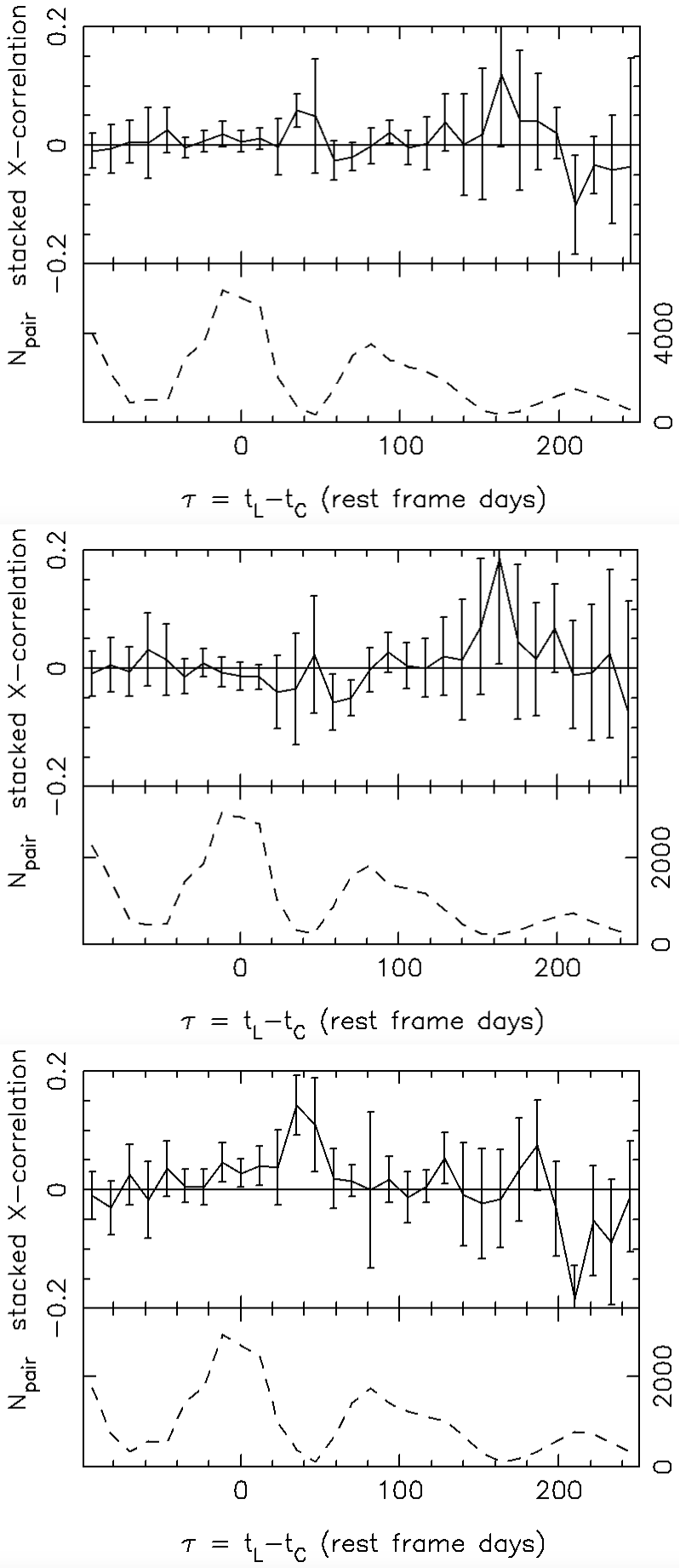

Figure 5.11: The stacked reverberation mapping result for optical to BLR variability, using the CIV broad line strength of QSOs in 17 of our eFEDS fields. Top: Full absolute magnitude range, Middle: Bright QSOs with $M_g < -25.5$, Bottom: Faint QSOs with $M_g > -25.5$.

in the middle and lower panels.

We can compare these results to those found for MgII and CIV by Fine et al. (2013), shown in their Figs. 2 and 5. For their 75 QSOs, Fine et al. (2013) find peaks in their cross-correlations at a lag of 125 ± 50 days for MgII compared to 59±28 days here and 70 ± 40 days for the CIV lag compared to 35 ± 25 days here. Given the wide peak widths of the Fine et al. (2013) lags it could be argued that the results are reasonably compatible with only a 66 ± 57 days difference for MgII and 35 ± 47 days for CIV. Even folding in a factor of 2 decrease in our lags due to our $\approx$ 1.5mag fainter average absolute magnitude (see Table 5.3) assuming a canonical R-L relation still only leads to a 95 ± 57 difference for MgII and a 52 ± 47 difference for CIV. Recalling that the QSO samples of Fine et al. (2013) are an order of magnitude smaller than those available here, we regard discrepancies at these levels as not being unexpected.

5.7.2 Continuum - X-ray stacked cross-covariance

We next cross-correlate light curves comprising up to 5 X-ray epochs of eROSITA X-ray imaging and optical light curves with 50 epochs of DECam r-band imaging between February 2020 - June 2022. This subset of 50 r-band epochs adequately covers the period when eROSITA observations were available between December 2019 - November 2021. The first X-ray epoch was done in the eFEDS field as the PV observation and therefore has an $\approx 10\times$ longer exposure than the 4 later X-ray exposures that were done as part of the eRASS all-sky survey. We limit the X-ray data at $S_X(0.2-2.3\mathrm{keV}) < 4.0 \times 10^{-14}$ ergs cm $^{-2}$ s^{-1} which is the limit of eRASS1234 X-ray epochs 2-5. This X-ray limit cuts the QSO sample from 2993 to 1104. The $\sigma_C < 0.075$ mag and $\sigma_X < 0.075$ mag combined cut plus the requirement that QSOs only detected at one X-ray epoch (i.e. the first epoch) can be included then cuts the sample from 1104 to 593 QSOs. These QSOs have a reasonably flat distribution of numbers of X-ray epochs between 2-5.

The cross-covariance results are shown in Fig. 5.12. Note that lags above zero days imply that the optical r continuum variation precedes the X-ray variation. In the full QSO sample in the top panel, a clear peak is seen at lag 35 ± 12 days at significance 4.0σ, the highest significance for a single peak in any of our analyses. The same peak is seen at 35 ± 6 days at 3.0σ in the bright subset of these quasars (middle panel) and at 47 ± 6 days in the cross-correlation result for the fainter QSOs shown in the bottom panel, although here the significance of the peak reduces to 2.7σ. We note that this 35 ± 12 day lag is similar to the 35 ± 24 day lag shown in the CIV cross-correlation, particularly in the fainter CIV QSO subset. We also

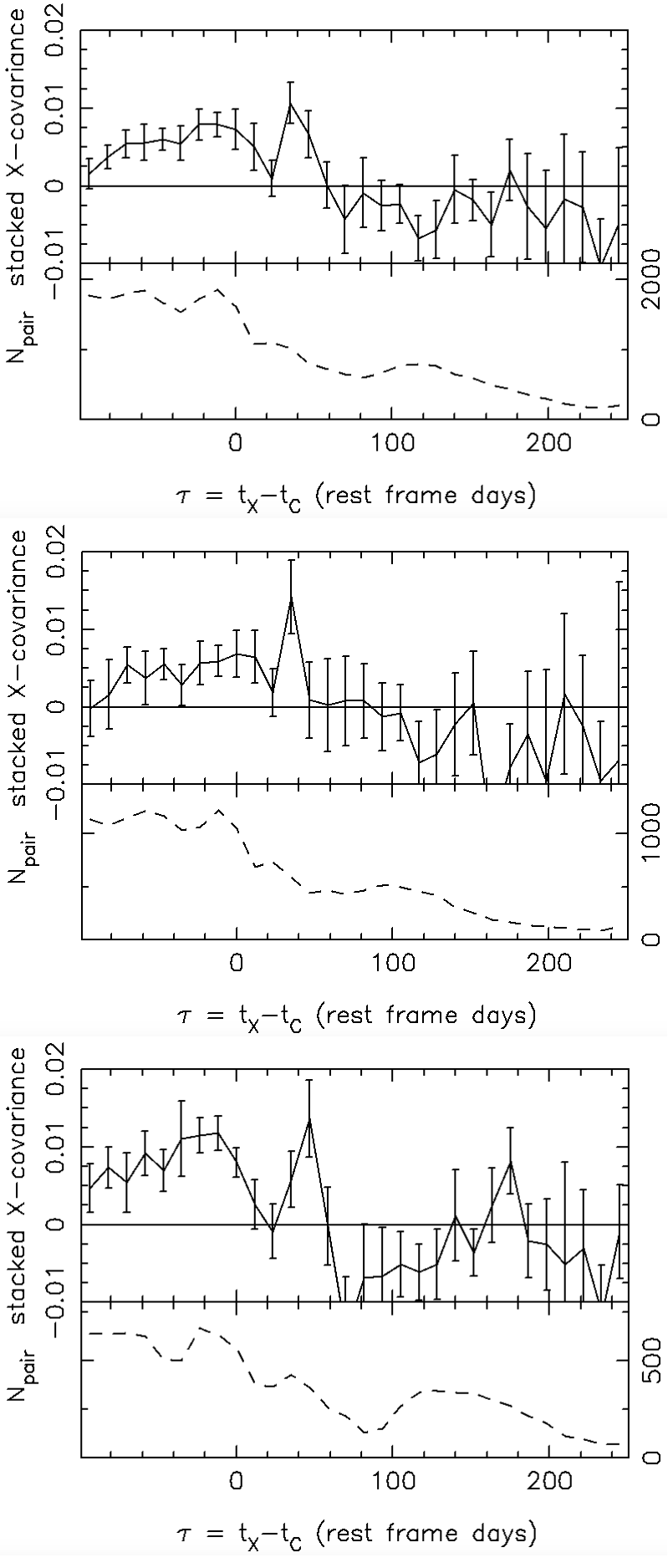

Figure 5.12: The stacked reverberation mapping result for optical to X-ray variability, using the eROSITA X-ray flux of QSOs in the 23 eFEDS fields. At positive lags, the continuum leads the X-rays and at negative lags X-rays lead the continuum. Top: Full absolute magnitude range, Middle: Bright QSOs with $M_a < -22.7$, Bottom: Faint QSOs with $M_a > -22.7$.

detect a further lower significance (2.0σ) X-ray-continuum peak at in this fainter QSO subset at 170 ± 3 days, again similar to the weaker 167 ± 20 day peak seen in the CIV data, although in CIV this peak was seen in the brighter QSO subset.

Finally, we also note the very strong, broad feature that extends from lag -100 to 0 days in all 3 panels of Fig. 5.12. Here the significance of individual points in this range reaches $> 4.0\sigma$ in the full and fainter QSO samples while reaching $> 3\sigma$ in the brighter QSO sample in the middle panel. Since this feature occurs at negative lags, this implies that the X-ray variation now precedes the r-continuum variation. We also note that the tendency for Broad Line-continuum peaks to occur near minima in the n_{pair} distribution, this broad X-ray-continuum feature appears near the maximum in n_{pair}. Indeed all the features in the X-ray-continuum cross-covariance benefit from much stronger statistical coverage by our observations than in the Broad Line-continuum case.

The Broad Line-continuum cross-correlation peaks are still at a level that need confirmation. The problems are that, although the MgII results do reproduce in the bright and faint samples, the CIV results do not, appearing only to arise in the fainter sub-sample. Also, the CIV and MgII Broad Line-continuum peaks are only in approximate agreement with the results of Fine et al. (2013). In the case of the X-ray data the strong, 4σ, peak at 35 days and the broader feature at lag =-100 and 0 days are reproducible in all 3 panels of Fig. 5.12. Indeed, further subdividing into 4 absolute magnitude bins rather than two then the 35 day and broad peak at negative lags reasonably reproduce in these bins as well. So although more data are certainly needed for the Broad Line-continuum peaks and for the weaker X-ray-continuum peak at 170 ± 3 days we can be reasonably confident about the reproducibility of these two X-ray-continuum features at $-100 <$lag< 40 days.

5.7.3 Cross-correlation results summary

Summarising the stacked cross-correlation results shown in Figs. 5.9, 5.10, 5.11, 5.12 and tabulated in Table 5.3:

1. The H_β line comes mainly from a BLR region 58 ± 39 light days from accretion disk and this result is in reasonable agreement with the 71 day lag predicted for our QSOs' $\approx 3 \times 10^{44}$ erg s^{-1} luminosity from previous observations at lower redshift (e.g. Kaspi et al. 2000). We do not regard the peaks in the faint and bright H_β sub-samples to be

reliably detected due to low N_{pairs} and so only the details for the full sample are given in Table 5.3.

2. The MgII line comes mainly from 59 ± 28 light days from the accretion disk, reasonably independent of QSO luminosity. This is similar to the result for H_β, although any interpretation will have to take into account that the MgII result is based on QSOs of luminosity 4×10^{45} erg s^{-1}, some 10× larger than the H_β sample. Assuming $R \propto L^{0.5}$ the MgII result would be 30 ± 28 light days at the luminosity of the H_β QSO sample.

3. The CIV line comes mainly from 35 ± 25 light days from the accretion disk and this line arises mostly from the fainter half of our QSO sample. A weaker cross-correlation peak is seen at lag 167 ± 22 days and this is only evident in the brighter half of the CIV QSO sample. Again it has to be taken into account that the CIV QSO sample has an average luminosity of 1×10^{46} erg s^{-1}, $\approx 2\times$ higher than the MgII sample and $\approx 20\times$ larger than the H_β sample.

4. Fig. 5.12 shows that X-rays come mainly from 35 ± 12 light days from the accretion disk, reasonably independent of luminosity within the 1×10^{44} erg s^{-1} - 2×10^{45} erg s^{-1} range. similar to CIV. The higher luminosity here at 2×10^{45} erg s^{-1} is comparable to the lower half of the CIV QSO range at 1×10^{45} erg s^{-1}. The question then arises as to the source of the X-rays from the 35 day lag peak and how can X-rays at $\approx 10^8$K at least *appear* to occupy the same volume as the lower temperature $\approx 10^4$K gas from which the CIV line originates. Below we present two Models A, B to address these issues.

5.7.4 Model A

We first suggest that the X-ray-continuum cross-correlation results in Fig. 5.12 support the following model suggested by B. Czerny (priv. comm.). Netzer (2022) has speculated that the longer than expected relative lags seen in optical *ugriz* inter-band RM (IBRM) results (Cackett et al., 2023; Edelson et al., 2019; Neustadt et al., 2024) suggests that the *ugriz* QSO continuum flux may be dominated by the BLR rather than the accretion disk. We now argue that this seems to be in line with our continuum-X-ray cross-correlation results where signal

is detected over far longer timescales than the few days expected for an accretion disc of size 2-3 light-days.

In model A, X-ray flares are only observed from the accretion disk. So the accretion disk first brightens and X-ray and optical light pulses head towards the observer (lag 0 days), while orthogonal to the line-of-sight, the optical beam ionises BLR CIV gas at 35 light days distance. This X-ray+r-band flare from the accretion disk can cause both this increase in CIV line luminosity from r-band after 35 days and X-ray heating of the BLR gas, peaking after ≈ 55 days. This causes an r-band flare from the BLR to arrive 35 days later at the accretion disk, causing another X-ray + r-band flare to be emitted. It is this latter X-ray flare in the accretion disk that corresponds to the +35 day peak in the continuum-X-ray cross-correlation. Thus model A naturally explains the continuum-X-ray and continuum-CIV having the same +35 day lag.

This model can also explain the 160 day peak seen in the fainter QSOs in the continuum-X-ray cross-correlation. An r-band flare starting in the BLR takes 35 days to reach the accretion disk and the resulting X-ray flare in the accretion disk takes 35 days to reach the BLR. After 55 days the r-band flare leaves the BLR arriving at the accretion disk after 35 days. So a continuum-X-ray peak is expected at lag=35+35+55+35=160 days as is possibly observed. This peak is only seen for fainter QSOs because in brighter QSOs, this secondary X-ray flare will only be a smaller fraction of the total X-ray flux.

The model can also explain why the 35 day continuum-CIV peak is mainly seen in fainter QSOs and the 160 day CIV peak is mainly seen in the brighter QSOs. The hypothesis would be that in bright QSOs, the accompanying X-ray heating of the BLR may be strong and fast enough to reduce the increase in CIV line strength caused by the continuum flare, resulting in only fainter QSOs showing the CIV peak on the first pass after 35 days. And conversely only the brightest QSOs would have a continuum flare, starting from the accretion disk, strong enough to cause an increase in CIV emission after 35+55+35+35=160 days.

Finally, model A may also produce some X-rays in the BLR which could be reflected from the disk, indicating the source of the X-ray 'soft excess' often seen in AGN (Czerny et al., 2003; Gierliński & Done, 2004; Ross & Fabian, 2005).

Thus, this model constitutes a continuous self-fuelling model for accretion disk and BLR flares. We further note that the ubiquity of the 35 day peak implies a small BH mass range for the QSOs we are observing despite their quite wide luminosity range. Indeed, this question may be prompted already by the apparent success of our stacked reverberation

mapping technique since we are averaging over wide QSO luminosity ranges in both X-ray and optical and if the accretion disk and BLR structures varied widely, we would not see the strength of cross-correlation signals we have seen because such features would be quickly smoothed away in this situation. This appears to confirm the conclusion of Shanks et al. (2011) and the results of Ch. 4.

5.7.5 Alternative Model B

C. Done and S. Scaringi (priv. comm.) have suggested an alternative model to explain these data. In this case, an r-band light pulse propagates from the outer to the inner accretion disk taking ≈ 35 days at a speed lower than the speed of light in vacuo as determined by the disk viscosity. This continuum pulse then perturbs the innermost accretion disk which causes an X-ray flare 35 days after the r-band flare, explaining the peak at +35 days in the continuum-X-ray cross-covariance. The X-ray flare is reprocessed in the disk to the optical as it moves outwards so that after ≈ 90 days, corresponding to $-100 < lag < -10$ day part of the cross-covariance, another optical pulse is seen. This repeating r-band flare then also ionises the CIV region of the BLR which coincidentally lies at 35 light days from the accretion disk.

The first issue with this model is that the r-band pulse being confined to the accretion disk cannot explain the CIV lag of 35 days being similar to the X-ray lag. Indeed, in this case we have to accept that the basic principle of RM as a route to the BLR radius and hence the central BH mass is compromised and at best only an upper limit to the BLR radius and BH mass can be achieved. There is also no connection with observations of reflection in X-ray spectra as there was in the above model. There is also the problem that X-ray variability usually occurs on 2-3 day (rest-frame) timescales and indeed this forms the basic argument for QSOs being powered by Black Holes. Therefore, in this model where optical and X-ray flares are only created in the accretion disk, it is unclear why the cross-correlation timescale between X-ray and optical is some $10\times$ longer than the accretion disk X-ray variability timescale.

For these reasons, we therefore prefer model A with its incorporation of a significant BLR contribution to the optical continuum of QSOs and no appeal to any disk reprocessing.

5.8 Conclusions

We have developed a dataset of QSOs in the eROSITA eFEDS field suitable for stacked reverberation mapping, with the twin aims of measuring the BLR radius-luminosity relation and QSO black hole masses (although the latter aim is now left for later work). This dataset is comprised of KiDS+DECaLS DR9 candidates along with eROSITA, DESI, eBOSS and 2SLAQ spectroscopically confirmed QSOs. Based on these QSOs, we performed a dedicated continuum and spectroscopic observing campaign over 4 years, creating highly sampled continuum light curves and more sparsely sampled emission line light curves (2-3 epochs). Although the initial aim was to measure BLR radii (and BH masses) in luminosity and redshift subsets, we found that our best results came from stacking the cross-correlation functions over all the QSOs where a particular emission line is visible and well measured. Anyway, the ranges for individual emission lines are relatively narrow, e.g. $z < 0.75$ for H_β, $0.7 < z < 1.7$ for MgII and $1.4 < z < 2.2$ for CIV. For the X-ray sample the redshift range is $.5 < z < 1.5$, similar to CIV but the range of luminosities is larger, a factor of ≈ 100.

Generally speaking, the errors on the BL cross-correlations are larger than for the X-ray because 5 X-ray epochs are available as opposed to only 2-3 epochs for the BLs. We find lags of 58 ± 39 days for H_β, 59 ± 28 days for MgII and 35 ± 25 days for CIV. For MgII the lag is seen in both bright and faint QSO subsamples whereas in CIV the peak is only seen in the fainter sub-sample. A much lower significance peak may also be seen at a lag of $\approx 167 \pm 29$ days in the bright QSO CIV sample. The H_β and CIV results are in good agreement with other authors. The MgII lag of 59 ± 28 days is lower than for other authors, including Fine et al. (2013) at lag $\approx 125 \pm 50$ days and Malik et al. (2023) at ≈ 100 days at our average luminosity of 4×10^{45} erg s^{-1}. The reason for this discrepancy is not known.

The X-ray-r-band continuum cross-correlations are detected at higher significance than the Broad Line-r-band continuum cross-correlations and are reproducible in 4 luminosity bin subsets. They show a narrow 35-day peak in the range of lags where continuum varies in advance of the X-rays and a much broader feature in the $-100 < lag < -10$ day range where X-rays vary in advance of the r-band continuum. Combining the BL and X-ray cross-correlations with the optical continuum seems to offer important clues to make a coherent picture of the core of an AGN including the structure of the accretion disk and the BLR.

Two models are therefore presented that may be suggested by these data. Model A builds on the work of Netzer (2022) who suggested that the longer than expected relative lags found in *ugriz* inter-band RM studies implies that the QSO continuum has a significant contribution

from BLR gas clouds as well as the accretion disk. So in model A, X-ray and optical flares are generated in the accretion disk and while the r-band flare increases the CIV emission line strength in the BLR at 35 light days distance, the X-ray flare heats the BLR gas, producing another optical flare that on arrival at the accretion disk produces further optical and X-ray flares. This model explains why the same 35 day lag is found in the continuum-CIV and continuum-X-ray cross-correlation functions. It also predicts the further 160 day peaks that may also be seen in the CIV and X-ray data and that the BLR may be the source of the reflection component of soft X-ray spectra. Model B suggests that all the activity takes place in the accretion disk starting with an optical flare at large radii propagating at speeds $v < c$ which on arrival at the disk centre, perturbs the X-ray corona, causing an X-ray pulse to propagate out to re-start the cycle by prompting a new optical flare. Thus both models generate a repeating cycle of activity in the quasar core. But for model B, the agreement of the 35 day peaks in the continuum-CIV and continuum-X-ray cross-correlations simply represents a coincidence and for that and other reasons such as the prediction of the admittedly weak 160 day peak in both CIV and X-ray cases and the prediction of the disk reflection component seen in AGN X-ray spectra, we prefer model A.

Finally, the reproducibility of peaks in both the BL and X-ray cross-correlations and the fact that they are not smeared out is a strong argument that over the luminosity and redshift ranges covered here, that the QSO BH mass and accretion disk structure may be broadly independent of these parameters. This tends to confirm the similar results found from QSO clustering (Shanks et al., 2011) and QSO-CMB lensing (Ch. 4). We leave the derivation of average line widths for our H_β, MgII and CIV QSO samples for future work. At that point we shall be able to estimate average BH masses for our BL sub-samples and further test the hypothesis that, in these samples at least, the QSO BH mass function is narrow and highly peaked.

Chapter 6

Summary and Future Work

The discovery of QSOs by Schmidt (1963, 1965) has led to the development of a large body of work dedicated to the understanding of the physical properties of QSOs as well as their use as tools to investigate the cosmological model. This thesis aims to contribute to this growing body of work in five main ways.

1. We exploit the multi-wavelength properties of QSOs to establish the VST ATLAS QSO catalogue. The catalogue covers $\sim 4700\text{deg}^2$ of the Southern sky and is based on VST ATLAS photometry in the *ugriz* bands as well as the unWISE neo6 $W1$ and $W2$ bands.
2. We utilize a restricted version this catalogue along with VST ATLAS galaxy clusters, galaxies, and LRGs to test whether the galaxy-QSO lensing signals we see in cross-correlations of these catalogues are caused by a higher Ω_m or whether a HOD model framework in the standard model can fit the results, after which we rule out the higher Ω_m model. We then show that the QSO autocorrelation function as well as QSO-CMB lensing cross-correlations can be fit by the same HOD models we use to fit these galaxy-QSO cross-correlations.
3. We infer the QSO halo mass function (and therefore the QSO BHMF) by multiplying the aforementioned HOD and with the ΛCDM halo mass function to find the QSO space density as a function of mass. This shows a narrow QSO BHMF with $\sim 2/3$ of QSOs halo masses lying within a small range of $12.2 < \log M < 13.15$ at an average redshift of $z = 1.7$ via the QSO acf and QSO-CMB lensing cross-correlations.
4. We test the QSO BHMF via optical to BLR and X-ray to optical stacked reverberation mapping. Stacked reverberation only works with the assumption that the QSOs have similar characteristics. Therefore, a peak in the stacked reverberation mapping results provides evidence to support a narrow QSO BHMF.

5. We also determine the radius of the BLR via optical to BLR stacked reverberation mapping. Though initially performed to determine the size of the accretion disk, the X-ray to optical stacked reverberation mapping resulted in longer than expected lags, leading to a discussion about various potential models for the inner region of QSOs.

Here, I summarize the main results and conclusions from each of these aims and discuss ongoing work as well as possible avenues for future work.

6.1 Results

6.1.1 The VST ATLAS QSO Catalogue

We presented the VST-ATLAS QSO catalogue in Chapter 2. Following the initial photometric QSO selection work of Chehade et al. (2016), we adjusted their selections to account for our greater sky coverage, depth, completeness in the u-band, and updated mid-IR data. We applied our selections to VST ATLAS $ugri$ + unWISE neo6 $W1$ and $W2$ data, resulting in the VST ATLAS QSO catalogue containing ~ 1.2 million QSO candidates with a sky density of $\sim$259 deg^{-2}. We use all available spectroscopically confirmed QSOs within the survey area as well as new, specially commissioned, 2dF observations of ATLAS QSO candidates to test our photometric selections. The results of our 2dF observations suggest that the ATLAS catalogue will reach a minimum QSO sky density of > 110 deg^{-2} at $z < 2.2$ and > 30 deg^{-2} at $z > 2.2$. Through the comparisons with 2QZ, 2QDESp, and eBOSS, we see a completeness of $\approx 88\%$, with the brightest, stellar, ATLAS selections giving $\approx 97\%$ completeness. We found a completeness of 70% with respect to confirmed DESI QSOs for our total candidate sample, with an efficiency of 48%.

Applying the ANNz2 algorithm of Sadeh et al. (2016) to our final QSO candidate catalogue provided photometric redshift estimates for all catalogue members. The resulting QSO candidate sky density over our full $\approx$4740 deg^2 is 194 deg^{-2} for the $z < 2.2$ 'tracer' QSO candidate catalogue and 66 deg^{-2} for the $z > 2.2$ LyA QSO candidate catalogue.

6.1.2 HOD vs. high Ω_m explanations for galaxy-QSO lensing results

We use the cross-correlation of galaxy clusters, galaxies, and LRGs with a conservative version of our VST ATLAS QSO catalogue to determine various model fits. We show that our galaxy

cluster-QSO and galaxy-QSO cross-correlation results are in good agreement with previous authors and that HOD models improve standard ΛCDM cosmology fits, in particular in the $17 < r < 21$ galaxy case compared to models where galaxies trace the mass. In the case of clusters, NFW mass profiles are preferred over SIS profiles, with NFW mass estimates compatible with previous results for both clusters and groups. CMB lensing results for clusters tended to be under-predicted by standard 2-halo models and this was also seen marginally in the CMB lensing of the $17 < r < 21$ galaxies. LRGs show the biggest discrepancies with a standard HOD model, where they under-predict w_{gq} by a factor of $\approx 2\times$ in the fainter QSO samples, while over-predicting the LRG-CMB lensing result by a smaller factor. Further investigation is required to see if improved HOD models can be found to address these anomalies at large and small scales in the galaxy, group and particularly LRG samples.

6.1.3 QSO HODs via QSO clustering and CMB lensing

The QSO 2-point angular correlation function was well modelled in 3-D by a correlation function with a power law form, $\xi(r) = (r/r_0)^{\gamma}$ with $r_0 = 5.2\mathrm{h}^{-1}$ Mpc and $\gamma = -1.75$. Then assuming a linear regime mass power spectrum in a ΛCDM model, we compared galaxy and mass auto-correlation functions within a $20\mathrm{h}^{-1}$ Mpc radius sphere (i.e. ξ_{20}) to find $b_Q = 2.09 \pm 0.09$ implying a QSO halo mass of $M_{halo} = 8.5 \pm 0.3 \times 10^{11} M_{\odot}$.

We then cross-correlated a restricted sample of our VST-ATLAS QSO catalogue with the CMB lensing maps of Planck Collaboration et al. (2018). We first used methods similar to those outlined by Geach et al. (2019) to measure the bias and halo mass via the lensing of the CMB by foreground quasars, where we were able to measure a QSO halo bias of $b_h = 2.08 \pm 0.24$ at an average redshift of $z = 1.7$, corresponding to a halo mass of $0.83 \times 10^{12} h^{-1} \mathrm{M}_{\odot}$. Our bias value is in excellent agreement with the quasar bias from quasar clustering in Chehade et al. (2016) as well as the QSO-CMB cross-correlation study of Petter et al. (2022). We then combined these two methods and fitted a HOD model to w_{qq} which could be tested for consistency using QSO-CMB lensing. This showns an average QSO halo mass at $z = 1.7$ of $\log M_{eff} = 12.4$. This HOD model from our w_{qq} was also found to be a good fit to our CMB lensing results, confirming consistency between these two independent observations.

6.1.4 QSO Halo Mass Function and BHMF

We determined the QSO halo mass function by multiplying the ΛCDM halo mass function with the QSO HOD. From the QSO mass function we find an average QSO halo mass at $z = 1.7$ of $\log M_{eff} = 12.4$, and that 67% of the $z = 1.7$ QSOs had halo masses that lie in the small halo mass range $12.2 < \log M < 13.15$. This narrow QSO halo mass function suggests that most QSOs have similar halo and hence black hole masses. A similar result can be found by combining the galaxy stellar mass function of Ilbert et al. (2013) and the probability of a galaxy hosting an X-ray AGN as a function of stellar mass as estimated by Aird et al. (2012). Here, 67% of $z = 1.7$ AGN are found to lie in the stellar mass range $10.0 < \log M_*(M_\odot) < 11.5$. Comparing the QSO halo mass functions at $z = 0.25$ and $z = 1.7$ showed that they appear to evolve to higher masses as redshift decreases as would be expected from gravitational growth.

We confirmed this narrow QSO black hole mass range via stacked reverberation mapping. Using the selection methods developed for the VST ATLAS QSO catalogue, we develop a dataset of QSOs in the eROSITA eFEDS field suitable for stacked reverberation mapping in order to measure black hole masses and investigate the radius-luminosity relation. This dataset is comprised of KiDS+DECaLS DR9 candidates along with eROSITA, DESI, eBOSS, and 2SLAQ QSOs. We then performed a dedicated continuum and spectroscopic observing campaign over 4 years in order to create continuum light curves and measure multiple epochs of spectroscopic line strengths. The technique of stacked reverberation mapping assumes that QSOs have similar masses and BLR radii. Therefore, the stacking of cross-correlations is able to amplify the lag signal. Our QSO sample spans a wide ($\sim 0 < z < 4$) redshift and luminosity range. The lags we recovered for H_β, MgII, CIV, and the X-ray thus provided significant evidence to support a narrow black hole mass and halo mass range for QSOs.

6.1.5 Inner Region of QSOs via Stacked Reverberation Mapping

We determined the radii of QSO Broad Line Region using the stacked reverberation mapping technique to the broad H_β, MgII and CIV emission lines in a large QSO sample. We find average lags of 58 ± 39 days for H_β, 59 ± 28 days for MgII and 35 ± 25 days for CIV. The results for H_β and CIV are in good agreement with other authors while the MgII lag is somewhat lower in these data than previous estimates. With 5 epochs of eROSITA X-ray observations also available, we further applied the stacked reverberation mapping technique

to X-ray-optical continuum time lags with the initial aim of measuring the size of the QSO accretion disk. A peak at an X-ray - continuum lag of 35 ± 12 days was detected in this cross-covariance at 3-4σ significance and a smoother more continuous feature was seen at negative lags between -100 and -10 days at similarly high significance. These lags are unexpectedly high given that X-ray variability is generally on a shorter, few day, timescale. Indeed, the lag of the sharp X-ray peak being close to the CIV lag seems to suggest that X-rays may be associated as much with BLR scales as those of an $\approx 10\times$ smaller accretion disk. This indication that QSO continuum light may have a significant contribution from BLR light has been independently suggested by Netzer (2022) because of the $5\times$ longer than expected *ugriz* lags found in AGN inter-band observations. An alternative model is considered where our long continuum-X-ray lags might be caused by UV + X-ray light being reprocessed on the small accretion disk scale but we argue that this model explains our observations less well than the more BLR dominant model. We note that the detection of significant peaks in stacked RM analyses is itself interesting since it suggests that similar BLR + accretion disk radii and potentially, M_{BH}, apply over wide QSO luminosity and redshift ranges.

6.2 Future Work

An ongoing aspect of our work is to finalize the target selection catalogue for the 4MOST Cosmology Redshift Survey. This work is introduced in Appendix D. As mentioned in Section 2.8.3, this QSO catalogue will be updated with the newer unWISE neo8 data release to enhance the selection, which is currently being done. The inclusion of eROSITA X-ray data in this area will also allow for a more complete QSO survey to be achieved. The long-term aim of this QSO survey is to probe the nature of dark energy and dark matter by primarily comparing gravitational lensing and redshift space distortion analyses (e.g. Kaiser 1987) but also via BAO using QSOs as tracers at $z < 2.2$ and the Lyman-α forest at $z > 2.2$ from the final 4MOST redshift surveys. The dark energy equation of state will thus be measured and tests of modified gravity models as an alternative explanation of the accelerating Universe will also be made.

The spectroscopic data which will be collected with 4MOST will allow for large scale studies such as the cross-correlation analyses and QSO acf work in Chapters 3 and 4 to be conducted with reduced errors as we still assume some contamination in our samples. Additionally, performing the CMB lensing cross-correlations with a higher resolution CMB lensing map (e.g. Atacama Cosmology Telescope CMB lensing maps; Madhavacheril et al. 2024) will

allow for the investigation of the 1-halo contribution to these lensing studies, as mentioned in Chapters 3 and 4.

Finally, larger scale stacked reverberation mapping studies can also be done if we are able to use two 4MOST spectroscopic epochs in conjunction with LSST bi-weekly *ugriz* optical monitoring. This can be combined with the X-ray when eROSITA starts up again.

We see a clear avenue for future work to be done within our stacked reverberation mapping project to derive the average line widths for the full H_β, MgII, and CIV QSO samples in order to determine the velocity dispersion of the BLR gass clouds. This will then allow for the estimation of at least average QSO black hole masses in redshift and luminosity sub-ranges, which continues to be an ongoing aim of the project.

Appendix A

WHDF X-ray and DESI QSOs

Here we list the QSO contents of the WHDF from the Chandra X-ray source list of Bielby et al. (2012) in Table A.1 and from preliminary DESI QSO redshift survey data in Table A.2.

Table A.1: Full colour, morphology and redshift information for the 15 X-ray QSOs from Bielby et al. (2012) found in the WHDF. X-ray absorbed QSOs are bolded. (D) in second column indicates also detected by DESI (see Table A.2). The *ugriz* magnitudes come from the SDSS Stripe 82 data, the W1 and W2 fluxes are from Timlin et al. (2016), and the X-ray fluxes are from Vallbé Mumbrú (2004).

ID	morph-ology	u	g	r	i	z	W1	W2	$S_X(0.5-10keV)$	Redshift
WHDFCH005	star	21.19	20.83	20.86	20.61	20.56	16.47	15.58	5.62×10^{-14}	0.52
WHDFCH007	galaxy	23.73	23.22	22.88	22.27	21.87	15.98	15.14	1.17×10^{-14}	1.33
WHDFCH008	galaxy	23.84	24.00	24.01	23.38	22.32	17.14	16.42	3.62×10^{-15}	2.12
WHDFCH016	star (D)	20.95	20.67	20.61	20.34	20.29	17.20	16.15	1.44×10^{-14}	1.73
WHDFCH017	star (D)	20.24	20.04	19.85	19.60	19.11	15.12	14.54	3.22×10^{-13}	0.40
WHDFCH020	galaxy	22.34	22.05	21.67	21.35	20.86	16.50	16.15	1.09×10^{-14}	0.95
WHDFCH036	star (D)	22.14	21.62	21.68	21.46	21.00	16.18	15.56	6.26×10^{-14}	0.83
WHDFCH044	star (D)	22.73	21.84	20.49	19.83	19.14	13.54	12.55	2.66×10^{-14}	0.79
WHDFCH048	galaxy (D)	23.16	22.57	22.13	21.67	21.76	16.30	15.42	2.15×10^{-14}	1.52
WHDFCH055	star	23.65	22.28	21.73	21.15	20.60	16.26	15.97	2.17×10^{-14}	0.74
WHDFCH090	star (D)	21.07	21.03	20.62	20.72	20.76	16.26	15.47	4.83×10^{-14}	1.32
WHDFCH099	star (D)	20.52	20.34	20.25	20.23	20.00	15.58	14.96	8.84×10^{-15}	0.82
WHDFCH109	star	18.39	18.07	18.14	18.00	18.13	13.80	12.95	6.69×10^{-14}	0.57
WHDFCH110	galaxy	22.73	21.91	21.22	20.59	19.95	15.50	15.42	2.20×10^{-14}	0.82
WHDFCH113	star (D)	22.19	21.56	21.51	21.59	21.44	18.30	17.47	5.99×10^{-15}	2.54

Table A.2: Photometric, morphological and redshift information for the 13 QSOs from DESI in the WHDF. In the first column, bracketed names are those for DESI sources detected in Chandra X-rays at $> 3\sigma$ by Vallbé Mumbrú (2004) but not listed by Bielby et al. (2012). In second column, (X) indicates also listed as an X-ray QSO by Bielby et al. (2012) (see Table A.1); Column 10: (-) indicates no X-ray detection at 3σ. All other fluxes not listed by Bielby et al. (2012) are from Vallbé Mumbrú (2004). We note that the DESI data used here is preliminary and subject to change in final, public, DESI data releases.

WHDF ID	morph-ology	u	g	r	i	z	W1	W2	$S_X(0.5-10keV)$	Redshift
1109	star	24.94	22.45	22.23	22.06	22.14	17.84	17.27	-	3.087
3630	star (X)	21.07	21.03	20.62	20.72	20.76	16.26	15.47	4.83×10^{-14}	1.334
2779 (WHD-FCH038)	star	23.47	21.26	21.05	21.11	21.24	19.00	17.68	6.30×10^{-15}	3.138
8222 (WHD-FCH014)	galaxy	23.22	22.34	21.96	21.82	21.46	17.24	16.68	7.10×10^{-15}	2.679
254	star	24.47	22.70	21.83	21.69	21.48	17.68	16.36	-	2.593
5964	star (X)	20.24	20.04	19.85	19.60	19.11	15.12	14.54	3.22×10^{-13}	0.397
10665	star (X)	22.73	21.84	20.49	19.83	19.14	13.54	12.55	2.66×10^{-14}	0.799
8779	star (X)	22.19	21.56	21.51	21.59	21.44	18.30	17.47	5.99×10^{-15}	2.544
14697	galaxy (X)	23.16	22.57	22.13	21.67	21.76	16.30	15.42	2.15×10^{-14}	1.539
14428	star (X)	22.14	21.62	21.68	21.46	21.00	16.18	15.56	6.26×10^{-14}	0.833
11642	star (X)	20.52	20.34	20.25	20.23	20.00	15.58	14.96	8.84×10^{-15}	0.820
5971	star (X)	20.95	20.67	20.61	20.34	20.29	17.20	16.15	1.44×10^{-14}	1.753
3081 (WHD-FCH052)	galaxy	21.77	21.73	21.56	21.62	21.66	17.26	16.59	1.20×10^{-14}	1.306

Appendix B

Catalogue Mask

B.1 Tycho Stars

Remove Tycho stars with $V_T < 12.0$ in circles with radii (arcsec converted to degrees):

read(20,*,end=100)ra$_t$(it),dec$_t$(it),vt$_{mag}$(it)

if(vt$_{mag}$(it).le.8.0d0)T$_{radiussq}$(it)=340.0d0/3600.0d0*340.0d0/3600.0d0

if(vt$_{mag}$(it).gt.8.0d0)T$_{radiussq}$(it)=80.0d0/3600.0d0*80.0d0/3600.0d0

if(vt$_{mag}$(it).gt.9.0d0)T$_{radiussq}$(it)=45.0d0/3600.0d0*45.0d0/3600.0d0

if(vt$_{mag}$(it).gt.10.0d0)T$_{radiussq}$(it)=30.0d0/3600.0d0*30.0d0/3600.0d0

if(vt$_{mag}$(it).gt.11.0d0.and.vt$_{mag}$(it).lt.12.0d0)T$_{radiussq}$(it)=20.0d0/3600.0d0*20.0d0/3600.0d0

B.2 Bright Galaxies

Remove objects in rectangular areas centred on bright galaxies etc in the NGC, shown in Table B.1 and the SGC, shown in Table B.2 with the following lines of code:

do iq=1,nq

do ibg=1,nbg

if(ra$_q$(iq).gt.ramin$_{deg}$(ibg).and.ra$_q$(iq).le.ramax$_{deg}$(ibg)* .and.dec$_q$(iq).gt.decmin$_{deg}$(ibg).and.dec$_q$(iq).le

enddo

enddo

write(*,*)' finished extra bgs'

Table B.1: NGC centre of the rectangle RA and Dec, the minimum and maximum RA (hms) of the rectangle, and the minimum and maximum Dec (dms) of the rectangle

RA (hms)	DEC (dms)	RA min (hms)	RA max (hms)	DEC min (dms)	DEC max (dms)
13 52 00	-28 20 00	13 38 00	14 05 20	-28 56 00	-27 54 00
10 10 30	-19 25 00	10 08 15	10 12 42	-19 59 00	-18 55 00
12 39 28	-26 44 38	12 38 50	12 40 05	-26 53 11	-26 35 29
15 17 25	-21 01 00	15 16 56	15 18 00	-21 06 30	-20 52 47
12 34 24	-23 23 00	12 33 47	12 34 52	-23 28 41	-23 16 17
14 16 08	-06 02 39	14 15 51	14 16 39	-06 07 30	-05 56 30
14 29 38	-05 58 56	14 29 15	14 29 58	-06 04 00	-05 54 00
15 12 22	-19 48 45	15 12 03	15 12 52	-19 52 40	-19 44 30
14 20 35	-29 14 39	14 20 21	14 20 48	-29 17 13	-29 10 47
12 00 34	-10 26 19	12 00 21	12 00 54	-10 29 50	-10 23 18
13 58 42	-24 55 57	13 58 28	13 58 55	-24 59 48	-24 52 41
12 20 39	-22 13 12	12 20 26	12 20 50	-22 16 32	-22 10 32
12 08 21	-24 43 16	12 08 05	12 08 52	-24 51 00	-24 39 00
11 11 47	-22 50 47	11 11 25	11 12 14	-22 56 30	-22 45 00

Table B.2: SGC centre of the rectangle RA and Dec, the minimum and maximum RA (hms) of the rectangle, and the minimum and maximum Dec (dms) of the rectangle

RA (hms)	DEC (dms)	RA min (hms)	RA max (hms)	DEC min (dms)	DEC max (dms)
00 00 45	-13 41 25	23 58 40	00 02 50	-14 12 00	-13 10 00
02 39 30	-34 30 00	02 36 00	02 43 30	-35 15 00	-33 45 00
00 47 05	-20 45 00	00 46 40	00 47 40	-21 00 00	-20 30 00
00 52 45	-26 36 00	00 50 00	00 53 30	-26 45 00	-26 22 00
00 47 33	-25 17 00	00 46 40	00 48 30	-25 30 00	-25 05 00
01 00 09	-33 42 00	00 58 00	01 02 00	-34 00 00	-33 25 00
00 54 51	-37 41 00	00 53 33	00 56 25	-37 58 00	-37 24 00
00 15 09	-39 13 00	00 13 48	00 16 43	-39 25 00	-39 00 00
21 40 20	-23 10 00	21 39 47	21 41 01	-23 18 01	-23 03 09
03 09 46	-20 34 46	03 09 19	03 10 20	-20 41 31	-20 28 09
03 02 28	-23 36 55	03 02 06	03 02 52	-23 40 48	-23 31 05
22 57 42	-29 37 50	22 56 00	22 59 30	-30 00 00	-29 17 00
23 09 30	-21 09 57	23 09 04	23 09 54	-21 15 00	-21 03 00
01 29 43	-21 37 54	01 29 22	01 30 07	-21 41 00	-21 33 00
23 44 15	-18 14 43	23 44 00	23 44 32	-18 18 00	-18 10 30
01 26 49	-32 32 17	01 26 28	01 27 17	-32 36 00	-32 28 30
00 14 11	-23 11 00	00 13 51	00 14 28	-23 16 51	-23 04 15
23 45 58	-18 42 00	23 45 43	23 46 13	-18 44 23	-18 36 44
00 40 25	-13 54 00	00 40 22	00 40 50	-13 56 00	-13 48 20
23 18 56	-13 25 01	23 18 40	23 19 20	-13 30 00	-13 21 00
00 30 12	-23 49 00	00 30 00	00 30 30	-23 50 00	-23 45 00
21 46 38	-21 15 00	21 46 28	21 46 50	-21 17 45	-21 12 00

B.3 Objects to r<21

Remove objects in fof clusters to r<21 eyeballed as such to Nmem>=40 plus those listed in 2MRS galaxy z survey with Nmem>=6.

Radius of hole with membership Nmem:

do it=1,nt
read(20,*,end=100)group$_t$(it),ra$_t$(it),dec$_t$(it),nmem$_t$(it)
T$_{radius}$ = factor*dsqrt(dfloat(nmem$_t$(it))/3.14159)/60.0d0 T$_{radiussq}$(it)
= T$_{radius}$*T$_{radius}$ if(nmem$_t$(it).lt.nmem$_{min}$)T$_{radiussq}$(it) = 0.0d0
enddo
100 continue

Table B.3: NGC cluster members

ID	RA (deg)	DEC (dec)	member number
3279898	204.3030813553814	-29.85575596412559	892
2958913	199.72440673794532	-21.03354270440251	477
114910	152.76981594805187	-4.69491793831169	308
4278912	219.9223341071429	-26.53768294897961	196
4392041	221.99731801342264	-14.273307536912755	149
3295327	204.50614267832162	-17.879687167832177	143
2276747	190.05399200000005	-5.7947934031007735	129
2899922	198.8729111249999	-23.980226757812495	128
2118277	187.76955616000004	-8.053675008000003	125
3722642	210.85685199193557	-6.051670758064511	124
2703230	196.05808848360655	-10.337562983606556	122
2983201	200.07301349586774	-24.441725462809906	121
3777297	211.64453011016948	-5.453457889830512	118
1687534	181.47745090350884	-14.525447877192983	114
4732403	228.45281229357786	-15.463854357798166	109
2137957	188.07357984999993	-7.566864649999998	100
2438836	192.34907701010107	-10.11961213131313	99
1439192	177.7498318979592	-28.804437561224493	98
3743713	211.18912416494837	-24.834968515463917	97
2517695	193.43760339583335	-6.620827812499998	96
1402995	177.18304741489368	-28.294456904255323	94
4746780	228.76255052173912	-10.093572358695655	92
1621019	180.48093513186814	-18.879942087912088	91
3138874	202.30612258888883	-33.17297045555555	90
1044731	171.2605087294119	-9.797936258823533	85
2527902	193.59619527380946	-10.5357425	84
1667331	181.17095414457836	-28.11527291566264	83
3061756	201.17744813750005	-19.695310162500007	80
1285263	170.88484047297297	-8.657945797297296	74
3012881	192.26876651388892	-8.659063486111108	72
5020749	216.48498516666666	-23.99205276388889	72
5441257	222.37540752857137	-10.169249685714286	70
5840337	228.4399946376812	-14.2766302173913	69
2942232	191.4227030735294	-6.070885617647056	68
4345382	208.02198436764698	-6.055230088235294	68
248418	154.65334270149256	-17.986653179104476	67
4782604	213.37590883582075	-29.593981208955224	67
3345869	196.1344944307692	-3.5736222000000004	65
4051043	204.54193478125	-9.799452484375	64
2251618	183.17317098333334	-28.619828916666663	60
4531502	210.26918011666672	-30.32942518333333	60
3357414	196.26871486666658	-8.162145983333332	60
4120617	205.40081658333327	-29.91287055	60
3256574	195.06872313333332	-12.34907715	60
4710170	212.43398331666666	-30.810755333333347	60
2325685	184.12112900000002	-11.528274366666668	60
4644455	211.6449588644067	-34.31482937288135	59
3505472	198.01982236206902	-6.998025689655175	58
684285	162.00983426315796	-20.846538105263164	57

Table B.4: NGC cluster members

ID	RA (deg)	DEC (dec)	member number
1044358	167.4687237894737	-23.72722694736842	57
3272128	195.24989743859643	-14.514280701754387	57
5575289	224.3373787857143	-19.213112250000002	56
3666152	199.95152163636368	-27.40836916363636	55
3043586	192.62272961111114	-10.855898925925924	54
2986685	191.9254914716981	-26.198444981132077	53
938682	165.93954350943395	-23.242229962264148	53
2445486	185.55351939622636	-33.48272705660377	53
2817826	190.02579328301888	-11.625414773584904	53
5381917	221.52201000000005	-18.023303037735847	53
5541874	223.83002711538455	-25.471869692307692	52
5344544	220.9850454038462	-18.48381734615384	52
1866189	178.59517184313725	-12.482856882352943	51
1722253	176.7697839215686	-16.854123921568632	51
5768923	227.31498934	-11.319487019999999	50
1858303	178.5010724285714	-20.56679004081633	49
4327270	207.83019030612243	-33.808764918367345	49
3320467	195.82386254166676	-17.425542354166673	48
3231168	194.77521237500005	-12.225542083333332	48
790528	163.66484233333338	-21.065085812499998	48
4537341	210.33602631914897	-33.066597191489365	47
5620189	225.03275636170216	-16.36845255319149	47
1027870	167.24925895744684	-28.36965548936171	47
5832203	228.31938557446813	-18.137715148936174	47
4541970	210.38591747826086	-25.252302043478256	46
3022123	192.35099793478264	-5.191411521739131	46
3643928	199.6687502608696	-8.44568845652174	46
1416992	172.68906991111115	-15.28874766666667	45
3476195	197.6949271555555	-23.864520644444447	45
5811295	227.95713375000003	-13.140219318181813	44
6070797	232.47650509302335	-18.622276511627913	43
2612249	187.56587195348843	-8.39720911627907	43
5953650	230.38825920930236	-7.451939906976744	43
2045376	180.72819295348836	-16.375528604651162	43
4088345	204.98601361904764	-31.639756404761908	42
2908695	191.0153323571428	-5.678389142857141	42
5943316	230.19471983333335	-18.34479	42
4035283	204.33006407142858	-28.04532361904762	42
4761427	213.09951973809518	-30.646854142857137	42
5410859	221.94641173809526	-19.080872428571425	42
3881772	202.49762285714286	-17.994142333333336	42
4932425	215.3204770731707	-29.264088341463417	41
4465196	209.4673533414634	-29.345838951219513	41
4403144	208.734024902439	-29.138739536585376	41
4674745	212.03325977499998	-6.090391675	40
3873552	202.41991494999996	-17.944346549999995	40
87189	151.66767268253972	-19.220797269841274	63
3128870	193.5917211041666	-29.011588770833324	48

Table B.5: NGC cluster members

ID	RA (deg)	DEC (dec)	member number
3400457	196.7893197291666	-28.224039749999992	48
4383280	208.49949477272727	-7.931694431818183	44
3352170	196.21222799999993	-30.48900730769231	39
3270516	195.23737210526315	-13.944915973684209	38
540509	159.71129811111106	-11.648649277777777	36
5680881	225.93480069444448	-3.302966166666666	36
1309299	171.22116468571429	-13.571127485714284	35
3709095	200.45816197142858	-13.206661057142856	35
2974723	191.81577814285714	-10.063159714285712	35
4525716	210.1927798000001	-34.22676271428573	35
5408028	221.89756057142858	-18.07181897142857	35
3269042	195.22050202941176	-13.452375676470592	34
3536115	198.3942782058824	-15.431245470588236	34
4080022	204.9066828484848	-11.497543727272728	33
3045404	192.66560990909093	-9.03044506060606	33
3665452	199.94472466666667	-21.903119818181818	33
489141	158.81997338709678	-17.276182419354836	31
4376985	208.4197493225806	-33.95271561290322	31
3289583	195.45426377419346	-27.125516451612906	31
4687763	212.17681064516134	-21.595621935483866	31
3154571	193.90345710000003	-8.05072086666667	30
3264255	195.16275370000008	-4.600716533333332	30
1430746	172.88632699999997	-2.307245206896552	29
4093696	205.08220141379311	-23.858248448275866	29
4896783	214.84794806896554	-27.37157362068966	29
3205848	194.48285389285715	-13.060772464285716	28
1560887	174.62431367857144	-8.977016392857141	28
3137927	193.71375967857145	-10.249520571428569	28
3662075	199.87835892857134	-33.48958785714285	28
3767038	201.14011564285713	-21.137529142857144	28
5472114	222.80521089285716	-26.632767571428573	28
4987883	216.05302807142863	-16.725936321428573	28
2449306	185.61780748148146	-22.34492451851852	27
691306	162.0981914074074	-25.163490666666668	27
3377225	196.49800726923075	-7.512767846153848	26
3314583	195.75161446153845	-8.086419846153847	26
4425719	208.99983530769228	-30.337639846153852	26
5398224	221.75208253846162	-16.95693303846154	26
1551941	174.49925699999994	-17.23183944	25
1225646	170.03776796000002	-3.0544556799999993	25
4098345	205.12687284	-33.65607804	25
3323702	195.87556288	-29.829253679999997	25
1690446	176.35930300000004	-10.101808083333331	24
5471572	222.79979545833336	-20.43983904166667	24
5600814	224.72938437499994	-19.242916250000004	24
4400670	208.70151350000003	-19.669939541666665	24
3058933	192.79218960869568	-22.538743565217388	23
718888	162.54098486956525	-17.24167382608696	23
2556272	186.91062926086957	-8.278622173913044	23
767511	163.30449826086956	-7.431449173913044	23

Table B.6: NGC cluster members

ID	RA (deg)	DEC (dec)	member number
5430674	222.2181360434783	-27.876491260869564	23
5363877	221.26066595652176	-13.944584434782605	23
1681084	176.21367518181816	-9.232363045454544	22
133463	152.53913345454546	-12.432589181818182	22
1050372	167.5559425454545	-6.585680227272727	22
5940579	230.1560518181818	-7.018821954545453	22
1858231	178.48801014285718	-23.167186095238097	21
2896001	190.89095561904767	-20.84450180952381	21
3016616	192.28594700000002	-11.408530666666667	21
3123183	193.5237259047619	-8.622822333333334	21
3340940	196.07900057142857	-7.647563333333333	21
699833	162.23856480952384	-4.762271666666666	21
3914813	202.8680920476191	-34.795367333333324	21
3982385	203.69548671428575	-34.31071885714285	21
3167183	194.04990538095234	-29.502299761904762	21
5405439	221.85767390476187	-22.40804714285714	21
5460509	222.65351723809528	-18.151704904761907	21
4167964	205.95580604761906	-19.82823314285714	21
4784433	213.40171257142862	-17.98474904761905	21
5487475	223.03331404761906	-2.529456857142857	21
4471508	209.53812175	-12.883457450000002	20
3312309	195.71740649999998	-2.5154554	20
731308	162.74151295000001	-2.14839865	20
492817	158.86369419999997	-24.384875650000005	20
3343976	196.09719809999996	-31.197946899999994	20
5593541	224.62211940000003	-6.8212706999999995	20
1135267	168.76508563157896	-28.393509684210528	19
1905287	179.03341952631578	-19.898835789473686	19
2468171	185.8396030526316	-5.684559263157896	19
3663383	199.90814963157896	-12.700539947368421	19
3758227	201.02929878947367	-31.669089105263154	19
4244980	206.86335410526317	-32.81919789473685	19
3193533	194.34450173684212	-30.36647684210526	19
3245019	194.94105115789475	-29.599982684210524	19
3837449	201.98074963157893	-25.85681805263158	19
4099682	205.14285431578944	-21.92965668421052	19
5917552	229.76920831578954	-15.99861463157895	19
4862914	214.41495278947366	-24.183638421052635	19
4581644	210.84102010526314	-22.555855263157888	19
5425453	222.15247826315792	-4.73731294736842	19
2990312	191.99010833333332	-22.267401333333336	18
1569598	174.7392215	-17.967776055555554	18
1654995	175.8754405555555	-16.796472500000004	18
1294745	170.9973876111111	-12.298288000000001	18
3268045	195.20281538888887	-12.008193277777776	18
4770423	213.2167703888889	-7.084871888888888	18
357827	156.59159472222225	-2.6201165555555557	18
4158011	205.84276799999998	-28.96846222222222	18
3895896	202.67084844444443	-28.149248444444442	18
4490913	209.7888654444444	-15.238980777777778	18
3514523	198.1460771764706	-17.54122288235294	17

Table B.7: NGC cluster members

ID	RA (deg)	DEC (dec)	member number
665044	161.67904788235293	-16.132952647058826	17
1899113	178.96246511764704	-18.19263688235294	17
1630526	175.5515935882353	-10.772221352941179	17
1827021	178.13153264705886	-3.872642235294117	17
1785635	177.5880004117647	-2.8136797647058818	17
3610131	199.26069347058822	-10.772028705882352	17
3177953	194.17178629411762	-7.565916294117646	17
3353345	196.23084758823526	-7.948015705882353	17
1021271	167.13076023529413	-10.491228764705882	17
76556	151.4501394117647	-17.435173882352945	17
4579372	210.81922835294117	-31.347985764705886	17
4981855	215.97738441176472	-28.68810729411765	17
5180970	218.6455869411765	-27.994165000000002	17
5540199	223.80360311764704	-19.66333635294118	17
5953104	230.38741735294118	-7.377622999999999	17
3242685	194.91643831250002	-14.967373375000001	16
997585	166.78574612500003	-18.026100687499998	16
1322655	171.404249625	-11.142372312499997	16
1232932	170.13258118750002	-9.014581499999998	16
2084139	181.19828793749997	-2.7185804375	16
3827301	201.85128743750002	-11.80764325	16
4607293	211.17873037499996	-9.7103841875	16
4108562	205.25275237499997	-10.7675703125	16
4102282	205.1795869375	-7.74961	16
3139683	193.7317963125	-10.064082	16
496371	158.93455924999998	-6.672456250000001	16
245755	154.61550368750002	-6.3105748749999995	16
256623	154.8036841875	-5.63191775	16
361335	156.64696275000003	-2.8275979375000007	16
1386900	172.28250531249998	-6.2096582499999995	16
3640658	199.62528468749997	-31.632029125	16
3132631	193.64988075000002	-29.07912	16
3942952	203.2299188125	-25.179018625	16
3804809	201.58700006249998	-22.628155874999997	16
5546898	223.907234375	-21.591724937499997	16
6021207	231.58754575	-6.938005125	16
5884529	229.19241281250004	-7.3667515	16
3560406	198.67655393333337	-18.77780286666667	15
3098133	193.2348882666667	-15.345782199999997	15
1000352	166.83151953333336	-19.556585000000002	15
860619	164.73130933333334	-14.961718866666669	15
2553708	186.87015226666662	-8.167452333333333	15
1373603	172.10039693333334	-11.373184399999998	15
1868230	178.60357519999997	-2.316021933333333	15
3887825	202.57184686666668	-10.053361066666668	15
3470052	197.6200815333333	-7.651105133333333	15
4997084	216.17711946666668	-3.2135898666666667	15
4359194	208.21434006666667	-2.6070583333333333	15
212949	154.041157	-15.790420733333333	15
259468	154.853005	-5.656517133333334	15
1266772	170.63136146666665	-7.056084400000002	15

Table B.8: NGC cluster members

ID	RA (deg)	DEC (dec)	member number
363035	156.6708945333333	-19.051379866666668	15
90963	151.72265166666665	-15.717463599999999	15
3547567	198.53510533333332	-33.773148733333336	15
3910852	202.84604086666664	-21.25106193333334	15
2877412	190.67737142857143	-29.618184714285714	14
1404257	172.51627107142855	-11.544935142857144	14
1715878	176.6861485714286	-3.847562928571429	14
4596673	211.04759371428568	-10.753154857142858	14
3985482	203.7242902142857	-8.444267857142856	14
3683312	200.15553214285714	-2.291562928571429	14
75032	151.4233645	-7.9818150714285725	14
26995	150.50621685714287	-15.282747428571428	14
47340	150.90374892857145	-15.111908285714286	14
3933572	203.111793	-33.137153285714284	14
3839942	201.98750078571433	-31.49246464285715	14
4003242	203.94866892857144	-30.876726285714273	14
3296099	195.53295471428572	-32.78792242857143	14
3345451	196.12229607142862	-32.25325621428571	14
3090183	193.15021971428575	-31.265108071428575	14
4873601	214.55918121428573	-19.979479785714283	14
4865341	214.44838507142856	-13.873009285714287	14
4802477	213.6318800714286	-10.705268857142858	14
5609196	224.85464521428577	-16.695787071428573	14
5613299	224.9181756428571	-16.180693714285717	14
5717173	226.50554007142858	-11.275611214285712	14
1877580	178.71403884615384	-31.57228438461538	13
2148563	181.9928819230769	-30.33719515384616	13
3102304	193.29624838461538	-27.46480184615385	13
3028214	192.44064576923074	-23.856568846153845	13
2633847	187.81910430769233	-26.290708000000002	13
3047539	192.67109346153848	-20.338590307692304	13
3203304	194.4545360769231	-17.27052453846154	13
2447773	185.59863584615388	-21.19568915384615	13
1627835	175.51810507692306	-16.462429615384615	13
926068	165.74789053846152	-16.289492923076924	13
2598826	187.4013723076923	-8.434659	13
3214980	194.59229453846154	-11.16715492307692	13
3257503	195.07870546153848	-8.086439461538461	13
2858080	190.460124	-7.169909307692308	13
551981	159.90305676923074	-10.542198153846153	13
53336	151.00876253846155	-6.475979538461538	13
6089370	232.87748930769234	-5.158188384615385	13
7666	150.14767846153848	-14.947911923076926	13
4281920	207.28150084615382	-30.822074769230763	13
3687840	200.20943115384614	-29.478397384615384	13
3363917	196.34814661538465	-30.103561307692303	13
3790854	201.41646061538458	-26.465773384615385	13
3842335	202.02821823076923	-20.964616846153845	13
5794278	227.69927184615383	-18.431375692307693	13
5225439	219.27361884615385	-23.982529846153845	13
4626860	211.42859146153847	-17.399115846153844	13

Table B.9: NGC cluster members

ID	RA (deg)	DEC (dec)	member number
2046527	180.7306049166667	-30.12700566666667	12
828325	164.23669916666665	-14.299226749999997	12
1024831	167.19182508333333	-10.96234375	12
4042281	204.42272050000003	-15.10274658333333	12
3839281	201.98273841666665	-13.424182000000002	12
3511747	198.09652908333334	-4.335307166666667	12
883876	165.09896999999998	-9.983962416666666	12
5944494	230.2313354166667	-2.578152166666667	12
559948	160.0333485	-23.81999841666666	12
624388	161.07527475	-22.827824	12
3754627	200.987311	-31.647692000000003	12
4262314	207.05920291666664	-30.54892733333333	12
4159307	205.8514075833333	-30.36828833333334	12
4454659	209.34156325	-27.17024866666667	12
3284950	195.40123341666668	-30.06781391666667	12
4049753	204.50882424999998	-22.923255083333334	12
5843640	228.49897950000002	-21.520962083333334	12
5957685	230.46567241666668	-17.727909666666665	12
5123303	217.88844566666666	-25.38657266666667	12
5432988	222.25672483333332	-20.848504750000004	12
4146635	205.70483825000002	-18.818304583333333	12
5559069	224.09610791666663	-5.885997833333333	12
5784167	227.54972341666664	-2.247892583333333	12
2144236	181.93296272727272	-32.018007	11
2069475	181.00273318181817	-31.599111999999998	11
2134179	181.81057445454547	-30.02739736363636	11
2237766	183.05759863636365	-27.109677727272732	11
3740805	200.8276643636364	-19.619748727272725	11
2531256	186.60361981818184	-13.68235881818182	11
3026418	192.4227295454546	-11.091128181818181	11
774866	163.41800927272726	-21.793987636363635	11
1197629	169.63152990909091	-14.44014690909091	11
1606714	175.24171245454545	-10.549812090909091	11
2381286	184.79490099999995	-5.022137999999999	11
4023755	204.18788763636363	-16.947420545454545	11
4009524	204.02281463636365	-14.902151909090907	11
4216592	206.5394950909091	-11.026134363636364	11
4755931	213.03045636363638	-10.07747709090909	11
4148888	205.7218768181818	-11.017928545454545	11
3048162	192.67770490909092	-8.768677545454546	11
3111208	193.39935436363638	-8.642319363636366	11
3468495	197.5954060909091	-7.172632181818181	11
4023094	204.18430172727275	-3.498795909090909	11
4774724	213.27495954545458	-7.8432806363636365	11
4863289	214.4214850909091	-7.418444545454546	11
5070027	217.15938109090908	-3.330987454545455	11
2867778	190.566663	-5.794040272727273	11
2834434	190.19093409090908	-5.3033269999999995	11
837413	164.37782627272728	-10.549694181818182	11
191577	153.67374327272728	-9.938861727272727	11
223581	154.22669636363636	-5.872223090909091	11

Table B.10: NGC cluster members

ID	RA (deg)	DEC (dec)	member number
322347	155.98281245454544	-3.182790727272727	11
1097423	168.21270372727273	-7.858735545454545	11
6085602	232.77766445454543	-5.0441497272727265	11
79632	151.50709018181817	-16.12274409090909	11
3753963	200.97542790909094	-34.65881572727272	11
3994666	203.83881109090908	-34.20598536363637	11
3757518	201.01025136363634	-32.34345818181819	11
3849340	202.10369572727274	-31.857368181818178	11
4428718	209.0287490909091	-29.311959545454545	11
3732619	200.7323698181818	-31.737951181818183	11
3137547	193.70415199999997	-29.16166336363636	11
3444025	197.29354363636364	-28.642021	11
3880267	202.47230590909092	-29.490199818181814	11
5151648	218.26281163636364	-29.48124081818182	11
5107560	217.6692929090909	-28.672663363636364	11
5505277	223.28742000000005	-21.39455236363636	11
5328122	220.73304436363637	-18.445967636363637	11
4063499	204.69410218181818	-20.335534454545453	11
5845550	228.54577999999998	-14.349135545454544	11
5626662	225.12482718181818	-13.917752090909094	11
5627831	225.14438900000002	-13.892871545454547	11
5972885	230.71605618181815	-5.000322636363636	11
2206381	182.6646584	-34.0596886	10
2561963	186.96723070000002	-30.0970415	10
2099030	181.3830035	-30.161532200000003	10
2322583	184.07310860000004	-26.6567818	10
1998389	180.13163290000006	-21.324599700000004	10
3026718	192.41722739999997	-25.161719699999995	10
3217562	194.61875980000002	-13.144193300000003	10
2919595	191.15761809999998	-10.081316	10
931081	165.8178131	-16.7611731	10
2142150	181.9084975	-14.9709267	10
4307645	207.58755100000005	-8.4561243	10
3187301	194.26662470000002	-10.761470399999999	10
3023708	192.3855408	-9.7384472	10
3156978	193.92738159999996	-9.0897116	10
3247232	194.9613007	-8.747910800000001	10
3428958	197.11906420000003	-6.372553299999999	10
3560657	198.6780808	-4.1763237	10
4969718	215.8034613	-5.3729109	10
2289325	183.6699667	-2.4493128000000004	10
344610	156.36038860000002	-15.3471024	10
244787	154.598173	-13.105921500000001	10
920619	165.65667739999995	-7.5116204	10
690191	162.0884703	-9.9448896	10
499165	158.9754182	-6.9295800000000005	10
1002341	166.85993390000002	-4.5984625999999995	10
40497	150.770183	-2.4008444	10
800356	163.80659740000002	-26.141784199999996	10
168768	153.2601423	-17.304260699999997	10
82541	151.56332290000003	-16.0244083	10

Table B.11: NGC cluster members

ID	RA (deg)	DEC (dec)	member number
3732862	200.7387202	-32.7292257	10
4358680	208.20913220000003	-30.7138956	10
4300592	207.5047245	-30.578885300000003	10
4159442	205.8608771	-29.805142199999995	10
3381078	196.54335490000003	-34.3186476	10
3299748	195.57249359999997	-32.377244600000004	10
3648659	199.7302487	-31.8175506	10
3484683	197.78741899999997	-25.8977621	10
3909674	202.8321538	-29.350783799999995	10
4156849	205.82635009999998	-25.2647566	10
4125654	205.45040680000002	-23.6122197	10
3784814	201.3473223	-25.383494	10
3904058	202.76215789999998	-20.5339788	10
4746072	212.9139381	-24.799925800000004	10
5365713	221.2936807	-20.9136597	10
5468005	222.74521540000003	-18.469229699999996	10
4977781	215.91746700000002	-19.4452569	10
4189885	206.2237623	-19.3693322	10
5970035	230.6734504	-14.036431599999998	10
5844693	228.52416170000004	-12.374991800000002	10
5510720	223.3556733	-4.7003124	10
1831381	178.1672241111111	-33.25947811111111	9
1712347	176.63304122222223	-30.100698666666666	9
1505624	173.8779791111111	-25.147086555555553	9
3134341	193.668236	-17.530277333333334	9
2602485	187.44285055555557	-19.915825111111115	9
2410862	185.15555377777775	-18.667119333333332	9
2445592	185.57034022222223	-17.988125777777782	9
3117482	193.46822188888888	-15.107254777777777	9
843695	164.46148622222225	-20.001596999999997	9
752626	163.06359366666666	-17.12955977777778	9
1334139	171.5729208888889	-14.278605888888888	9
1630785	175.56146222222222	-13.866953777777777	9
1980317	179.9136763333333	-12.394371444444443	9
1895341	178.91843944444446	-12.029574333333333	9
2392225	184.92849844444441	-12.226802777777777	9
1537753	174.30382066666664	-11.555417444444442	9
1530236	174.20736277777777	-9.566537777777777	9
1417939	172.70250444444446	-8.817227222222222	9
1378623	172.16998366666667	-8.798246777777779	9
1530123	174.2066968888889	-8.58468411111111	9
1645310	175.74084833333333	-8.335701333333335	9
1412801	172.63209599999996	-8.042680777777779	9
4519068	210.11151977777777	-7.957885999999999	9
3301680	195.5965566666667	-12.341022333333337	9
3090086	193.14850266666664	-9.775931555555557	9
3446409	197.322184	-5.272715000000001	9
4717755	212.55755388888886	-6.821179000000001	9
4616580	211.29647533333335	-3.3702826666666668	9
2944591	191.44996588888887	-7.0675143333333335	9
2913389	191.08171666666667	-7.1979196666666665	9

Table B.12: NGC cluster members

ID	RA (deg)	DEC (dec)	member number
2781738	189.56771044444446	-4.773989	9
979521	166.53344133333331	-8.876328444444445	9
347680	156.4158155555556	-3.588144333333334	9
415013	157.54528388888892	-3.1611439999999997	9
916302	165.60183011111113	-6.704226555555556	9
1029147	167.24528866666665	-4.582661666666667	9
847412	164.52488044444442	-4.7566793333333335	9
970833	166.40244633333336	-2.139172777777778	9
611164	160.86638899999997	-25.867935222222226	9
627110	161.10917811111113	-25.379605333333334	9
7129	150.13526566666667	-19.661470777777776	9
46206	150.8709258888889	-15.501823777777776	9
4001740	203.9303367777778	-31.89962222222222	9
4654529	211.7660364444444	-30.01682466666667	9
4249974	206.92522466666668	-30.358567555555556	9
4184157	206.14846666666665	-29.935986888888888	9
3183801	194.24209233333332	-31.33007566666667	9
3275049	195.28365033333333	-30.81379566666666	9
3859642	202.2336488888889	-27.93709022222222	9
4004124	203.95048011111112	-28.11287088888889	9
3838289	201.98094966666667	-24.497128777777778	9
3896706	202.67805633333336	-23.502698777777777	9
3897456	202.67865944444443	-22.419217555555555	9
4084676	204.9583548888889	-22.026774222222222	9
5030848	216.62591777777777	-29.70340766666667	9
5498109	223.17454388888888	-24.807499333333332	9
5314322	220.52831177777776	-9.010430333333334	9
2015749	180.336982	-33.879979000000006	8
2677377	188.35258574999997	-31.365994750000002	8
3090928	193.16010999999997	-26.697872000000004	8
2785413	189.613086375	-23.641181625	8
3309672	195.685760375	-22.068183625	8
3185033	194.2529525	-20.482030625	8
3543755	198.47600437500003	-16.494723500000003	8
2551257	186.83346375000002	-17.90821525	8
3129974	193.62226074999998	-16.349025375000004	8
1924376	179.24352312500002	-19.858638375	8
722172	162.591071875	-22.319760374999998	8
593906	160.5819465	-17.647505125000002	8
1080562	167.991258375	-16.92894725	8
871549	164.906638	-15.526888625	8
2154456	182.06021925000002	-15.718162375	8
2512559	186.3815605	-7.236072625	8
1605265	175.22101325	-10.721628375	8
1361182	171.93609012500002	-9.163654375	8
2087445	181.23223437500002	-3.198722875	8
3716776	200.54548375000002	-16.098225875	8
4121610	205.41073300000002	-12.100688375	8
4605237	211.14885762499998	-10.217157000000002	8
3252924	195.02396275	-10.492233125000002	8
3289926	195.45841125000004	-8.335594	8

Table B.13: NGC cluster members

ID	RA (deg)	DEC (dec)	member number
5100662	217.57353150000003	-5.251473125	8
2965300	191.68732162499998	-8.790905500000001	8
3047912	192.681888875	-4.15680375	8
492234	158.8605545	-14.130631999999999	8
757029	163.130985875	-7.924962375000001	8
869186	164.859100375	-7.54696	8
328588	156.089409875	-6.0425785	8
273352	155.10698212499997	-6.525474000000001	8
401478	157.310778125	-2.5116586250000004	8
1405391	172.532290875	-5.3759901249999995	8
1471138	173.408615	-4.940177125000001	8
1062823	167.743094625	-3.57328675	8
1571307	174.76729137499999	-4.320269375	8
13116	150.25646825	-15.361665375	8
4782881	213.37561737499996	-30.488232125000003	8
3178474	194.18061225000002	-34.704977375	8
3639449	199.612662625	-33.302210375	8
3834980	201.94246387500004	-31.80059125	8
4434629	209.09327937499998	-34.11258325000001	8
4264030	207.06525212499997	-30.574323375000002	8
4406350	208.76686012499997	-26.779214500000005	8
3282063	195.36940625	-32.333135250000005	8
3341027	196.06908525	-29.409854375000002	8
3899425	202.70717275	-25.334760125000003	8
4061242	204.65848212499998	-24.147314124999998	8
3747859	200.91083925000004	-26.012846000000003	8
3759255	201.040542375	-23.876986374999998	8
3938783	203.17137749999998	-23.513439874999996	8
4538387	210.33543562500003	-25.437873625	8
4598532	211.06706900000003	-25.637934500000004	8
4675785	212.0326085	-24.158306249999995	8
4830801	213.99284500000002	-22.592827	8
4527805	210.222119375	-21.341431250000003	8
4603117	211.11180699999997	-14.5464385	8
5531694	223.670526625	-17.404420000000002	8
5886187	229.2224715	-13.419031874999998	8
5713621	226.44935625	-14.96428425	8
5715069	226.472346125	-14.151721625	8
5373997	221.402464875	-11.807901874999999	8
5087180	217.38864849999996	-9.562790625	8
5680439	225.928601625	-3.907620625	8
2126828	181.71629714285712	-31.947981285714285	7
2692564	188.52761471428573	-31.216913999999996	7
2262814	183.34528799999998	-30.954910428571434	7
1931255	179.32320171428566	-28.07236842857143	7
1981997	179.93483600000002	-20.972309714285714	7
2014459	180.325082	-20.507695142857145	7
1975917	179.860005	-20.447968285714285	7
3113556	193.420984	-26.65353257142857	7
3057741	192.79054142857146	-25.54846885714285	7
2883806	190.74864785714286	-24.727591857142855	7

Table B.14: NGC cluster members

ID	RA (deg)	DEC (dec)	member number
3089883	193.14913657142858	-21.914967285714283	7
3710185	200.46760957142857	-17.671330571428573	7
3202981	194.45626371428574	-17.545419285714285	7
3193678	194.34836514285715	-15.649778285714286	7
3294984	195.51473471428574	-14.879340857142857	7
3050943	192.71442414285713	-14.494202	7
3065930	192.8854842857143	-14.222543	7
928891	165.78735114285712	-24.90969114285714	7
839537	164.41002642857146	-25.505206714285716	7
874997	164.96062914285716	-25.494662428571427	7
1082092	168.01021342857146	-22.303772428571428	7
1572976	174.78814671428574	-23.301080285714285	7
1410250	172.59392800000003	-21.985302428571423	7
1174776	169.32111057142856	-14.523183714285715	7
1030896	167.26752485714286	-13.95481757142857	7
1903947	179.01144299999999	-15.802422285714284	7
2823729	190.06523900000002	-9.30016257142857	7
1651721	175.8299142857143	-12.875856714285716	7
1344856	171.72044628571427	-8.091144428571429	7
1531574	174.22578857142855	-8.376349714285714	7
3945684	203.25743342857143	-16.24693614285714	7
4077041	204.85356814285714	-11.546603428571428	7
4278839	207.24692757142859	-7.19501642857143	7
4292788	207.41225099999994	-6.105995142857142	7
3022330	192.37270328571427	-8.848000285714285	7
3987524	203.74609257142856	-8.089315285714285	7
4790957	213.48209200000002	-8.476622142857142	7
2740666	189.09101014285716	-3.920265714285714	7
3600843	199.15176785714283	-2.0923144285714286	7
453228	158.185976	-12.638952999999997	7
802029	163.83553085714286	-5.817095428571429	7
63861	151.20705242857142	-6.726308	7
518847	159.3324065714286	-3.358529428571429	7
289886	155.40804114285714	-4.312074285714286	7
240466	154.5238074285714	-2.562267	7
168013	153.250389	-2.662574857142857	7
6050	150.12682214285715	-2.1622681428571426	7
330474	156.12962157142857	-21.790099285714287	7
71575	151.3582842857143	-17.799209285714287	7
27800	150.52143485714288	-15.299311857142857	7
4506599	209.96519785714287	-34.32079342857143	7
4122111	205.41920442857145	-34.43386971428571	7
3711639	200.48249728571423	-34.60726957142857	7
3656840	199.8297322857143	-33.46973742857143	7
3843329	202.03992185714284	-34.03845971428572	7
3785973	201.36192171428576	-33.79710642857143	7
3753849	200.97966328571428	-32.179390285714284	7
4219488	206.56606342857143	-32.975472571428575	7
4590950	210.96353371428575	-31.94847085714286	7
4015298	204.0863028571429	-31.008695999999997	7
3917928	202.93350499999997	-29.809577428571426	7

Table B.15: NGC cluster members

ID	RA (deg)	DEC (dec)	member number
3546002	198.50913085714282	-33.89252314285714	7
3299894	195.57400142857142	-32.76410628571429	7
3401909	196.79863528571425	-31.701035714285712	7
3805658	201.59246100000001	-30.584551999999995	7
3183184	194.23582885714282	-29.480202857142853	7
3237197	194.84280500000003	-27.42485742857143	7
3839758	201.99853485714286	-27.357458714285713	7
3696610	200.30493971428572	-27.557230142857144	7
3551037	198.56171757142855	-23.390409571428574	7
3800441	201.53442085714286	-21.033016000000007	7
5633082	225.22069957142858	-25.206379428571424	7
5336643	220.86007985714286	-23.443917142857142	7
5543682	223.85970371428573	-23.28163785714286	7
5577131	224.36619457142857	-21.666321142857146	7
5629654	225.16081842857145	-21.717461285714286	7
4663277	211.8762084285714	-27.021052714285716	7
4480399	209.65580728571425	-24.46846342857143	7
4543942	210.39473085714286	-23.140711999999997	7
5407930	221.88951614285716	-19.33379971428571	7
4891448	214.79050585714285	-19.478204571428574	7
4507828	209.98440785714288	-22.845988	7
4552158	210.49614485714287	-22.363275	7
4191700	206.24547614285714	-17.027589	7
4717732	212.55896157142854	-17.83665442857143	7
6030626	231.75174557142861	-12.98308214285714	7
5818204	228.080671	-10.277342714285714	7
2440770	185.50890416666664	-32.309106166666666	6
2034655	180.57657933333334	-29.515043333333335	6
2197270	182.5584553333333	-29.73391816666667	6
2390646	184.90552716666667	-29.065115833333337	6
2003449	180.18248566666668	-20.832880999999997	6
2616350	187.6094698333333	-26.458680166666667	6
2998286	192.0891266666667	-20.29286933333333	6
3483300	197.76992149999995	-21.685999666666667	6
3178829	194.1813865	-21.020315833333328	6
3226082	194.71178533333332	-18.534685666666668	6
3352640	196.20917749999998	-17.2999905	6
2398223	184.99923166666665	-17.393623666666663	6
3089107	193.1382526666667	-15.518259166666667	6
3052982	192.73944683333332	-13.457294333333333	6
1859622	178.506621	-19.565352833333332	6
1629717	175.54086099999998	-18.169893166666668	6
846392	164.50416333333334	-18.427099166666665	6
1201389	169.69144666666668	-17.8595085	6
1044540	167.46737583333334	-14.972928666666666	6
1096696	168.21194316666666	-12.320937499999998	6
1845398	178.344379	-13.263230833333333	6
2383777	184.82308533333332	-13.24803533333333	6
2834670	190.18629833333335	-10.256324333333335	6
1649256	175.805141	-12.763828333333331	6
1365593	171.9953598333333	-11.718041	6

Table B.16: NGC cluster members

ID	RA (deg)	DEC (dec)	member number
1669216	176.06944816666666	-5.963307666666667	6
3989272	203.7739998333333	-15.866576333333335	6
3711433	200.48840066666668	-16.935291999999997	6
3684183	200.15501683333335	-16.916574	6
3704405	200.40083550000003	-16.285956000000002	6
3675905	200.05886833333332	-14.296009333333334	6
3803734	201.57118233333333	-12.617863833333333	6
3281679	195.35585883333334	-9.3650405	6
3162668	193.9957015	-8.075046	6
3446918	197.3301045	-6.8754610000000005	6
3230831	194.775464	-7.729558333333333	6
3317856	195.77563733333332	-5.980473166666666	6
4025357	204.20689716666666	-6.1173306666666685	6
3774754	201.22171733333334	-4.0786865	6
4720579	212.59378766666669	-7.343644666666666	6
4470482	209.52817866666666	-4.088765833333334	6
2971876	191.76590350000004	-8.737510333333335	6
2940009	191.39270233333335	-8.092572333333335	6
3113310	193.42129716666665	-4.8850745	6
375626	156.8722205	-18.809741499999998	6
635737	161.23161383333334	-16.0863175	6
237029	154.455949	-15.484803833333336	6
151371	152.90820866666667	-14.694918333333334	6
228438	154.311686	-7.898804666666665	6
370515	156.79377266666668	-3.3178089999999996	6
312151	155.8025796666667	-3.234797166666667	6
354524	156.528911	-2.7743131666666665	6
1271888	170.68259833333335	-7.676263000000001	6
1273402	170.71155066666668	-7.589680166666666	6
1042455	167.43706433333332	-7.5903236666666665	6
1360519	171.93057383333334	-5.108837333333333	6
1405567	172.53470916666666	-4.031081833333333	6
1106808	168.35364733333333	-4.094044666666667	6
671084	161.78546233333336	-2.3594093333333332	6
156308	153.0088825	-2.1447688333333335	6
269608	155.03130416666667	-21.694487666666664	6
3182458	194.22517083333335	-33.66943	6
2934486	191.332346	-34.701722000000004	6
3763989	201.092638	-31.70963216666667	6
4259849	207.02594	-33.46428016666667	6
4282263	207.29200633333332	-33.094982	6
4634260	211.510303	-31.464318000000002	6
4056763	204.60526233333334	-31.266802166666665	6
4258197	207.00989700000002	-30.787297500000005	6
4383330	208.49334799999997	-27.46027	6
3245854	194.95103433333335	-33.67363266666667	6
3354269	196.22950350000002	-32.10591516666666	6
3739911	200.81002133333334	-31.45992133333333	6
3650578	199.750932	-27.632142499999997	6
3241836	194.90267099999997	-29.26212416666667	6
2958032	191.6015575	-29.726354000000004	6

Table B.17: NGC cluster members

ID	RA (deg)	DEC (dec)	member number
4029838	204.26208200000002	-26.049567000000007	6
3807024	201.6087966666667	-25.407426333333337	6
3858594	202.2162828333333	-24.150549	6
3871692	202.37319383333335	-23.667441999999998	6
3948512	203.287409	-23.54279783333333	6
3897399	202.68075466666667	-20.9510525	6
5023868	216.53772066666667	-29.588828166666662	6
4774491	213.2682955	-28.859123166666667	6
4877639	214.61232816666669	-27.377513166666667	6
4658503	211.8122101666667	-27.161216166666666	6
4620078	211.33737550000004	-25.24504166666667	6
4452445	209.31584933333335	-25.38976866666667	6
4467671	209.49942833333336	-24.678982500000004	6
4576205	210.7774491666667	-23.201899833333332	6
4606018	211.1567376666667	-22.489218166666667	6
4812605	213.75870933333331	-24.4053295	6
4370797	208.34390016666666	-20.114121	6
4473731	209.5698298333333	-15.752670499999999	6
4670681	211.96601966666668	-16.779845166666664	6
4632672	211.490684	-12.0722625	6
5619840	225.01935466666666	-16.092774333333335	6
5852543	228.66245333333333	-13.266020833333332	6
5953550	230.39007166666667	-13.090391333333335	6
5938970	230.13952650000002	-8.528938333333334	6
4969641	215.80398533333334	-10.849879666666665	6
5601529	224.74136950000002	-6.670543666666666	6
5586582	224.4963346666667	-6.726222333333333	6
5783946	227.54113083333334	-5.885438166666666	6
5624051	225.08375766666666	-4.774803166666667	6
5640303	225.32612200000003	-4.553117666666667	6

Table B.18: SGC cluster members

ID	RA (deg)	DEC (dec)	member number
2222281	-0.5373881180487806	-32.58669424487808	1025
2287512	0.4906925062500008	-15.447324956250013	640
4674978	41.571242786476894	-30.26792159074733	281
4906873	45.657593459821456	-22.85539917857145	224
1880226	-6.389274966346151	-36.110873254807714	208
3024199	13.235829893203885	-26.54188410194175	206
5699815	59.428185892045484	-13.411284977272723	176
5343393	53.38870946357617	-36.15420288741721	151
2954909	12.026766783783783	-25.182599729729738	148
1486272	-12.886811211267606	-15.600296887323942	142
5061538	48.384271028776986	-25.7256594820144	139
3632314	23.573031936507945	-29.41732830158729	126
5149419	49.92750214285714	-19.406413453781518	119
2014646	-4.056705455357144	-31.957687705357145	112
3576615	22.62287764197532	-22.670806308641986	81
3078998	14.17632043209877	-9.916760234567898	81
1309907	344.14815098734175	-37.02990860759493	79
2075712	356.96726710958905	-30.52171856164384	73
1001777	338.94349240298504	-26.054504268656714	67
5344384	53.43098058208955	-21.477767656716413	67
908185	337.33818531818184	-20.843338484848495	66
4348958	35.78089407575757	-21.231817590909092	66
4907108	45.66314212500001	-18.896550125	64
2470134	3.560550951612903	-23.216144854838706	62
2701161	7.564972950000002	-33.265949033333335	60
1757936	351.61312205172413	-32.38843110344827	58
2942670	11.793751206896554	-20.642785896551725	58
5560073	57.06146008928571	-21.471499964285712	56
3849962	27.294090763636362	-10.05947230909091	55
5542618	56.76670107547171	-33.71245075471698	53
4429152	37.137636519230774	-19.04207546153846	52
5473582	55.55322742307693	-29.897049846153845	52
1111971	340.8230745098039	-39.872082176470585	51
3496172	21.206889139999994	-31.764540919999995	50
291709	327.0798867346939	-34.95143316326531	49
607133	332.29223199999996	-27.167069416666667	48
2755291	8.507689958333335	-9.708103312500004	48
4807701	43.91626793750001	-27.42150960416667	48
1392888	345.54180287234044	-39.572591234042555	47
5480280	55.736184130434786	-19.01814204347826	46
2758156	8.545216155555558	-30.773277688888882	45
5422546	54.73038446666668	-26.346076933333336	45
5474515	55.629046444444434	-13.492002955555552	45
501425	330.5266564090909	-32.889372181818175	44
2797397	9.213266727272728	-28.36703911363637	44
5064422	48.42256818181819	-25.193090681818187	44
4229812	33.73780041860464	-20.21962620930232	43
5419240	54.638164348837215	-35.45548909302325	43
1099471	340.58167997619046	-30.069153714285708	42
5192175	50.73193004761904	-11.203901238095238	42
5223457	51.30380111904763	-36.371941952380936	42

Table B.19: SGC cluster members

ID	RA (deg)	DEC (dec)	member number
5439550	55.034584071428576	-35.622481333333326	42
4591753	40.031981925000004	-25.202888325000004	40
1945165	354.7366508974359	-12.96171017948718	39
622347	332.54699157894737	-16.664380526315792	38
1906098	354.06579883783786	-37.93828605405405	37
5113743	49.30547533333334	-32.575118916666675	36
4396446	36.590743416666676	-24.287603805555555	36
2951431	11.94577882857143	-11.467748599999998	35
3878122	27.7650394	-9.705573285714285	35
1153106	341.5169326	-11.002039800000002	35
4971469	46.79185345714286	-9.589450657142857	35
4192935	33.12230038235294	-22.469064823529404	34
3112044	14.741089249999998	-18.7414274375	32
2384219	2.1439505483870964	-33.85479203225807	31
4378774	36.265787967741936	-24.791477451612902	31
2404547	2.4850833	-24.965793633333345	30
3281693	17.65151356666667	-30.2214146	30
4838333	44.45120153333333	-36.717350866666656	30
5417070	54.623211966666666	-23.028778733333336	30
425124	329.279403862069	-34.58220165517241	29
876498	336.8011714827586	-35.13947389655173	29
510136	330.6717116206896	-33.801856413793104	29
5353068	53.57322240740742	-30.73018651851851	27
2828507	9.783744230769233	-14.175434000000001	26
2326797	1.1918720384615387	-16.031683461538464	26
525567	330.94598469230766	-32.28581734615384	26
1052530	339.79687256	-17.344079679999997	25
628393	332.64434496	-22.6569434	25
4556196	39.39866604166666	-32.92512179166667	24
4382420	36.297811083333336	-29.477605499999996	24
4876887	45.1338325	-15.736900166666663	24
1278311	343.60756691304346	-20.36146147826087	23
3607033	23.11216886956522	-38.67920230434782	23
3486680	21.06567656521739	-37.336252739130444	23
3642808	23.717880304347826	-36.48795791304348	23
4973056	46.80405082608694	-31.396919739130436	23
2015544	355.9510095	-36.713427318181814	22
3255078	17.196568636363633	-15.843053318181818	22
1490072	347.14943013636366	-19.8936165	22
1336663	344.6212632727273	-32.23965754545455	22
5166535	50.26838514285714	-37.10060561904762	21
4483485	38.07348866666667	-35.03071914285714	21
5339468	53.32174866666665	-13.664379428571426	21
4886271	45.30079233333334	-10.89832842857143	21
632595	332.7265026190476	-25.07325680952381	21
2083612	357.08300575	-28.23329065	20
3718099	25.000445399999997	-14.8589749	20
3515659	21.525279250000004	-37.9637832	20
947284	338.03255485	-25.400473350000002	20
2609906	5.974200578947369	-32.53511631578947	19
2792854	9.120428263157894	-10.107989526315789	19

Table B.20: SGC cluster members

ID	RA (deg)	DEC (dec)	member number
5206755	51.004321	-39.485143263157894	19
3665165	24.111907263157896	-36.37983499999999	19
4792966	43.637323736842106	-10.025199368421053	19
638384	332.81010115789474	-30.56438678947368	19
980542	338.5863947222222	-10.354832499999997	18
3520061	21.640683777777777	-23.222518555555553	18
2057890	356.6834018888889	-38.46811811111111	18
1918470	354.2826725	-37.71566611111111	18
953554	338.12375794444443	-25.665657388888892	18
1702024	350.64730529411764	-13.094585941176469	17
3663212	24.0776945882353	-13.692941823529413	17
5456364	55.311253	-23.839174117647058	17
4372828	36.171054294117646	-19.143483	17
4494573	38.26501664705882	-10.758732	17
162712	324.9676357647059	-36.03343788235294	17
2227349	359.50586075	-34.29239125000001	16
3502685	21.33776375	-18.161413375000002	16
3656432	23.960667	-9.999518499999999	16
983290	338.6363229375	-12.934093625	16
3016843	13.09515825	-35.001084500000005	16
2870034	10.484768125	-32.972949	16
3316313	18.2363544375	-31.450281062499997	16
4682214	41.67391231249999	-25.3465038125	16
5570956	57.2382833125	-22.129249125	16
4330582	35.42030775	-27.28033475	16
4814598	44.02303000000001	-14.1863315	16
5202423	50.911586375	-11.19813525	16
4438744	37.2979466875	-11.0270136875	16
212675	325.8006095	-38.969648437500005	16
325234	327.607423	-30.996081375000003	16
690106	333.6643446875	-27.464574875	16
617022	332.4638475	-27.5360994375	16
1973417	355.22307973333335	-28.33642853333333	15
2285277	0.48282973333333334	-27.626644799999998	15
2592767	5.6588668	-24.125529399999994	15
2715223	7.782826200000001	-22.617982933333337	15
4024469	30.293245133333333	-33.208725400000006	15
5577670	57.356066933333345	-18.562855133333336	15
4815021	44.045445333333326	-15.3988938	15
101655	323.95639073333336	-30.313351333333333	15
1516455	347.561239	-10.796237571428572	14
2700700	7.5320243571428565	-11.11406892857143	14
3612796	23.217785071428576	-14.81410414285714	14
5640398	58.40595414285715	-9.45413357142857	14
4459312	37.65761578571429	-34.26392435714286	14
3646932	23.795468500000005	-39.14683457142857	14
3340087	18.63072364285714	-32.26298335714285	14
4671537	41.49135607142857	-28.268277714285713	14
4576000	39.76795121428572	-27.443023571428572	14
5515917	56.32180185714286	-23.000849357142858	14
4598025	40.162387285714296	-21.00474985714286	14
1628355	349.4184574285714	-34.787950428571435	14

Table B.21: SGC cluster members

ID	RA (deg)	DEC (dec)	member number
987909	338.7090258571429	-25.67346285714286	14
477933	330.1249991428571	-24.62925642857143	14
193170	325.4807302857143	-20.786165999999998	14
497773	330.46664914285714	-22.484614357142856	14
2219572	359.36848623076924	-29.04964161538462	13
2807895	9.395191461538463	-22.546759692307695	13
3431256	20.15251307692308	-17.38676392307692	13
3260317	17.277479230769234	-15.998900692307691	13
1688930	350.4306562307692	-26.293166153846155	13
1051001	339.77421284615383	-19.661219538461538	13
1266168	343.4174234615385	-17.477150692307692	13
3054474	13.749184461538464	-35.51200276923077	13
3330478	18.464276384615385	-31.786823692307696	13
5569335	57.21246546153846	-18.979428076923075	13
5341767	53.36917992307692	-18.147393230769232	13
4284990	34.64581676923078	-25.757730769230772	13
4450651	37.498097692307695	-13.265481307692307	13
4842676	44.529403230769226	-10.361962153846154	13
5178835	50.48283561538462	-13.649053076923076	13
359249	328.16499892307695	-36.499904	13
1045522	339.6924223846154	-36.742030615384614	13
751106	334.69088876923075	-36.801957615384616	13
517962	330.8037902307692	-26.40602269230769	13
2775803	8.846639916666668	-23.37572666666667	12
3033049	13.38033475	-13.113637333333335	12
1648923	349.7630481666667	-22.717292583333336	12
1142577	341.33001575000003	-16.097333916666663	12
2352132	1.6151525833333333	-13.41769575	12
4035508	30.463443	-10.470191166666664	12
4060364	30.881414833333327	-9.935421999999999	12
3066580	13.96751141666667	-9.989023333333334	12
1179089	341.9485226666667	-11.815811166666665	12
1441402	346.3447345	-10.220467583333333	12
3651734	23.876880333333336	-39.38588333333334	12
5047408	48.114692500000004	-27.141725500000003	12
5496211	56.00180483333334	-14.358485750000002	12
378604	328.49575158333334	-29.287800583333333	12
1111806	340.8065330833333	-25.825836666666664	12
857186	336.4817673333333	-24.728131083333334	12
172358	325.12043175	-26.529955583333333	12
471592	330.018868	-19.204089583333335	12
2540466	4.771907090909091	-22.93697718181818	11
1919002	354.27705436363635	-20.462708454545457	11
3853572	27.344869181818186	-14.126300909090908	11
5671871	58.93127136363636	-9.579570363636362	11
3770860	25.905925454545457	-33.70651954545455	11
3442646	20.332706545454545	-34.06317963636364	11
3603934	23.057740000000003	-33.49560281818182	11
5607941	57.87307427272727	-23.235884454545456	11
4228273	33.70740009090909	-24.853701727272725	11
4656561	41.22144427272726	-17.657633272727274	11

Table B.22: SGC cluster members

ID	RA (deg)	DEC (dec)	member number
4471285	37.86087372727273	-17.65480881818182	11
4163604	32.61758345454545	-16.832717727272726	11
5212891	51.107561454545454	-11.670264454545455	11
4600689	40.22425636363635	-13.312869181818181	11
4556844	39.39496872727273	-11.024553363636363	11
622568	332.5395280909091	-36.09105418181818	11
685537	333.5991650909091	-29.981697	11
8898	322.4811557272727	-30.036555909090914	11
139208	324.57142436363637	-27.55852945454545	11
24951	322.7374398181818	-23.818567818181815	11
587262	331.96296245454545	-18.245321727272724	11
2798866	9.246205300000002	-29.475552600000004	10
2065880	356.8124533	-27.960484700000002	10
2512035	4.2918931	-19.303247	10
1644170	349.6818457	-27.132072	10
1273599	343.5393735	-15.238600999999997	10
2066732	356.8194133	-15.305152000000001	10
2883789	10.723938299999999	-9.229952199999998	10
1771577	351.8120164	-9.386327699999999	10
3513733	21.5253384	-13.419932999999999	10
3711762	24.893129999999996	-12.076383199999999	10
3871739	27.662928299999997	-12.6805808	10
1087590	340.4016507	-12.997648700000001	10
855339	336.4448641	-13.165035399999999	10
1012842	339.1227812	-12.5653857	10
5263304	51.99349959999999	-37.149182	10
5274981	52.20369240000001	-35.1779454	10
5666827	58.84459730000001	-28.1594159	10
3923705	28.5639055	-37.78567699999999	10
3191203	16.0780377	-35.1186561	10
3641633	23.712002400000003	-36.13880270000001	10
3830299	26.935415900000006	-33.59956	10
3943786	28.9187731	-29.922744700000003	10
4716220	42.2652865	-31.174447999999998	10
4966626	46.6924819	-25.716632099999995	10
5007868	47.4001995	-25.250912800000002	10
5692293	59.29396829999999	-18.779319799999996	10
4384770	36.368526100000004	-25.639213499999997	10
4471339	37.86089219999999	-23.003190200000002	10
4254429	34.1351472	-11.348851999999999	10
210942	325.7716886	-36.739910900000005	10
1466740	346.7784495	-28.611853500000002	10
588451	331.9769617	-35.505098600000004	10
459891	329.8335087	-31.882499	10
673269	333.3795526	-27.559366300000004	10
445749	329.5958926	-20.1048236	10
527762	330.964292	-19.880792300000003	10
656328	333.1065931	-17.721723100000002	10
196693	325.5342673	-18.881460999999998	10
1906791	354.0674725555556	-31.603141888888892	9
1814497	352.5268105555555	-31.12765922222222	9

Table B.23: SGC cluster members

ID	RA (deg)	DEC (dec)	member number
1828708	352.7568497777778	-29.767875222222223	9
2843262	10.024959666666666	-22.827067000000003	9
3273325	17.50312	-15.622088777777776	9
2808907	9.426518888888888	-14.179567555555556	9
2631388	6.329444333333333	-14.555884444444445	9
1141466	341.3089008888889	-22.73144466666667	9
2333823	1.3019667777777775	-11.500611666666668	9
3636318	23.605907	-15.81732377777778	9
3613511	23.22261188888889	-12.189742444444445	9
3850507	27.296266888888887	-10.42786488888889	9
3924406	28.57775911111111	-9.715360888888888	9
2931658	11.568203444444444	-9.289464666666667	9
3547651	22.097278111111113	-35.991153777777775	9
3404311	19.689427000000002	-23.944772333333336	9
5283100	52.335207999999994	-28.13281	9
4738023	42.649222333333334	-31.51797511111111	9
4717570	42.286450444444455	-31.289311555555557	9
5571570	57.251880666666665	-22.242354999999996	9
5453136	55.258330333333326	-22.718617111111108	9
5426154	54.79341111111111	-22.388809	9
5476905	55.664839888888885	-13.292538000000002	9
5510062	56.23380066666666	-9.854918333333332	9
3916665	28.442138444444442	-23.76133566666667	9
4165197	32.65532877777778	-15.777045333333332	9
4667978	41.41930711111112	-15.361179444444444	9
4493485	38.24976455555555	-10.972665444444443	9
1787052	352.07658888888886	-36.41985566666666	9
186810	325.3681363333333	-39.765367222222224	9
506581	330.60560555555554	-35.791246888888885	9
1494508	347.229565	-30.855609777777776	9
721436	334.1793113333333	-25.754980111111113	9
720824	334.1651615555555	-21.48778877777778	9
280340	326.89856355555554	-13.182298	9
2129699	357.877592625	-34.453766625	8
2270972	0.245780375	-33.609921875	8
2145111	358.130919875	-30.181758750000004	8
2148433	358.184954125	-28.573516750000003	8
1844839	353.01384125	-27.72754475	8
2942745	11.781570625	-24.369458124999998	8
2949140	11.896486750000001	-20.428040499999998	8
3240638	16.947086000000002	-17.508108625	8
1653034	349.830709875	-28.942747750000002	8
1312111	344.18968125	-24.953066875	8
2738085	8.17489	-11.319545625	8
938030	337.854060875	-19.032909125	8
900126	337.199265125	-15.070844125	8
1154475	341.531594625	-10.368074625	8
531757	331.03595025	-11.36295275	8
5220864	51.245292875000004	-37.010117625	8
3886843	27.920108374999998	-36.187330625	8
4012021	30.078555124999998	-34.31582575	8

Table B.24: SGC cluster members

ID	RA (deg)	DEC (dec)	member number
3874954	27.718707875000003	-36.011206	8
3491496	21.14588825	-33.170941	8
3471870	20.812511750000002	-32.841203125	8
3853948	27.352514250000002	-26.745293624999995	8
3293743	17.844385	-29.23451425	8
4632358	40.786336625	-32.798666125000004	8
4777951	43.36939387500001	-30.860264374999996	8
4666942	41.404633125	-27.960870749999994	8
5652799	58.617724875	-20.424530125	8
5652152	58.599651249999994	-19.192636750000002	8
5303042	52.69844249999999	-21.05871875	8
5486870	55.83554037500001	-18.476555875	8
5468172	55.515584000000004	-17.523898499999998	8
5441241	55.050199125	-15.610773625000002	8
5607213	57.85236175	-15.404549750000001	8
5308532	52.79433325000001	-14.637623125000001	8
4391428	36.49472875	-24.70885025	8
4614964	40.478482	-20.962562124999998	8
4596452	40.13114325	-20.369816125	8
4797530	43.72108012499999	-15.651314500000002	8
4790558	43.588984375	-13.948385625000002	8
4815414	44.040504125	-13.690678499999997	8
4702186	42.023437375	-13.958655875000002	8
4831220	44.3272275	-10.99048825	8
5142938	49.823467625	-12.104408000000001	8
1202734	342.34761175	-37.470622000000006	8
1272024	343.515018125	-34.060618749999996	8
682113	333.53701925	-33.23516275	8
385073	328.596030875	-31.97091225	8
810167	335.67838975	-27.353807749999998	8
802283	335.545567625	-23.602826375	8
65270	323.374041875	-29.50553675	8
642849	332.883595375	-22.952824125	8
668636	333.303978375	-19.7590745	8
666323	333.271967625	-16.64317925	8
374568	328.42388275	-13.291976250000001	8
2344943	1.497726142857143	-36.133999857142854	7
1995031	355.5920472857143	-36.41313371428573	7
2156613	358.319954	-34.05294057142857	7
2326345	1.1752359999999997	-30.481065142857137	7
3036158	13.430811857142857	-27.050695	7
2802452	9.306850571428571	-22.586845571428572	7
3408633	19.75983028571429	-17.061675142857144	7
2432454	2.9485859999999997	-21.908101714285714	7
2822791	9.664268285714284	-15.420218714285713	7
2872717	10.532542428571428	-14.124983857142857	7
2724366	7.939661285714288	-13.341124714285716	7
2933099	11.601324428571427	-13.441882142857143	7
1693698	350.5047941428571	-23.508972000000004	7
1610012	349.11013214285714	-22.152802	7
2092691	357.2543642857143	-19.691738142857144	7

Table B.25: SGC cluster members

ID	RA (deg)	DEC (dec)	member number
1948157	354.78774571428573	-16.925694714285715	7
1152197	341.4937777142857	-17.624771714285718	7
1825039	352.6978054285714	-13.482585	7
2334442	1.3174301428571427	-16.476172142857145	7
2581303	5.463753142857143	-9.494360285714286	7
3668828	24.16860157142857	-13.888843000000001	7
3902978	28.198462142857142	-14.274731857142857	7
522094	330.86775314285717	-10.720732142857141	7
495866	330.43602142857145	-9.895452857142857	7
5708003	59.55581928571428	-35.444508285714285	7
4336866	35.53156528571429	-34.435284857142854	7
3924168	28.572216571428573	-35.673545000000004	7
3298354	17.926291142857146	-30.028538571428573	7
3256627	17.212656999999997	-28.59942657142857	7
3582820	22.702524285714286	-27.36490657142857	7
4856534	44.758726571428575	-37.24513428571428	7
5098093	49.022153571428575	-34.362896142857146	7
5541171	56.741575	-25.519908857142855	7
5700692	59.43123857142859	-16.846927428571426	7
4067264	30.982675428571433	-23.311184285714283	7
4185029	32.984839	-20.373339714285713	7
4793144	43.64040442857143	-18.63500942857143	7
4353740	35.83022185714285	-18.83845057142857	7
4445311	37.41071371428571	-17.04402342857143	7
5098854	49.03789628571429	-10.672479714285716	7
1929002	354.45617785714285	-37.227507857142854	7
425234	329.2592484285714	-36.992172571428576	7
500097	330.50508142857143	-36.02200542857143	7
999237	338.8958207142857	-37.36280028571429	7
776201	335.105061	-32.68668171428572	7
848859	336.33722485714287	-31.354127428571427	7
1345319	344.74487928571426	-30.494662428571427	7
501071	330.515912	-31.97085714285715	7
525813	330.93546071428574	-27.79685942857143	7
974865	338.4879535714286	-25.76451857142857	7
767297	334.95650814285716	-26.341960285714283	7
808833	335.65462242857143	-21.736103857142854	7
515704	330.7619385714286	-22.51548257142857	7
800330	335.51154685714283	-19.57130857142857	7
481547	330.1788071428571	-19.810981714285717	7
181067	325.26655757142856	-16.692861142857144	7
481580	330.1863095714286	-14.881832142857144	7
2015143	355.945853	-34.9075395	6
2352347	1.6225828333333332	-31.953773	6
2563005	5.1513531666666665	-31.370095666666668	6
2685466	7.266257499999999	-30.843152499999995	6
1904477	354.031992	-32.50842933333333	6
2110977	357.55459183333335	-29.011305333333333	6
2136040	357.97885933333333	-27.930197333333336	6
2222029	359.4194763333333	-21.576509666666666	6
2877723	10.615393166666667	-23.629894833333335	6

Table B.26: SGC cluster members

ID	RA (deg)	DEC (dec)	member number
3184607	15.965928833333333	-20.609289	6
3289877	17.774305500000004	-18.14671966666667	6
2710873	7.710655000000001	-12.723998666666665	6
1586978	348.7251851666667	-20.996192666666666	6
1934716	354.55203033333333	-20.784443666666665	6
1559490	348.2648511666667	-11.856596	6
3547393	22.100705833333333	-13.570386833333336	6
3679738	24.343354166666664	-9.269056166666669	6
892078	337.0661523333333	-16.39552116666667	6
1300515	343.9980903333333	-12.368996333333333	6
714972	334.0677821666667	-9.333046	6
5520631	56.405538166666666	-9.236769666666667	6
4203983	33.30101466666667	-33.63065183333334	6
3110445	14.710622333333331	-35.118477999999996	6
3501408	21.31152366666667	-33.405313666666665	6
3589171	22.806543499999997	-26.863325999999994	6
5089863	48.8592015	-31.517015499999996	6
4426860	37.0877025	-31.87875183333334	6
5045558	48.07409616666667	-24.618979833333334	6
4703011	42.034161166666664	-22.75501566666667	6
5654220	58.63456433333333	-27.080149666666667	6
5341418	53.3615005	-23.712262333333335	6
5665254	58.81562966666666	-21.854757333333332	6
5663619	58.78892599999999	-17.470921666666666	6
5347575	53.47174766666667	-20.28236083333333	6
5012665	47.480511166666666	-20.087803	6
5201544	50.890213	-16.779046500000003	6
5458049	55.34522533333333	-17.759925499999998	6
5365843	53.778424666666666	-15.829064	6
4030249	30.37800833333334	-24.9251385	6
4304484	34.981874166666664	-21.390341333333332	6
4248897	34.04648883333333	-11.924711166666667	6
5153391	50.015108000000005	-14.000744500000001	6
4935702	46.15217133333333	-13.511263666666666	6
4633859	40.816898	-15.2640865	6
4963684	46.63570666666667	-12.380726666666664	6
4800698	43.77808316666667	-10.752186	6
5075201	48.601934666666665	-10.754963333333333	6
5025588	47.71849699999999	-9.212064500000002	6
4591120	40.032831333333334	-11.735607000000003	6
4509791	38.531333999999994	-11.038281166666668	6
4808501	43.920074666666665	-10.489065666666667	6
4606739	40.324680333333326	-9.930921	6
1359960	344.9859181666667	-34.238627666666666	6
1531977	347.8220785	-32.45032716666666	6
235802	326.17295433333334	-39.18491166666667	6
315647	327.45601266666665	-37.78410683333333	6
1058299	339.8880995	-36.40273133333333	6
430518	329.35044883333336	-31.69291083333333	6
572714	331.71154366666667	-28.9476955	6
892867	337.07217233333336	-22.434139166666668	6
202426	325.6388161666667	-29.368454166666666	6

Table B.27: SGC cluster members

ID	RA (deg)	DEC (dec)	member number
325171	327.6115245	-23.992753999999998	6
150663	324.7628398333333	-22.79053733333333	6
163261	324.97880733333335	-22.613999500000002	6
522200	330.8731915	-20.315392999999997	6
225743	326.0076603333333	-15.518637666666665	6

Appendix C

New Spectroscopically Identified QSOs

Table C.1: 272 QSO redshifts measured by 2dF in the eFEDS area, excluding those already measured by DESI or SDSS

ID	RA (deg)	Dec (deg)	r-band	redshift
J085607.338+025411.88	134.03	2.90	21.74	3.94
J085455.236+025230.38	133.73	2.87	22.35	2.25
J085435.505+025127.12	133.64	2.85	20.97	1.63
J085508.027+024707.91	133.78	2.78	21.98	2.42
J085302.197+025045.42	133.25	2.84	21.29	1.94
J085359.089+024325.12	133.49	2.72	21.95	1.72
J085434.929+022625.43	133.64	2.44	22.41	1.73
J085233.832+024936.44	133.14	2.82	19.96	0.65
J085209.596+024822.32	133.03	2.80	21.29	2.14
J085201.384+024909.72	133.00	2.81	22.04	2.08
J085209.931+024339.74	133.04	2.72	21.49	1.71
J085117.253+020031.84	132.82	2.00	20.25	0.99
J085033.499+020807.20	132.63	2.13	21.19	1.43
J085007.951+021033.30	132.53	2.17	19.58	2.15
J084912.470+023149.55	132.30	2.53	21.45	2.01
J085015.265+024455.70	132.56	2.74	21.19	1.93
J085002.889+024343.67	132.51	2.72	19.25	1.18
J084851.067+024349.50	132.21	2.73	21.96	1.62
J084852.717+024529.52	132.21	2.75	20.32	0.92
J091100.494+024213.50	137.75	2.70	20.92	1.71
J091104.574+023320.82	137.76	2.55	20.85	2.29
J090819.523+025811.85	137.08	2.96	21.74	1.94
J090811.006+024322.52	137.04	2.72	21.79	1.71
J090837.445+023125.17	137.15	2.52	21.75	2.07
J090815.291+022136.99	137.06	2.36	21.47	3.01
J090807.268+023225.98	137.03	2.54	21.19	1.86
J090748.882+025342.54	136.95	2.89	21.57	2.37
J090719.690+022930.44	136.83	2.49	21.76	3.57
J090644.637+020728.30	136.68	2.12	21.5	1.96
J090509.546+021837.18	136.28	2.31	20.88	2.10
J090546.834+023709.21	136.44	2.61	21.28	1.77
J090511.382+023610.17	136.29	2.60	19.56	1.60
J090643.974+025001.72	136.68	2.83	22.06	1.79
J090620.500+025108.03	136.58	2.85	21.79	1.63
J090555.705+025236.80	136.48	2.87	20.4	0.90
J090503.028+025335.21	136.26	2.89	21.83	2.43
J090536.767+025512.08	136.40	2.92	21.92	1.84
J090422.818+025522.51	136.09	2.92	20.89	2.47
J091848.585+021321.86	139.70	2.22	19.33	1.36
J091723.021+023542.39	139.34	2.59	20.97	1.68
J091453.918+023220.31	138.72	2.53	21.12	1.72
J091404.181+023913.00	138.51	2.65	22.14	1.83
J091310.439+023625.89	138.29	2.60	21.96	1.92
J091217.524+023312.44	138.07	2.55	21.44	1.92
J091220.247+023425.08	138.08	2.57	21.15	0.39
J091310.180+024245.33	138.29	2.71	22.39	2.43

Table C.2: QSO redshifts measured by 2dF in the eFEDS area, excluding those already measured by DESI or SDSS

ID	RA (deg)	Dec (deg)	r-band	redshift
J091217.824+024951.57	138.07	2.83	21.42	1.92
J084151.756+004407.94	130.46	0.73	18.03	0.54
J084124.917+004214.74	130.35	0.70	20.4	0.62
J084011.808+005125.05	130.04	0.85	20.16	1.40
J084229.661+010003.06	130.62	1.00	19.06	0.85
J084139.837+010235.08	130.41	1.04	20.16	2.50
J084157.449+011347.72	130.48	1.22	21.34	1.69
J084411.598+011332.99	131.04	1.22	21.24	1.90
J084427.040+010052.81	131.11	1.01	20.7	2.45
J084409.071+010205.50	131.03	1.03	22.24	2.13
J085513.845+004016.22	133.80	0.67	19.73	1.63
J085439.361+004142.52	133.66	0.69	19.27	0.43
J085429.139+002318.00	133.62	0.38	20.0	1.17
J085218.603+004200.39	133.07	0.70	19.91	1.26
J085208.870+003418.05	133.03	0.57	20.36	1.91
J085215.441+001155.39	133.06	0.19	21.27	2.42
J085151.800+002410.15	132.96	0.40	20.53	1.44
J085126.835+001342.04	132.86	0.22	17.83	1.34
J085132.429+005144.87	132.88	0.86	21.98	2.09
J084957.460+005200.12	132.48	0.86	20.88	2.42
J084948.320+005423.54	132.45	0.90	21.48	1.89
J084837.400+013241.17	132.15	1.54	21.27	2.43
J085113.085+012342.81	132.80	1.39	20.3	1.34
J085134.885+011713.26	132.89	1.28	19.44	1.29
J085145.264+011452.31	132.93	1.24	20.7	0.73
J085117.253+020031.84	132.82	2.00	20.25	0.61
J085156.140+011946.65	132.98	1.32	20.34	1.67
J085231.376+013333.42	133.13	1.55	21.19	1.47
J085307.318+014523.11	133.28	1.75	17.61	1.96
J085336.386+014659.28	133.40	1.78	19.41	0.44
J085343.322+014851.01	133.43	1.81	18.67	0.80
J085338.488+014127.87	133.41	1.69	19.15	1.94
J085424.272+014433.75	133.60	1.74	20.85	1.28
J085345.398+012754.93	133.43	1.46	20.76	1.32
J085347.486+011918.13	133.44	1.32	20.86	1.41
J085347.788+011417.33	133.44	1.23	21.12	1.53
J085429.078+012424.69	133.62	1.40	19.42	0.94
J085508.964+013113.35	133.78	1.52	19.38	1.02
J085509.154+012322.32	133.78	1.38	19.36	1.56
J085511.991+011933.25	133.79	1.32	20.96	1.01
J085422.449+011136.52	133.59	1.19	21.17	1.45
J090026.565+003109.03	135.11	0.51	21.29	1.92
J090035.675+001529.77	135.14	0.25	21.14	1.86
J085951.173+003753.40	134.96	0.63	20.73	1.02
J085806.000+001236.05	134.52	0.20	19.95	1.69
J085834.049+002339.35	134.64	0.39	19.84	1.59

Table C.3: QSO redshifts measured by 2dF in the eFEDS area, excluding those already measured by DESI or SDSS

ID	RA (deg)	Dec (deg)	r-band	redshift
J085941.004+005328.87	134.92	0.89	21.37	1.57
J085813.398+004328.37	134.55	0.72	22.03	2.40
J085759.348+004703.94	134.49	0.78	21.69	1.72
J085726.008+004507.00	134.35	0.75	20.48	1.41
J085753.296+005057.20	134.47	0.84	21.06	1.52
J085656.037+004759.17	134.23	0.79	19.36	2.41
J085650.213+005013.99	134.20	0.83	20.65	2.69
J085554.795+004821.04	133.97	0.80	20.81	1.68
J085632.345+005932.57	134.13	0.99	20.14	1.91
J085805.535+005833.52	134.52	0.97	20.88	1.20
J085802.627+010556.27	134.51	1.09	20.7	1.36
J085757.474+011541.42	134.48	1.26	20.56	1.67
J085736.692+012456.63	134.40	1.41	22.48	0.94
J085727.856+012802.23	134.36	1.46	18.05	1.36
J085725.201+012949.72	134.35	1.49	20.76	1.64
J085829.734+012522.09	134.62	1.42	19.61	2.55
J085813.071+014329.94	134.55	1.72	19.55	1.59
J085853.266+013836.36	134.72	1.64	20.54	2.10
J085839.495+015324.39	134.66	1.89	22.41	1.50
J090040.009+014355.39	135.16	1.73	19.83	2.33
J090039.774+013505.08	135.16	1.58	20.36	1.67
J090105.670+014151.05	135.27	1.69	20.03	1.87
J090144.670+015431.51	135.43	1.90	20.16	2.58
J090110.097+013810.77	135.29	1.63	21.14	0.92
J090148.914+014741.44	135.45	1.79	20.79	1.92
J090047.052+012009.70	135.19	1.33	20.9	2.60
J090207.258+014427.04	135.53	1.74	21.81	1.66
J090242.371+013955.83	135.67	1.66	22.44	2.08
J090146.630+011547.77	135.44	1.26	20.31	1.88
J090329.225+013401.38	135.87	1.56	20.35	1.80
J090314.785+010708.33	135.81	1.12	21.6	2.51
J090350.446+010645.41	135.96	1.11	22.5	0.59
J090852.210+005516.33	137.21	0.92	22.41	0.03
J091003.752+002426.59	137.51	0.40	20.77	1.54
J090852.668+003653.66	137.21	0.61	21.7	1.67
J090657.666+003105.56	136.74	0.52	22.07	2.65
J090422.509+003035.07	136.09	0.51	20.72	0.90
J090801.737+005841.70	137.00	0.98	22.34	2.03
J090548.903+010003.50	136.45	1.00	20.07	0.89
J090630.384+010905.03	136.62	1.15	21.36	1.91
J090453.390+011835.75	136.22	1.30	18.82	3.19
J090512.388+011802.20	136.30	1.31	18.82	0.25
J090452.004+012609.66	136.21	1.44	20.39	1.24
J090444.316+013436.51	136.18	1.58	19.53	0.82
J090614.370+012231.12	136.55	1.37	22.11	2.46
J090639.735+011324.48	136.66	1.22	21.3	1.49

Table C.4: QSO redshifts measured by 2dF in the eFEDS area, excluding those already measured by DESI or SDSS

ID	RA (deg)	Dec (deg)	r-band	redshift
J090611.210+013642.30	136.54	1.61	21.42	1.36
J090732.898+013740.55	136.88	1.63	20.93	0.82
J090729.984+015447.48	136.87	1.91	21.9	0.57
J090915.723+013212.18	137.31	1.53	20.49	1.66
J090941.468+011356.57	137.42	1.23	22.36	1.98
J091139.585+011608.05	137.91	1.27	19.44	0.63
J090905.059+005752.24	137.27	0.96	21.0	2.65
J091623.401+001846.77	139.09	0.31	19.27	1.34
J091533.896+013433.46	138.89	1.58	21.32	1.38
J091635.840+012330.11	139.14	1.39	20.41	0.58
J091645.025+010101.61	139.18	1.02	20.69	0.92
J084225.675-010332.74	130.60	-1.06	21.88	2.00
J084030.870-010542.25	130.12	-1.09	20.91	0.75
J084112.157-012253.37	130.30	-1.38	21.06	1.77
J084053.431-012805.92	130.22	-1.47	22.13	1.21
J083957.159-013346.40	129.98	-1.56	21.38	1.15
J083951.886-013841.64	129.96	-1.64	22.22	1.26
J083718.086-011652.58	129.32	-1.28	21.82	2.28
J083719.159-005748.37	129.32	-0.96	21.31	4.94
J083616.971-003931.78	129.07	-0.66	19.98	0.98
J083749.532-004359.89	129.45	-0.73	21.27	1.86
J083920.400-002748.62	129.83	-0.46	21.44	2.43
J084028.002-003532.13	130.11	-0.59	20.91	1.40
J084315.396-002129.37	130.81	-0.35	20.96	0.95
J084314.957-003053.54	130.81	-0.51	21.35	2.24
J085832.697-013111.15	134.63	-1.51	19.39	0.64
J085759.681-012724.41	134.49	-1.45	20.88	2.61
J085651.514-012707.85	134.21	-1.45	21.73	1.43
J085716.435-012839.05	134.31	-1.47	20.39	1.14
J085627.459-010824.88	134.11	-1.14	19.64	0.61
J085613.829-010827.79	134.05	-1.14	21.68	2.61
J085613.259-011223.88	134.05	-1.20	20.8	0.57
J085631.084-014246.82	134.12	-1.71	22.36	2.40
J085613.607-015209.65	134.05	-1.86	20.05	1.45
J085626.012-010548.42	134.10	-1.09	22.07	1.90
J085535.154-014330.41	133.89	-1.72	21.33	2.20
J085527.852-015033.84	133.86	-1.84	20.99	1.91
J085553.609-011208.53	133.97	-1.20	21.47	1.76
J085526.076-013935.57	133.85	-1.65	21.2	1.85
J085522.220-012850.80	133.84	-1.48	19.45	2.24
J085543.748-011045.65	133.93	-1.17	20.91	1.80
J085444.976-011210.53	133.68	-1.20	19.55	0.97
J085515.829-011826.18	133.81	-1.30	21.23	1.71
J085349.736-014405.22	133.45	-1.73	20.4	1.80
J085458.251-011347.14	133.74	-1.22	21.66	2.54

Table C.5: QSO redshifts measured by 2dF in the eFEDS area, excluding those already measured by DESI or SDSS

ID	RA (deg)	Dec (deg)	r-band	redshift
J085354.929-012302.50	133.47	-1.38	20.4	1.78
J085512.572-010158.97	133.80	-1.03	22.01	2.02
J085422.879-005659.71	133.59	-0.95	19.55	1.39
J085442.535-005951.12	133.67	-0.99	19.45	1.31
J085241.780-002509.19	133.17	-0.41	19.98	1.66
J085525.651-005049.32	133.85	-0.84	20.7	0.57
J085430.949-003018.02	133.62	-0.50	20.46	1.97
J085413.242-001149.47	133.55	-0.19	21.94	2.55
J085450.765-001756.27	133.71	-0.29	20.66	1.98
J085509.292-001404.46	133.78	-0.23	20.7	1.54
J085536.484-001952.53	133.90	-0.33	20.27	1.55
J085610.108-004922.93	134.04	-0.82	20.59	1.81
J085709.545-001851.85	134.28	-0.31	20.65	2.03
J085700.274-003145.75	134.25	-0.52	21.26	1.36
J085718.516-002427.83	134.32	-0.40	21.33	1.81
J085804.695-001558.91	134.51	-0.26	20.21	2.51
J085704.261-005605.89	134.26	-0.93	20.56	1.18
J085723.277-005531.09	134.34	-0.92	21.2	0.62
J085857.669-005124.50	134.74	-0.85	22.12	1.74
J085643.389-005943.47	134.18	-0.99	20.88	1.32
J091447.647-011444.13	138.69	-1.24	20.52	1.41
J091339.884-011358.17	138.41	-1.23	21.31	2.09
J091347.066-015140.58	138.44	-1.86	20.53	1.37
J091253.729-013925.09	138.22	-1.65	21.05	2.51
J091303.327-015312.27	138.26	-1.88	19.58	1.01
J091239.267-014027.80	138.16	-1.67	18.08	0.57
J091214.875-013718.97	138.06	-1.62	19.2	1.09
J091246.255-015415.06	138.19	-1.90	19.35	2.59
J091219.660-013534.59	138.08	-1.59	20.28	1.72
J091220.891-015425.90	138.08	-1.90	20.54	1.51
J091159.554-013710.84	137.99	-1.61	19.97	2.11
J091152.261-013109.90	137.96	-1.51	18.44	2.01
J091208.805-012809.86	138.03	-1.46	20.53	1.89
J091140.906-013012.28	137.92	-1.50	19.94	1.27
J091131.782-014021.66	137.88	-1.67	20.0	1.27
J091129.379-014727.07	137.87	-1.79	17.88	1.37
J091114.969-015002.94	137.81	-1.83	18.8	1.29
J085046.099-011522.59	132.69	-1.25	22.43	0.23
J084934.717-011437.54	132.39	-1.24	20.74	1.15
J084927.408-011415.80	132.36	-1.23	19.83	2.46
J084923.174-013633.36	132.34	-1.60	20.11	1.23
J084849.238-013437.92	132.20	-1.57	21.67	1.81
J084752.356-011310.76	131.96	-1.21	22.05	1.12
J084655.259-014042.15	131.73	-1.67	22.35	0.06
J084638.840-013412.01	131.66	-1.57	22.18	2.50

Table C.6: QSO redshifts measured by 2dF in the eFEDS area, excluding those already measured by DESI or SDSS

ID	RA (deg)	Dec (deg)	r-band	redshift
J084620.597-013025.33	131.58	-1.50	20.2	0.76
J084554.588-013730.61	131.47	-1.62	18.74	0.86
J084637.262-012228.67	131.65	-1.37	21.86	0.77
J084710.317-011010.19	131.79	-1.16	21.91	2.04
J084500.642-011548.84	131.25	-1.26	20.31	0.72
J084648.528-005251.47	131.70	-0.88	21.52	1.23
J084405.857-011513.01	131.02	-1.25	21.27	1.30
J084423.680-010058.92	131.09	-1.01	21.88	2.53
J084358.823-005735.67	130.99	-0.95	20.05	1.35
J084359.498-004535.60	130.99	-0.75	21.06	1.75
J084617.490-004653.76	131.57	-0.78	19.2	1.81
J084538.179-003241.06	131.40	-0.54	21.91	0.92
J084614.874-002228.90	131.56	-0.37	20.53	0.86
J084625.070-002108.72	131.60	-0.35	22.45	1.04
J084725.533-001620.48	131.85	-0.27	20.54	1.80
J084743.759-001829.15	131.93	-0.30	19.78	0.63
J084805.341-002231.94	132.02	-0.37	19.9	1.40
J084809.215-004310.99	132.03	-0.71	20.76	2.02
J084830.452-001117.64	132.12	-0.18	19.73	2.14
J084839.283-001121.39	132.16	-0.19	20.82	1.75
J084817.721-002225.82	132.07	-0.37	20.87	1.05
J084844.076-001215.51	132.18	-0.20	19.09	0.24
J084856.353-000815.67	132.23	-0.13	19.19	2.50
J084928.872-002156.16	132.37	-0.36	21.71	2.49
J085036.043-001525.29	132.65	-0.25	20.6	0.74
J085055.314-001932.83	132.73	-0.32	20.34	2.63
J084927.887-004103.35	132.36	-0.68	19.55	1.24
J085103.390-002230.94	132.76	-0.37	20.32	1.40
J085046.763-004447.20	132.69	-0.74	20.99	0.70
J084859.521-005600.48	132.24	-0.93	22.05	1.20
J092304.313-011700.67	140.76	-1.28	21.32	1.46
J092306.909-012037.42	140.77	-1.34	21.41	2.67
J092143.560-011517.78	140.43	-1.25	21.3	1.68
J092229.959-013240.84	140.62	-1.54	19.54	0.66
J092153.113-013659.19	140.47	-1.61	22.32	1.22
J092105.976-012715.58	140.27	-1.45	21.25	1.90
J092057.834-013127.13	140.24	-1.52	18.95	2.06
J091941.245-014953.55	139.92	-1.83	20.78	1.69
J091736.795-014624.80	139.40	-1.77	20.34	2.27
J091730.835-014609.30	139.37	-1.76	19.76	1.52
J091629.874-013105.77	139.12	-1.51	18.95	1.80
J091629.565-012425.08	139.12	-1.40	20.14	1.99
J091806.276-011125.61	139.52	-1.19	21.05	1.87
J091846.858-005928.97	139.69	-0.99	19.16	0.36

Appendix D

4MOST Cosmology Redshift Survey QSO Catalogue

D.1 Introduction

The 4-meter Multi-Object Spectroscopic Telescope (4MOST) will do a 5 year survey, with additional 5 year surveys planned in its future, and is designed to provide spectroscopic data covering over 17000 deg^2 of the Southern sky. Especially of interest are the possibilities for the spectroscopic data which will be gathered with 4MOST to work together with other facilities currently being built for the Southern hemisphere such as LSST. The 4MOST survey has three main science interests; cosmology and galaxy evolution, the high-energy sky, and galactic archeology. To achieve it's science goals, the survey is split into 18 main consortium surveys, each with specific scientific aims, along with an additional number of smaller community surveys (de Jong et al. (2014) de Jong et al. (2019)).

This thesis work contributes to the 4MOST Consortium Survey 8: Cosmology Redshift Survey (4CRS) through the creation and submission of the 4CRS QSO target catalogue. The main goal of 4CRS is to perform cosmological tests through spectroscopic clustering measurements of bright galaxies, luminous red galaxies (LRGs), and QSOs. We utilize the VST ATLAS QSO survey as well as an additional selection using Legacy Survey DR10 data to create the $z<2.2$ as well as the $z>2.2$ Lyα QSO target selection over the full footprint of 4CRS. This chapter we will present an introduction to the 4MOST instrument and consortium processes, the 4CRS sub-survey, and finally the QSO target catalogue we have generated for 4CRS.

D.2 4MOST Instrument

4MOST is being developed as a high-multiplex, wide-field spectroscopic survey facility for the Visible and Infrared Survey Telescope for Astronomy (VISTA) at Paranal Observatory in Chile. It has a large, 4.2 deg^2 field of view, comprised of 2436 fibers that have a fiber positioning accuracy of better than 0.2 arcseconds. Of these 2436 fibers, 1624 are low-resolution (R=$\lambda/\Delta\lambda \sim$ 6500) spectrograph fibers, amounting to approximately 400 deg^{-2}, and 812 high-resolution (R$\sim$ 20000) spectrograph fibers, amounting to $\approx$ 200 deg^{-2} (de Jong et al. (2019), Tempel et al. (2020)). The sensitivity of the instrument is such that it is capable of obtaining redshifts of r = 22.5 magnitudes (AB) galaxies and active galactic nuclei (AGN) with a 120 minute exposure time (de Jong et al. (2019)). A diagram of the instrument is shown in Figure 1 of de Jong et al. (2019) and shown here in D.1. Here we can see the main subsystems of the telescope.

The operations of 4MOST function such that all science teams submit their targets which will then be evaluated for overlaps and exposure time requirements so that multiple science teams' targets can then be observed simultaneously for greater efficiency where possible. The consortium as a whole therefore plans all of the observations and will also be reducing, analysing, and publishing the data. Each consortium sub-survey is responsible for detailing their science case and submitting mock catalogues at first (followed by real target catalogues) with a figure of merit which details the spectral success criteria required for the proposed science goals. This then enables consortium wide simulations to take place via the 4MOST Facility Simulator (4FS) (Tempel et al. (2020)). Through 4FS the ETC is calculated, fiber targets are assigned, and the 5-year survey strategy is planned.

D.3 4MOST Survey 8: Cosmology Redshift Survey

The scientific goals and survey strategy of the 4MOST Cosmology Redshift Survey are outlined in (Richard et al. (2019)), summarized here. The main aim is to test gravitational physics via lensing and to investigate the cosmological model. To do this, 4CRS is aiming to target $\approx$8 million galaxies, LRGs, and QSOs in the $0.15 < z < 3.5$ redshift range, therefore constructing a map of large scale structure across the southern sky. The main aim for the QSO survey is to support the redshifting of galaxies at redshifts $z > 1.5$, through the cross-correlation with QSOs, in order to define the galaxy n(z). Further various cosmological tests

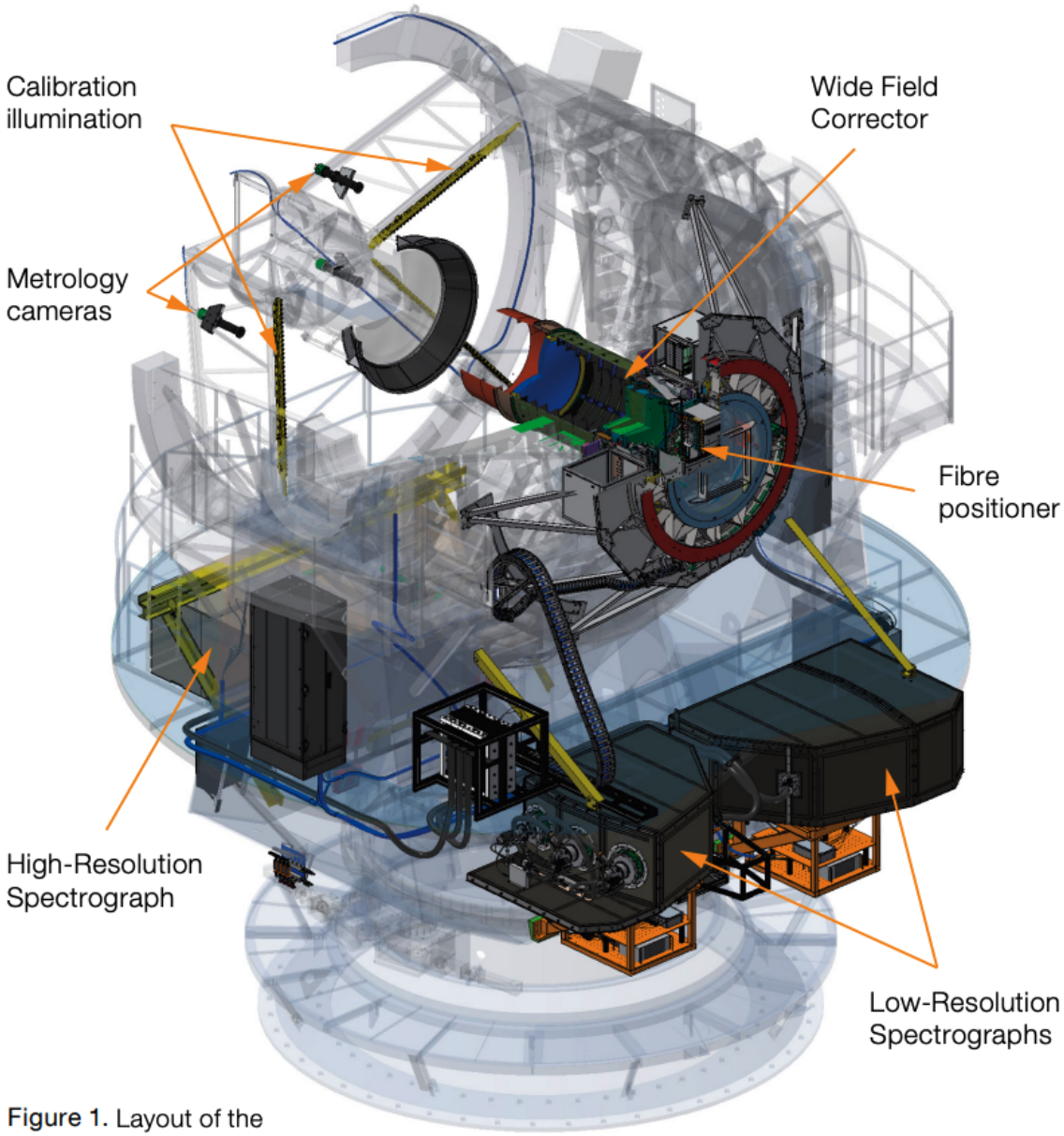

Figure 1. Layout of the different subsystems of 4MOST on the VISTA telescope.

Figure D.1: Diagram of the 4MOST instrument, taken from de Jong et al. (2019), Figure 1.

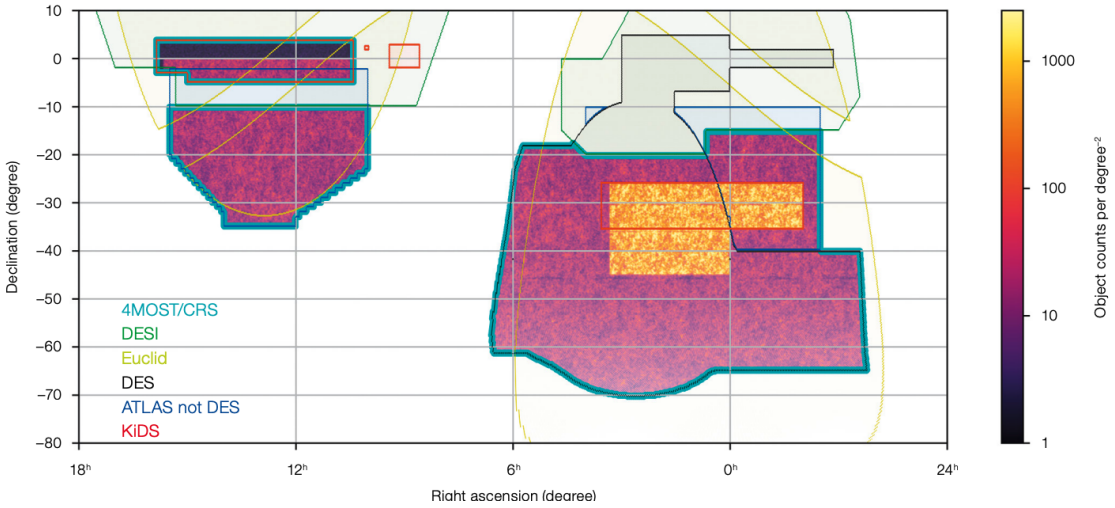

Figure D.2: A map of the overlapping surveys with the 4MOST footprint, taken from Richard et al. (2019), Figure 1.

can then also be conducted via galaxy-galaxy lensing, galaxy-QSO lensing, and the lensing of the CMB by these objects. A number of metrics can then be measured such as both the QSO and galaxy bias, galaxy peculiar velocities, and the SunyaevZel'dovich and integrated Sachs-Wolfe effects. Not only can these measurements be made on large scales, but they can be used as tests for each other, verifying results and reducing statistical uncertainties (Richard et al. (2019)). The mapping of large scale structure across the sky also lends itself to various auxiliary science such as testing BAO measurements and redshift space distortions (RSD). These science goals require multiple overlapping datasets, which the 4MOST 5-year plan is particularly suited for. As we will see in Chapter 3, weak gravitational lensing analyses are a powerful probe of the cosmological model, especially in conjunction with the overlapping imaging surveys in the southern sky, such as ATLAS, KiDS, DES, the upcoming LSST, as well as various measurements of the cosmic microwave background (e.g. Planck Collaboration et al. 2018, Madhavacheril et al. 2024). However, the largest source for error in the weak lensing analyses done with imaging data is source redshift. Therefore, this spectroscopic survey will allow for the photometric redshift to be calibrated for the the galaxies and QSOs, a map of which is shown in Figure 1 of (Richard et al. (2019)), shown here in Fig. D.2.

In order to achieve these science goals, 4CRS requested a minimum survey are of 6000 degrees, with the currently defined 4CRS footprint being 7500 deg^2, with target densities defined for each object class large enough to not be limited by Poisson noise For QSOs, a spectroscopic

success rate of greater than 50% is required. Spectroscopic success for QSOs is defined as S/N>0.7 per Angstrom.

D.4 Data

In order to cover the full 7500 deg^2 4CRS footprint, we use a combination of VST ATLAS and Legacy Survey DR10 data to create our target catalogues. As VST ATLAS has a more uniform coverage to g<22.5 in the required area, we utilize the full ∼4700deg^2 ATLAS footprint and supplement with Legacy Survey DR10 in the SGC where there is no ATLAS data.

D.4.1 VST ATLAS

We base our VST ATLAS QSO target catalogue for 4CRS on the catalogue created in Chapter 2. The submitted target catalogue also splits the targets into Priority 1, 2, and 3 candidates. Priority 1 candidates are the same targets as those in the Priority 1 subset, described in Section 2.4. These require both our UVX and mid-IR (grW) selections.

Our Priority 2 candidates are described as the grW& non-UVX selection in Section 2.4 by Equation 2.4.5. This defines a set of objects included in the white dwarf and grW selections (with W2-band detection required), but are NOT within our UVX selections.

Finally, our Priority 3 candidates are objects that were classified in Section 2.4 as extended cuts, which are designed to select targets that we believe have been (mis-)classified as galaxies. These cuts are described in Equation 2.4.6.

We utilize the catalogue described in Chapter 2 as a preliminary target catalogue, on which the candidate density and required exposure time figures, Fig. D.5, D.7, and D.6, are based. However, an updated version of this target catalogue which uses the neo8 release of the unWISE catalogue (Meisner et al., 2021), is currently being created.

D.4.2 DECaLS Legacy Survey DR10

Quasar Selection

In order to cover the full 4CRS footprint, we use data from an internal version of DECaLS Legacy Survey DR10 prior to it's public release (Dey et al. (2019b)) to create a QSO target catalogue for the area outside of the ATLAS footprint in the SGC. This data has the g-, r-, i-, and z-bands photometry in AB magnitudes as well as WISE (Wright et al. (2010)) fluxes for the W1-, and W2-bands in Vega magnitudes from the year 7 release of NEOWISE, the year 6 release of which is described in Section 2.2.1. As this catalogue does not have u-band photometry, we adapt the selections we use for VST ATLAS to create a comparable QSO catalogue.

For this DR10 target catalogue, we create one subset for the candidates as we cannot distinguish between UVX and non-UVX objects. Additionally, each object has a "Type" attributed to it for the star/galaxy separation, rather than a s/g determination made for each photometric band. To start our selections, we define our 'stellar' selection with Type="PSF". We find that this has a high density of targets and therefore do not supplement with an additional selection of objects that may have been mis-classified as an extended source. Then, we utilize EBV corrected magnitudes to make the following photometric cuts.

We define the same base selection we use for our VST ATLAS catalogue along with the grW selection:

$$\begin{aligned} & 16 < g \leq 22.5 \ \& \ -0.4 \leq (g-r) \leq 1.1 \ \& \\ & not \ [0.4385(g-r) - 0.1681 < (r-i) < 0.4385(g-r) - 0.0181 \\ & \& \ (g-r) < -0.05)] \\ & \& \ (r-W1) > 0.75(g-r) + 2.1 \end{aligned} \tag{D.4.1}$$

As with our VST ATLAS selections, we found that the W2-band restriction has a large effect on the target density as well as the depth of the catalogue. Therefore, we create one last cut requiring $(W1-W2) > 0.4$ for all objects that have a detection in W2. However, for objects that do not have a detection in W2 only the other selections are made.

Finally, we attempted to clean the catalogue using various masks that are in the catalogue, such as ANYMASK and ALLMASK (described on `https://www.legacysurvey.org/dr10/`

`bitmasks/#allmask-x-anymask-x`), and realized that the multi-exposure transient flag was removing too many actual QSOs when we looked at those positions on the legacy viewer. Therefore, we decided to use MASKBITS=0 as a data quality flag, which removes bright stars, galaxies, clusters, and saturated objects. The full 4CRS candidate catalogues are therefore also consistent throughout as this is the mask used by the other groups in 4CRS who are creating the galaxy, LRG, and ELG catalogues as well. This final selection has a target density very similar to the target density of our VST ATLAS P1, P2, and P3 selections combined. We use ANNz2 (Sadeh et al. (2016)), as described in Section 2.7, in order to determine photometric redshifts for each of our candidates.

Legacy Survey DR10 Candidate Completeness and Efficiency

We first test our DR10 target selection by comparing it to our VST ATLAS catalogue. To do this, we select an area between $30 < RA < 60$ and $-20 < DEC < -10$ where we have an overlap of the DR10 and ATLAS data as well as partial coverage by DESI spectroscopically confirmed QSOs (described in Section 2.5.1). In this area, there are 64563 ATLAS QSO candidates and 50927 DECaLS DR10 candidates, with an overlap of 30872 candidates between the two catalogues. There are 29944 ATLAS candidates that DR10 does not pick up as candidates. 80% of these are not picked up because DR10 classifies them as galaxies. Of the 14444 DR10 candidates that ATLAS doesn't select as candidates, 46% are classified as ATLAS galaxies. Of the remainder, 65% are kicked out in our initial white dwarf cut. Therefore, we note that the largest difference in the two catalogues is the star/galaxy separation that is used. Furthermore, we notice a slight difference in the photometry, with the biggest difference being in the W1- and W2-bands, as shown in Figure D.3. This difference is likely due to the forced photometry used in the DECaLS W1 and W2. From the partial spectroscopic coverage in the area, we can determine that there are 12203 ATLAS candidates and 13700 DR10 candidates that are DESI spectroscopically confirmed QSOs. Of those confirmed QSOs, ATLAS and DR10 have 9838 in common.

In order to test the spectroscopic completeness and efficiency of our sample in more detail, we select an area between $34 < RA < 40$ and $-9 < DEC < -4$, where we have full coverage of DESI spectra from the internal iron release. In this area, we have 6070 DR10 candidates. There is a match of 4299 DESI spectroscopically confirmed QSOs when performing a one to one match with all objects in the DR10 catalogue in the $16 < g < 22.5$ magnitude

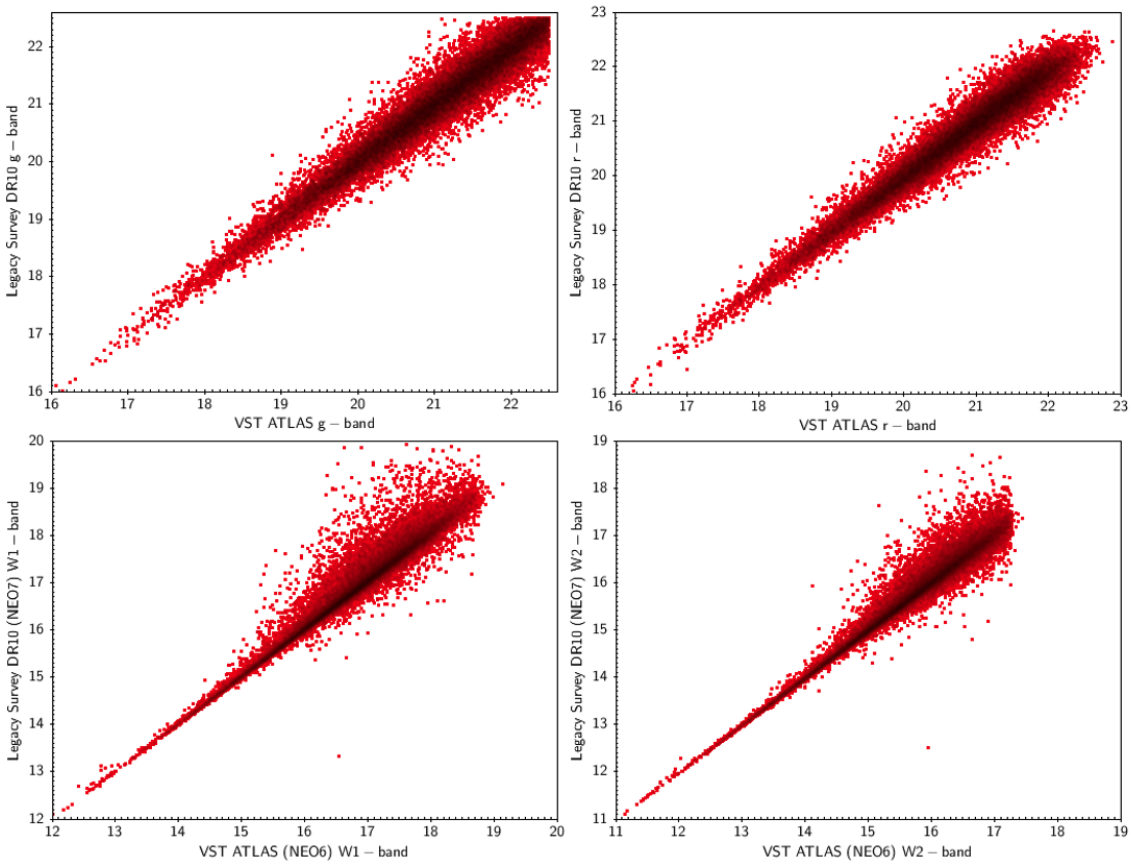

Figure D.3: A comparison of the Legacy Survey DR10 and VST ATLAS photometry in the g- and r-band along with the neo6 and neo7 versions of the NEOWISE W1- and W2-band.

range. Of these 4299 QSOs, our selections pick up 3570 objects, giving us 83% spectroscopic completeness with respect to DESI. Of the 729 objects that our selections don't pick up, 51% are thrown out due to not being classified as a point source by DR10. To check the contamination in our sample, we also match our candidate list to the list of DESI objects that have non-QSO spectra. We find a match to 240 non-QSO objects, indicating a mimimum contamination of 4%.

D.5 Final Catalogue

We combine our full VST ATLAS candidate catalogue and the Legacy Survey DR10 target catalogue in the SGC area not covered by ATLAS to create the 4CRS QSO candidate catalogue over the full target area. This gives a total of 1,755,327 candidates with a target density of approximately 204 deg^{-2}, with the full redshift distribution of the candidates shown in Figure D.4. This catalogue is then divided as 4CRS requires two separate catalogues, one

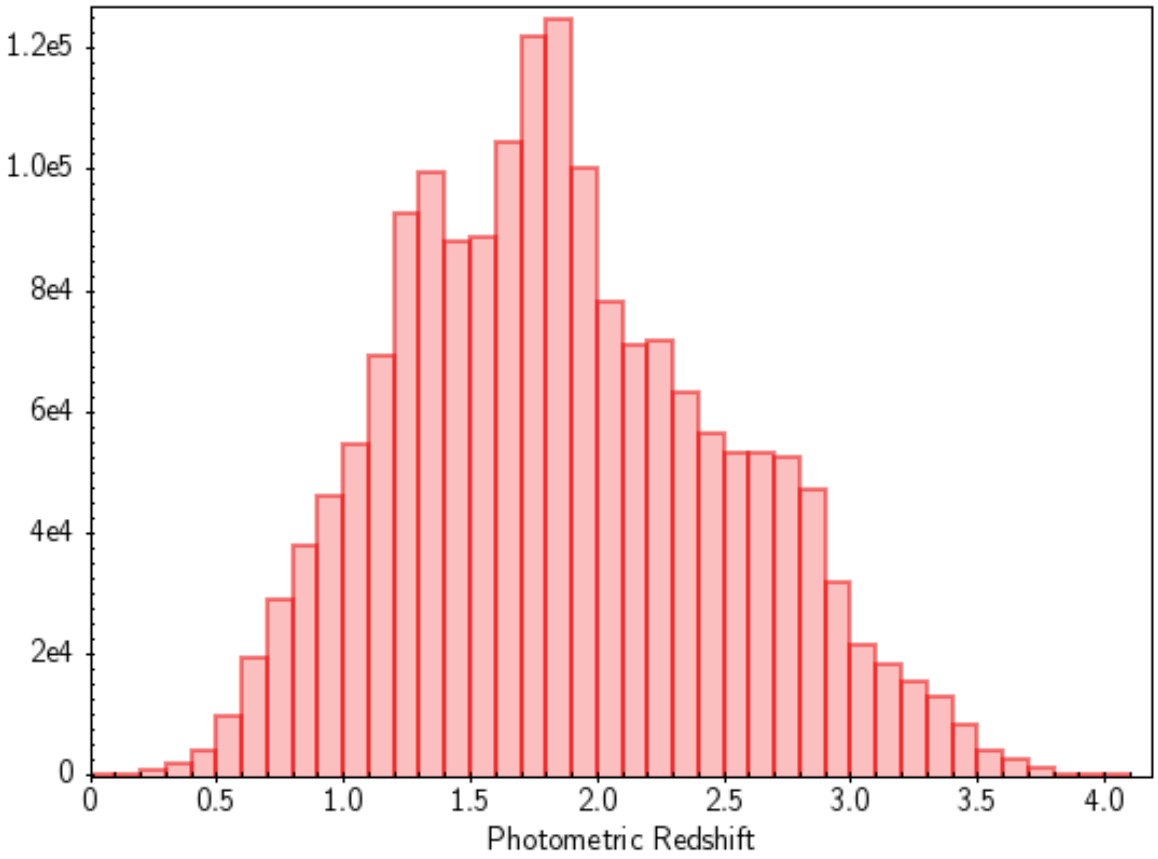

Figure D.4: Photometric redshift distribution of the full 4CRS QSO sample.

for objects at redshifts z<2.2 and one for the Lyα QSOs at redshifts z>2.2, for the various science cases. The z<2.2 tracer QSO candidate catalogue (labeled S0803) has a total of 1,241,574 candidates with a target density of approximately 145 deg^{-2}. The Lyα QSO candidate catalogue (labeled S0804) has a total of 513,753 candidates with a target density of approximately 60 deg^{-2}. The density of targets in both catalogues are shown in Figure D.5. We do notice an increase in candidates near the galactic plane and near the Large Magellenic Cloud (LMC), especially for our Lyα QSO candidate sample at redshifts of z>2.2, which can be seen in Figure D.5b. This is likely due to an increased star contamination in those areas. In Chapter 2, we mention the extensive work done to try to reduce contamination due to the galactic plane through various colour selections and especially via adjustments to the star/galaxy separation based on seeing for VST ATLAS. However, some contamination is expected, especially at higher redshifts and closer to the photometric limit of g<22.5. The exposure times required to achieve spectroscopic success rate for the candidates are calculated using 4FS and shown in Figures D.6 and D.7.

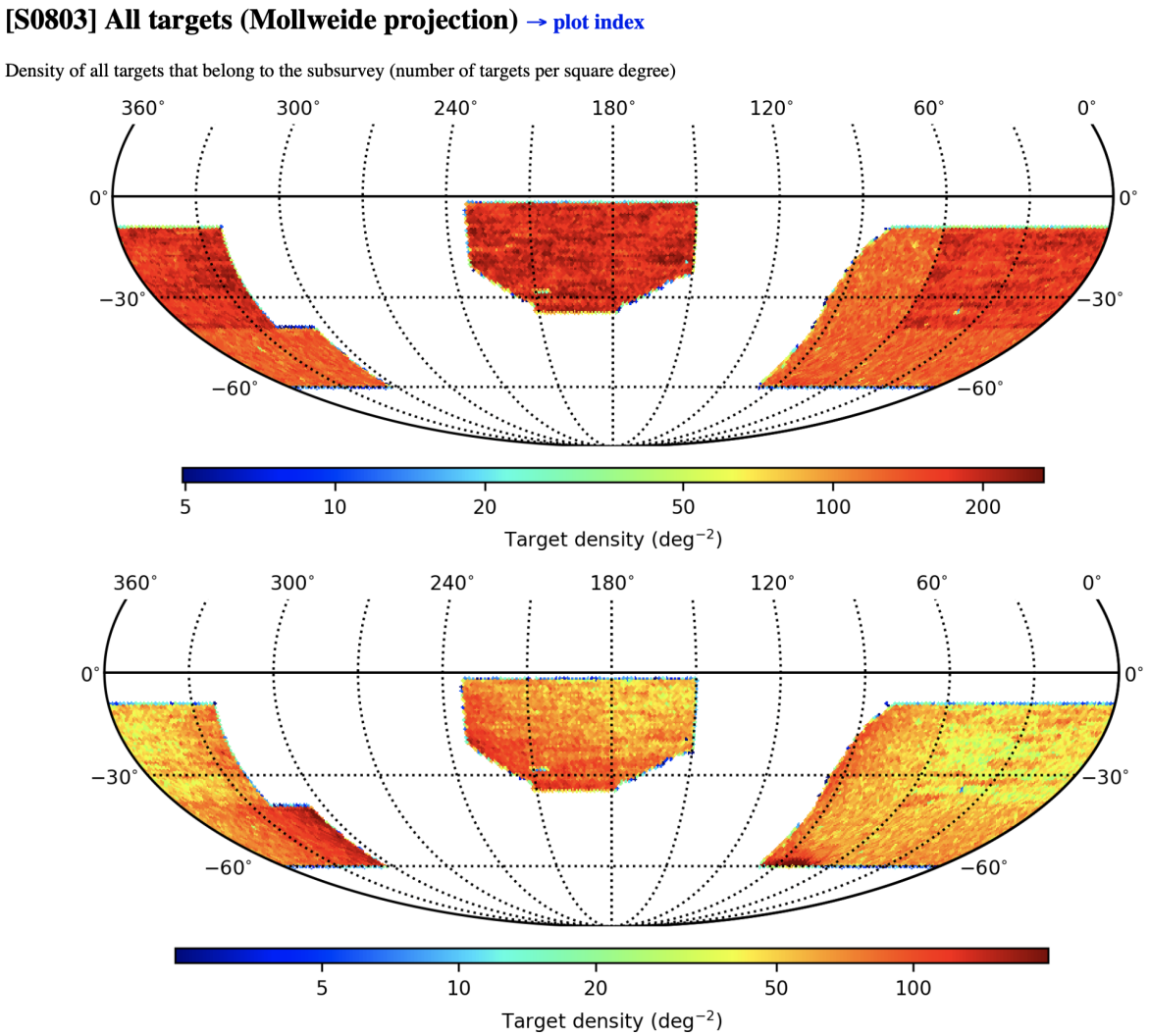

Figure D.5: (a) Map of the $z < 2.2$ quasar candidate density over the full 4CRS footprint. (b) Map of the $z > 2.2$ Lyα quasar candidate density over the full 4CRS footprint.

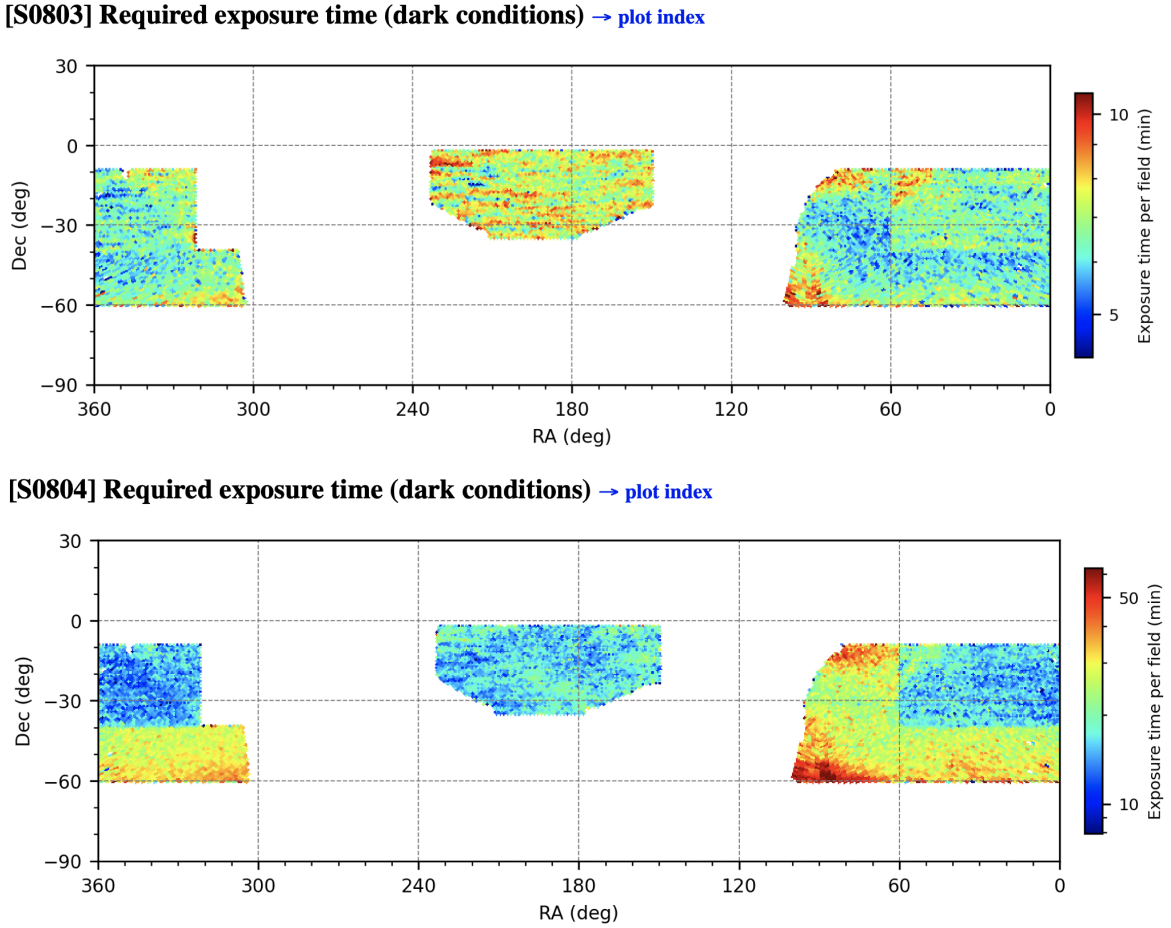

Figure D.6: (a) Map of the $z < 2.2$ quasar candidate exposure time (dark conditions) over the full 4CRS footprint. (b) Map of the $z > 2.2$ Lyα quasar candidate exposure time (dark conditions) over the full 4CRS footprint.

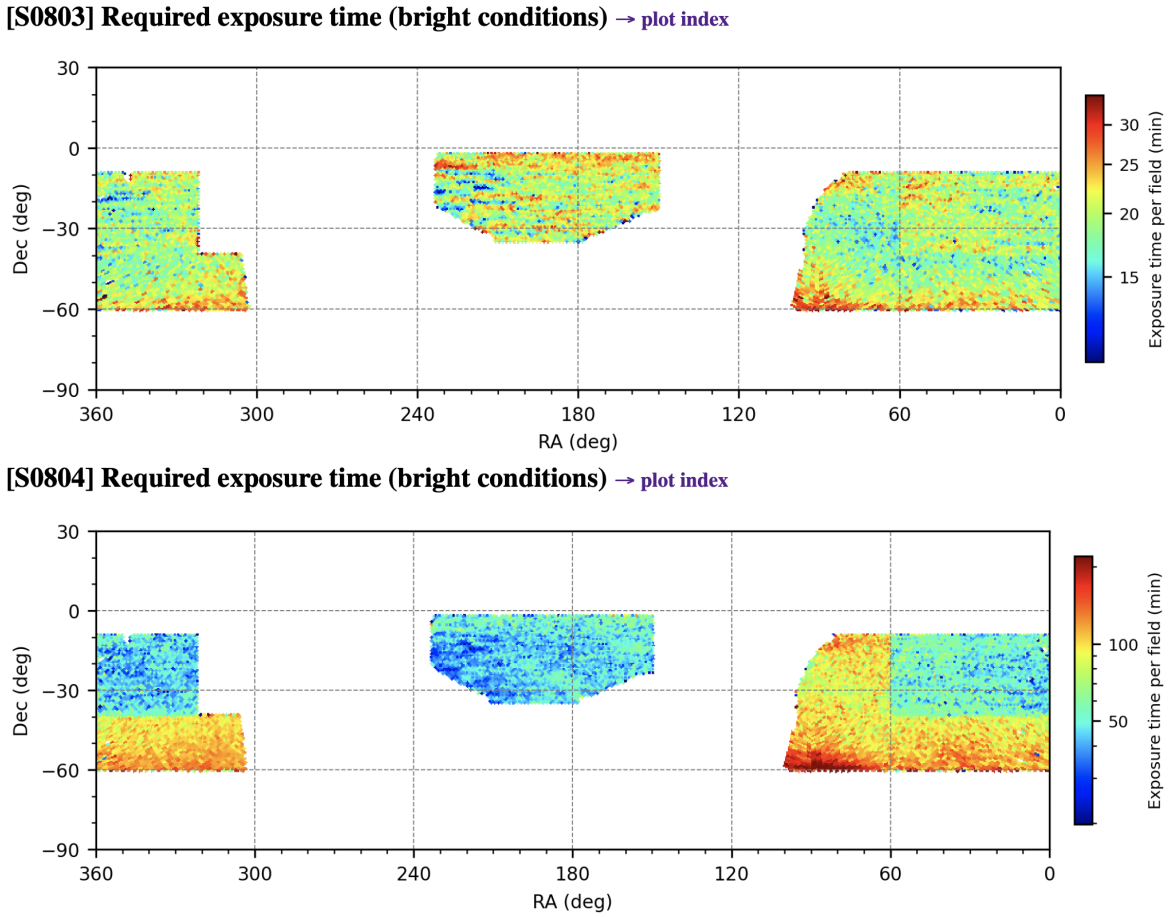

Figure D.7: (a) Map of the $z < 2.2$ quasar candidate exposure time (bright conditions) over the full 4CRS footprint. (b) Map of the $z > 2.2$ Lyα quasar candidate exposure time (bright conditions) over the full 4CRS footprint.

Bibliography

Ahumada, R., Allende Prieto, C., Almeida, A., et al. *The 16th Data Release of the Sloan Digital Sky Surveys: First Release from the APOGEE-2 Southern Survey and Full Release of eBOSS Spectra.* ApJS, **249**(1) (2020), 3. 1912.02905.

Aird, J., Coil, A.L., Moustakas, J., et al. *PRIMUS: The Dependence of AGN Accretion on Host Stellar Mass and Color.* ApJ, **746**(1) (2012), 90. 1107.4368.

Alam, S., Albareti, F.D., Allende Prieto, C., et al. *The Eleventh and Twelfth Data Releases of the Sloan Digital Sky Survey: Final Data from SDSS-III.* ApJS, **219**(1) (2015), 12. 1501.00963.

Alexander, D.M., Davis, T.M., Chaussidon, E., et al. *The DESI Survey Validation: Results from Visual Inspection of the Quasar Survey Spectra.* arXiv e-prints (2022), arXiv:2208.08517. 2208.08517.

Alexander, D.M., Hickox, R.C. *What drives the growth of black holes?* New A Rev., **56**(4) (2012), 93. 1112.1949.

Alonso, D. *CUTE solutions for two-point correlation functions from large cosmological datasets.* arXiv e-prints (2012), arXiv:1210.1833. 1210.1833.

Ansarinejad, B., Murphy, D., Shanks, T., et al. *VST ATLAS galaxy cluster catalogue I: cluster detection and mass calibration.* MNRAS, **520**(1) (2023), 1371. 2207.03725.

Ansarinejad, B., Murphy, D.N.A., Shanks, T., et al. *VST ATLAS Galaxy Cluster Catalogue I: cluster detection and mass calibration.* arXiv e-prints (2022), arXiv:2207.03725. 2207.03725.

Antonucci, R. *Unified models for active galactic nuclei and quasars.* ARA&A, **31** (1993), 473.

Bahcall, N.A., Cen, R. *Galaxy Clusters and Cold Dark Matter: A Low-Density Unbiased Universe?* ApJ, **398** (1992), L81.

Bahcall, N.A., Cen, R. *The Mass Function of Clusters of Galaxies.* ApJ, **407** (1993), L49.

Baldry, I.K., Robotham, A.S.G., Hill, D.T., et al. *Galaxy And Mass Assembly (GAMA): the input catalogue and star-galaxy separation.* MNRAS, **404**(1) (2010), 86. 0910.5120.

Beckmann, V., Shrader, C.R. *The AGN phenomenon: open issues* (2013). 1302.1397.

Berlind, A.A., Weinberg, D.H., Benson, A.J., et al. *The Halo Occupation Distribution and the Physics of Galaxy Formation.* ApJ, **593**(1) (2003), 1. astro-ph/0212357.

Bertin, E., Arnouts, S. *SExtractor: Software for source extraction.* A&AS, **117** (1996), 393.

Bielby, R.M., Hill, M.D., Metcalfe, N., et al. *Submillimetre observations of X-ray active galactic nuclei in the William Herschel Deep Field.* MNRAS, **419**(2) (2012), 1315. 1108.3934.

Blandford, R.D., McKee, C.F. *Reverberation mapping of the emission line regions of Seyfert galaxies and quasars.* ApJ, **255** (1982), 419.

Boyle, B.J., Croom, S.M., Shanks, T., et al. *The 2dF QSO Redshift Survey.* In N. Metcalfe, T. Shanks, editors, *A New Era in Cosmology*, volume 283 of *Astronomical Society of the Pacific Conference Series* (2002), page 72.

Boyle, B.J., Fong, R., Shanks, T. *On the correlation of UVX QSOs with galaxies.* MNRAS, **231** (1988a), 897.

Boyle, B.J., Shanks, T., Georgantopoulos, I., et al. *A Deep ROSAT Survey - Part Four - the Evolution of X-Ray Selected QSOS.* MNRAS, **271** (1994), 639. astro-ph/9410078.

Boyle, B.J., Shanks, T., Peterson, B.A. *The evolution of optically selected QSOs - II.* MNRAS, **235** (1988b), 935.

Broadhurst, T.J., Taylor, A.N., Peacock, J.A. *Mapping Cluster Mass Distributions via Gravitational Lensing of Background Galaxies.* ApJ, **438** (1995), 49. astro-ph/9406052.

Brunner, H., Liu, T., Lamer, G., et al. *The eROSITA Final Equatorial Depth Survey (eFEDS). X-ray catalogue.* A&A, **661** (2022), A1. 2106.14517.

Bullock, J.S., Kolatt, T.S., Sigad, Y., et al. *Profiles of dark haloes: evolution, scatter and environment.* MNRAS, **321**(3) (2001), 559. astro-ph/9908159.

Cackett, E.M., Gelbord, J., Barth, A.J., et al. *AGN STORM 2. IV. Swift X-Ray and Ultraviolet/Optical Monitoring of Mrk 817.* ApJ, **958**(2) (2023), 195. 2306.17663.

Cackett, E.M., Gelbord, J., Li, Y.R., et al. *Supermassive Black Holes with High Accretion Rates in Active Galactic Nuclei. XI. Accretion Disk Reverberation Mapping of Mrk 142.* ApJ, **896**(1) (2020), 1. 2005.03685.

Capaccioli, M., Schipani, P. *The VLT Survey Telescope Opens to the Sky: History of a Commissioning.* The Messenger, **146** (2011), 2.

Chaussidon, E., Yèche, C., Palanque-Delabrouille, N., et al. *Angular clustering properties of the DESI QSO target selection using DR9 Legacy Imaging Surveys.* MNRAS, **509**(3) (2022a), 3904. 2108.03640.

Chaussidon, E., Yèche, C., Palanque-Delabrouille, N., et al. *Target Selection and Validation of DESI Quasars.* arXiv e-prints (2022b), arXiv:2208.08511. 2208.08511.

Chehade, B., Shanks, T., Findlay, J., et al. *The 2QDES Pilot: the luminosity and redshift dependence of quasar clustering.* MNRAS, **459**(2) (2016), 1179. 1603.04849.

Colless, M., Dalton, G., Maddox, S., et al. *The 2dF Galaxy Redshift Survey: spectra and redshifts.* MNRAS, **328**(4) (2001), 1039. astro-ph/0106498.

Croom, S.M. Ph.D. thesis, - (1997).

Croom, S.M., Boyle, B.J., Shanks, T., et al. *The 2dF QSO Redshift Survey - XIV. Structure and evolution from the two-point correlation function.* MNRAS, **356**(2) (2005), 415. astro-ph/0409314.

Croom, S.M., Richards, G.T., Shanks, T., et al. *The 2dF-SDSS LRG and QSO Survey: the spectroscopic QSO catalogue.* MNRAS, **392**(1) (2009), 19. 0810.4955.

Croom, S.M., Smith, R.J., Boyle, B.J., et al. *The 2dF QSO Redshift Survey - V. The 10k catalogue.* MNRAS, **322**(4) (2001), L29. astro-ph/0104095.

Croom, S.M., Smith, R.J., Boyle, B.J., et al. *The 2dF QSO Redshift Survey - XII. The spectroscopic catalogue and luminosity function.* MNRAS, **349**(4) (2004), 1397. astro-ph/0403040.

Czerny, B., Nikołajuk, M., Różańska, A., et al. *Universal spectral shape of high accretion rate AGN.* A&A, **412** (2003), 317. astro-ph/0309242.

Dark Energy Survey Collaboration, Abbott, T., Abdalla, F.B., et al. *The Dark Energy Survey: more than dark energy – an overview.* MNRAS, **460**(2) (2016), 1270. ISSN 0035-8711. https://academic.oup.com/mnras/article-pdf/460/2/1270/8117541/stw641.pdf.

Dawson, K.S., Kneib, J.P., Percival, W.J., et al. *The SDSS-IV Extended Baryon Oscillation Spectroscopic Survey: Overview and Early Data.* AJ, **151**(2) (2016), 44. 1508.04473.

Dawson, K.S., Schlegel, D.J., Ahn, C.P., et al. *The Baryon Oscillation Spectroscopic Survey of SDSS-III.* AJ, **145**(1) (2013), 10. 1208.0022.

de Jong, J.T.A., Verdoes Kleijn, G.A., Kuijken, K.H., et al. *The Kilo-Degree Survey.* Experimental Astronomy, **35**(1-2) (2013), 25. 1206.1254.

de Jong, R.S., Agertz, O., Berbel, A.A., et al. *4MOST: Project overview and information for the First Call for Proposals.* The Messenger, **175** (2019), 3. 1903.02464.

de Jong, R.S., Barden, S., Bellido-Tirado, O., et al. *4MOST: 4-metre Multi-Object Spectroscopic Telescope.* In S.K. Ramsay, I.S. McLean, H. Takami, editors, *Ground-based and Airborne Instrumentation for Astronomy V*, volume 9147 of *Society of Photo-Optical Instrumentation Engineers (SPIE) Conference Series* (2014), page 91470M.

DESI Collaboration, Aghamousa, A., Aguilar, J., et al. *The DESI Experiment Part I: Science,Targeting, and Survey Design.* arXiv e-prints (2016), arXiv:1611.00036. 1611.00036.

Dey, A., Schlegel, D.J., Lang, D., et al. *Overview of the DESI Legacy Imaging Surveys.* AJ, **157**(5) (2019a), 168. 1804.08657.

Dey, A., Schlegel, D.J., Lang, D., et al. *Overview of the DESI Legacy Imaging Surveys.* AJ, **157**(5) (2019b), 168. 1804.08657.

Diehl, H.T., Dark Energy Survey Collaboration. *The Dark Energy Survey & Camera (DECam).* In *American Astronomical Society Meeting Abstracts #219*, volume 219 of *American Astronomical Society Meeting Abstracts* (2012), page 413.05.

Driver, S.P., Hill, D.T., Kelvin, L.S., et al. *Galaxy and Mass Assembly (GAMA): survey diagnostics and core data release.* MNRAS, **413**(2) (2011), 971. 1009.0614.

Edelson, R., Gelbord, J., Cackett, E., et al. *The First Swift Intensive AGN Accretion Disk Reverberation Mapping Survey.* ApJ, **870**(2) (2019), 123. 1811.07956.

Efstathiou, G., Rosenberg, E., Poulin, V. *Improved Planck constraints on axion-like early dark energy as a resolution of the Hubble tension.* arXiv e-prints (2023), arXiv:2311.00524. 2311.00524.

Eftekharzadeh, S., Myers, A.D., White, M., et al. *Clustering of intermediate redshift quasars using the final SDSS III-BOSS sample.* MNRAS, **453**(3) (2015), 2779. 1507.08380.

Einstein, A. *Die Grundlage der allgemeinen Relativitätstheorie.* Annalen der Physik, **354**(7) (1916), 769.

Einstein, A. *Kosmologische Betrachtungen zur allgemeinen Relativitätstheorie.* Sitzungsberichte der Königlich Preussischen Akademie der Wissenschaften (1917), 142.

Eisenstein, D.J., Annis, J., Gunn, J.E., et al. *Spectroscopic Target Selection for the Sloan Digital Sky Survey: The Luminous Red Galaxy Sample.* AJ, **122**(5) (2001), 2267. astro-ph/0108153.

Event Horizon Telescope Collaboration, Akiyama, K., Alberdi, A., et al. *First M87 Event Horizon Telescope Results. I. The Shadow of the Supermassive Black Hole.* ApJ, **875**(1) (2019), L1. 1906.11238.

Ferrarese, L. *Beyond the Bulge: A Fundamental Relation between Supermassive Black Holes and Dark Matter Halos.* ApJ, **578**(1) (2002), 90. astro-ph/0203469.

Fine, S., Shanks, T., Croom, S.M., et al. *Composite reverberation mapping.* MNRAS, **427**(4) (2012), 2701. 1205.1401.

Fine, S., Shanks, T., Green, P., et al. *Stacked reverberation mapping.* MNRAS, **434** (2013), L16. 1305.1803.

Flaugher, B., Diehl, H.T., Honscheid, K., et al. *The Dark Energy Camera.* AJ, **150**(5) (2015), 150. 1504.02900.

Friedmann, A. *Über die Krümmung des Raumes.* Zeitschrift fur Physik, **10** (1922), 377.

Fry, J.N. *The Evolution of Bias.* ApJ, **461** (1996), L65.

Gaia Collaboration, Brown, A.G.A., Vallenari, A., et al. *Gaia Data Release 2. Summary of the contents and survey properties.* A&A, **616** (2018), A1. 1804.09365.

Geach, J.E., Peacock, J.A. *Cluster richness-mass calibration with cosmic microwave background lensing.* Nature Astronomy, **1** (2017), 795. 1707.09369.

Geach, J.E., Peacock, J.A., Myers, A.D., et al. *The Halo Mass of Optically Luminous Quasars at $z \approx$ 1-2 Measured via Gravitational Deflection of the Cosmic Microwave Background.* ApJ, **874**(1) (2019), 85. 1902.06955.

Gierliński, M., Done, C. *Is the soft excess in active galactic nuclei real?* MNRAS, **349**(1) (2004), L7. astro-ph/0312271.

González-Solares, E.A., Walton, N.A., Greimel, R., et al. *Initial data release from the INT Photometric Hα Survey of the Northern Galactic Plane (IPHAS).* MNRAS, **388** (2008), 89. 0712.0384.

Hahn, C., Wilson, M.J., Ruiz-Macias, O., et al. *DESI Bright Galaxy Survey: Final Target Selection, Design, and Validation.* arXiv e-prints (2022), arXiv:2208.08512. 2208.08512.

Han, J., Ferraro, S., Giusarma, E., et al. *Probing gravitational lensing of the CMB with SDSS-IV quasars.* MNRAS, **485**(2) (2019), 1720. 1809.04196.

Harrison, C. *Observational constraints on the influence of active galactic nuclei on the evolution of galaxies.* Ph.D. thesis, Durham University, UK (2014).

Heymans, C., Tröster, T., Asgari, M., et al. *KiDS-1000 Cosmology: Multi-probe weak gravitational lensing and spectroscopic galaxy clustering constraints.* A&A, **646** (2021), A140. 2007.15632.

Hickox, R.C., Alexander, D.M. *Obscured Active Galactic Nuclei.* ARA&A, **56** (2018), 625. 1806.04680.

Hinton, S., Davis, T., Lidman, C., et al. *MARZ: Manual and Automatic Redshifting Software.* Astronomy and Computing, **15** (2016).

Hinton, S.R., Davis, T.M., Lidman, C., et al. *MARZ: Manual and automatic redshifting software.* Astronomy and Computing, **15** (2016), 61. 1603.09438.

Honscheid, K., DePoy, D.L. *The Dark Energy Camera (DECam).* arXiv e-prints (2008), arXiv:0810.3600. 0810.3600.

Hoormann, J.K., Martini, P., Davis, T.M., et al. *C IV black hole mass measurements with the Australian Dark Energy Survey (OzDES).* MNRAS, **487**(3) (2019), 3650. 1902.04206.

Hubble, E. *A Relation between Distance and Radial Velocity among Extra-Galactic Nebulae.* Proceedings of the National Academy of Science, **15**(3) (1929), 168.

Ilbert, O., McCracken, H.J., Le Fèvre, O., et al. *Mass assembly in quiescent and star-forming galaxies since z 4 from UltraVISTA.* A&A, **556** (2013), A55. 1301.3157.

Jain, B., Scranton, R., Sheth, R.K. *Quasar-galaxy and galaxy-galaxy cross-correlations: model predictions with realistic galaxies.* MNRAS, **345**(1) (2003), 62. astro-ph/0304203.

Kaiser, N. *On the spatial correlations of Abell clusters.* ApJ, **284** (1984), L9.

Kaiser, N. *Clustering in real space and in redshift space.* MNRAS, **227** (1987), 1.

Kaiser, N. *Weak Lensing and Cosmology.* ApJ, **498**(1) (1998), 26. astro-ph/9610120.

Kaiser, N., Squires, G. *Mapping the dark matter with weak gravitational lensing.* ApJ, **404** (1993), 441.

Kaspi, S., Maoz, D., Netzer, H., et al. *The Relationship between Luminosity and Broad-Line Region Size in Active Galactic Nuclei.* ApJ, **629**(1) (2005), 61. astro-ph/0504484.

Kaspi, S., Smith, P.S., Netzer, H., et al. *Reverberation Measurements for 17 Quasars and the Size-Mass-Luminosity Relations in Active Galactic Nuclei.* ApJ, **533**(2) (2000), 631. astro-ph/9911476.

Kirshner, R.P. *Hubble's diagram and cosmic expansion.* Proceedings of the National Academy of Science, **101**(1) (2004), 8.

Kuijken, K. *OmegaCAM: ESO's Newest Imager.* The Messenger, **146** (2011), 8.

Kuijken, K., Bender, R., Cappellaro, E., et al. *OmegaCAM: the 16k×16k CCD camera for the VLT survey telescope.* The Messenger, **110** (2002), 15.

Landy, S.D., Szalay, A.S. *Bias and Variance of Angular Correlation Functions.* ApJ, **412** (1993), 64.

Lewis, I.J., Cannon, R.D., Taylor, K., et al. *The Anglo-Australian Observatory 2dF facility.* MNRAS, **333**(2) (2002), 279. astro-ph/0202175.

Limber, D.N. *The Analysis of Counts of the Extragalactic Nebulae in Terms of a Fluctuating Density Field.* ApJ, **117** (1953), 134.

Liu, T., Buchner, J., Nandra, K., et al. *The eROSITA Final Equatorial-Depth Survey (eFEDS). The AGN catalog and its X-ray spectral properties.* A&A, **661** (2022), A5. 2106.14522.

Longair, M.S. *On the interpretation of radio source counts.* MNRAS, **133** (1966), 421.

Lynden-Bell, D., Rees, M.J. *On quasars, dust and the galactic centre.* MNRAS, **152** (1971), 461.

Lynds, R., Petrosian, V. *Giant Luminous Arcs in Galaxy Clusters.* In *Bulletin of the American Astronomical Society*, volume 18 (1986), page 1014.

Madhavacheril, M.S., Qu, F.J., Sherwin, B.D., et al. *The Atacama Cosmology Telescope: DR6 Gravitational Lensing Map and Cosmological Parameters.* ApJ, **962**(2) (2024), 113. 2304.05203.

Malik, U., Sharp, R., Penton, A., et al. *OzDES Reverberation Mapping Program: Hβ lags from the 6-yr survey.* MNRAS, **520**(2) (2023), 2009. 2210.03977.

Marshall, H.L. *The evolution of optically selected quasars with Z < 2.2 and B <20.* ApJ, **299** (1985), 109.

Martini, P., Weinberg, D.H. *Quasar Clustering and the Lifetime of Quasars.* ApJ, **547**(1) (2001), 12. astro-ph/0002384.

McFarland, J.P., Verdoes-Kleijn, G., Sikkema, G., et al. *The Astro-WISE optical image pipeline. Development and implementation.* Experimental Astronomy, **35**(1-2) (2013), 45.

Mead, A.J., Verde, L. *Including beyond-linear halo bias in halo models.* MNRAS, **503**(2) (2021), 3095. 2011.08858.

Meisner, A.M., Lang, D., Schlafly, E.F., et al. *Full-sky unWISE Coadds at Seven Years' Depth.* Research Notes of the American Astronomical Society, **5**(9) (2021), 200.

Ménard, B., Wild, V., Nestor, D., et al. *Probing star formation across cosmic time with absorption-line systems.* MNRAS, **417**(2) (2011), 801. 0912.3263.

Merloni, A., Predehl, P., Becker, W., et al. *eROSITA Science Book: Mapping the Structure of the Energetic Universe.* arXiv e-prints (2012), arXiv:1209.3114. 1209.3114.

Metcalfe, N., Shanks, T., Campos, A., et al. *Galaxy number counts - V. Ultradeep counts: the Herschel and Hubble Deep Fields.* MNRAS, **323** (2001), 795. astro-ph/0010153.

Metcalfe, N., Shanks, T., Weilbacher, P.M., et al. *Galaxy number counts - VI. An H-band survey of the Herschel Deep Field.* MNRAS, **370** (2006), 1257. astro-ph/0509540.

Mountrichas, G., Sawangwit, U., Shanks, T., et al. *QSO-LRG two-point cross-correlation function and redshift-space distortions.* MNRAS, **394**(4) (2009), 2050. 0801.1816.

Mountrichas, G., Shanks, T. *QSO lensing magnification: a comparison of 2QZ and Sloan Digital Sky Survey results.* MNRAS, **380**(1) (2007), 113. astro-ph/0701870.

Murphy, D.N.A., Geach, J.E., Bower, R.G. *ORCA: The Overdense Red-sequence Cluster Algorithm.* MNRAS, **420**(3) (2012), 1861. 1109.3182.

Murray, S.G., Diemer, B., Chen, Z., et al. *THEHALOMOD: An online calculator for the halo model.* Astronomy and Computing, **36** (2021), 100487. 2009.14066.

Myers, A.D., Moustakas, J., Bailey, S., et al. *The Target Selection Pipeline for the Dark Energy Spectroscopic Instrument.* arXiv e-prints (2022), arXiv:2208.08518. 2208.08518.

Myers, A.D., Outram, P.J., Shanks, T., et al. *The 2dF QSO Redshift Survey - X. Lensing of background QSOs by galaxy groups.* MNRAS, **342**(2) (2003), 467. astro-ph/0211624.

Myers, A.D., Outram, P.J., Shanks, T., et al. *On statistical lensing and the anticorrelation between 2dF QSOs and foreground galaxies.* MNRAS, **359**(2) (2005), 741. astro-ph/0502481.

Myers, A.D., Palanque-Delabrouille, N., Prakash, A., et al. *The SDSS-IV Extended Baryon Oscillation Spectroscopic Survey: Quasar Target Selection.* ApJS, **221**(2) (2015), 27. 1508.04472.

Narayan, R. *Gravitational Lensing and Quasar-Galaxy Correlations.* ApJ, **339** (1989), L53.

Narayan, R., Nityananda, R. *Gravitational Lenses-The Multiple Scattering Limit.* In V.K. Kapahi, editor, *Extragalactic Energetic Sources* (1985), page 149.

Navarro, J.F., Frenk, C.S., White, S.D.M. *The Structure of Cold Dark Matter Halos.* ApJ, **462** (1996), 563. astro-ph/9508025.

Netzer, H. *Continuum reverberation mapping and a new lag-luminosity relationship for AGN.* MNRAS, **509**(2) (2022), 2637. 2110.05512.

Neustadt, J.M.M., Kochanek, C.S., Montano, J., et al. *AGN STORM 2. VI. Mapping Temperature Fluctuations in the Accretion Disk of Mrk 817.* ApJ, **961**(2) (2024), 219. 2310.01497.

Padovani, P. *Active Galactic Nuclei at all wavelengths and from all angles.* Frontiers in Astronomy and Space Sciences, **4** (2017), 35.

Palanque-Delabrouille, N., Magneville, C., Yèche, C., et al. *The extended Baryon Oscillation Spectroscopic Survey: Variability selection and quasar luminosity function.* A&A, **587** (2016), A41. 1509.05607.

Peacock, J.A. *Cosmological Physics* (1999).

Peebles, P.J.E. *The Gravitational-Instability Picture and the Nature of the Distribution of Galaxies.* ApJ, **189** (1974), L51.

Peebles, P.J.E. *The large-scale structure of the universe* (1980).

Peterson, B.M. *Variability of Active Galactic Nuclei.* In I. Aretxaga, D. Kunth, R. Mújica, editors, *Advanced Lectures on the Starburst-AGN* (2001), page 3. astro-ph/0109495.

Peterson, B.M. *Black hole masses from reverberation measurements.* In T. Storchi-Bergmann, L.C. Ho, H.R. Schmitt, editors, *The Interplay Among Black Holes, Stars and ISM in Galactic Nuclei*, volume 222 (2004), pages 15–20. astro-ph/0404539.

Petter, G.C., Hickox, R.C., Alexander, D.M., et al. *Host Dark Matter Halos of SDSS Red and Blue Quasars: No Significant Difference in Large-scale Environment.* ApJ, **927**(1) (2022), 16. 2201.07803.

Petter, G.C., Hickox, R.C., Alexander, D.M., et al. *Host Dark Matter Halos of Wide-field Infrared Survey Explorer-selected Obscured and Unobscured Quasars: Evidence for Evolution.* ApJ, **946**(1) (2023), 27. 2302.00690.

Phillipps, S., Fong, R., Ellis, R.S., et al. *Correlation analysis deep galaxy samples - 1. Techniques with applications to a two-colour sample.* MNRAS, **182** (1978), 673.

Pier, J.R., Munn, J.A., Hindsley, R.B., et al. *Astrometric Calibration of the Sloan Digital Sky Survey.* The Astronomical Journal, **125**(3) (2003), 1559. URL https://doi.org/10.1086/346138.

Planck Collaboration, Abergel, A., Ade, P.A.R., et al. *Planck 2013 results. XI. All-sky model of thermal dust emission.* A&A, **571** (2014), A11. 1312.1300.

Planck Collaboration, Aghanim, N., Akrami, Y., et al. *Planck 2018 results. VIII. Gravitational lensing.* arXiv e-prints (2018), arXiv:1807.06210. 1807.06210.

Planck Collaboration, Aghanim, N., Akrami, Y., et al. *Planck 2018 results. VI. Cosmological parameters.* A&A, **641** (2020), A6. 1807.06209.

Predehl, P., Andritschke, R., Arefiev, V., et al. *The eROSITA X-ray telescope on SRG.* A&A, **647** (2021), A1. 2010.03477.

Press, W.H., Schechter, P. *Formation of Galaxies and Clusters of Galaxies by Self-Similar Gravitational Condensation.* ApJ, **187** (1974), 425.

Raichoor, A., Moustakas, J., Newman, J.A., et al. *Target Selection and Validation of DESI Emission Line Galaxies.* arXiv e-prints (2022), arXiv:2208.08513. 2208.08513.

Ramos Almeida, C., Ricci, C. *Nuclear obscuration in active galactic nuclei.* Nature Astronomy, **1** (2017), 679. 1709.00019.

Richard, J., Kneib, J.P., Blake, C., et al. *4MOST Consortium Survey 8: Cosmology Redshift Survey (CRS).* The Messenger, **175** (2019), 50. 1903.02474.

Richards, G.T., Nichol, R.C., Gray, A.G., et al. *Efficient Photometric Selection of Quasars from the Sloan Digital Sky Survey: 100,000 $z < 3$ Quasars from Data Release One.* ApJS, **155**(2) (2004), 257. astro-ph/0408505.

Riess, A.G., Yuan, W., Macri, L.M., et al. *A Comprehensive Measurement of the Local Value of the Hubble Constant with 1 km s^{-1} Mpc^{-1} Uncertainty from the Hubble Space Telescope and the SH0ES Team.* ApJ, **934**(1) (2022), L7. 2112.04510.

Robertson, H.P. *Kinematics and World-Structure.* ApJ, **82** (1935), 284.

Ross, N.P., Myers, A.D., Sheldon, E.S., et al. *The SDSS-III Baryon Oscillation Spectroscopic Survey: Quasar Target Selection for Data Release Nine.* ApJS, **199**(1) (2012), 3. 1105.0606.

Ross, R.R., Fabian, A.C. *A comprehensive range of X-ray ionized-reflection models.* MNRAS, **358**(1) (2005), 211. astro-ph/0501116.

Rubin, V.C., Thonnard, N., Ford, W. K., J. *Extended rotation curves of high-luminosity spiral galaxies. I. The angle between the rotation axis of the nucleus and the outer disk of NGC 3672.* ApJ, **217** (1977), L1.

Ryden, B. *Introduction to Cosmology* (2016).

Sadeh, I., Abdalla, F.B., Lahav, O. *ANNz2: Photometric Redshift and Probability Distribution Function Estimation using Machine Learning.* PASP, **128**(968) (2016), 104502. 1507.00490.

Sánchez, C., Carrasco Kind, M., Lin, H., et al. *Photometric redshift analysis in the Dark Energy Survey Science Verification data.* MNRAS, **445**(2) (2014), 1482. 1406.4407.

Schlafly, E.F., Meisner, A.M., Green, G.M. *The unWISE Catalog: Two Billion Infrared Sources from Five Years of WISE Imaging.* ApJS, **240**(2) (2019), 30. 1901.03337.

Schmidt, M. *3C 273 : A Star-Like Object with Large Red-Shift.* Nature, **197**(4872) (1963), 1040.

Schmidt, M. *Large Redshifts of Five Quasi-Stellar Sources.* ApJ, **141** (1965), 1295.

Schneider, D.P., Hall, P.B., Richards, G.T., et al. *The Sloan Digital Sky Survey Quasar Catalog. IV. Fifth Data Release.* AJ, **134**(1) (2007), 102. 0704.0806.

Scranton, R., Ménard, B., Richards, G.T., et al. *Detection of Cosmic Magnification with the Sloan Digital Sky Survey.* ApJ, **633**(2) (2005), 589. astro-ph/0504510.

Seldner, M., Peebles, P.J.E. *Statistical analysis of catalogs of extragalactic objects. XI. Evidence of correlation of QSOs and Lick galaxy counts.* ApJ, **227** (1979), 30.

Shakura, N.I., Sunyaev, R.A. *Black holes in binary systems. Observational appearance.* A&A, **24** (1973), 337.

Shankar, F., Weinberg, D.H., Miralda-Escudé, J. *Self-Consistent Models of the AGN and Black Hole Populations: Duty Cycles, Accretion Rates, and the Mean Radiative Efficiency.* ApJ, **690**(1) (2009), 20. 0710.4488.

Shanks, T., Ansarinejad, B., Bielby, R.M., et al. *The nature of sub-millimetre galaxies I: a comparison of AGN and star-forming galaxy SED fits.* MNRAS, **505**(1) (2021), 1509. 2010.07934.

Shanks, T., Croom, S.M., Fine, S., et al. *Do all QSOs have the same black hole mass?* MNRAS, **416**(1) (2011), 650. 1105.2547.

Shanks, T., Metcalfe, N., Chehade, B., et al. *The VLT Survey Telescope ATLAS.* MNRAS, **451**(4) (2015), 4238. 1502.05432.

Sharp, R., Saunders, W., Smith, G., et al. *Performance of AAOmega: the AAT multi-purpose fiber-fed spectrograph.* In I.S. McLean, M. Iye, editors, *Society of Photo-Optical Instrumentation Engineers (SPIE) Conference Series*, volume 6269 of *Society of Photo-Optical Instrumentation Engineers (SPIE) Conference Series* (2006), page 62690G. astro-ph/0606137.

Shen, Y., Greene, J.E., Ho, L.C., et al. *The Sloan Digital Sky Survey Reverberation Mapping Project: No Evidence for Evolution in the M• -σ_* Relation to z$\sim$ 1.* ApJ, **805**(2) (2015), 96. 1502.01034.

Shen, Y., Grier, C.J., Horne, K., et al. *The Sloan Digital Sky Survey Reverberation Mapping Project: Improving Lag Detection with an Extended Multiyear Baseline.* ApJ, **883**(1) (2019), L14. 1908.00027.

Smee, S.A., Gunn, J.E., Uomoto, A., et al. *The Multi-object, Fiber-fed Spectrographs for the Sloan Digital Sky Survey and the Baryon Oscillation Spectroscopic Survey.* AJ, **146**(2) (2013), 32. 1208.2233.

Taylor, K., Bailey, J., Wilkins, T., et al. *Design-Led Software Strategy for the 2dF Survey Spectrograph.* In G.H. Jacoby, J. Barnes, editors, *Astronomical Data Analysis Software and Systems V*, volume 101 of *Astronomical Society of the Pacific Conference Series* (1996), page 195.

Taylor, M.B. *TOPCAT & STIL: Starlink Table/VOTable Processing Software.* In P. Shopbell, M. Britton, R. Ebert, editors, *Astronomical Data Analysis Software and Systems XIV*, volume 347 of *Astronomical Society of the Pacific Conference Series* (2005), page 29.

Tempel, E., Tuvikene, T., Muru, M.M., et al. *An optimized tiling pattern for multiobject spectroscopic surveys: application to the 4MOST survey.* MNRAS, **497**(4) (2020), 4626. 2007.03307.

Timlin, J.D., Ross, N.P., Richards, G.T., et al. *SpIES: The Spitzer IRAC Equatorial Survey.* ApJS, **225**(1) (2016), 1. 1603.08488.

Tinker, J.L., Robertson, B.E., Kravtsov, A.V., et al. *The Large-scale Bias of Dark Matter Halos: Numerical Calibration and Model Tests.* ApJ, **724**(2) (2010), 878. 1001.3162.

Tyson, J.A., Valdes, F., Wenk, R.A. *Detection of Systematic Gravitational Lens Galaxy Image Alignments: Mapping Dark Matter in Galaxy Clusters.* ApJ, **349** (1990), L1.

Valdes, F., Gruendl, R., DES Project. *The DECam Community Pipeline.* In N. Manset, P. Forshay, editors, *Astronomical Data Analysis Software and Systems XXIII*, volume 485 of *Astronomical Society of the Pacific Conference Series* (2014), page 379.

Vallbé Mumbrú, M. *The evolution of galaxies and AGN from deep x-ray and optical surveys.* Ph.D. thesis, Durham University (2004).

Vestergaard, M., Fan, X., Tremonti, C.A., et al. *Mass Functions of the Active Black Holes in Distant Quasars from the Sloan Digital Sky Survey Data Release 3.* ApJ, **674**(1) (2008), L1. 0801.0243.

Walker, A.G. *On Milne's Theory of World-Structure.* Proceedings of the London Mathematical Society, **42** (1937), 90.

Walsh, D., Carswell, R.F., Weymann, R.J. *0957+561 A, B: twin quasistellar objects or gravitational lens?* Nature, **279** (1979), 381.

Wang, Y., Brunner, R.J., Dolence, J.C. *The SDSS galaxy angular two-point correlation function.* MNRAS, **432**(3) (2013), 1961. 1303.2432.

Williams, L.L.R., Irwin, M. *Angular correlations between LBQS and APM: weak lensing by the large-scale structure.* MNRAS, **298**(2) (1998), 378. astro-ph/9804032.

Wright, E.L., Eisenhardt, P.R.M., Mainzer, A.K., et al. *The Wide-field Infrared Survey Explorer (WISE): Mission Description and Initial On-orbit Performance.* AJ, **140** (2010), 1868. 1008.0031.

Yang, Q., Wu, X.B., Fan, X., et al. *Quasar Photometric Redshifts and Candidate Selection: A New Algorithm Based on Optical and Mid-infrared Photometric Data.* AJ, **154**(6) (2017), 269. 1710.09155.

Yèche, C., Palanque-Delabrouille, N., Claveau, C.A., et al. *Preliminary Target Selection for the DESI Quasar (QSO) Sample.* Research Notes of the American Astronomical Society, **4**(10) (2020), 179. 2010.11280.

York, D.G., Adelman, J., Anderson, John E., J., et al. *The Sloan Digital Sky Survey: Technical Summary.* AJ, **120**(3) (2000), 1579. astro-ph/0006396.

Yuan, H.B., Liu, X.W., Xiang, M.S. *Empirical extinction coefficients for the GALEX, SDSS, 2MASS and WISE passbands.* MNRAS, **430**(3) (2013), 2188. 1301.1427.

Zehavi, I., Zheng, Z., Weinberg, D.H., et al. *Galaxy Clustering in the Completed SDSS Redshift Survey: The Dependence on Color and Luminosity.* ApJ, **736**(1) (2011), 59. 1005.2413.

Zheng, Z., Berlind, A.A., Weinberg, D.H., et al. *Theoretical Models of the Halo Occupation Distribution: Separating Central and Satellite Galaxies.* ApJ, **633**(2) (2005), 791. astro-ph/0408564.

Zheng, Z., Coil, A.L., Zehavi, I. *Galaxy Evolution from Halo Occupation Distribution Modeling of DEEP2 and SDSS Galaxy Clustering.* ApJ, **667**(2) (2007), 760. astro-ph/0703457.

Zheng, Z., Weinberg, D.H. *Breaking the Degeneracies between Cosmology and Galaxy Bias.* ApJ, **659**(1) (2007), 1. astro-ph/0512071.

Zheng, Z., Zehavi, I., Eisenstein, D.J., et al. *Halo Occupation Distribution Modeling of Clustering of Luminous Red Galaxies.* ApJ, **707**(1) (2009), 554. 0809.1868.

Zhou, R., Dey, B., Newman, J.A., et al. *Target Selection and Validation of DESI Luminous Red Galaxies.* arXiv e-prints (2022), arXiv:2208.08515. 2208.08515.

Zwicky, F. *Die Rotverschiebung von extragalaktischen Nebeln.* Helvetica Physica Acta, **6** (1933), 110.